

**DIRECT NUMERICAL SIMULATION OF SOOT  
FORMATION AND TRANSPORT IN  
TURBULENT NONPREMIXED  
ETHYLENE FLAMES**

by

David Owen Lignell

A dissertation submitted to the faculty of  
The University of Utah  
in partial fulfillment of the requirements for the degree of

Doctor of Philosophy

Department of Chemical Engineering

The University of Utah

May 2008

Copyright © David Owen Lignell 2008

All Rights Reserved

THE UNIVERSITY OF UTAH GRADUATE SCHOOL

**SUPERVISORY COMMITTEE APPROVAL**

of a dissertation submitted by

David Owen Lignell

This dissertation has been read by each member of the following supervisory committee and by majority vote has been found to be satisfactory.

---

Chair: Philip J. Smith

---

Jacqueline H. Chen

---

Eric G. Eddings

---

Jost O. L. Wendt

---

Milind D. Deo

THE UNIVERSITY OF UTAH GRADUATE SCHOOL

**FINAL READING APPROVAL**

To the Graduate Council of the University of Utah:

I have read the dissertation of David Owen Lignell in its final form and have found that (1) its format, citations, and bibliographic style are consistent and acceptable; (2) its illustrative materials including figures, tables, and charts are in place; and (3) the final manuscript is satisfactory to the Supervisory Committee and is ready for submission to The Graduate School.

\_\_\_\_\_  
Date

\_\_\_\_\_  
Philip J. Smith  
Chair, Supervisory Committee

Approved for the Major Department

\_\_\_\_\_  
JoAnn S. Lighty  
Chair/Dean

Approved for the Graduate Council

\_\_\_\_\_  
David S. Chapman  
Dean of The Graduate School

## ABSTRACT

Combustion is central to society and accounts for the majority of the world's energy production. Soot formation, transport, and emission from turbulent flames are an important process in nonpremixed combustion. Soot is a major air pollutant with adverse health effects; its emission reduces combustion efficiencies associated with unburned fuel; and soot interacts strongly with the composition and temperature fields of flames, contributing to the bulk of radiative heat transfer. Simulation of combustion is an important and emerging discipline that compliments theoretical and experimental investigations and can provide fundamental insight into turbulent combustion environments and aid in engineering design of practical equipment. Simulations of practical combustion environments cannot fully resolve all flow and chemical phenomena due to the wide range of timescales and lengthscales present and must rely on models to capture the effects of unresolved turbulent transport and turbulence-chemistry interactions.

Very little is known about soot formation in turbulent flames due to the difficulty of experimental measurements and the computational cost of simulation. Direct numerical simulation (DNS) resolves all relevant flow and chemical structures in turbulent flames, requiring no turbulence closure models. DNS of soot formation with realistic combustion chemistry and soot formation is presented in this dissertation. A series of increasingly complex flow configurations is investigated including one-dimensional relaxing diffusion flames, two-dimensional mixing layers and decaying turbulence simulations, and a three-dimensional temporally evolving jet flame. A reduced ethylene mechanism consisting of 19 transported species is coupled to a four-step soot model using the method of moments.

The DNS are used to quantify soot formation and transport in turbulent flames. The proximity of soot to a flame is important, as this impacts the soot reaction and radiation rates. Differential diffusion between soot and the mixture fraction is very important. Multidimensional flame dynamic effects including flame curvature are shown to influence the direction of soot transport relative to a flame. The DNS provide a database by which turbulent combustion models may be validated and developed. Soot formation in the laminar flamelet and conditional moment closure models is examined.

To my wife Jennifer and to our sons Isaac, Andrew, and Luke

# CONTENTS

<b>ABSTRACT</b> .....	<b>iv</b>
<b>LIST OF TABLES</b> .....	<b>ix</b>
<b>ACKNOWLEDGEMENTS</b> .....	<b>x</b>
<b>CHAPTERS</b>	
<b>1. INTRODUCTION</b> .....	<b>1</b>
1.1 RANS and LES Simulation .....	6
1.2 Combustion Modeling .....	8
1.2.1 Direct PDF Methods .....	9
1.2.2 Equilibrium Models .....	9
1.2.3 Flamelet Models .....	10
1.2.4 Unsteady Flamelet Models .....	12
1.2.5 CMC Models .....	12
1.2.6 Progress Variable Approaches .....	13
1.2.7 Other Combustion Models .....	14
1.3 Review of Turbulent Simulations with Soot Formation .....	15
1.4 Direct Numerical Simulation .....	17
1.4.1 Review of DNS of Turbulent Combustion .....	19
<b>2. DNS FORMULATION, MODELS, AND NUMERICS</b> .....	<b>23</b>
2.1 Grid Resolution .....	27
2.2 Parallel Scaling .....	30
2.3 Ethylene Chemical Mechanism .....	34
2.3.1 Reduced Mechanism Description .....	34
2.3.2 Computational Costs and Speedup .....	35
2.3.3 Mechanism Validations .....	37
2.3.3.1 Ignition Tests .....	38
2.3.3.2 PSR Extinction .....	38
2.3.3.3 Laminar Premixed Flame Speed .....	40
2.3.3.4 Opposed Jet Diffusion Flame Comparisons .....	41
2.3.4 One-Step Ethylene Mechanism .....	45
2.4 Soot Model .....	48
2.5 The Method of Moments .....	52
2.5.1 Nucleation .....	53
2.5.2 Growth .....	54
2.5.3 Coagulation .....	57
2.5.4 Closure Approaches .....	61

2.5.4.1	Monodispersed Size Distribution . . . . .	62
2.5.4.2	Lognormal Distribution . . . . .	64
2.5.4.3	Lognormal Plus Power Law Distribution . . . . .	67
2.5.4.4	Quadrature Method of Moments . . . . .	67
2.5.4.5	Verification of Quadrature Implementation . . . . .	69
2.5.5	Implementation and Results . . . . .	71
2.5.5.1	Moment Scaling . . . . .	73
2.5.5.2	Comparison of the Number of Moments . . . . .	74
2.5.5.3	Effect of the Approximate Coagulation Source . . . . .	76
2.5.5.4	Sensitivity to Source Rates . . . . .	77
2.5.5.5	PSR Tests . . . . .	78
<b>3.</b>	<b>ONE-DIMENSIONAL SIMULATIONS . . . . .</b>	<b>81</b>
3.1	Configuration . . . . .	81
3.1.1	Flame Initialization . . . . .	82
3.2	Results . . . . .	89
3.2.1	Thermophoretic Diffusion Effects . . . . .	91
3.2.2	Radiative Effects . . . . .	95
3.2.3	Comparison of Gas-Phase Chemical Mechanisms . . . . .	98
<b>4.</b>	<b>TWO-DIMENSIONAL MIXING LAYER SIMULATIONS . . . . .</b>	<b>102</b>
4.1	Introduction . . . . .	102
4.2	Configuration and Initialization . . . . .	104
4.2.1	Simulation Parameters . . . . .	106
4.3	Results . . . . .	107
4.3.1	Mixing Layer Structure . . . . .	107
4.3.1.1	Mixture Fraction Profiles . . . . .	108
4.3.1.2	Flame Location . . . . .	110
4.3.2	Soot Formation and Transport . . . . .	111
<b>5.</b>	<b>TWO-DIMENSIONAL TURBULENT FLAMES . . . . .</b>	<b>117</b>
5.1	Introduction . . . . .	117
5.2	Configuration and Initial Conditions . . . . .	119
5.3	Flame Analysis . . . . .	122
5.4	Results . . . . .	125
5.4.1	Overview and Observations . . . . .	125
5.4.2	Global Statistics . . . . .	128
5.4.3	Flame Displacement Velocity . . . . .	129
5.4.4	Flame Normals . . . . .	132
5.4.5	Soot-Flame Breakthrough . . . . .	135
5.4.6	Normal Statistics . . . . .	139
5.4.7	Temporal Evolution of Mean Flame Quantities . . . . .	144
5.4.8	Temporal Evolution of Total Soot and Radiation . . . . .	146
5.4.9	Soot Transport . . . . .	147
5.5	Discussion . . . . .	149

<b>6.</b>	<b>THREE-DIMENSIONAL ETHYLENE JET SIMULATION</b>	<b>153</b>
6.1	Initial Conditions and Configuration	154
6.2	Results	156
6.2.1	Overview	156
6.2.2	Conditional Means and Scatter	158
6.2.2.1	Scalar Dissipation Rate	162
6.2.3	Mixture Fraction PDF and Soot Transport	164
6.2.4	Mixture Fraction Dynamics and Soot-Flame Diffusion	167
6.2.5	The Flame Displacement Velocity and Its Terms	169
6.2.6	Thermophoretic Diffusion Velocity	174
6.3	Discussion	175
<b>7.</b>	<b>FLAMELET AND CMC MODELING</b>	<b>178</b>
7.1	Laminar Flamelets with Soot	178
7.1.1	Soot Flamelet Formulation	179
7.1.2	Results and Discussion	181
7.2	Quantification of the Temperature Flamelet Equation	186
7.3	A-Priori Analysis of CMC Modeling	190
7.3.1	CMC Formulation	191
7.3.2	Results	195
7.3.2.1	Soot Mass Fraction Equation	195
7.3.2.2	Gaseous Species	198
<b>8.</b>	<b>CONCLUSIONS AND FUTURE WORK</b>	<b>201</b>
8.1	DNS of Soot Formation and Transport	201
8.1.1	One-Dimensional Simulations	201
8.1.2	Two-Dimensional Mixing Layer Simulations	201
8.1.3	Two-Dimensional Decaying Turbulence Simulations	202
8.1.4	Three-Dimensional Temporal Jet Simulation	203
8.2	Flamelet and CMC Modeling	204
8.3	Future Work	205
<b>APPENDICES</b>		
<b>A.</b>	<b>FINITE DIFFERENCE PROGRAM</b>	<b>207</b>
<b>B.</b>	<b>PRODUCT DIFFERENCE ALGORITHM</b>	<b>209</b>
<b>C.</b>	<b>MIXING LAYER INSTABILITY</b>	<b>210</b>
<b>D.</b>	<b>DERIVATION OF THE CMC EQUATIONS</b>	<b>219</b>
<b>REFERENCES</b>		<b>226</b>

## LIST OF TABLES

2.1	First-order derivative finite difference coefficients. . . . .	29
2.2	Parallel scaling results. . . . .	33
2.3	Fuel and oxidizer stream compositions. . . . .	38
4.1	Simulation parameters of mixing layer Case 1. . . . .	107
4.2	Comparison of bulk sooting properties of Case 1 with two experimental configurations. Case 1 is at 10 ms. . . . .	115
5.1	Simulation parameters and timescales. . . . .	121
6.1	Temporal ethylene jet simulation parameters. . . . .	155
6.2	Positive fraction of stoichiometric surface quantities. . . . .	172

## ACKNOWLEDGEMENTS

This work could not have been performed without the support of my family, advisors, and friends. I express sincere appreciation to my two advisors Professor Philip J. Smith and Dr. Jaqueline H. Chen. Professor Smith's enthusiasm and excitement and optimism cannot be overstated and have been a real inspiration to me. I am very grateful to Dr. Chen for her support and her attention to detail, technical insight, and many enlightening discussions. The opportunity to do graduate research at the Combustion Research Facility (CRF) has been a real pleasure, and I thank my advisors for providing this unique experience. I want to thank the many students, postdocs, and staff members I have been able to work with and learn from and who have been my friends.

The financial support of many organizations is greatly appreciated. Thanks to Sandia for providing my internship, the University of Utah College of Engineering for the Wayne Brown Fellowship, and the John Zink Company for their generous scholarship support.

Most of all I thank my wife Jennifer for her love and devotion and my sons Isaac, Andrew, and Luke. The quiet sacrifice of my family is undeserved and I will always be indebted to them.

This work was supported by the U.S. Department of Energy, Office of Basic Energy Sciences, Division of Chemical Sciences, Geosciences, and Biosciences. Simulations were performed at Sandia National Laboratories on the Thunderbird and Redstorm supercomputers. Sandia National Laboratories is a multiprogram laboratory operated by Sandia Corporation, a Lockheed Martin Company, for the United States Department of Energy under Contract DE-AC04-94-AL85000.

# CHAPTER 1

## INTRODUCTION

Combustion of fossil fuels and their derivatives is the single most important source of energy in society. We light our homes, drive our cars, cook our food, and develop materials and goods with the energy of the flame. In 2006, approximately 85% of the energy consumed in the United States was from combustion sources [1]. Nearly all transportation is by combustion engines, be it diesel, spark ignition, or gas turbines. Sixty-nine percent of U.S. energy consumption for electricity generation derives from the burning of coal and natural gas [1].

The importance of combustion has prompted intense research efforts to understand and control the fundamental and applied aspects of flames and combustion devices. Fossil fuels are limited commodities, and the design of efficient engines, burners, and boilers saves fuel costs and reduces emissions of greenhouse gases (e.g.,  $\text{CO}_2$ ) and air pollutants such as unburned hydrocarbons, sulfur oxides, nitrogen oxides, carbon monoxide, and particulate matter.

Combustion is a very complicated process involving a wide variety of simultaneous and interacting physical phenomenon including turbulent fluid dynamics, thermodynamics, convective and radiative heat transfer, multiphase flow, and complex chemical kinetics involving tens to thousands of chemical species. These phenomena occur on lengthscales and timescales that vary over many orders of magnitude: from nanoseconds for fast chemical reaction of radical species, to tens of milliseconds for pollutant formation, to seconds for large-scale flow structures. These processes are highly nonlinear, complicating model development and application.

Combustion generally occurs as nonpremixed flames, as premixed flames, or as a flameless mode [2]. Most flames are turbulent because of the high Reynolds numbers of flows in combustion devices, but more practically, because turbulence enhances mixing of fuel and oxidizer enabling large combustion heat release rates in a small volume. In addition, most flames are nonpremixed, where fuel and oxidizer are introduced in separate

streams. The streams mix via diffusive transport, and a thin reaction zone exists at the location where fuel and oxidizer are in stoichiometric proportions. This stream separation has the advantage of allowing greater control of the flame, while avoiding safety concerns associated with flashback and unwanted spontaneous ignition as may occur in premixed flames (where fuel and oxidizer are mixed to flammable proportions prior to entering the combustion environment). Conversely, nonpremixed flames have higher peak temperatures since the flame exists at a stoichiometric mixture, which tends to maximize the formation of pollutants, such as  $\text{NO}_x$ . In addition, as the fuel approaches the flame front in the absence of oxygen, it pyrolyzes and forms soot and other products of incomplete combustion.

Soot is a major component of most nonpremixed hydrocarbon flames and plays an important role in practical aspects of a flame. Soot accounts for a flame's luminosity, and for a large fraction of the radiative heat transfer from a flame or fire to surrounding objects. This heat transfer is desirable in steam boilers and other heating applications but is also a mechanism for fire spread in wildfires or other fire hazards. Soot formation is a product of the chemical industry with uses such as tire filler and printer toner [3]. Soot emission from flames is also an air pollutant and health hazard. Many fine particulates in the atmosphere of a size less than  $2.5 \mu\text{m}$ , (termed PM 2.5) are formed from hydrocarbon combustion. When breathed, these particles are able to penetrate deeply into the lungs. Many scientific studies have been performed linking exposure to fine particulates to health problems including aggravated asthma, chronic bronchitis, decreased lung function including shortness of breath, and even premature death. In addition, fine particulates, including soot, result in haze and reduced visibility in the atmosphere. An extensive review of the health and environmental effects of particulate matter is presented in the 2004 United States Environmental Protection Agency report on "Air Quality Criteria for Particulate Matter" [4].

Soot is formed on the fuel-rich side of a nonpremixed flame where oxidizing species concentrations are low. Soot exists as a nominally solid particulate phase with a particle size distribution (PSD). The soot formation process is complex and is the subject of ongoing research. Soot is nucleated as polyaromatic hydrocarbons (PAH) are formed and grow mainly via addition of acetylene and other molecules. As a particulate phase, soot has low molecular diffusivity, and the transport of soot occurs mainly via convection and thermophoretic diffusion (driven by a temperature gradient). As soot is transported

towards or away from a flame, the temperature and composition of the surrounding gases change. These impact the growth rate of soot, and hence its concentration and composition. The radiative emission rate of soot directly depends on its temperature and concentration. If soot is transported from the fuel-rich growth regions across the flame to fuel-lean regions, the high temperature and presence of oxidizing species burn the soot. This process is observed in laminar candle flames in which soot is formed on the inside of the hollow flame cone and transported upwards where it crosses through the flame and is oxidized. In some cases, soot is incompletely oxidized, or the flame partially extinguishes, and soot is observed to break through the flame in what are known as soot wings, leading to soot emission into the cool, surrounding environment.

Typical soot volume fractions in atmospheric nonpremixed flames are on the order of 1 ppmv (part per million, by volume) [5, 6, 7], which corresponds to a mass fraction of approximately 1%, (or 5% of the fuel mass). Concentrations in diesel engines and fires can be significantly higher. The complex formation chemistry of soot results in formation timescales that are relatively long compared to those responsible for most of the heat release rate of flames. These formation timescales overlap the diffusive and convective timescales in laminar and turbulent flames. This poses a significant challenge for the modeling and simulation of sooting flames because the soot cannot simply be decoupled from the fluid flow, as is often done for fast combustion chemistry. Unlike passive pollutant species, such as  $\text{NO}_x$ , soot interacts strongly with the flame temperature field through radiation, and with the composition field through reaction with intermediate combustion products. Hence, soot fields must be simulated in conjunction with the reacting flow.

Several problems exist in our current understanding of turbulent sooting flames. Large-scale fires are known to emit large quantities of smoke, which can shield surrounding objects from the radiative heat transfer of a fire. The exact mechanism for this process is not fully understood at the present time, and the ability to simulate such a process accurately is not possible. More generally, very little at all is known about soot-flame interactions in turbulent flows. Turbulent flows are unsteady (by definition) and involve complex flame-flow interactions that wrinkle and contort flame surfaces. These dynamic fluid motions result in a range of flame curvatures and strain rates that directly impact soot formation rates and transport into and out of reaction zones. A detailed view of the soot-flame-flow processes that occur in turbulent flames, along with the statistics of these processes, is needed to enable the development and validation of models for turbulent

soot formation.

Most detailed analyses of sooting flames have been confined to relatively simple, canonical flow configurations such as perfectly stirred reactors [8], one-dimensional freely propagating premixed flames [9], and laminar diffusion flames [5, 10, 11, 12], which have allowed detailed experimental investigation and comparison to computational models. These configurations are ideal for model development and validation. However, the vast majority of practical situations are turbulent. Experiments of turbulent sooting flames have provided mainly averaged quantities of soot and temperature fields, but have been unable to capture temporally and spatially-resolved scalar fields [13, 14, 15, 7].

Modeling and simulation of turbulent nonpremixed flames are becoming more and more relevant to practical engineering design of combustion equipment and to the evaluation and characterization of fire hazards. Simulation is complementary to experimental investigation and can provide insights that are either not possible or not economical to obtain experimentally. However, the fidelity of simulation depends upon the quality of the underlying algorithms that define it. Hence, in order to apply simulation with confidence, an understanding of the relevant physics is important.

Due to computational costs, simulations of practical turbulent configurations have been confined to Reynolds averaged Navier-Stokes (RANS) and large eddy simulation (LES) approaches. RANS and LES cannot resolve all of the timescales and lengthscales present in a flow and must rely on subgrid models for closure of mean and filtered terms representing unresolved turbulent transport that appear in the governing equations. Turbulence-chemistry interactions are also important and require mixing and reaction models for simulation of practical configurations.

Direct numerical simulation (DNS) is a computational approach in which all lengthscales and timescales are fully resolved. DNS requires no turbulence models and utilizes highly accurate numerical methods to minimize computational error. As a result, computational costs are very high for DNS, and application is presently limited to canonical turbulent configurations at moderate Reynolds number (i.e., in combustion, small domain sizes). However, DNS provides precise, detailed information of a chemically reacting flow including complete spatial and temporal fields of temperature, pressure, composition, and velocity, and may be used in lieu of experimental data. It is noted that DNS results are direct in the sense that all of the turbulent scales arising from solution to the governing transport equations are resolved. However, the accuracy of the simulation depends upon

the accuracy of the chemical mechanism and molecular transport models for heat and mass transfer employed.

This dissertation presents results of DNS applied to soot formation in turbulent nonpremixed ethylene flames. DNS of turbulent, nonpremixed, sooting flames is an original contribution to the field of combustion simulation. The primary objective of this work is to increase fundamental understanding of soot formation and transport in turbulent flames and to provide data for validation and development of combustion models that can be used in practical configurations. The remainder of this chapter presents a discussion of RANS and LES simulation approaches, a review of simulations with soot formation, and a review of DNS simulation of reacting flows. Chapter 2 describes the DNS formulation and the combustion chemistry and soot model applied. A series of simulations has been performed of increasing complexity:

- One-dimensional simulations of unsteady, relaxing diffusion flames. This configuration allows investigation of fundamental processes of soot-flame interaction in a simple flowfield with few competing and complicating transport effects.
- Two-dimensional simulations of a Kelvin-Helmholtz instability representing the rollup of a single vortex-eddy. This flow is a fundamental unit in more complex turbulence and arises in many practical configurations at the interface between shear layers. The configuration highlights the interaction between flame and fluid structures as well as the importance of soot location in a flame.
- Two-dimensional simulations of decaying isotropic turbulence that lend insight into soot-flame interaction in a simplified turbulent flow allowing realistic timescales and transport processes.
- Three-dimensional simulation of soot formation in a temporally evolving jet flame, providing statistical data describing flame and soot dynamics.

These simulation results are presented in Chapters 3-6, respectively, followed by a discussion of modeling results obtained, notably the laminar flamelet, and conditional moment closure models, presented in Chapter 7. Finally, conclusions and opportunities for future research directions are given in Chapter 8.

## 1.1 RANS and LES Simulation

RANS is widely used in commercial engineering applications as a tool to aid in the design and development of a variety of equipment—everything from airplanes to power plant boilers. The RANS equations are obtained from the Navier-Stokes equations by writing instantaneous flow variables (such as velocity) as the sum of a local mean value and a fluctuation, where for a statistically steady flow

$$\phi(x, t) = \bar{\phi}(x) + \phi'(x, t). \quad (1.1)$$

Here,  $\bar{\phi}$  is the time-average of a variable,  $\phi$ , at a point  $x$ , and  $\phi'(x, t)$  is its fluctuation about the mean value, whose time-average is zero. The time-averaged variable  $\bar{\phi}$  is defined as

$$\bar{\phi}(x) = \lim_{\tau \rightarrow \infty} \frac{1}{\tau} \int_0^{\tau} \phi(x, t) dt, \quad (1.2)$$

where  $\tau$  is much larger than the largest timescale associated with the turbulent flow field. The filtering operation of Eq. (1.2) removes small timescales so that they do not need to be resolved by the simulation. The RANS equations appear very similar to the Navier-Stokes equations. In RANS, the average values of flow variables are computed on a coarse grid, and the effects of the unresolved turbulent motions are accounted for through extra terms containing the so-called Reynolds stresses in the governing equations. These terms must be modeled, and the RANS equations are *closed* by writing the Reynolds stresses in terms of the mean flow components. RANS suffers from the fact that no closure model for the Reynolds stresses can give accurate results for all flows because universally applicable closure models do not exist. Hence model constants usually have to be tuned to fit a particular flow [16].

In contrast to RANS, the LES equations are derived by applying a spatial filter to the governing flow equations. The smallest turbulent eddies and their associated timescales are filtered out, while the large, energy containing eddies are resolved. LES has the advantage that closure models for terms arising from the unresolved scales are less dependent upon the flow configuration due to scale similarity of smaller-scale turbulent eddies [17]. The spatial filter applied is of the form [18]

$$\bar{f}(\mathbf{x}) = \int_D f(\mathbf{x}') G(\mathbf{x} - \mathbf{x}') d\mathbf{x}'. \quad (1.3)$$

Here, the integration is carried out over the whole domain, and  $G$  is a filter function with a characteristic filter width  $\Delta$ . Common functional forms for  $G$  are the tophat, Gaussian, and sharp Fourier cutoff filter [18]. Application of the tophat filter is equivalent to simply taking the average value of  $f$  over the filter width  $\Delta$ . Figure 1.1 illustrates the filtering approach. On the left of the figure, an unresolved turbulent field in each grid cell is represented by its filtered (average) value at a given point. On the right, a tophat filter is applied to a random signal. As the filter width increases, the signal becomes smoother, and only larger structures are resolved.

Equation 1.3 is applied to the Navier-Stokes equations to obtain the LES equations, which resemble the original equations but with an additional term that must be closed. The incompressible, constant property (e.g., viscosity) LES equations for continuity and momentum are, respectively,

$$\frac{\partial \bar{v}_i}{\partial x_i} = 0, \quad (1.4)$$

$$\frac{\partial \bar{v}_i}{\partial t} + \frac{\partial(\bar{v}_i \bar{v}_j)}{\partial x_j} = -\frac{1}{\rho} \frac{\partial \bar{P}}{\partial x_i} + \nu \frac{\partial^2 \bar{v}_i}{\partial x_j \partial x_j} - \frac{\partial \tau_{ij}^{sgs}}{\partial x_j}. \quad (1.5)$$

Here,  $\tau_{ij}^{sgs} = \overline{v_i v_j} - \bar{v}_i \bar{v}_j$  is a new unclosed term that represents momentum flux due to unresolved turbulent inertia. The RANS equations have a similar term. Index notation is used in these equations: subscripts  $i$  and  $j$  refer to orthogonal coordinate directions.

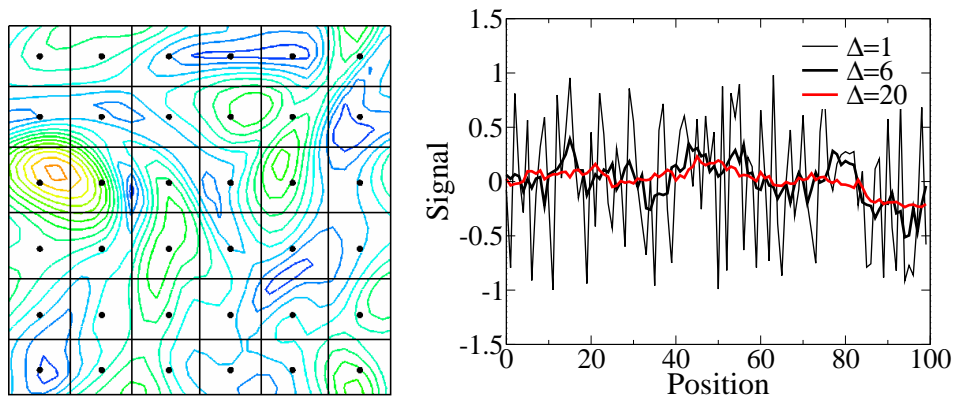


**Figure 1.1.** Illustration of LES filtering.

A repeated subscript on any given term implies summation, and a single occurrence of a subscript in a term implies a vector component [19].

## 1.2 Combustion Modeling

Incorporation of combustion chemistry into a flow simulation significantly increases the complexity in two important ways. First, combustion chemistry requires consideration of many chemical species, which must either be transported or otherwise accounted for. Combustion reactions involve small timescales (e.g., among radical species) that do not overlap with flow timescales, resulting in numerical stiffness. Solving an additional transport equation for each chemical species would severely limit a simulation. Reducing this chemical load by reducing the number of transport equations to be solved is termed *reaction modeling*. Second, unresolved turbulence-chemistry interactions arising from fluctuations of scalar fields are significant and must be modeled. The Favre (density weighted) averaged [20] transport equation for a reactive scalar  $\phi$  is

$$\frac{\partial(\bar{\rho}\tilde{\phi})}{\partial t} + \frac{\partial(\bar{\rho}\tilde{v}_i\tilde{\phi})}{\partial x_i} = -\frac{\partial\bar{j}_\phi}{\partial x_i} - \frac{\partial(\bar{\rho}\widetilde{\phi''v_i''})}{\partial x_i} + \bar{\omega}_\phi. \quad (1.6)$$

The fourth term in this equation represents transport of scalar  $\phi$  by unresolved turbulence and is often closed using a gradient transport assumption using a turbulent diffusivity [20]. Modeling of the last term in Eq. (1.6) is much more challenging because the reaction rate term is highly nonlinear. As a result, the average rate cannot simply be computed using the average quantities it depends upon. For a second-order irreversible reaction,



the average rate expression for species  $A$  is given by

$$\bar{\omega}_A = \overline{c_A c_B k_o \exp(-E/RT)} \neq \bar{c}_A \bar{c}_B k_o \exp(-E/R\bar{T}). \quad (1.8)$$

Here, the inequality holds except in the limit of reaction timescales being much greater than turbulent timescales (low Damköhler number) [21], which is rare in combustion.

Instead, for a given chemical state vector  $\phi$  (consisting of, e.g., T, P, and composition), the average reaction rate for a species  $i$ , which is a function of  $\phi$ , must be computed as

$$\bar{\omega}_i = \int_{\phi} \omega_i(\phi) P(\phi) d\phi, \quad (1.9)$$

where  $P(\phi)$  is the joint probability density function (PDF) of  $\phi$ , representing the subgrid fluctuations in the chemical state. The method of solving Eq. (1.9) or its equivalent (i.e., the equation holds for other scalars, not just the reaction rate) is termed a *mixing model*.

Two goals of combustion modeling are:

1. To reduce the complexity of the problem by reducing the number of transport equations necessary to accurately describe the chemistry.
2. To find ways to simplify modeling of the subgrid mixing effects.

The first goal is attempted by directly reducing chemical mechanisms or by applying subgrid reaction models that represent the chemistry in terms of a few parameters that are solved on the computational grid. This latter approach involves taking advantage of scale separation between grid-resolved phenomena and (faster) subgrid phenomena. A significant scale separation allows decoupling of fast combustion reactions from slower convective processes. Transport and subgrid mixing closure is then applied to the reduced parameterization. The application of a mixing model when the joint PDF is considered is much simpler when the number of parameters (dimensions of the joint PDF) is small. The first and second goals, listed above, are often intertwined with little explicit distinction.

### 1.2.1 Direct PDF Methods

In direct PDF methods, a transport equation is solved for the joint PDF itself, and reaction rates appear in closed form (no modeling is required). Direct PDF methods are usually performed using Lagrangian *particles* in a Monte-Carlo simulation due to the high dimensionality of the PDF [22]. Direct PDF methods are computationally intensive, however, and require modeling of transport terms appearing in the governing PDF transport equation.

### 1.2.2 Equilibrium Models

In the limit of very high Damköhler number (fast reaction), the reaction timescales are much smaller than mixing timescales, and hence, the chemistry can be decoupled

from the fluid dynamics. In this situation, all reactive scalars are related to the mixture fraction,  $\xi$ , which is a conserved scalar commonly defined as the local mass fraction of gas originating in the fuel stream. The mixture fraction quantifies the degree of mixing between the fuel and air streams, and linear relationships exist between conserved scalars and the mixture fraction. For a conserved scalar  $\varphi$  such as an elemental mass fraction, or enthalpy in an adiabatic system,  $\varphi = (\xi)\varphi_{\xi=1} + (1 - \xi)\varphi_{\xi=0}$ . Strictly, this assumes all species and heat have equal diffusivities ( $Le_i = 1$ ), with single-species driving forces, and (for enthalpy) that other Shvab-Zeldovich assumptions hold [2]. For a given value of mixture fraction, enthalpy and elemental composition is known, and the equilibrium state of a system can be computed and tabulated as  $\phi_i(\xi)$  (where  $\phi_i$  is a chemical state variable, such as temperature). A transport equation for the time-averaged or filtered mixture fraction is then solved on a computational grid, and scalars  $\bar{\phi}_i$  can be computed as

$$\bar{\phi}_i = \int \phi_i(\xi)P(\xi)d\xi. \quad (1.10)$$

Here the PDF of mixture fraction is needed, which is often computed using an assumed-shape PDF (usually a clipped Gaussian or  $\beta$ -PDF), requiring the mean and variance of mixture fraction. The latter can be modeled in several ways [23] and  $\bar{\phi}_i$  can be tabulated as a function of mixture fraction and its variance. Here, complex combustion requiring transport and mixing closure of all species has been reduced to transport of only mixture fraction and its variance. Of course, the tabulation does not need to be an equilibrium tabulation, any  $\phi_i(\xi)$  (such as from experimental data) could be used.

### 1.2.3 Flamelet Models

Flamelet models incorporate some of the effects of finite-rate chemistry not captured in equilibrium models by adding a parameter that can capture additional timescales. Unresolved combustion is assumed to take place between fuel and oxidizer in a collection of laminar flamelets whose chemical rates are assumed fast enough that the flame thickness is smaller than Kolmogorov scales, and turbulence only wrinkles the flames. The flamelets are described by the one-dimensional convective/diffusive equations that are transformed from physical to mixture fraction space using a coordinate transformation [24, 25]. Figure 1.2 is a schematic of the physical configuration. The flamelet equations rely on the

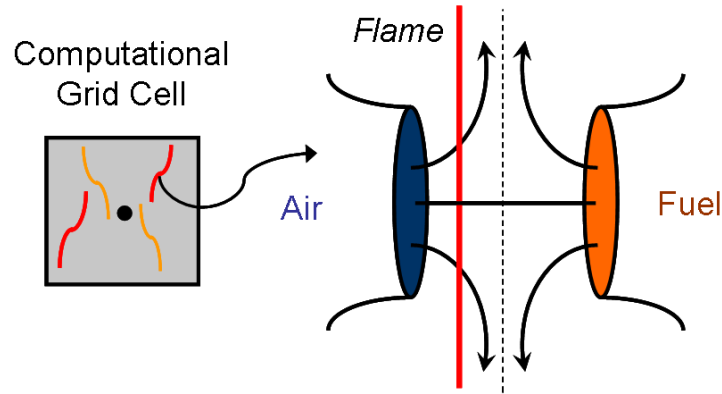


**Figure 1.2.** Flamelet model schematic.

assumption of unity Lewis numbers (equal species and thermal diffusivities) and Fickian diffusion, as well as the one-dimensional flame structure, and are given by

$$\rho \frac{\partial Y_i}{\partial \tau} = \frac{\rho \chi}{2} \frac{\partial^2 Y_i}{\partial \xi^2} + \dot{m}_i''' , \quad (1.11)$$

where

$$\chi = 2D_\xi \left( \frac{\partial \xi}{\partial y} \right)^2 \quad (1.12)$$

is the scalar dissipation rate, which relates the physical and mixture fraction coordinates. The scalar dissipation rate characterizes the intensity of turbulent flame straining and is usually specified as a known function of the mixture fraction:  $\chi = \chi_o g(\xi)$ , where  $\chi_o$  is a constant. Adiabatic enthalpy is also a known function of mixture fraction, and temperature can be computed from the enthalpy and composition. The flamelet equations can be solved to steady state and tabulated by the natural parameters  $\xi$  and  $\chi_o$ . A grid-averaged quantity  $\bar{\phi}_i$  can then be computed as

$$\bar{\phi}_i = \int_{\xi} \int_{\chi_o} \phi_i(\xi, \chi_o) P(\xi, \chi_o) d\chi_o d\xi. \quad (1.13)$$

Here, the joint PDF of  $\xi$  and  $\chi_o$  is needed. Usually it is assumed that  $\xi$  and  $\chi_o$  are statistically independent so the joint PDF is split into a product of marginal PDFs  $P(\xi, \chi_o) = P(\xi)P(\chi_o)$ . Linearity between  $\phi_i$  and  $\chi_o$  is also assumed so that the integration

above is just over  $P(\xi)$ , and  $\phi_i$  is evaluated as  $\phi_i(\xi, \bar{\chi}_o)$  in Eq. (1.13) [26]. Alternatively, a lognormal distribution for  $P(\chi)$  is used [27, 28].

#### 1.2.4 Unsteady Flamelet Models

Steady flamelet models incorporate some finite-rate chemistry through the subgrid reaction-diffusion balance, but unsteady effects such as flame extinction and ignition are not captured. Also, grid-resolved time-history effects involving chemical species whose reactive timescales overlap with grid scales (such as  $\text{NO}_x$  or soot formation) will not be accurately captured using steady flamelets. The flamelet equations can be solved in unsteady form using time as an additional parameter. Often,  $\chi_o$  is given some temporal profile and the unsteady flamelet equations are solved from some specified initial condition. The timescale of the subgrid flamelet simulation may then overlap with the computational fluid dynamics (CFD) grid-resolved timescales, and the subgrid flamelet can be thought of as moving through the computational grid in a Lagrangian sense. Some method of linking the flamelet time to the corresponding time on the CFD grid is required. Pitsch et al. [29, 30] have used a decaying profile for  $\chi$  as would be found in a turbulent jet. The flamelet time is then linked to the axial position in the jet based on the axial jet velocity and position.

#### 1.2.5 CMC Models

The conditional moment closure (CMC) model is based on the observation that most fluctuations of scalars in turbulent nonpremixed combustion are associated with the mixture fraction (local stoichiometry). A review of CMC is presented by Klimenko and Bilger in [31]. Rather than taking traditional averages of scalars in the RANS or LES equations, averages are conditioned on the mixture fraction. In first-order CMC, fluctuations of conditional scalars are ignored. The resulting transport equation for a scalar (say some reactive species)  $\phi_i$  is

$$\rho_\eta \frac{\partial Q_i}{\partial t} = -\rho_\eta \mathbf{v}_\eta \cdot \nabla Q_i + \rho_\eta \frac{\chi_\eta}{2} \frac{\partial^2 Q_i}{\partial \eta^2} + \langle \omega_i | \eta \rangle + e_y + e_Q, \quad (1.14)$$

with

$$e_Q = \left\langle \nabla \cdot (\rho D \nabla Q_i) + \rho D \nabla \xi \cdot \nabla \left( \frac{\partial Q_i}{\partial \eta} \right) \Big| \eta \right\rangle, \quad (1.15)$$

$$e_Y = - \left\langle \rho \frac{\partial Y''}{\partial t} + \rho \mathbf{v} \cdot \nabla Y'' - \nabla \cdot (D\rho \nabla Y'') \middle| \eta \right\rangle. \quad (1.16)$$

Here subscript  $\eta$  denotes a variable conditionally-averaged on mixture fraction  $\xi$  having value  $\eta$  ( $\eta$  is the sample space variable for the random variable  $\xi$ ). For example,  $Q_i = \langle \phi_i | \eta \rangle$  is the conditional average of  $\phi_i$ . The last two terms in Eq. (1.14) require closure models as do the conditional velocity ( $\mathbf{v}_\eta$ ) and conditional scalar dissipation rate ( $\chi_\eta$ ). The CMC model increases the dimensionality of the problem by one, with the mixture fraction appearing as an independent coordinate. The reaction rate, however, appears in closed form with  $\langle \omega_i(\phi) | \eta \rangle = \omega_i(\langle \phi | \eta \rangle)$ . Mean grid values of unconditional scalars are recovered from

$$\bar{\phi}_i = \int Q_i P(\xi) d\xi. \quad (1.17)$$

A transport equation is solved for the mean mixture fraction with  $P(\xi)$  obtained from the mean and variance of mixture fraction when using an assumed-shape PDF for  $P(\xi)$ . The CMC equations are expensive because of the increased dimensionality of the problem if detailed chemistry is used, but the reaction source closure problem is avoided. Often, the dimensionality is reduced by integrating across some of the spatial dimensions. In jets, for example, one can preserve the axial direction and cross-stream average through the radial direction [32]. It is also possible to solve the CMC equations on a coarser grid than the flow equations. For homogeneous flows, the spatial dependence of Eq. (1.14) drops out, and the CMC equations resemble the flamelet equations. Because of the spatial and temporal dependence in Eq. (1.14), chemical history effects can be captured and longer chemical timescales explicitly resolved.

### 1.2.6 Progress Variable Approaches

Desam [33] developed a novel approach to unsteady flamelets called the reaction time flamelet model. The model was developed for  $\text{NO}_x$  formation in which the subgrid flamelet time was monotonically correlated to NO concentration, which was then used as the “time” parameter and transported on the CFD grid. A similar progress variable approach was used by Pierce and Moin [34] in which a steady flamelet-like library was parameterized by mixture fraction and a progress variable, with both being transported on the CFD grid. In [34], the progress variable approach was able to capture a wider range of the accessed

state space than a typical flamelet model and included some ignition and extinction effects.

Subgrid models based on one-dimensional flows have been discussed above, but other configurations for subgrid turbulence-chemistry interactions are possible. Canonical reactors are appealing because they are easy to model and parameterize. CSTR (continuous stirred tank reactor) models and premixed flame models have been applied to tabulate the chemical state as a function of mixture fraction and some progress variable, such as combustion product concentrations:  $\text{H}_2\text{O}+\text{CO}_2$  or  $\text{CO}_2+\text{CO}$  [35].

The ILDM (intrinsic low-dimensional manifold) model, developed by Maas and Pope [36], is a rigorous and elegant method of reducing a chemical mechanism in which fast chemical processes are assumed to exist in local equilibrium with the evolution of longer timescale processes. The evolution of the slower processes occurs in a reduced space within the full thermochemical state space that can be represented by an arbitrary number of parameters depending on desired accuracy. These parameters are then transported on the CFD level, with other species. In the canonical reactor sense, the ILDM model corresponds to a batch reactor and, hence, does not account for transport effects at the subgrid level.

Most of the above models assumed detailed chemical mechanisms were used in describing the combustion reactions. However, reduced mechanisms using partial equilibrium and pseudo-steady state assumptions [2] which involve fewer chemical species could be used. Indeed, ILDM or other parameterizations may be coupled to existing combustion models such as the CMC equations, where, rather than solve the CMC equations for species, they could be solved for a few ILDM parameters.

### 1.2.7 Other Combustion Models

Other models for turbulent combustion have been developed such as the stochastic linear eddy and one-dimensional turbulence models (LEM, ODT) in which mixing is simulated on a one-dimensional domain that may be embedded in the flow. These models are characterized by the solution of one-dimensional reactive diffusive equations and periodic statistical rearrangement events (e.g., triplet maps) simulating the effect of turbulent eddies [37, 38]. Other, simpler models employing “mixed is burned” assumptions are common such as the eddy breakup model.

### 1.3 Review of Turbulent Simulations with Soot Formation

Modeling soot formation in turbulent nonpremixed flames has been a challenge due to the complex chemical mechanisms and long timescales governing soot formation. Unlike other pollutants, such as  $\text{NO}_x$ , which can be effectively postprocessed on established flow fields, soot can strongly interact with temperature and composition fields. The need to bridge the resolved and subgrid scales and account for radiative effects has led to a progression in applied models. Most computations of turbulent sooting flames are RANS simulations of jet flames. The fuels are typically methane, acetylene, ethylene, or propane. Generally, the soot is modeled by the addition of two transport equations for the first two moments of the soot size distribution. These moments represent particle number density and soot mass per unit volume,  $\rho Y_s$ , or soot volume fraction  $f_v = \rho Y_s / \rho_s$ , where  $\rho_s$  is the soot particle density (assumed constant).

The soot sources for these moments  $\omega_n$ ,  $\omega_s$  are closed in several ways. Usually, no mixing model of the form of Eq. (1.9) is applied, rather  $\bar{\omega}(\phi)$  is treated as  $\omega(\bar{\phi})$ . Often, the gas phase chemistry is totally decoupled from the soot chemistry and gas species are computed using one of the combustion models discussed above. Gas chemistry ranges from single-step to detailed schemes including PAH growth, though the treatment is usually subgrid using, e.g., the flamelet model. A full range of soot models are applied. Heat loss is also often decoupled, with treatments ranging from specification of  $T(\xi)$  profiles from experimental data or laminar flame calculations, to specification of a fixed fractional loss of sensible enthalpy, termed heat loss. Radiation models, when applied, are usually the optically thin model, or the discrete ordinates model. Often, the gas phase subgrid chemistry model is taken to be adiabatic. Sometimes heat losses are accounted for through a heat loss parameter or the optically thin model. Heat loss effects are never accounted for in the joint PDF, rather  $P(\xi, \gamma) \approx P(\xi)P(\gamma) \approx P(\xi)\delta(\gamma - \bar{\gamma})$  is assumed, where  $\gamma$  represents the heat loss parameter.

Early simulations of sooting flames did not treat soot explicitly. Jeng et al. [39] modeled methane and propane flames using equilibrium gas chemistry in 1982. A fixed fraction of the sensible enthalpy in the flame was removed to account for radiative losses (see also [40]). Gore et al. [40] did a calculation in which chemical species and soot were specified as experimental state relationships with mixture fraction in 1992. Radiative losses were computed on the grid with temperature inferred from enthalpy

and composition. In 1995, Young and Moss [41] simulated an ethylene flame where soot number density and mass fraction were transported in the CFD simulation with soot rates computed from a four-step mechanism. Soot was both postprocessed onto the flow field using an experimental temperature-mixture fraction relation, and by computing the soot as part of the flow calculation with heat loss obtained from an optically thin model coupled to the experimental temperature-mixture fraction profile perturbed by a heat loss parameter. Four-step soot models consist of nucleation, surface growth, oxidation, and coagulation processes.

Bressloff et al. [42] modeled a methane jet using a one-step gas reaction modeled using an eddy breakup combustion model (1996). The soot number density and mass fraction were transported with a three-step soot mechanism (no soot oxidation was employed). Gaseous intermediates for soot were computed from an adiabatic flamelet model. Brookes and Moss [15], in 1999, did similar calculations using laminar flamelets for gas chemistry. Soot oxidation by OH was included and subgrid heat losses were coupled to grid-level radiation through a heat loss parameter. Yan and Holmstedt [43] simulated a propane jet flame using experimental correlations between gas compositions and mixture fraction (1999). The two soot moments were transported with a four-step chemistry model. Likewise, Morvan et al. [44] simulated a line fire interacting with a crosswind using one-step gas reaction with a laminar flamelet model (2001), and Guenberger et al. [45] simulated a rich natural gas furnace using equilibrium gas chemistry (2002).

Several researchers have simulated ethylene jets with the gas state obtained from the laminar flamelet model with a heat loss parameter coupled to the grid-resolved radiative heat losses (using the optically thin model). Only the soot volume (or mass) fraction was transported on the grid and its reaction rate closed using the product of the grid soot volume fraction and the subgrid soot rate normalized by volume fraction (where the normalized soot rate was assumed independent of the amount of soot). Hence, a partial splitting of the soot rate between subgrid and resolved scales was done. Detailed gas chemistry and the HACA (hydrogen abstraction, acetylene addition) soot mechanism was used in [28, 46]. Balthasar [47] took a similar approach in 1996, but postprocessed the soot on an established flow field. The flamelet model applied included optically thin radiative losses, but the CFD simulation did not account for the higher heat losses associated with increased soot at the grid level.

Wang et al. [48] modeled an oxygen-enriched propane jet flame using a detailed gas

mechanism with PAH formation (2005). Turbulence-chemistry interactions were treated using an eddy-breakup model and soot was modeled by transporting the first six moments of the particle size distribution with the HACA mechanism used for surface reactions.

Desjardin and Frenkel [49] simulated an acetylene-air jet flame using LES (1999). The soot mass fraction and number density were transported with a four-step reaction mechanism. One-step combustion was used as well as the discrete ordinates radiation model with no coupling to the subgrid gas chemistry.

Kronenburg et al. [32] modeled soot formation in a methane jet using CMC in 2000. Only the axial spatial dimension was retained in the CMC equations. Soot mass fraction and number density were transported with five-step soot rates ( $O_2$  and  $OH$  oxidation). Reduced and detailed methane chemical mechanisms and the optically thin radiation model were applied.

Pitsch et al. [30] modeled an ethylene flame where both the soot and gas chemistry were treated subgrid using an unsteady flamelet model, which allowed for the longer timescale of the soot formation process (2000). Optically thin radiation was used in the subgrid model. Detailed gas chemistry for aromatic growth up to pyrene was used and soot was treated using the first two moments and the HACA mechanism.

None of these simulations included turbulence-chemistry interactions in closing the soot rates, and a large variation in the level of detail attempted in the models is observed. Lindstedt and Louloudi [50], however, simulated turbulent ethylene flames with a transported PDF method in which turbulence-chemistry interactions were accounted for (2005).

At present, only one DNS with soot formation has been performed, while the present work was in progress. In 2007, Yoo et al. [51] simulated soot formation in a two-dimensional, turbulent, counterflow, ethylene-air flame, with one-step combustion chemistry, and a four-step, two-moment soot model. The discrete ordinates radiation model was used in the simulation.

## 1.4 Direct Numerical Simulation

Direct numerical simulation (DNS) resolves all of the scales of turbulent motion, from the integral scales characterized by the flow configuration to the Kolmogorov scales where turbulent energy is dissipated by viscous effects. The size of the difference between these scales dictates the size of a computational grid for numerical simulation. The ratio of the largest to the smallest eddies in isotropic, homogeneous, turbulent flow,  $(L/\eta)$ ,

scales as  $Re_L^{3/4}$ , where  $Re_L$  is the Reynolds number based on the integral scale of the flow [17]. Thus, as  $Re_L$  increases, the disparity in lengthscales between the largest and smallest eddies increases. If all of the scales of motion are to be resolved, the number of grid points required in each direction increases in proportion to  $Re_L^{3/4}$  as  $Re_L$  increases [17, 52]. In three-dimensional flow, the number of grid points is proportional to  $Re_L^{9/4}$ . In addition, the flow timescales are proportional to the lengthscales and the combined effect of spatial and temporal resolution requirements gives computational costs that scale approximately as  $Re_L^3$  for three-dimensional flow. For this reason DNS is limited to moderate Reynolds number flow and simulation of practical combustion environments are not feasible currently.

The incorporation of detailed chemical kinetics into a DNS simulation substantially increases the complexity. In addition to solving the standard Navier-Stokes equations consisting of continuity and momentum, transport equations for one less than all chemical species, and an energy equation are required. Also, thermochemical properties vary as a function of composition and temperature and are not constant in reacting flows. For combustion simulations, in addition to resolution of the lengthscales and timescales of the turbulent flow, all continuum chemical scales must be resolved. As noted above, combustion chemistry can involve many species and reactions. In a DNS, gradients in all chemical species must be resolved, requiring ten or more grid points across a flame front [53, 54] resulting in very small grid spacings ( $O(10\ \mu m)$ ). For this reason, DNS simulations of combustion chemistry are limited to small computational domains on the order of centimeters.

DNS is also characterized by a high degree of numerical fidelity. For turbulent flow simulations, it is important that truncation errors in the numerical scheme are minimized so that numerical diffusion of turbulent energy does not compete with the physical process of viscous dissipation [52]. For this reason, high-order finite difference approximations ( $6^{th}$ - $8^{th}$ ) of derivatives appearing in the governing flow equations are used for spatial coordinates. In spectral methods, time advancement of the solution takes place in wave number space rather than physical space. The efficient fast Fourier transform (FFT) is used to convert between physical and wave number space. Approximation of derivatives in spectral methods is exact and accuracy is dictated by the number of discrete Fourier modes retained. However, spectral methods require periodicity in the domain in the direction of application of the method. For flow configurations with more

complex boundary conditions, high-order finite difference methods are used [55, 56]. Time advancement is accomplished using methods for ordinary differential equations (e.g., Runge-Kutta, Adams-Bashforth). Explicit methods are usually used since implicit methods have a high computational cost per timestep, and many timesteps are required to resolve the evolution of the flow [55].

Although DNS cannot simulate flows of engineering interest, it is an ideal tool for obtaining mechanistic insight into turbulent reacting flows and in the evaluation and development of closure models for LES and RANS. DNS provides a level of detail of flow/flame interactions unrivaled by any other means (albeit at a small scale). Data from DNS simulations are often used in two ways [55]. First, in so-called a-posteriori tests, the DNS results are used as “experimental” data, for which RANS and LES simulations can be compared. Using DNS data rather than experimental results has the advantages that (1) experimental results may not be available or feasible, (2) the boundary and initial conditions are known exactly, and (3) more detailed information may be obtainable from DNS than is available experimentally. The drawbacks were noted above, that is, computational cost and simple configurations. Second, in a-priori testing, DNS data are used directly to evaluate model performance. For example, the DNS data can be filtered to obtain the subgrid turbulent stress  $\tau_{ij}^{sgs} = \overline{v_i v_j} - \bar{v}_i \bar{v}_j$ . The filtered data could then be used as input to a given model for  $\tau_{ij}^{sgs}$  and the results compared. In combustion, the equilibrium reaction model, for example, could be tested by comparing the chemical state obtained by the DNS to the equilibrium state using the DNS values of the mixture fraction and enthalpy [57]. In this way, performance of a given simplification of the chemistry can be isolated from turbulent mixing effects. DNS data are also used directly to quantify important turbulence-chemistry interactions such as the effects of flame strain and curvature, effects of multicomponent mass transfer, and transient finite-rate chemistry effects such as flame extinction and ignition [58, 59].

#### 1.4.1 Review of DNS of Turbulent Combustion

Several reviews summarizing DNS of nonpremixed combustion have appeared [59, 53, 58, 60]. Progress in DNS of combustion over the last 20 years or so has consisted of increasing the amount of physical phenomena accounted for in the simulation. As noted above, incorporation of chemical reaction in a flow simulation greatly increases computational costs, and tradeoffs in the level of physical detail in different parts of

the simulation have been made as a compromise between computational costs, physical models, and achieving the goals of the end use of the simulation. Turbulence is assumed to be two- or three-dimensional. Combustion chemistry models range from single-step irreversible reaction, to global multistep schemes, to reduced or skeletal mechanisms, to detailed kinetics. Flow configurations range from simple mixing layers, to periodic isotropic decaying turbulence, to temporally or spatially evolving jets. Transport models range from specification of Schmidt numbers, to mixture-averaged species transport with a single species driving force (e.g., Fickian), to full multicomponent mass transfer (e.g., the Maxwell-Stefan equations) [61, 59].

In 1985, McMurtry et al. [37] simulated a two-dimensional, temporally evolving, reacting mixing layer using single-step, irreversible chemistry with heat release. A computational domain of  $64 \times 64$  grid cells was used. The Schmidt, Prandtl, Reynolds, and Damköhler numbers were fixed in these simulations. Similar studies were conducted by Givi et al. [62] in 1991 using a grid of  $128^2$  or  $256^2$  points and a temperature dependent reaction rate. In 1994, Miller et al. [63] performed simulations in three dimensions.

Many studies have been done of the interaction of nonpremixed flames with decaying isotropic turbulence in a box. Three-dimensional, constant property, isothermal reaction with periodic boundary conditions were done in the early 1990's [64, 65, 66]. Lee and Pope [67] in 1994, and later Jaber et al. [68] in 1997 studied three-dimensional isotropic turbulence with external forcing to obtain statistically stationary results using the above assumptions. Mahalingam et al. [54] allowed for heat release and Arrhenius reaction rates for one- and two-step global reaction schemes. The boundaries in the plane of the flame were nonreflecting to allow an open domain, avoiding pressure buildup. Bushe and Bilger [69] performed similar calculations using forced isotropic turbulence and a three-step global mechanism: two steps for methane oxidation and one for NO production.

In 1997, Montgomery et al. [70] simulated three-dimensional isotropic decaying turbulence with periodic boundaries using a low-Mach formulation and a reduced hydrogen mechanism consisting of four transported species. Reaction zones were widened by running at low pressure, preheating the reactants, and using reduced Schmidt numbers to reduce resolution costs. Two-dimensional simulations with detailed hydrogen chemistry, mixture-averaged transport (Fickian) with thermal diffusion, and nonreflecting boundary conditions have also been performed [71, 72]. Baum et al. [73] performed two-dimensional premixed DNS in isotropic turbulence with periodic boundaries in one direction and non-

reflecting boundaries in the other. Detailed  $\text{H}_2$  chemistry and mixture-averaged transport properties with Fickian diffusion were applied. Van Kalmthout and Veynante [74] studied a two-dimensional mixing layer using a one-step reaction with heat release. Nonreflecting boundaries were used in the cross stream direction and homogeneous isotropic turbulence was injected into the domain to attain a spatially-developing flow.

A four-step global mechanism for  $\text{NO}_x$  (one-step methane oxidation, three-step  $\text{NO}_x$  formation) was applied in two- and three-dimensional decaying isotropic turbulence with periodic and nonreflecting boundaries. The chemical mechanism was constructed to minimize computational cost while attempting to preserve flame temperature, burning velocity, and species profiles, and to account for unsteady effects [75]. DNS of three-dimensional isotropic decaying turbulence with a four-step n-heptane mechanism [76] were also performed. Thevenin et al. [77] present results of a premixed calculation using a DNS code with a low Mach assumption and a pressure projection to remove the acoustic CFL restriction. An intrinsic low-dimensional manifold method (ILDm) [36] coupled to a flame prolongation method was used to reduce the chemistry.

In 2002, a three-dimensional lifted hydrogen jet diffusion flame was simulated using 22.8 million points, detailed chemistry and Fickian mass transfer with mixture-averaged coefficients, and nonreflecting boundary conditions [78]. The numerics were much coarser than usual for DNS: a finite volume scheme with TVD upwinding was used with a second-order Runge-Kutta integrator [78]. In 2004, Sutherland [57] simulated two-dimensional spatially evolving jets using detailed syngas (12 species) and reduced methane (17 species) reaction mechanisms, along with Fickian diffusion with mixture-averaged coefficients. Turbulence was injected at the inlet and nonreflecting boundary conditions were applied. In 2003, Pantano et al. [79] performed three-dimensional DNS of a turbulent, temporally evolving mixing layer to study the effects of heat release on turbulence and mixing. Simplified chemistry and transport properties were used. The grid size consisted of 38 million cells.

More recently, in 2007 large-scale DNS of combustion with detailed chemistry in three dimensions has been reported. Sankaran et al. [80] performed three-dimensional simulations of a statistically stationary lean premixed methane Bunsen flame in the thin reaction zones regime with a 13-species reduced mechanism on a computational mesh of 51.84 million cells. Hawkes et al. [81] performed a parametric study of extinction and reignition of temporally evolving  $\text{CO}/\text{H}_2$  jet flames with Reynolds numbers up to 9,000

and up to 500 million grid cells. Yoo et al. [82] performed a DNS of a lifted hydrogen jet flame with a heated coflow, consisting of nearly one billion grid cells.

## CHAPTER 2

### DNS FORMULATION, MODELS, AND NUMERICS

The DNS code is called S3D and was developed at Sandia National Laboratories. The code is written in Fortran 90 and parallelized with MPI. S3D solves the fully compressible, three-dimensional reacting Navier-Stokes equations on a uniform Cartesian grid. Equations for continuity, momentum, total energy, and chemical species mass fractions are solved in their conservative form. The ideal gas law equation of state is used throughout to compute the pressure from the density, temperature, and composition. A fourth-order, six-stage explicit Runge-Kutta method is used for time advancement [83]. Spatial derivatives are evaluated using eighth-order central difference approximations derived from Taylor series. A tenth-order spatial filter is applied to remove high wavenumber content and reduce aliasing errors at each timestep [84]. The boundary conditions of Sutherland and Kennedy are used in S3D [85]. All thermodynamic and transport properties are composition and temperature dependent and are evaluated using Chemkin III [86]. In all simulations presented, mixture-averaged effective diffusivities are used, with each species driven by its own mole fraction gradient (Fick-style). The code can also compute species diffusivities assuming constant Lewis numbers. The mass fraction of the last chemical species,  $N_2$  is computed to ensure conservation of mass, and thus the diffusion flux of  $N_2$  implicitly enforces a null sum of species diffusion fluxes as required by continuity.

The governing equations solved are given (in index notation) by

$$\text{continuity:} \quad \frac{\partial \rho}{\partial t} = -\frac{\partial(\rho v_i)}{\partial x_i}, \quad (2.1)$$

$$\text{momentum:} \quad \frac{\partial(\rho v_i)}{\partial t} = -\frac{\partial(\rho v_j v_i)}{\partial x_j} - \frac{\partial P}{\partial x_i} + \frac{\partial \tau_{i,j}}{\partial x_j}, \quad (2.2)$$

$$\text{energy:} \quad \frac{\partial(\rho e_o)}{\partial t} = -\frac{\partial(\rho e_o v_i)}{\partial x_i} - \frac{\partial(P v_i)}{\partial x_i} + \frac{\partial(\tau_{i,j} \cdot v_j)}{\partial x_i} - \frac{\partial q_i}{\partial x_i}, \quad (2.3)$$

$$\text{species:} \quad \frac{\partial(\rho Y_k)}{\partial t} = -\frac{\partial(\rho Y_k v_i)}{\partial x_i} - \frac{\partial(j_{k,i})}{\partial x_i} + \omega_k. \quad (2.4)$$

In these equations  $\rho$  is density,  $v_i$  is velocity,  $t$  is time,  $x_i$  is position,  $P$  is pressure,  $\tau_{i,j}$  is the viscous stress tensor,  $Y_k$  is the mass fraction of species  $k$ , and  $\omega_k$  is the species reaction rate. In addition,  $e_o$ ,  $q_i$ , and  $j_{k,i}$  are the specific total energy, heat flux vector, and species diffusion flux vector, respectively. The first two of these quantities are defined as

$$e_o = \frac{v_i v_i}{2} + h - \frac{P}{\rho}, \quad (2.5)$$

$$q_i = -\lambda \frac{\partial T}{\partial x_i} + \sum_k h_k j_{k,i} + Q_{rad,i}, \quad (2.6)$$

where  $\lambda$  is the thermal conductivity,  $T$  is temperature,  $h$  and  $h_k$  are specific enthalpies of the mixture and species, respectively, and  $Q_{rad,i}$  is the radiative heat flux vector. The transport equations are closed with constitutive relations for the species diffusivities and the stress tensor, a thermodynamic relation linking enthalpy and temperature,  $h = h(T)$ , and an equation of state, here the ideal gas law:

$$P = \frac{\rho R T}{W}, \quad (2.7)$$

where  $R$  is the universal gas constant and  $W$  is the mean molecular weight.

There are many possible forms for the species diffusion coefficients [61]. In S3D, a mixture-averaged formulation based on a form of Fick's law is used:

$$j_{k,i} = \rho Y_k V_{k,i}, \quad (2.8)$$

$$= -\frac{\rho Y_k D_k}{X_k} \frac{\partial X_k}{\partial x_i}, \quad (2.9)$$

$$= -\rho D_k \frac{\partial Y_k}{\partial x_i} - \frac{\rho D_k Y_k}{W} \frac{\partial W}{\partial x_i}, \quad (2.10)$$

where  $D_k$  is a mixture-averaged diffusion coefficient, computed using the Chemkin Transport package [87],  $X_k$  is the mole fraction of species  $k$ , and  $V_{k,i}$  is the diffusion velocity of species  $k$ . The form of  $V_{k,i}$  is a simplification of the Maxwell-Stefan equations and suggests a diffusion velocity relative to a molar-averaged velocity [61]. However, the form of  $j_{k,i}$  in Eq. (2.9) implies a mass-averaged velocity if the sum of the diffusion fluxes is

equal to zero. This inconsistency is not severe given the mixture-averaged approximation, however. S3D transports all gaseous species except nitrogen, which is computed so as to satisfy continuity (that is,  $Y_{N_2} = 1 - \sum_{k \neq N_2} Y_k$ ). This approach implicitly forces a null sum of the species diffusivities, which is not true as written in Eq. (2.10).

The viscous stress tensor is computed in S3D as

$$\tau_{i,j} = \mu \left( \frac{\partial v_i}{\partial x_j} + \frac{\partial v_j}{\partial x_i} - \frac{2}{3} \delta_{i,j} \frac{\partial v_l}{\partial x_l} \right), \quad (2.11)$$

where  $\mu$  is the viscosity, and  $\delta_{i,j}$  is the Kronecker delta, which equals unity if  $i = j$ , and zero otherwise.

The solution algorithm of S3D is as follows:

1. Initialize  $T$ ,  $P$ ,  $Y_k$ , and  $v_i$  fields throughout the domain. These variables are the primitive variables.
2. From the primitive variables, initialize conserved, transported variables:  $\rho$ ,  $\rho v_i$ ,  $\rho e_o$ ,  $\rho Y_k$ . The average molecular weight is computed from the composition field using  $W = (\sum_k Y_k / W_k)^{-1}$ . Density is computed from the ideal gas law  $\rho = WP/RT$ . Total energy is computed from Eq. (2.5), where  $h = \sum_k Y_k h_k$ , and  $h_k = h_{k,ref} + \int_{T_{ref}}^T C_{p,k}(T) dT$ . A lookup table is computed using Chemkin for all species enthalpies and heat capacities as a function of temperature. Values of  $C_{p,k}$ , and  $h_k$  are then linearly interpolated from the tables.
3. The solution field is integrated in time by evaluating the right-hand side (RHS) of the governing transport equations, Eqs. (2.1)-(2.4), shown above.
4. Periodically (usually after each step) the solution (conserved variables) are filtered to remove any high wavenumber content.
5. Primitive variables are then computed from the conserved variables, which are used in computing constitutive relations for fluxes, and thermodynamic and transport properties (such as viscosity).
6. Integration then continues with step 3 to the end of the simulation.

The timestep size is either set manually at an accurate and safe level, based on the estimated error reported by the embedded Runge-Kutta solver, or set by a PID controller

that adjusts the timestep size to maintain a given error threshold. Runtime parameters can be adjusted during the simulation through an active file that is read periodically during the integration. Parameters include error tolerances, ending timestep, frequency to save output files and solution monitors, and timestep size. Three types of output are reported:

1. A save file (the primary output), which also serves as a restart file and consists of the temperature, pressure, velocity, and composition fields at a given time. A single file is saved for the fields of each processor.
2. Runtime output including the time, timestep, and integration error. Also, files consisting of maximum and minimum field values during the integration, as well as information on the acoustic CFL timestep, and the location and source of peak errors are created.
3. Visualization files for examination and processing of solution fields including quantities such as reaction rates, vorticity fields, and other scalar fields.

S3D is operated in two modes: solve mode and postprocessing mode. The solve mode was described above. Postprocessing is done by looping over a selected list of savefiles, loading the primitive variables, and performing user-defined operations on the fields. This processing is performed to compute many derived quantities, such as flame dynamics and statistical quantities. The postprocessing is not usually computationally intensive, compared to the solution itself. In some cases, temporal quantities available only as the solution progresses are of interest, in which case additional output would be required as the solution progresses.

S3D uses several systems of units. The base system is SI, but interfacing with Chemkin requires conversion to CGS units at the point of the interface. S3D itself nondimensionalizes solution variables within the code, and SI units are used for input and output only. However, it is not true that S3D is a nondimensional code in the traditional sense. Generally, nondimensionalization is performed on the governing equations, transforming them to new equations in which dimensionless groups such as the Reynolds number and Mach numbers appear in coefficients to the terms in the governing PDEs. These terms are not present in S3D, and Eqs. (2.1)-(2.4) are solved as shown. The traditional nondimensionalization is performed using physically relevant reference quantities, such that the partial derivative terms are all order unity, and coefficients to those terms with

the dimensionless numbers contain the magnitude of the whole term. For example, the constant-property, incompressible Navier-Stokes equations are given by

$$\frac{\partial v_i}{\partial x_i} = 0, \quad (2.12)$$

$$v_i \frac{\partial v_j}{\partial x_i} = -\frac{1}{\rho} \frac{\partial P}{\partial x_i} + \nu \frac{\partial^2 v_j}{\partial x_j \partial x_i}. \quad (2.13)$$

If velocity is scaled by  $V_r$ , length by  $L_r$ , and pressure by  $\rho V_r^2$ , the result is

$$\frac{\partial v_i^*}{\partial x_i^*} = 0, \quad (2.14)$$

$$v_i^* \frac{\partial v_j^*}{\partial x_i^*} = -\frac{1}{\rho} \frac{\partial P^*}{\partial x_i^*} + \left( \frac{1}{Re} \right) \frac{\partial^2 v_j^*}{\partial x_j^* \partial x_i^*}, \quad (2.15)$$

where starred quantities are nondimensional (e.g.,  $v_i^* = v_i/V_r$ ). One may think of S3D as a dimensional code using *S3D units* rather than SI units. In practice, however, the unit conversion in S3D is performed to minimize the disparity in ranges of magnitude of the transported and primitive quantities.

## 2.1 Grid Resolution

One of the features of DNS is the resolution of the important physics present in the problem. In order to minimize numerical diffusion, which could compete with viscous diffusion, a fine computational grid is required with an associated high computational cost. To minimize the number of grid points required (and computational roundoff errors), higher-order finite difference approximations to derivative terms are employed. Finite difference methods are in contrast to spectral methods in which derivatives are evaluated exactly in the frequency domain, and errors arise only through the finite number of wavenumbers (and roundoff error). Finite difference methods allow more general boundary conditions than spectral methods, which are limited to periodic boundary conditions in the spectral directions. Finite differences are also local in physical space, which increases parallel communication efficiency.

When applying finite difference methods, it is important to quantify the truncation error. Often, this is done by successive grid refinement on a full simulation scale. Here the relative error of four central difference schemes of increasing order are computed in terms of Fourier modes. We can consider functions that evolve as the solution to the

Navier-Stokes equations as being representable by a complex Fourier series of which a given term  $n$  is

$$\phi_n(x) = c_n \cdot e^{i\kappa_n x}, \quad (2.16)$$

where  $\kappa$  is the wavenumber of the mode and  $c$  is a complex coefficient multiplying the mode. The subscript  $n$  is dropped here for convenience.

The derivative of  $\phi$  with respect to  $x$  is exactly given by

$$\frac{d\phi}{dx} = c_n i\kappa e^{i\kappa x}. \quad (2.17)$$

The discrete approximation to a derivative is represented as

$$\left(\frac{\delta\phi}{\delta x}\right)_j = \frac{\sum_k a_k \phi_{j+k}}{\Delta x}, \quad (2.18)$$

where the summation is over some finite number of grid points in the vicinity of  $x_j$ ,  $a_k$  are constant coefficients, and  $\phi_{j+k}$  are values  $\phi(x_{j+k})$  at the grid points, where  $x_j = j\Delta x$ . The coefficients  $a_k$  are determined using Taylor series. The number of grid points in the discrete derivative increases with the order of accuracy of the approximation. Lomax outlines a method of determining the coefficients  $a_k$  for any order derivative for any order approximation using a ‘‘Taylor Table’’ [88]. A short Matlab script was written to generalize the method and is listed in Appendix A. The script computes coefficients for any order derivative, to any order of accuracy, with the base point at any position in the grid stencil. Here, only central differences are considered of order 2, 4, 6, and 8. Table 2.1 gives the coefficients of the points in the stencil computed using the program.

The relative error of the approximate derivative is obtained by substituting (2.16) into (2.18) and comparing to (2.17). The substitution yields

$$\left(\frac{\delta\phi}{\delta x}\right)_j = \frac{c}{\Delta x} \sum_k a_k \cdot e^{i\kappa\Delta x \cdot (j+k)}, \quad (2.19)$$

$$= \frac{c \cdot e^{i\kappa x_j}}{\Delta x} \sum_k a_k e^{i\kappa\Delta x \cdot k}. \quad (2.20)$$

**Table 2.1.** First-order derivative finite difference coefficients.

Position, k	$a_k$			
	2 <sup>nd</sup>	4 <sup>th</sup>	6 <sup>th</sup>	8 <sup>th</sup>
-4	0	0	0	1/280
-3	0	0	-1/60	-4/105
-2	0	1/12	3/20	1/5
-1	-1/2	-2/3	-3/4	-4/5
0	0	0	0	0
1	1/2	2/3	3/4	4/5
2	0	-1/12	-3/20	-1/5
3	0	0	1/60	4/105
4	0	0	0	-1/280

The relative error of the derivative then is

$$\epsilon = 1 - \frac{1}{i\kappa\Delta x} \sum_k a_k e^{i\kappa\Delta x \cdot k}. \quad (2.21)$$

This equation is simplified by first expanding the complex exponential using the Euler formula  $\exp(\pm iz) = \cos(z) \pm i \sin(z)$ . Since  $a_k = -a_{-k}$  in Table 2.1, the cosine terms will drop out of Eq. (2.21). For the same reason, the sine terms of equal magnitude  $k$  are additive and result in (for central differences):

$$\epsilon = 1 - \frac{2}{\kappa\Delta x} \sum_{k \geq 0} a_k \sin(\kappa\Delta x \cdot k). \quad (2.22)$$

Figure 2.1 shows the logarithm of the relative error versus  $\kappa\Delta x$ , which is allowed to vary up to  $\pi$ , as dictated by the Nyquist limit. That is, one grid spacing can handle no less than half a wavelength, or one grid cell for half a wave. Of interest is the number of grid points required for half a wave (from peak to trough). This number is given by

$$N_{1/2} = \left\lceil \frac{\pi}{\kappa\Delta x} \right\rceil. \quad (2.23)$$

An error of 0.1% for the second-, fourth-, sixth-, and eighth-order approximations gives  $N_{1/2}$  of 41.9, 7.7, 4.3, and 3.2 points, respectively (to be rounded up). So, for an eighth-order stencil we can expect to commit just over 0.1% error if we have three intervals, or four points from peak-to-peak on a given Fourier mode.

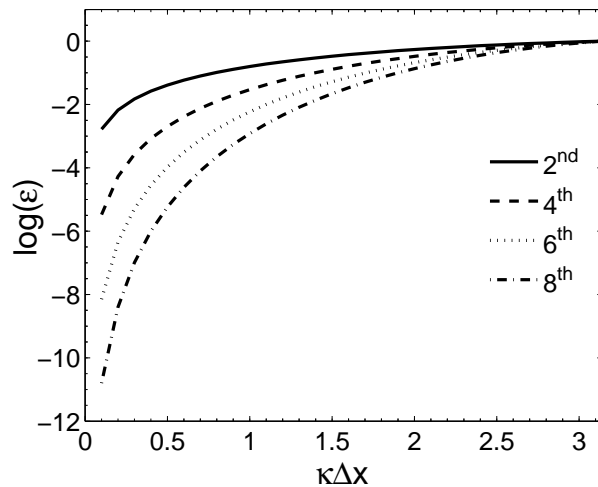


**Figure 2.1.** Relative error of centered finite differences of indicated order for a single Fourier mode.

Clearly, there is a huge discrepancy in resolution requirements between the high- and low-order methods. In general, a given signal will be composed of many Fourier modes, many of which will not be resolvable, and the issue becomes one of making sure that the amount of spectral energy in the high wavenumber region of the signal is very small. In high-order codes with low numerical diffusion, high wavenumber content must be filtered out to prevent aliasing errors. Aliasing errors occur when a solution produces high wavenumbers that, because they cannot be resolved on the grid, show up at lower wavenumbers. For example, take a function with frequency  $f_o$ , sampled at a frequency  $f_s$  (at points  $nT_s = n/f_s$ ,  $n = 0, 1, 2, \dots$ ), such as  $\sin(2\pi f_o n T_s)$ . The same function is obtained by adding a multiple of  $2\pi$  to the argument:  $\sin(2\pi f_o n T_s + 2\pi m)$ . This is true for any integer  $m$ , so take  $m$  as a multiple of  $n$ , and rearrange the second expression to get

$$\sin(2\pi f_o n T_s) = \sin(2\pi(f_o + k/T_s)n T_s), \quad (2.24)$$

where  $k$  is an integer. Figure 2.2 shows an example for  $f_o = 2$ ,  $f_s = 1.4f_o$ , and  $k = 1$ .

## 2.2 Parallel Scaling

S3D is a massively parallel DNS code that is highly portable and maintains high parallel efficiency on tens of thousands of processors. S3D is parallelized with MPI

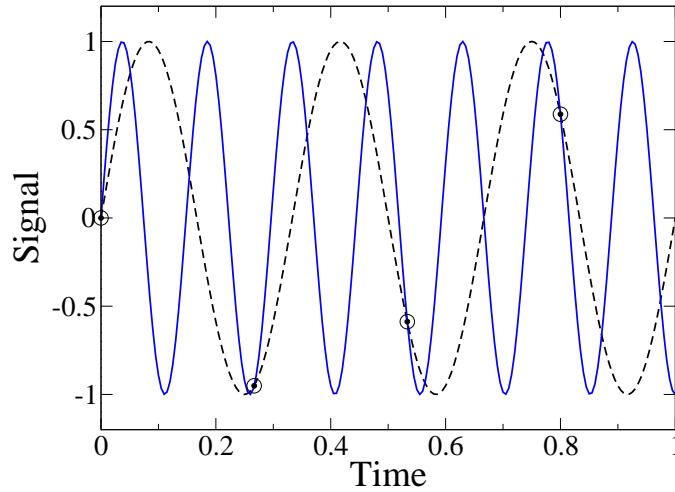


**Figure 2.2.** Example of aliasing of two periodic functions. The functions are the same at the uniformly spaced sample points shown.

through a rectangular-prism (i.e., a stretched cube) domain decomposition in which each processor operates on the same number of grid cells. The finite difference stencils and explicit time integration require only nearest-neighbor communication between processor domains. As a result, good parallel efficiency is maintained as the number of processors increases for a fixed grid density per processor. The parallel efficiency is often defined as

$$E = \frac{t_{serial}}{N_p \cdot t_{parallel}}. \quad (2.25)$$

Efficiency is decreased through parallel costs (primarily message passing among processors) that does not directly contribute to the computation of the problem. There are two important parallel scaling tests termed *weak* and *strong* scaling. In a strong scaling test, the efficiency is measured as the number of processors increases for a *fixed* problem size. In this mode, the communication-to-computation ratio increases and a point is reached where further parallelization is not beneficial as efficiency becomes low. Analogous to the parallel efficiency is the speedup factor

$$S = \frac{t_{serial}}{t_{parallel}}. \quad (2.26)$$

Strong parallel scaling is subject to Amdahl's law which relates the maximum theoretical speedup for a fixed problem size. If  $f$  is the fraction of a given problem that must be

computed serially (that is, cannot benefit from parallelization) and  $(1 - f)$  is the fraction that can be parallelized, then Amdahl's law states

$$S = \frac{t_{serial}}{ft_{serial} + (1 - f)t_{serial}/N_p}. \quad (2.27)$$

As the number of processors increases, the speedup factor approaches  $1/f$ , giving an upper bound on the possible speedup. For example, if  $f = 0.01$ , the maximum speedup factor is 100.

Most practical problems are not parallelized with a fixed computation size, but rather, the problem size is increased as the number of processors increases. A weak scaling test maintains a fixed computation density per processor as the number of processors increases. In this case, efficiency decreases primarily as the communication-to-computation ratio increases for a given problem. S3D contains very little global communication and maintains nearly constant normalized computational cost (i.e., CPU-hours per grid point, per timestep) as the number of processors increases to as high as 20,000.

A series of test cases was conducted to examine the scaling efficiency of S3D on a parallel Linux cluster called Jet. This machine consists of 141 nodes, with two processors each. The processors are 2 GHz AMD Opterons and each node has 2 GB memory with a fast Infiniband switch for communications. Generally, the S3D code tends to be CPU limited as opposed to memory limited. Common application of DNS involves a very large number of grid points due to high spatial resolution requirement and domain size. Because of the fine grid, the timestep size is small due to the acoustic CFL. The upper bound of the acoustic speed is relatively constant at the flame temperature, and the maximum timestep size is proportional to the grid spacing. As a result, relatively short runtimes are computed. For cell spacings on the order of 20  $\mu\text{m}$ , run times of a millisecond or less are common, corresponding to order 100,000 timesteps.

Soot calculations differ from gas-only cases in that one would like to maximize the simulation time to maximize the soot growth. For constant overall computational cost, longer times (e.g., a large number of timesteps) result in fewer grid cells. Hence, the computational domain size can decrease, or the cell spacing can increase. At longer run times, the flow velocity can be smaller because the same number of flow-through times can be maintained. This lower velocity is helpful in that the corresponding strain rates

are lower; hence both flames and soot layers are thicker, resulting in decreased resolution requirements.

As a matter of parallel efficiency, to run to longer times requires more processors for a given wall-clock time, but more processors means the number of grid points per processor decreases. As this occurs, the communication-to-computation ratio may be expected to increase, with corresponding decreases in the parallel efficiency. Here, efficiency as the grid density per processor changes is examined.

The simulation is that of a two-dimensional temporal mixing layer, described later. The grid size is  $256 \times 512$  for 131,072 total grid cells. Two hundred timesteps were performed. The grid size is  $39 \mu\text{m}$  in both directions. Twenty-two transport equations are solved corresponding to mass, two momentum components, energy, and 18 transported chemical species. For these calculations, sixth-order derivatives were used, with an eighth-order spatial filter. Input and output were suppressed for everything except printing of the output statistics and reading of the active file, which are expected to be a small part of the overall run time. Five cases were considered using 4 to 64 processors. Table 2.2 shows the processors, the number of nodes per processor, and the run time. The average computational cost is  $3 \times 10^{-9}$  CPU-hrs/ $N_{grid}N_pN_{eqns}$ .

As shown in the table, for 64 processors, the grid density is relatively small. For isoefficiency, a plot of the log of the run time versus the log of the number of processors should be linear. Figure 2.3 shows this to be true for the scaling results. Hence, even for a relatively low grid density, a good parallel efficiency is obtained, indicating that the simulations are far from the limit where communication costs begin to dominate. These results are conservative compared to three-dimensional cases in which much higher grid densities are used (typically  $30^3$  to  $50^3$  grid cells per processor), reducing the communication-to-computation cost with nearest-neighbor communication.

**Table 2.2.** Parallel scaling results.

$N_p$	$N_{grid}/N_p$	$t_{run}$ (min)
4	32768	28.75
8	16384	13.4
16	8192	7.6
32	4096	3.5
64	2048	1.63

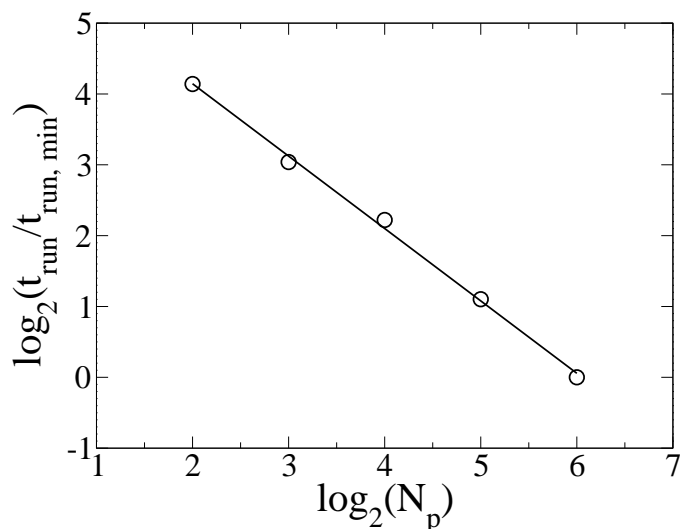


**Figure 2.3.** Plot of parallel run time versus number of processors.

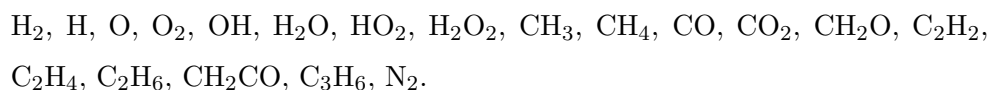
## 2.3 Ethylene Chemical Mechanism

In combustion of typical hydrocarbon flames, the number of chemical species required to describe the reacting system ranges from around ten for hydrogen, to around 1000 for higher hydrocarbons, such as those comprising a typical JP8 jet fuel. Currently, it is not feasible to transport large numbers of chemical species for combustion simulations, and reduced mechanisms are employed which reduce the number of chemical species, as well as the number of reactions among those species. These mechanisms will often make use of steady state and partial equilibrium assumptions [2], which reduce the dimensionality (number of species) by taking advantage of timescale separation. There are many approaches and methods for generating a reduced description of a chemical mechanism, including computational singular perturbation theory [89], intrinsic low-dimensional manifold methods [36], rate controlled constrained equilibrium [90], directed relation graph methods [91], sensitivity analysis, and principle components analysis [92]. For a review, see [93]. Here, a description of a reduced ethylene mechanism, which is used in all simulations, is given. In addition, a one-step mechanism was used for some preliminary case setups, and is briefly described.

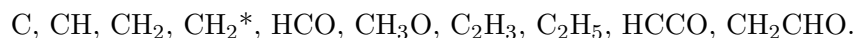
### 2.3.1 Reduced Mechanism Description

Ethylene is of interest as a fuel for two reasons. First, it is one of the smallest hydrocarbons with appreciable sooting tendency. Second, it is a small hydrocarbon that also exhibits complexities not present in hydrogen and carbon monoxide systems, such

as bimodal extinction/ignition behavior. The reduced ethylene mechanism used here was developed by Lu and Law [94]. The mechanism consists of 15 global reaction steps, and the following 19 transported species:



In addition, the following quasi-steady state species are included:



The mechanism is based on a detailed mechanism consisting of 70 chemical species and 463 chemical reactions [95]. The first step in the mechanism reduction, termed skeletal reduction, is to eliminate unimportant species and reactions. This is done throughout, with the constraint that the mechanism should transport gaseous species that are needed for soot reactions, namely,  $\text{C}_2\text{H}_2$ ,  $\text{H}_2$ ,  $\text{CO}$ ,  $\text{O}_2$ , and  $\text{OH}$ . The skeletal reduction was performed using the directed relation graph method [91]. This was followed by sensitivity analysis to further reduce the number of crucial chemical species. The resulting number of chemical species retained at this stage was 29, with 167 elementary reactions. Of these 29 species, 10 were approximated to be in quasi-steady state (QSS) by using computational singular perturbation [96]. QSS species concentrations are required to compute the reaction rates of transported species, and the former are computed as functions of the latter. It is important, however, that this functional relationship can be computed analytically. Often, the QSS species concentrations must be computed by numerical inversion of a nonlinear system, which is costly. This numerical approach can cause problems when used in a reacting flow code, since failure to fully converge the nonlinear solve can result in instability. These problems are eliminated in the present reduced mechanism by computing the QSS species concentrations analytically. This was done using a linearized QSS approximation with a QSS graph method [97].

### 2.3.2 Computational Costs and Speedup

As noted above, computational costs are associated with the number of chemical species retained in a mechanism, as well as the corresponding complexity in evaluating the chemical source terms (which usually increases nonlinearly with increasing number of species). In addition, computational costs arise from chemical stiffness associated with very small timescales. This is especially evident when explicit integration methods

are used, which is the case in the present DNS context. The third major source of computational cost is in resolving the lengthscales of species. If a mechanism includes species that are very thin in physical space, the number of DNS grid points required for numerical accuracy and stability increases. In summary, the three major sources of computational cost associated with a chemical mechanism arise from

1. the number of chemical species transported and the associated computational cost of computing reaction source terms, as well as transport properties, such as viscosities and diffusivities.
2. the chemical timescales of the reaction mechanism, which dictate the largest possible timestep: smaller scales required more steps.
3. the lengthscales of minor species profiles: smaller scales require more grid points.

The speedup factor associated with these three sources of computational costs are significant. In three-dimensional DNS, the number of transport equations is  $5+N_{sp} = 75$  for the detailed mechanism, and 24 for the reduced mechanism, giving a factor of 3 cost reduction. The chemical stiffness was found to be reduced by a factor of 10 with the reduced mechanism. This value was computed from one-dimensional ignition tests consisting of a temporal-spatial ignition from a temperature spike (600-1800 K) on an open domain with a  $10 \mu\text{m}$  grid spacing. After ignition, and during the diffusive propagation of the flame, the acoustic CFL was  $2.74 \times 10^{-8}$  s, and an accurate timestep size with the reduced mechanism was  $6.1 \times 10^{-9}$  s. For this case, the timestep size approached the acoustic CFL whereas the detailed mechanism was limited by chemical stiffness to a timestep size approximated ten times smaller. Finally, the reduced mechanism was found to require about 1.5 times fewer grid points, for the same resolution (e.g., number of grid points across the thinnest structures), than the detailed mechanism. In each direction, this results in a three-dimensional speedup factor of about 3.4. The overall speedup factor of the reduced mechanism, then, is about 100 for three-dimensional calculations and about 67 in two dimensions. These results do not include likely speedup associated with reduced cost of calculation of chemical source terms and transport properties for the reduced mechanism over the detailed mechanism.

DNS computational costs scale approximately as  $Re^3$  (with three space dimensions and time) [17]. A computational savings of 100 equates to a factor of 4.7 increase in Reynolds number or similar increases in domain size for constant run time/step size. The large

computational savings make realistic, fully resolved combustion simulations with complex chemistry possible and allow the extension of DNS with realistic chemistry to the domain of three-dimensional simulations. A three-dimensional temporal jet on a  $1.6 \times 1 \times 0.8$  cm domain with a  $25 \mu\text{m}$  grid spacing, run to 1 ms with the reduced mechanism, currently costs about 1 million CPU hours on current machines, so a factor of 100 speedup over the detailed mechanism is important. The two-dimensional decaying turbulence simulations presented later required 32,500 CPU-hours to run to 5 ms on a 2 GHz, 64 bit AMD Opteron Linux Cluster (Sandia National Laboratories' Thunderbird machine), with a  $25 \mu\text{m}$  grid, a  $2 \times 3$  cm domain, and an average step size of 15 ns. Clearly, the same calculation with the detailed mechanism would be prohibitive.

### 2.3.3 Mechanism Validations

The reduced chemical mechanism was extensively validated for the range of conditions experienced in the DNS including extinction/ignition, laminar flame speed, and diffusion flame solutions. Some of these results were repeated and are presented here. There are three sets of conditions which are of interest when testing the mechanism, corresponding to three gas conditions studied. These are listed in Table 2.3. The first is simply a pure fuel and air mixture with streams at 300 K. The second consists of streams at 550 K, a stoichiometric mixture fraction of 0.17, and slight oxygen enrichment at the stoichiometric point. The third set of conditions is intermediate and consists of preheating to 550 K, with a stoichiometric mixture fraction of 0.25, but no oxygen enrichment. This third set of conditions is not explicitly tested here. The first condition is used in one-dimensional relaxing, sooting flame studies, two-dimensional temporal mixing layers, and two-dimensional decaying turbulence. The second condition was used in three-dimensional extinction/ignition studies, and the third condition is used in the three-dimensional sooting study. Only in diffusion flame contexts does the value of the stoichiometric mixture fraction have meaning. The stoichiometric mixture fraction is varied by systematically moving nitrogen from the air stream to the fuel stream, resulting in a change in the position of the flame in the mixture coordinate, while maintaining a constant adiabatic flame temperature. This can have important impacts on flame dynamics but, of course, does not show up in premixed or 0-D configurations. The effect of preheating and oxygen enrichment is expected to have the strongest impact on the validity of the reduced mechanism.

**Table 2.3.** Fuel and oxidizer stream compositions.

Configuration	Stream	Mole Fractions			
		$C_2H_4$	$N_2$	$O_2$	T (K)
1	Fuel	1.0	0	—	300
	Oxidizer	—	0.79	0.21	300
2	Fuel	0.2546	0.7454	—	550
	Oxidizer	—	0.7359	0.2641	550
3	Fuel	0.42205	0.57795	—	550
	Oxidizer	—	0.73806	0.26914	550

Results comparing the detailed and reduced mechanisms are shown in canonical configurations consisting of opposed jet diffusion flames, premixed diffusion flames, perfectly stirred reactors (PSR), and batch reactors. All calculations are performed using the Chemkin suite of programs: Oppdif, Premix, PSR, and Senkin [86]. Here the overall flame behavior is primarily of concern, and not so much emphasis is placed on specific species profiles. However, species profiles are the focus of the opposed jet calculations, which are the most directly relevant quantities to the present DNS simulations.

### 2.3.3.1 Ignition Tests

The Senkin program represents a 0-D batch reactor and was used to compute ignition delay times for gas conditions 1 and 2 as a function of temperature. Figure 2.4 shows the results. Clearly, the effect of preheating is built into these calculations since temperature (actually, scaled inverse temperature) is the abscissa. The ignition results are practically the same for the two gas conditions and show very good agreement between the reduced and detailed mechanisms. In both conditions, the detailed ignition delay is a little higher than the reduced delay time, with the spacing between the detailed and reduced curves being about the same for both sets of gas conditions.

### 2.3.3.2 PSR Extinction

Figure 2.5 shows the extinction residence time in a PSR as a function of the equivalence ratio of the mixture. The PSR residence time is the volume of the PSR divided by the volumetric flow rate of the PSR (exit) gases. The point of extinction is just the point at which the temperature is discontinuous as the residence time is decreased (i.e., when the chemical state jumps from the burning to the unburning branch of the famed *S-curve*. Conditions 1 are at a lower temperature than conditions 2 and tolerate a lower residence

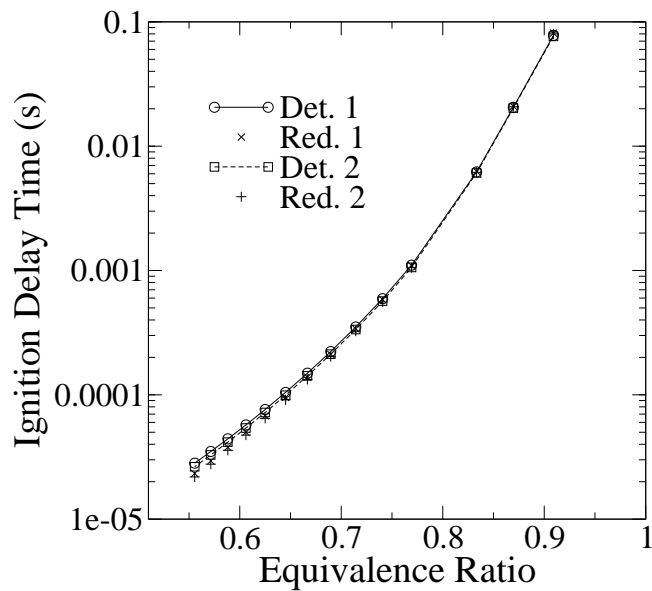


**Figure 2.4.** Comparison of detailed and reduced mechanism ignition delay time under two sets of gas conditions.

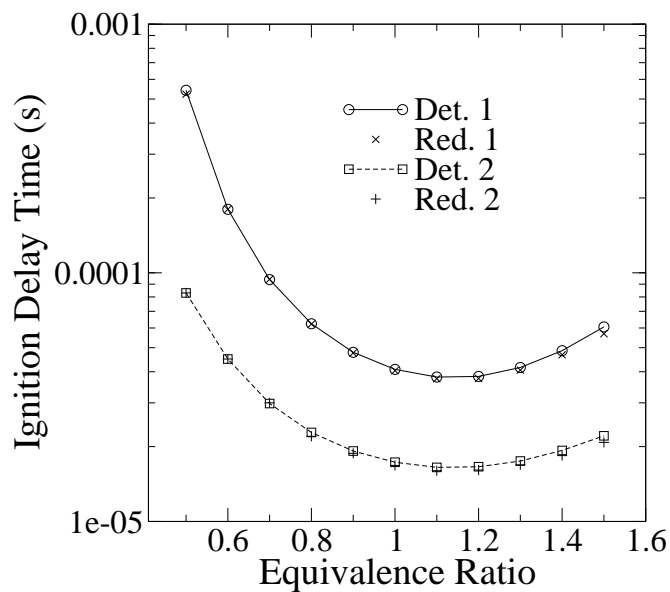


**Figure 2.5.** Comparison of detailed and reduced mechanism PSR extinction residence time.

time (higher flow, hence mixing, rate). The shape of the two curves is the same, and the agreement between the reduced and detailed mechanism is excellent, but slightly better for conditions 1. Here it is noted that the abscissa is the equivalence ratio. Here, a much wider range of fuel-oxygen ratio is exercised than occurs due to the oxygen enrichment in gas conditions 2 (which is achieved by reducing the stoichiometric nitrogen by about 15%). Hence, given only a validation of conditions 1, the validity of conditions 2 would not be a surprise. Of course, temperature may have a strong impact, but the validity of the ignition tests showed that temperature effects are nicely handled.

### 2.3.3.3 Laminar Premixed Flame Speed

While premixed flames are not explicitly investigated, three-dimensional turbulent combustion may have significant premixed flame propagation. This is especially true in regions of flame extinction where substantial interstream mixing may occur before ignition processes take over. Figure 2.6 shows the laminar premixed flame velocity for the two gas conditions, for the reduced and detailed mechanisms. The flame velocity is simply the unburned velocity that causes a steady flame (in the viewer's coordinates), or, in flame coordinates, the flame velocity is the velocity at which the unburned reactants

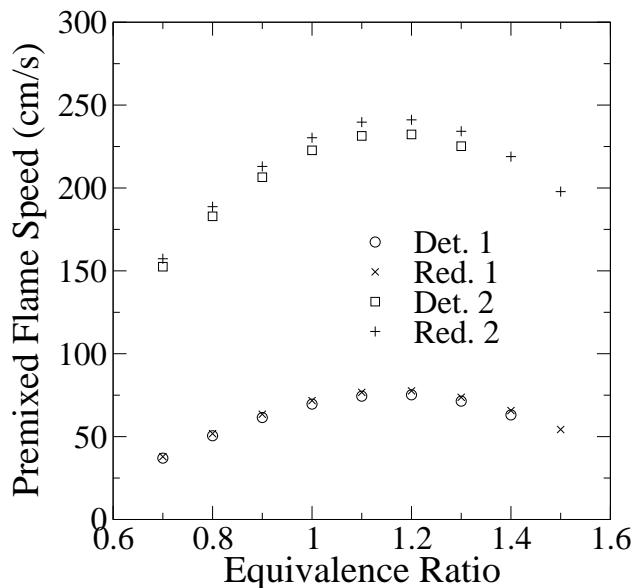


**Figure 2.6.** Comparison of detailed and reduced mechanism laminar premixed flame velocity.

approach the flame. This configuration includes effects of both reaction and diffusion, and the latter will depend (slightly) on the species differences in the mechanisms. The flame velocity is greater for conditions 2 because of the preheating of the mixture. The agreement is good for both cases, but better for conditions 1. However, the reduced mechanism is within 4% of the detailed mechanism under conditions 2. As expected, the flame speed peaks rich of stoichiometric. Premixed species profiles for conditions 1 (not shown) are also in excellent agreement. The detailed mechanism calculations did not converge at the highest values of the equivalence ratio.

### 2.3.3.4 Opposed Jet Diffusion Flame Comparisons

The previous computational configurations most directly exercise the reaction mechanism, but the opposed jet diffusion flame configuration most directly approximate the conditions of the DNS code. Four simulations were conducted: for each gas condition, two values of strain rate were compared. Temperature results are shown in Fig. 2.7. Under conditions 1, the mean extinction strain rate is 850 and 950  $\text{s}^{-1}$  for the detailed and reduced mechanisms, respectively. For the reduced mechanism, the mean extinction strain rate was 3650 and 4050  $\text{s}^{-1}$ . These results represent about a 10% difference under both gas conditions. For both gas conditions, the low strain value of 100  $\text{s}^{-1}$  is used, whereas the 850  $\text{s}^{-1}$  is used as the high strain value for conditions 1, and 3650  $\text{s}^{-1}$  is

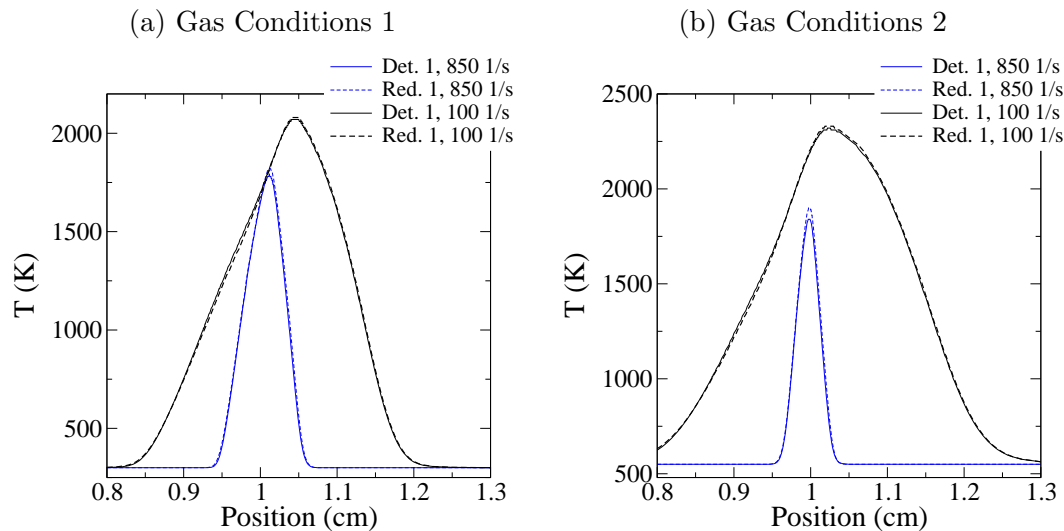


**Figure 2.7.** Comparison of temperature profiles for detailed and reduced mechanisms in an opposed jet diffusion flame calculation.

used as the high strain value for conditions 2. These latter values are at extinction for the detailed mechanism and within 10% of extinction for the reduced mechanism. Most simulations presented are designed to minimize extinction and ignition, but these are rigorous tests of the validity of the chemical mechanism. Here, the mean strain rate is reported, which is calculated as the velocity difference between the streams divided by the stream separation distance.

The temperature profiles in Fig. 2.7 for the four cases show that the results are within about 5% between the two mechanisms, with greater discrepancy at higher strain. The temperature differences will directly result in differences in the species concentrations.

Figures 2.8 and 2.9 show major and minor species profiles, respectively, for the four cases. Here, several important observations are made:

- Major species profiles show generally good agreement between the reduced and detailed mechanisms.
- Major and minor species profiles are in better agreement at low strain than high strain.
- Major species profiles are in slightly better agreement at gas conditions 1 than gas conditions 2.
- Minor species profiles generally follow the same trend as major species profiles with respect to the strain level and gas conditions.
- The minor species show noticeable differences between the detailed and reduced mechanisms. This is likely due to the effects of the raw mechanism differences, but enhanced by the temperature differences shown previously.
- The minor species profiles are in fairly good agreement for all species shown except acetylene. Certainly the agreement would be within experimental errors and errors between the detailed mechanism and experimental data.
- The acetylene profile is higher for the reduced mechanism since the reduced mechanism does not contain pathways to higher hydrocarbons. These pathways would act as a sink to the acetylene concentration. This overprediction is unfortunate from the point of view of soot calculations since acetylene acts as the soot nucleation and growth species. However, again, the error is reasonable, especially with respect

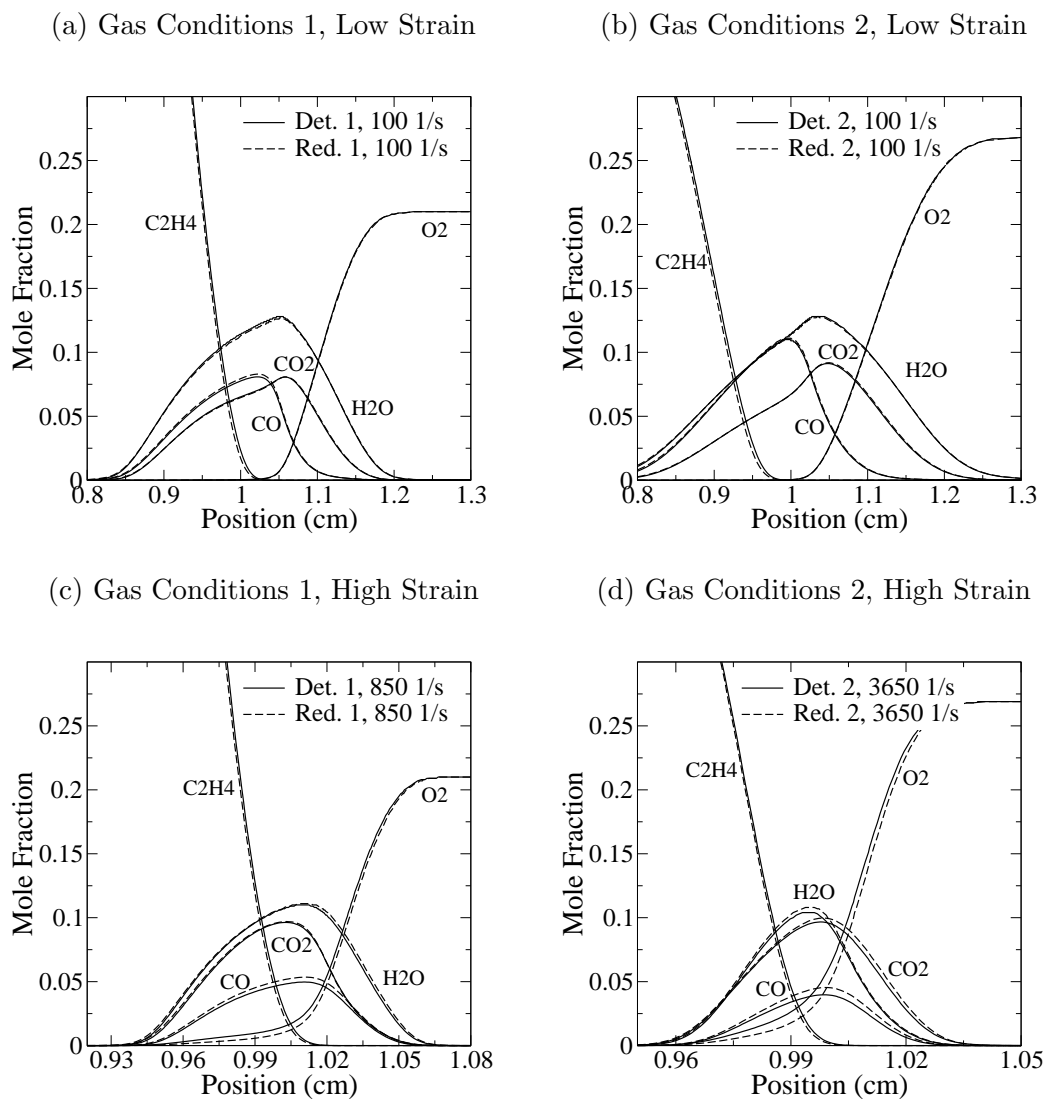


**Figure 2.8.** Comparison of major species profiles for opposed jet diffusion flames under two sets of gas conditions and at two levels of strain, as indicated.

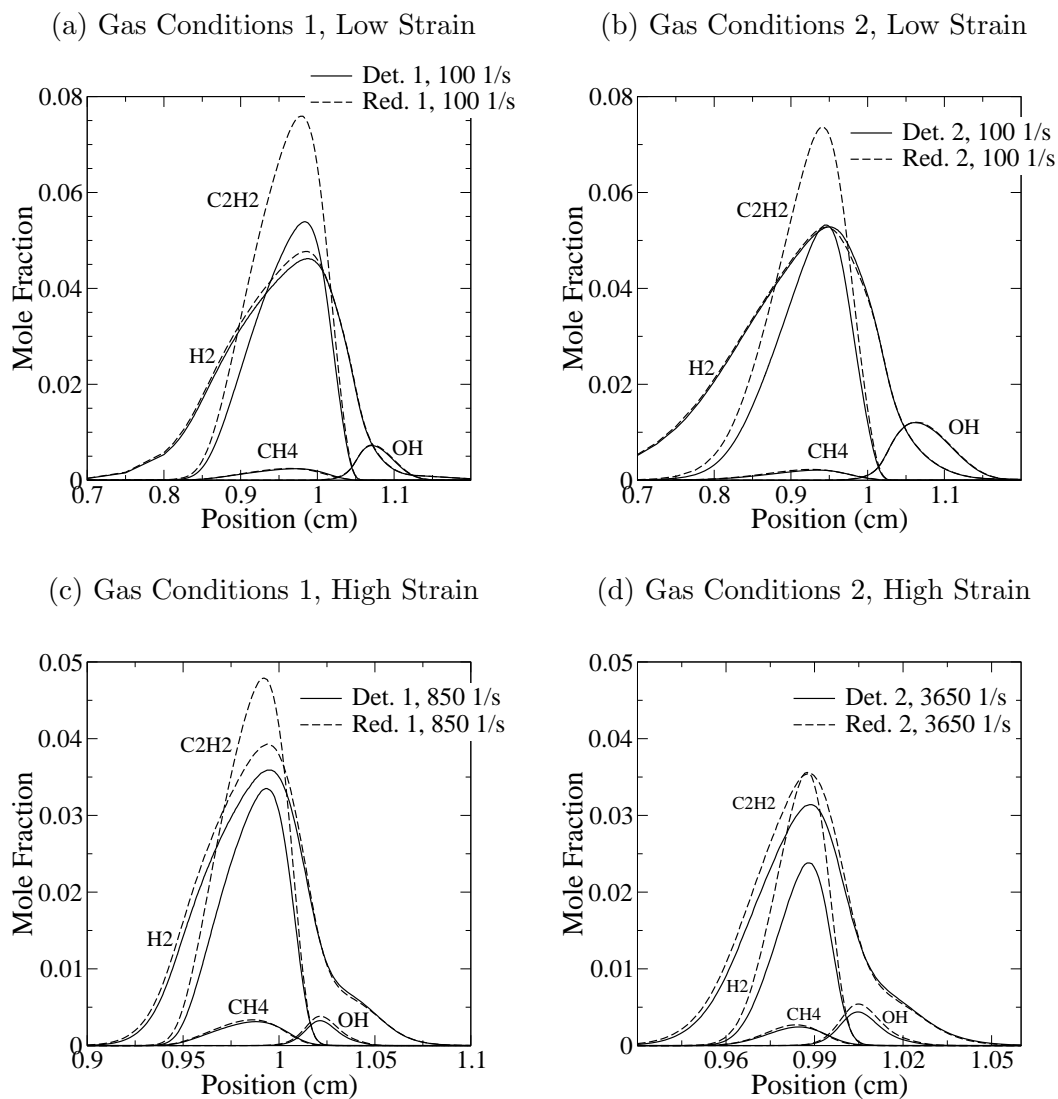


**Figure 2.9.** Comparison of minor species profiles for opposed jet diffusion flames under two sets of gas conditions and at two levels of strain, as indicated.

to uncertainties in current soot mechanisms. Likewise, acetylene is a global soot reaction species, taking the place of a much more complicated reaction system involving many higher hydrocarbons and pyrolyzing species.

The reduced ethylene mechanism presented here is shown to be very robust for all combustion conditions encountered in the DNS. Validations performed of both global flame properties, as well as individual species profiles, lend confidence in applying the mechanism to DNS simulation, with the ability to obtain quantitative results that are accurate representations of the real flow configurations. In addition, the reduced mechanism is shown to provide substantial computational cost savings, allowing more complex chemistry in turbulent combustion modeling and simulation.

### 2.3.4 One-Step Ethylene Mechanism

In order to speed up the turnaround time for setup of DNS simulations involving detailed chemistry, a one-step ethylene mechanism was tested. This allows fast exploration of the impact of turbulent scales, run time, domain size, and other important parameters that, to first order, only depend on the presence of a flame, and not the *right* flame. The single-step mechanism for ethylene combustion by Westbrook and Dryer [98] is



The rate expression for this reaction is given by

$$\frac{d[C_2H_4]}{dt} = -2 \times 10^{12} \cdot \exp(-15098/T) [C_2H_4]^{0.1} [O_2]^{1.65}, \quad (2.29)$$

with concentrations in units of mole per cubic centimeter and temperature units of Kelvin.

This mechanism was implemented in S3D and run in a two-dimensional temporal mixing layer. The results were poor. Very small timesteps were required to maintain stability, indicating severe chemical stiffness. For reference, timesteps of  $1 \times 10^{-9}$  seconds gave unacceptable integration errors while the acoustic CFL was  $1.5 \times 10^{-7}$  s on a 60  $\mu\text{m}$  grid—more than a factor of 60 higher. This behavior was unexpected. The activation energy is not too large (a large value tending to decrease flame thickness, requiring smaller grid sizes). As a simple test of the mechanism, the chemical timescale was estimated as

$$\tau = \frac{\Delta[C_2H_4]_{max}}{\left| \frac{d[C_2H_4]}{dt} \right|_{max}}. \quad (2.30)$$

When this expression is evaluated at 2000 K, with a stoichiometric unburned composition, the estimated timescale is  $1 \times 10^{-5}$  s, which is much larger than the timesteps taken in the DNS run.

It turns out that the problem is due to the subunity reaction order on the ethylene concentration. Chun Sang Yoo [99] provided an identical version of the above reaction with the following modification. Instead of a reaction order of 0.1, the expression  $0.1 + 0.9 \exp(-800Y_{C_2H_4})$  was used. This modification is explained here as follows. It is not immediately obvious that the low reaction order will not work. The revised formula transitions between 0.1 at a large concentration of ethylene and unity at small ethylene concentrations. At very small ethylene concentrations, it is not important to get the right rate, since the overall composition profile is what is desired, not the rate.

Figure 2.10 shows the normalized reaction rate of ethylene versus ethylene concentration at constant temperature and oxygen concentration. The dashed line shows the original rate, which is linear on the log scale, and has a slope of 0.1. The solid line is the variable-order rate showing two regions of constant slope with a smooth variation.

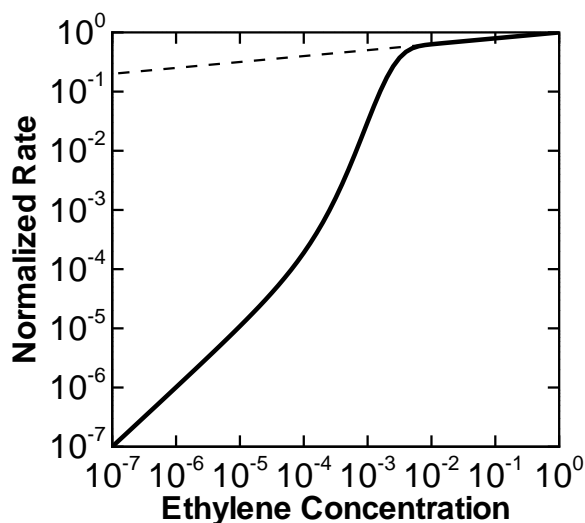


**Figure 2.10.** Plot of the normalized rate at constant temperature and oxygen concentration versus ethylene concentration. The dashed line is the original 0.1 order curve. Solid line is the revised variable-order curve.

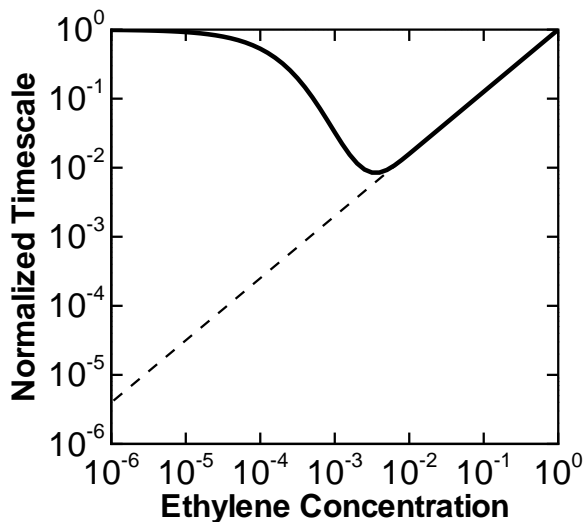
This figure is only intended to show the shape of the curves, not the magnitudes. At low concentration, the slope becomes 1, corresponding to the unity reaction order. The point of these figures is that the rate of the original formulation drops much slower with concentration than the revised formulation. Qualitatively, the rate is still relatively large when the composition is small, which makes the system very sensitive to the timestep size. Comparing the curves for a given timestep, at low concentration, the fractional change in the ethylene concentration will be much larger in the original 0.1 order case than for the unity order curve, or, in other words, for equal fractional changes in concentration, the order 0.1 curve will require a smaller timestep than the order 1 curve, due to the larger rate of the former.

Figure 2.11 shows more quantitatively the reason for this. Applying expression in Eq. (2.30) to the reaction rate gives

$$\tau_{orig} = \frac{[C_2H_4]}{[C_2H_4]^{0.1}} = [C_2H_4]^{0.9}, \quad (2.31)$$

$$\tau_{new} = \frac{[C_2H_4]}{[C_2H_4]^{0.1+0.9 \exp(-800Y_{C_2H_4})}} = [C_2H_4]^{0.9(1-\exp(-800Y_{C_2H_4}))}. \quad (2.32)$$

In the original case, the timescale goes to zero as the concentration goes to zero, but as the chemical timescale decreases, the timestep size must also decrease, which increases



**Figure 2.11.** Plot of the normalized timescale versus the ethylene concentration. The dashed line is the original 0.1 order curve. Solid line is the revised variable-order curve.

the stiffness, all else being equal (e.g., flow properties). In the variable-order case, at large concentration, the timescale decreases as in the original case, but as the concentration of ethylene goes to zero, the timescale becomes finite because the exponent becomes zero. Hence, the stiffness goes away at small concentrations. Figure 2.11 shows the behavior graphically. This same trouble may be expected to occur, in general, for reactants with reaction orders less than one. The solution is a neat trick that works under the assumption that at near-zero concentration the rate can and should be near zero, even if the rate expression indicates otherwise. Part of the problem, of course, is that the rate expression is being applied in flame regions of low ethylene concentration, which is likely outside the range of the global model anyway.

The approach considered here lends ideas of how to approach stiffness-related problems in other settings. For example, it may be feasible to use unity Lewis number soot diffusion in regions of little or no soot to aid stability induced by low diffusivity and/or the form of the soot diffusion term.

## 2.4 Soot Model

Soot forms at high temperatures on the fuel-rich side of diffusion flames where there is insufficient oxygen for complete combustion. In these regions, the fuel is pyrolyzed to unsaturated hydrocarbon species, which react to form aromatic species. These aromatics then grow by the addition of other aromatics and smaller alkyl species, such as acetylene, to form polyaromatic hydrocarbons (PAH), which, upon further growth, form the smallest soot particles on the order of 1 nm in size and containing on the order of a hundred carbon atoms [100]. These particles grow, coagulate, and oxidize (by mainly  $O_2$  and  $OH$ ) in a flame. Figure 2.12 is a schematic of the soot evolution adapted from Bockhorn [3]. Soot begins as gas phase species and grows to become solid particles. Several reviews detailing soot chemistry have been published [101, 102, 100].

Soot models consist of two important components:

1. Description of the soot nucleation and growth/oxidation mechanisms, and
2. Representation of the particle size distribution (PSD).

Because of the highly complex nature of soot formation, many attempts have been made to simplify the chemistry to account for only the most important aspects. For example, in practical applications, one is not interested in a highly detailed description

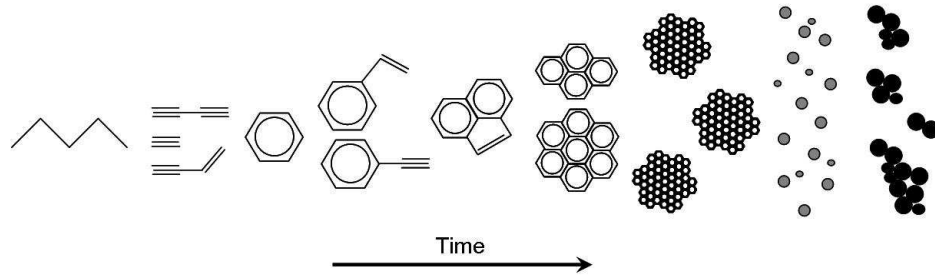


**Figure 2.12.** Schematic of soot evolution: nucleation, growth/oxidation, coagulation. Adapted from Ref. [3]

of the chemistry, but rather with the amount of soot formed and the impact this has on temperature and radiative properties of the flame. The level of chemistry included is dictated by the satisfactory representation of desired quantities. Kennedy (1997) has reviewed at least 33 soot models which range from empirical correlations based on the local mixture fraction, to semiempirical multistep global schemes, to detailed mechanisms for PAH and soot growth [100].

A common approach in soot modeling is to consider a four-process mechanism consisting of nucleation, growth, oxidation, and particle coagulation. Each process may consist of many individual reaction steps (e.g., oxidation in terms of O<sub>2</sub> and OH), but often, the processes are written explicitly as individual steps. Here, simulations with soot are based on the model of Leung and Lindstedt [5], which has been widely applied in simulations of turbulent sooting flames. The model assumes a monodispersed size distribution defined in terms of the particle number density,  $n$ , and soot mass fraction,  $Y_s$ . The four reaction steps are given by

1. nucleation:  $C_2H_2 \rightarrow 2C(s) + H_2$
2. growth:  $nC(s) + C_2H_2 \rightarrow (n + 2)C(s) + H_2$
3. oxidation:  $C(s) + \frac{1}{2}O_2 \rightarrow CO$
4. coagulation:  $(n) \rightarrow (n - 1)$

Here, C(s) represents soot ( $n$  denoting  $n$  carbons) and a mole of soot is taken as a mole of carbon atoms. There are four gaseous species involved, C<sub>2</sub>H<sub>2</sub>, O<sub>2</sub>, H<sub>2</sub>, and CO. The following reactions rates are given for each of the above reactions:

$$R_1 = 0.1 \times 10^5 e^{-21100/T} [C_2H_2], \quad (2.33)$$

$$R_2 = 0.6 \times 10^4 e^{-12100/T} [C_2H_2] \sqrt{A_s}, \quad (2.34)$$

$$R_3 = 0.1 \times 10^5 T^{1/2} e^{-19680/T} [O_2] A_s, \quad (2.35)$$

$$R_4 = 2C_a \left( \frac{6W_c}{\pi\rho_s} \right)^{1/6} \left( \frac{6k_bT}{\rho_s} \right)^{1/2} \left( \frac{\rho Y_s}{W_c} \right)^{1/6} n^{11/6}. \quad (2.36)$$

The units of reactions 1-3 are kilomole per cubic meter per second, and the coagulation rate is given in units of number per cubic meter per second. The quantity  $A_s$  is the particle surface area per unit volume, given by

$$A_s = \pi \left( \frac{6\rho Y_s}{\pi\rho_s} \right)^{2/3} n^{1/3}, \quad (2.37)$$

where  $\rho_s$  is the soot density. Soot particles are assumed spherical, all carbon, and with a constant particle density of 1850 kg/m<sup>3</sup>. The first nucleated soot particle is assumed to consist of 100 carbon atoms, and the parameter  $C_a$  is taken to be 9.0. Since soot particles are small enough,  $O(50 \text{ nm})$ , and the Stokes number is much smaller than unity, the soot particles are assumed to follow the gas velocity without any impact on the overall fluid momentum. The three-dimensional simulations transport three moments, as discussed below. For the one-dimensional and two-dimensional simulations, the following two transport equations were added to the set given by Eqs. (2.1)-(2.4):

$$\text{soot mass fraction:} \quad \frac{\partial(\rho Y_s)}{\partial t} = -\frac{\partial(\rho Y_s v_i)}{\partial x_i} - \frac{\partial j_{s,i}}{\partial x} + S_{Y_s}, \quad (2.38)$$

$$\text{particle number density:} \quad \frac{\partial n}{\partial t} = -\frac{\partial(nv_i)}{\partial x_i} - \frac{\partial j_{n,i}}{\partial x} + S_n. \quad (2.39)$$

The soot reactions are fully coupled to the gas reactions through additional source terms added to the species transport equations for C<sub>2</sub>H<sub>2</sub>, O<sub>2</sub>, H<sub>2</sub>, and CO. The reaction source terms for soot reactions are given by

$$\text{number density:} \quad S_n = \frac{2N_a R_1}{C_{min}} - R_4, \quad (2.40)$$

$$\text{soot mass fraction:} \quad S_{Y_s} = W_c \cdot (2R_1 + 2R_2 - R_3), \quad (2.41)$$

$$\text{C}_2\text{H}_2: \quad S_{C_2H_2} = -W_{C_2H_2} \cdot (R_1 + R_2), \quad (2.42)$$

$$\text{O}_2: \quad S_{O_2} = -W_{O_2} \cdot R_3/2, \quad (2.43)$$

$$\text{H}_2: \quad S_{H_2} = -W_{H_2} \cdot (R_1 + R_2), \quad (2.44)$$

$$\text{CO:} \quad S_{CO} = W_{CO} \cdot R_3. \quad (2.45)$$

With the addition of soot, density in the governing equations refers to the total density (gas + soot), as does the total energy. The internal energy is computed using the ideal mixing rule  $e = Y_g e_g + Y_s e_s$ . The heat capacity is computed similarly. The soot energy and heat capacity are computed assuming the soot exists as graphite. The system pressure is computed as in Eq. (2.7), but there,  $\rho = \rho_g$ , with

$$\rho_g = \frac{\rho(1 - Y_s)}{1 - \frac{\rho Y_s}{\rho_s}}, \quad (2.46)$$

where  $\rho Y_s / \rho_s = f_v$ . Here, the denominator is included, but expected to depart from unity only in the sixth decimal place or smaller since soot volume fractions are on the order of 1 ppmv or less. The heat flux vector in Eq. (2.6) is modified by the addition of the term  $h_s j_s$ .

The soot diffusion flux was computed from

$$j_M = -\rho D_{p1} \nabla \left( \frac{1}{Le_s} \frac{M}{\rho} \right) - 0.556 M \frac{\nu}{T} \nabla T, \quad (2.47)$$

where  $M$  is either  $n$  or  $\rho Y_s$ . The first term represents Brownian diffusion, and the second term accounts for thermophoresis. This expression was derived similar to [30] from the general transport equation for the  $k^{\text{th}}$  particle size and applying the definition of the  $r^{\text{th}}$  soot mass-moment  $M_r = \sum_{k=1}^{\infty} m_1^r k^r n_k$ , (with  $m_k = k m_1$ ). Assuming the soot particle diffusivity in the free-molecular regime varies inversely as the square of the particle diameter as in [103],  $D_{p,k} \propto k^{-2/3}$ , so  $D_{p,k} = D_{p,1} k^{-2/3}$ . This results in fractional moments ( $M_{1/3}$  and  $M_{-2/3}$ ) in the diffusion flux of the transport equations, which are closed by logarithmic interpolation of  $M_0$  and  $M_1$ . Equation (2.47) results from assuming a unity Lewis number for particles of size  $k = 1$ ,  $Le_s = k^{2/3} = (\rho Y_s / n m_1)^{2/3}$ , where  $k$  is the number of carbons in the mean soot size defined by  $M_0$  and  $M_1$ . The first term in Eq. (2.47) is negligible [30], but is included for completeness. For example, nominal conditions of 1500 K and a volume fraction of 1 ppmv, and a number density of  $1 \times 10^{17} \text{ m}^{-3}$ , give  $Le_s \approx 9500$ . As implemented,  $Le_s$  is assumed to be locally constant and, therefore, taken outside the gradient.

## 2.5 The Method of Moments

As noted above, the representation of the particle size distribution is important in soot modeling. Two-moment models assume a monodispersed size distribution in terms of the number density and soot mass fraction, but often, they are not rigorously formulated as moment methods. The three-dimensional soot simulation transports three moments, assuming a lognormal particle size distribution, and the method of moments is described here in more detail. A particle size distribution can be written in a discrete form or a continuous form. Here, the discrete form is emphasized since this is more physically relevant for real particles composed of atoms. A continuous representation is also applied when convenient.

Several approaches are employed for representing the PSD, listed below in decreasing order of computational cost:

- Direct methods, in which all particle sizes are accounted for.
- Sectional methods, in which a few representative (lumped) particle sizes are tracked.
- Moment methods, in which a few (usually two to six) moments of the PSD are tracked.

Direct methods are not employed in spatially varying flows for soot formation. Sectional methods have been employed in two-dimensional simulations of soot formation in laminar flames [104, 11]. By far the most common approach for turbulent simulations is the method of moments since this method requires the fewest transport equations (one for each moment considered).

The starting point for the method is the balance equation for the number density, written as

$$\frac{\partial n_i}{\partial t} + \frac{\partial v_k n_i}{\partial x_k} = -\frac{\partial n_j V_{j,k}}{\partial x_k} + S_i, \quad (2.48)$$

where  $n_i$  has units of number per cubic meter,  $V_{j,k}$  is the diffusion velocity of particle size  $i$ , and  $S_i = N_i + G_i + C_i$  is the reaction source term with nucleation, net growth, and coagulation components, respectively, with units of number per cubic meter per second. Moments of the size distribution are defined as

$$M_r = \sum_{i=1}^{\infty} m_i^r n_i, \quad (2.49)$$

where  $M_r$  is the  $r^{th}$  moment, and  $m_i$  is the mass of particle  $i$ . This expression defines a mass-moment, which is primarily used here although other moments are possible and useful. The particle masses are assumed to differ by a single carbon atom so that  $m_i = i \cdot m_1$ . In Eq. (2.49), if  $m_i$  is replaced by  $d_i$ , a size-moment is obtained, and if  $m_i$  is replaced by  $i$ , a monomer-moment is obtained. A continuous version of Eq. (2.49) is

$$M_r = \int_0^\infty m^r f(m) dm, \quad (2.50)$$

where  $f(m)$  is the analog of  $n_i$  and is a number density proper, having units of number per cubic meter per kilogram.

The moment equations are derived by applying Eq. (2.49) to Eq. (2.48):

$$\frac{\partial M_r}{\partial t} + \frac{\partial v_k M_r}{\partial x_k} = - \frac{\partial M_r V_k}{\partial x_k} + S_r. \quad (2.51)$$

Here, the velocity and diffusion velocity are assumed independent of particle size, which is true of small soot particles transported by convection and thermophoresis. Evaluation of the moment sources  $N_r$ ,  $G_r$ , and  $C_r$  is the primary challenge in the method. As shown below, the moment equations are exact but contain unclosed terms, whose computation requires a knowledge of the size distribution. Since the size distribution is generally unknown, models or approximations are needed to express the terms as functions of the known, transported moments.

### 2.5.1 Nucleation

Nucleation occurs as the result of gas phase reactions. In soot formation, there is no distinct mass at which gaseous molecules grow to become soot. Generally, a representative nucleation rate is written with an assumed minimum particle size. Here, it assumed that particles are nucleated with acetylene to produce a particle with  $C_{min}$  carbon atoms, where  $C_{min}$  might be 100. Other nucleation species could be used, such as pyrene. Here is the reaction used for example:



The nucleation rate in Eq. (2.48) is given by

$$N_i = S_{nuc}\delta(m_i - m_{min}), \quad (2.53)$$

where  $S_{nuc}$  has units of number per cubic meter per second,  $m_{min} = m_1 * C_{min}$ , and  $\delta(m_i - m_{min})$  is zero except where  $m_i = m_{min}$ ; that is, nucleation is zero for all sizes except the smallest.  $S_{nuc}$  can be written for the above nucleation reaction, Eq. (2.52), as

$$S_{nuc} = \frac{2N_a R_{nuc}}{C_{min}}, \quad (2.54)$$

where  $N_a$  is the Avogadro number, the factor 2 is a molar conversion, and  $R_{nuc}$  is the reaction rate constant with units of kilomole per cubic meter per second.

Applying the moment definition Eq. (2.49) to the nucleation portion of the source term Eq. (2.53) of Eq. (2.48) yields

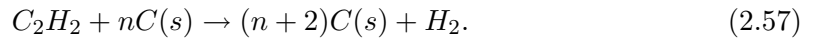
$$\sum_i m_i^r N_i = m_{min}^r S_{nuc}, \quad (2.55)$$

$$N_r = m_{min}^r S_{nuc}. \quad (2.56)$$

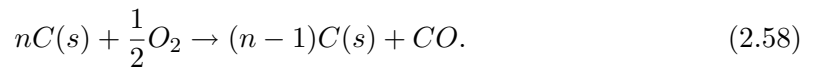
This result can easily be extended to more complex nucleation steps involving, possibly many, nucleation species.

### 2.5.2 Growth

Particle growth arises from the rate at which gaseous species react with the ideally solid particles to form larger particles. A common growth reaction written with acetylene as the growth species is given by



An oxidation reaction in terms of oxygen is given by



In these equations,  $n$  just refers to soot with  $n$  carbons. Particle sizes are assumed to be spaced by single carbon atoms, so the net growth rate of a given size  $i$  is the rate at

which carbon atoms are added to particles of size  $i - 1$  , minus the rate at which carbon atoms are added to particles of size  $i$ . The rate of growth is assumed to be proportional to the surface area of the particle and is given by

$$G_i = \frac{k_s}{m_1} (n_{i-1} S_{i-1} - n_i S_i), \quad (2.59)$$

with terms having the following units:

$$G (=) \frac{\text{particles}}{m^3 s}, \quad (2.60)$$

$$k_s (=) \frac{kg}{m^2 s}, \quad (2.61)$$

$$m_1 (=) \frac{kg}{\text{carbon atom}}, \quad (2.62)$$

$$n (=) \frac{\text{particles}}{m^3}, \quad (2.63)$$

$$S (=) \frac{m^2}{\text{particle}}. \quad (2.64)$$

Particles are assumed spherical and the surface area of a particle is given by

$$S_i = \pi d_i^2 = \pi \left[ \left( \frac{6v_i}{\pi} \right)^{1/3} \right]^2 = \pi \left( \frac{6}{\rho_s \pi} \right)^{2/3} m_i^{2/3}, \quad (2.65)$$

where  $v_i$  is particle volume, and  $\rho_s$  is the particle density. Define  $\gamma$  as

$$\gamma = \frac{k_s}{m_1} \pi \left( \frac{6}{\rho_s \pi} \right)^{2/3}, \quad (2.66)$$

in Eq. (2.59) to give

$$G_i = \gamma (n_{i-1} m_{i-1}^{2/3} - n_i m_i^{2/3}). \quad (2.67)$$

Apply Eq. (2.49) to Eq. (2.48), considering just the growth term, as was done for the nucleation term to yield

$$G_r = \gamma \sum_i m_i^r n_{i-1} m_{i-1}^{2/3} - \gamma \sum_i m_i^r n_i m_i^{2/3}. \quad (2.68)$$

The second term is just  $\gamma M_{r+2/3}$  and is denoted by  $(T)$  below. At this point it is easier to split the masses as  $m_i = im_1$ :

$$G_r = \gamma m_1^{r+2/3} \sum_i n_{i-1} i^r (i-1)^{2/3} - (T). \quad (2.69)$$

Variables are changed using

$$u = i - 1, \quad (2.70)$$

$$i = u + 1. \quad (2.71)$$

Hence, Eq. (2.69) becomes

$$G_r = \gamma m_1^{r+2/3} \sum_u (u+1)^r u^{2/3} n_u - (T). \quad (2.72)$$

Now use the binomial expansion defined as (with generic notation):

$$(x+a)^n = \sum_{k=0}^n \binom{n}{k} x^k a^{n-k}, \quad (2.73)$$

$$\binom{n}{k} = \frac{n!}{k!(n-k)!}, \quad (2.74)$$

so that

$$(u+1)^r = \sum_{k=0}^r \binom{r}{k} u^k. \quad (2.75)$$

Inserting this expression into Eq. (2.72) yields

$$G_r = \gamma m_1^{r+2/3} \sum_u \sum_{k=0}^r \binom{r}{k} u^{k+2/3} n_u - (T), \quad (2.76)$$

$$= \gamma m_1^{r+2/3} \sum_{k=0}^r \binom{r}{k} \sum_u u^{k+2/3} n_u - (T), \quad (2.77)$$

$$= \gamma m_1^{r+2/3} \sum_{k=0}^r \binom{r}{k} M_{k+2/3} m_1^{-k-2/3} - (T), \quad (2.78)$$

$$= \gamma \sum_{k=0}^{r-1} \binom{r}{k} M_{k+2/3} m_1^{r-k}. \quad (2.79)$$

In the second step, the definition of the moment is used (where  $u$  has units of monomer; multiply and divide by  $m_1^{k+2/3}$  with  $m_1^{-k-2/3}$  left over). In the third step, (T) cancels with the last term in the sum. The continuous version was derived as well and gives the same result if only the last term in the summation is kept. Here, this assumption is made since the particle size distribution is practically continuous (a 30 nm particle has about one million carbons), and the moment growth term is given by

$$G_r = \pi \left( \frac{6}{\rho_s \pi} \right)^{2/3} k_s r M_{r-1/3}. \quad (2.80)$$

The fractional moment,  $M_{r-1/3}$ , appears in the equation. This moment must be written in terms of the other (integer) moments to obtain a closed-form solution.

### 2.5.3 Coagulation

Soot particles are small compared to the mean free path of the gas, so the particle interactions are assumed to occur in the free molecular regime. The coagulation rate of spherical particles in this regime is given by

$$C_i = \frac{1}{2} \sum_{j=1}^{i-1} \beta_{j,i-j} n_j n_{i-j} - n_i \sum_{j=1}^{\infty} \beta_{i,j} n_j. \quad (2.81)$$

The first term is a source of particles of size  $i$  from collisions among smaller particles, and the second term is a sink of particles of size  $i$  from collisions with particles of size  $i$  and all other sizes. The  $\frac{1}{2}$  factor in the first term corrects for double counting. For example, particle size 8 is formed from sizes 5 and 3, but the summation gives  $\beta_{3,5} n_3 n_5$  for  $j = 3$ , but also  $\beta_{5,3} n_5 n_3$  for  $j = 5$ . Multiplying by half counts just one of the terms. The coagulation rate is proportional to the concentrations of the colliding particles and a frequency factor,  $\beta$ , which is given by

$$\beta_{i,j} = \epsilon \left( \frac{6k_b T}{\rho_s} \right)^{1/2} \left( \frac{3}{4\pi \rho_s} \right)^{1/6} \left( \frac{1}{m_i} + \frac{1}{m_j} \right)^{1/2} (m_i^{1/3} + m_j^{1/3})^2 \quad (2.82)$$

$$= K_f \cdot \left( \frac{1}{m_i} + \frac{1}{m_j} \right)^{1/2} (m_i^{1/3} + m_j^{1/3})^2. \quad (2.83)$$

Here,  $\epsilon$  is an agglomeration rate constant in the range of 3-9,  $k_b$  is the Boltzmann constant, and  $K_f$  is a grouping of terms. The following approximation is applied in this equation and relaxed later on

$$\left(\frac{1}{m_i} + \frac{1}{m_j}\right)^{1/2} = b \cdot \left(\frac{1}{m_i^{1/2}} + \frac{1}{m_j^{1/2}}\right), \quad (2.84)$$

where  $b$  is a constant. This approach was used by Pratsinis [105] and greatly simplifies the calculation of the moments. The factor  $b$  is bounded between  $1/\sqrt{2}$  and 1 (or 0.707 and 1). The ratio approaches unity when the colliding particles have widely different sizes and approaches  $1/\sqrt{2}$  when the particles are the same size. Since particle size distributions are often approximately lognormal, the size range varies widely (also, particle collisions space particles geometrically), so we may expect to use  $b \approx 1$  and obtain reasonable results. If  $b$  is taken as the average of its bounds, at worst a 15% error results. The moment derivation is simplified by using the continuous particle size distribution. The equation for  $\beta$  is the same, but particle masses are not discrete. The corresponding expression for Eq. (2.81) is

$$C(m) = \frac{1}{2} \int_0^m \beta(\mu, m - \mu) f(\mu) f(m - \mu) d\mu - \int_0^\infty \beta(\mu, m) f(\mu) f(m) d\mu. \quad (2.85)$$

Here,  $\mu$  and  $m$  are the masses of two particles.

Applying Eq. (2.50) to this equation to obtain the moment source is straightforward but tedious (the final result is given in Eqs. (2.105)-(2.110)):

$$C_r = \frac{1}{2} \int_0^\infty m^r \left( \int_0^m \beta(m - \mu, \mu) f(m - \mu) f(\mu) d\mu \right) dm - \int_0^\infty m^r \int_0^\infty \beta(m, \mu) f(m) f(\mu) d\mu dm. \quad (2.86)$$

With the first term, the double integral amounts to finding the volume above an area in the  $\mu, m$  plane. If  $\mu$  is the y-axis and  $m$  is the x-axis, the region is below the  $\mu = m$  line. The inner integration above *marches* vertically along lines of constant  $m$ , and the outer

integration increments these lines towards  $m \rightarrow \infty$ . The integration bounds on the first term are inverted to cover the same region:

$$C_r = \frac{1}{2} \int_0^\infty \left( \int_\mu^\infty m^r \beta(m - \mu, \mu) f(m - \mu) dm \right) f(\mu) d\mu - (T). \quad (2.87)$$

Here, the inner integral marches along horizontal lines of constant  $\mu$  from  $\mu = m$  towards infinity, whereas the outer integral moves these lines from  $\mu = 0$  towards  $\infty$ . These two cases are illustrated in Fig. 2.13 on the right and left, respectively. Changing variables on the inner integral in Eq. (2.87), and the corresponding integration limits gives

$$u = m - \mu, \quad (2.88)$$

$$du = dm, \quad (2.89)$$

$$m = \mu \rightarrow u = 0, \quad (2.90)$$

$$m = \infty \rightarrow u = \infty - \mu = \infty, \quad (2.91)$$

$$C_r = \frac{1}{2} \int_0^\infty \left( \int_0^\infty (u + \mu)^r \beta(u, \mu) f(u) du \right) f(\mu) d\mu - (T), \quad (2.92)$$

$$= \frac{1}{2} \int_0^\infty \left( \int_0^\infty \sum_{k=0}^r \binom{r}{k} u^k \mu^{r-k} \beta(u, \mu) f(u) du \right) f(\mu) d\mu - (T). \quad (2.93)$$

The last step uses the binomial expansion, Eq. (2.73). The variable  $u$  is notational and can be replaced by  $m$ . Rearranging the expression for  $C_r$ , and bringing (T) back in gives

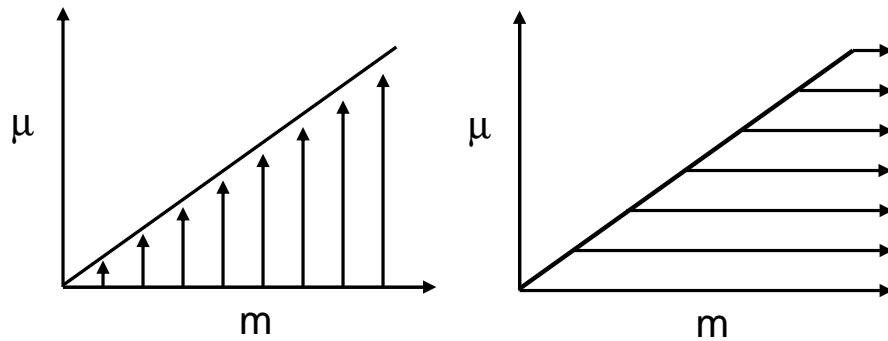


**Figure 2.13.** Schematic illustrating integration bounds.

$$C_r = \frac{1}{2} \int_0^\infty \int_0^\infty f(m)f(\mu)\beta(m,\mu) \left( \sum_{k=0}^r \binom{r}{k} \mu^{r-k} m^k \right) \quad (2.94)$$

$$- 2f(m)f(\mu)m^r\beta(m,\mu)dmd\mu,$$

$$= \frac{1}{2} \int_0^\infty \int_0^\infty f(m)f(\mu)\beta(m,\mu) \left[ -2m^r + \sum_{k=0}^r \binom{r}{k} m^k \mu^{r-k} \right] dmd\mu, \quad (2.95)$$

$$= \int_0^\infty \int_0^\infty f(m)f(\mu)\beta(m,\mu) \left[ -m^r + \frac{1}{2} \sum_{k=0}^r \binom{r}{k} m^k \mu^{r-k} \right] dmd\mu. \quad (2.96)$$

The term in brackets in this last equation is expanded below for the first six moments  $r = 0$  to  $r = 5$ .

$$r = 0 : \left[ -\frac{1}{2} \right], \quad (2.97)$$

$$r = 1 : \left[ -m + \frac{1}{2}\mu + \frac{1}{2}m \right], \quad (2.98)$$

$$r = 2 : \left[ -m^2 + \frac{1}{2}\mu^2 + m\mu + \frac{1}{2}m^2 \right], \quad (2.99)$$

$$r = 3 : \left[ -m^3 + \frac{1}{2}\mu^3 + \frac{3}{2}m\mu^2 + \frac{3}{2}m^2\mu + \frac{1}{2}m^3 \right], \quad (2.100)$$

$$r = 4 : \left[ -m^4 + \frac{1}{2}\mu^4 + 2m\mu^3 + 3m^2\mu^2 + 2m^3\mu + \frac{1}{2}m^4 \right], \quad (2.101)$$

$$r = 5 : \left[ -m^5 + \frac{1}{2}\mu^5 + \frac{5}{2}m\mu^4 + 5m^2\mu^3 + 5m^3\mu^2 + \frac{5}{2}m^4\mu + \frac{1}{2}m^5 \right]. \quad (2.102)$$

The coefficients of these terms follow Pascal's triangle. To compute  $C_r$ , the approximate expression for  $\beta$  is expanded to

$$\begin{aligned} \beta(m,\mu) = K_f \cdot b \cdot (m^{1/6} + 2m^{-1/6}\mu^{1/3} + m^{-1/2}\mu^{2/3} \\ + m^{2/3}\mu^{-1/2} + 2m^{1/3}\mu^{-1/6} + \mu^{1/6}), \end{aligned} \quad (2.103)$$

and inserted, along with the expanded terms in brackets, into Eq. (2.96). By inspection one can see that the result will be a sum of products of fractional moments. The symmetry of the expression for  $\beta$  and the integration in Eq. (2.96) with respect to  $m$  and  $\mu$  allow substantial simplifications in the calculation. For example, for  $r = 5$ , the first, second, and last terms in brackets in Eq. (2.102) cancel, while the third and sixth terms add together, along with the fourth and fifth terms. The result is

$$\begin{aligned}
C_5 &= 10 \int_0^\infty \int_0^\infty m^2 \mu^3 f(m) f(\mu) \beta(m, \mu) dm d\mu \\
&\quad + 5 \int_0^\infty \int_0^\infty m \mu^4 f(m) f(\mu) \beta(m, \mu) dm d\mu.
\end{aligned} \tag{2.104}$$

Expanding  $\beta$  and performing the integration for all  $r$  listed gives

$$C_0 = -K_f b (M_0 M_{1/6} + 2M_{1/3} M_{-1/6} + M_{2/3} M_{-1/2}), \tag{2.105}$$

$$C_1 = 0, \tag{2.106}$$

$$C_2 = 2K_f b (M_1 M_{7/6} + 2M_{4/3} M_{5/6} + M_{5/3} M_{1/2}), \tag{2.107}$$

$$C_3 = 3K_f b (M_1 M_{13/6} + 2M_{4/3} M_{11/6} + M_{5/3} M_{3/2} \tag{2.108}$$

$$+ M_{1/2} M_{8/3} + 2M_{5/6} M_{7/3} + M_{7/6} M_2),$$

$$C_4 = 4K_f b (M_1 M_{19/6} + 2M_{17/6} M_{4/3} + M_{5/2} M_{5/3} \tag{2.109}$$

$$+ M_{11/3} M_{1/2} + M_{10/3} M_{5/6} + M_3 M_{7/6})$$

$$+ 3K_f b (2M_2 M_{13/6} + 4M_{11/6} M_{7/3} + 2 * M_{3/2} M_{8/3}),$$

$$C_5 = 10K_f b (M_{13/6} M_3 + 2M_{11/6} M_{10/3} + M_{3/2} M_{11/3} + \tag{2.110}$$

$$+ M_{8/3} M_{5/2} + 2M_{7/3} M_{17/6} + M_2 M_{19/6})$$

$$+ 5K_f b (M_{7/6} M_4 + 2M_{5/6} M_{13/3} + M_{1/2} M_{14/3}$$

$$+ M_{5/3} M_{7/2} + 2M_{4/3} M_{23/6} + M_1 M_{25/6}).$$

The sum of the fractions on each term for a given  $C_r$  should be the same.  $C_1$  is zero because this moment is physically the mass of soot per unit volume, which is unchanged by coagulation.

#### 2.5.4 Closure Approaches

The fractional moments that have appeared in the growth and coagulation terms must be written in terms of the integer moments in order to use the method of moments. This presents a closure problem and there are many ways to obtain closure. These include

- interpolation and extrapolation between whole moments [106],
- assumed-shape size distribution where parameters defining the size distribution (such as the mean and standard deviation) are written in terms of the fractional moments [105],

- quadrature closure where the integrals defining the moments are computed using a form of quadrature where the weighting function and evaluation points are written in terms of the moments [107],
- approximations usually involving further simplifications of the growth and nucleation rates (e.g., assuming a size independent growth rate) [108].

Here, the goal is not to do an exhaustive search and comparison of the various methods but to find some that work and compare those. The focus here is on assumed-shape size distributions relevant for soot formation, as well as quadrature closure (QMOM). The later is probably the most general of all closure methods, but it requires an even number of moments.

#### 2.5.4.1 Monodispersed Size Distribution

The first two mass-moments of the particle size distribution are the particle number density ( $n = M_0$ ) and the soot mass per unit volume ( $\rho Y_s = M_1$ ). These two quantities are sufficient to define a mean particle size:

$$d = \left( \frac{6M_1}{\pi\rho_s M_0} \right)^{1/3}. \quad (2.111)$$

The monodispersed assumption in terms of two moments is a popular starting point for theoretically-based soot models because it is simple and allows basing reaction rates on a mean particle size (e.g., surface area). Models are often not written explicitly in terms of the first two moments as moments but consider the number density and soot mass fraction, or volume fraction ( $f_v = \rho Y_s / \rho_s$ ). The previously derived expressions for  $N_r$ ,  $G_r$ , and  $C_r$  are valid for the monodispersed assumption. It turns out that fractional moments computed by logarithmic interpolation between the first two moments are equivalent to using the mean particle size defined by those two moments. That is, using the known size distribution  $n(m) = M_0 \cdot \delta(m - m_m)$ , where  $m_m$  is the mean particle mass  $M_1/M_0$ . This is illustrated simply below.

The growth rate in Eq. (2.80) for  $r = 0$  is 0, and for  $r = 1$  is

$$G_1 = \pi \left( \frac{6}{\rho_s \pi} \right)^{2/3} k_s M_{2/3}. \quad (2.112)$$

Logarithmic interpolation for a fractional moment  $M_k$  is defined as

$$M_k = M_a \left( \frac{M_b}{M_a} \right)^{(k-a)/(b-a)}, \quad (2.113)$$

where  $a$  and  $b$  are integers, and  $k$  is between  $a$  and  $b$  for interpolation, or outside the range of  $a$  and  $b$  for extrapolation. For  $a = 0$ ,  $b = 1$ , and  $k = 2/3$ ,

$$M_{2/3} = M_0 \left( \frac{M_1}{M_0} \right)^{2/3}. \quad (2.114)$$

Using this expression in Eq. (2.112), and using Eq. (2.111) with  $A_p = \pi d^2$  results in

$$G_1 = M_0 \cdot A_p \cdot k_s. \quad (2.115)$$

The growth rate is the number of particles per unit volume, times the mean surface area per particle, times the rate per area, which makes sense for a monodisperse distribution. This is the expression used in the Leung and Lindstedt model [5], except that  $M_0 A_p$  is replaced with  $(M_0 A_p)^{1/2}$ .

The same thing can be done for the coagulation rate  $C_0$  in Eq. (2.105), using logarithmic interpolation for the fractional moments. The result is the same if the mean particle size is used in the rate expression Eq. (2.81). For the monodisperse distribution, the factor  $b$  in the approximation for  $\beta$  is identically  $1/\sqrt{2}$ .

Here are the rate expressions for the monodisperse distribution:

$$N_0 = S_{nuc}, \quad (2.116)$$

$$N_1 = m_{min} S_{nuc}, \quad (2.117)$$

$$G_0 = 0, \quad (2.118)$$

$$G_1 = \pi \left( \frac{6M_1}{\pi \rho_s M_0} \right)^{2/3} M_0 k_s, \quad (2.119)$$

$$C_0 = -4K_f \cdot b \cdot M_0^{11/6} M_1^{1/6}, \quad (2.120)$$

$$C_1 = 0. \quad (2.121)$$

### 2.5.4.2 Lognormal Distribution

Aerosol particle size distributions undergoing free molecular collisions are known to be well approximated by the lognormal size distribution. This is also a good approximation for soot including nucleation and surface growth. If a lognormal size distribution is assumed, all fractional moments can be written explicitly in terms of the parameters of the lognormal distribution. The distribution in continuous form, with diameter as the size variable is

$$f(\log d) = \frac{dF(\log d)}{d \log d} = \frac{M_0}{\sigma\sqrt{2\pi}} \exp\left(-\frac{\log^2(d/\bar{d})}{2\sigma^2}\right). \quad (2.122)$$

This is the classic normal distribution multiplied by  $M_0$ , where  $\log d$  is the independent variable,  $f$  is the size distribution and  $F$  is the cumulative size distribution. Notation is important here and  $\sigma$  is the standard deviation of the distribution with  $\log d$  as the independent variable. Sometimes one sees  $\sigma$  replaced with  $\log \sigma$ , and in both cases  $\sigma$  is called the standard deviation, which can cause confusion. In Eq. (2.122),  $d$  can be used as the independent variable using  $d \log d = \frac{1}{d} dd$  (where  $d \log d$  is the differential of  $\log d$ , and  $dd$  is the differential of  $d$ ):

$$f(d) = \frac{dF(d)}{dd} = \frac{M_0}{\sigma\sqrt{2\pi}} \frac{1}{d} \exp\left(-\frac{\log^2(d/\bar{d})}{2\sigma^2}\right). \quad (2.123)$$

Using  $m = \frac{\pi}{6} d^3 \rho_s$  and  $dd = \frac{2}{\pi \rho_s d^2} dm$  and  $d \log m = \frac{1}{m} dm$  yields

$$f(m) = \frac{dF(m)}{dm} = \frac{M_0}{3\sigma\sqrt{2\pi}} \frac{1}{m} \exp\left(-\frac{\log^2(m/\bar{m})}{18\sigma^2}\right), \quad (2.124)$$

$$f(\log m) = \frac{dF(\log m)}{d \log m} = \frac{M_0}{3\sigma\sqrt{2\pi}} \exp\left(-\frac{\log^2(m/\bar{m})}{18\sigma^2}\right). \quad (2.125)$$

This last expression is like Eq. (2.122), but with the 1/3 factor. The quantity  $3\sigma$  here is the standard deviation of  $f(\log m)$  with  $\log m$  as the independent variable. If  $3\sigma$  is replaced with  $\sigma$ , a lognormal distribution in  $\log m$  like  $\log d$  in Eq. (2.122) results, but the form given is more common (confusing) and will be used. At any rate,  $\sigma$  is written as it appears in Eq. (2.124) in terms of moments. The actual form only matters insofar as the distribution is reconstructed from the moments.

The moments of the lognormal distribution are found by multiplying Eq. (2.124) by  $m^k$  and integrating over all  $m$  as in Eq. (2.50):

$$M_k = \frac{M_0}{3\sqrt{2\pi}\sigma} \int_0^\infty m^{k-1} \exp\left(-\frac{\log^2(m/\bar{m})}{18\sigma^2}\right) dm. \quad (2.126)$$

Changing the integration variable to  $\log m$ ,  $dm = m d \log m$ , yields

$$M_k = \frac{M_0}{3\sqrt{2\pi}\sigma} \int_{-\infty}^\infty m^k \exp\left(-\frac{\log^2(m/\bar{m})}{18\sigma^2}\right) d \log m. \quad (2.127)$$

Next, change variables as

$$z = \left(\frac{\log(m/\bar{m})}{3\sqrt{2}\sigma}\right), \quad (2.128)$$

$$d \log m = 3\sqrt{2}\sigma dz, \quad (2.129)$$

$$M_k = \frac{M_0}{3\sqrt{2\pi}\sigma} \int_{-\infty}^\infty 3\sqrt{2}\sigma m^k \exp(-z^2) dz, \quad (2.130)$$

$$= \frac{M_0}{3\sqrt{2\pi}\sigma} \int_{-\infty}^\infty 3\sqrt{2}\sigma \left(\frac{m}{\bar{m}}\right)^k \bar{m}^k \exp(-z^2) dz. \quad (2.131)$$

Insert  $(m/\bar{m})^k = \exp(3\sqrt{2}\sigma z k)$  from Eq. (2.128) and let  $\alpha = 3\sqrt{2}k\sigma$ :

$$M_k = M_0 \frac{\bar{m}}{\sqrt{\pi}} \int_{-\infty}^\infty \exp(-z^2 + \alpha z) dz, \quad (2.132)$$

$$= M_0 \frac{\bar{m}}{\sqrt{\pi}} \int_{-\infty}^\infty \exp\left[-\left(z - \frac{\alpha}{2}\right)^2 + \left(\frac{\alpha}{2}\right)^2\right] dz, \quad (2.133)$$

$$= M_0 \frac{\bar{m}}{\sqrt{\pi}} \exp\left(\frac{\alpha^2}{4}\right) \int_{-\infty}^\infty \exp\left[-\left(z - \frac{\alpha}{2}\right)^2\right] dz, \quad (2.134)$$

$$= M_0 \frac{\bar{m}}{\sqrt{\pi}} \exp\left(\frac{\alpha^2}{4}\right) \int_{-\infty}^\infty \exp[-p^2] dp, \quad (2.135)$$

$$M_k = M_0 \bar{m}^k \exp\left(\frac{9}{2}k^2\sigma^2\right). \quad (2.136)$$

The first step of this equation consists of completing the square, moving it outside the integral in step 2, changing the integration variable in step 3, and simplifying the result, where the final integral equals  $\sqrt{\pi}$ .

Equation (2.136) gives any moment in terms of  $\bar{m}$  and  $\sigma$ .  $M_k$  is needed terms of  $M_0$ ,  $M_1$ , and  $M_2$ , which is done as follows:

$$M_1 = M_0 \bar{m} \exp\left(\frac{9}{2}\sigma^2\right), \quad (2.137)$$

$$\bar{m} = \frac{M_1}{M_0} \exp\left(-\frac{9}{2}\sigma^2\right), \quad (2.138)$$

$$\frac{M_0 \bar{m}}{M_1} = \exp\left(-\frac{9}{2}\sigma^2\right), \quad (2.139)$$

$$M_2 = M_0 \bar{m}^2 \exp\left(4\frac{9}{2}\sigma^2\right), \quad (2.140)$$

$$M_2 = M_0 \bar{m}^2 \left(\exp\left(\frac{9}{2}\sigma^2\right)\right)^4, \quad (2.141)$$

$$\left(\frac{M_2}{M_0 \bar{m}^2}\right)^{1/4} = \exp\left(\frac{9}{2}\sigma^2\right). \quad (2.142)$$

Equate Eq. (2.139) and the inverse of Eq. (2.142) and solve for  $\bar{m}$ :

$$\bar{m} = \frac{M_1^2}{M_0^{3/2} M_2^{1/2}}. \quad (2.143)$$

Now insert this expression in Eq. (2.139) and solve for  $\sigma$ :

$$\sigma^2 = \frac{1}{9} \log\left(\frac{M_0 M_2}{M_1^2}\right). \quad (2.144)$$

Equations (2.143) and (2.144) are used in Eq. (2.136) to yield

$$M_k = M_0^{1-\frac{3}{2}k+\frac{1}{2}k^2} M_1^{2k-k^2} M_2^{\frac{1}{2}k^2-\frac{1}{2}k}. \quad (2.145)$$

This equation can be used to find all required fractional moments in  $N_r$ ,  $G_r$ , and  $C_r$ .

Here are the rate expressions for the three-moment, lognormal closure:

$$N_0 = S_{nuc}, \quad (2.146)$$

$$N_1 = m_{min} S_{nuc}, \quad (2.147)$$

$$N_2 = m_{min}^2 S_{nuc}, \quad (2.148)$$

$$G_0 = 0, \quad (2.149)$$

$$G_1 = \pi \left(\frac{6}{\rho_s \pi}\right)^{2/3} k_s M_{2/3}, \quad (2.150)$$

$$G_2 = \pi \left( \frac{6}{\rho_s \pi} \right)^{2/3} \cdot 2 \cdot k_s M_{5/3}, \quad (2.151)$$

$$C_0 = -K_f b (M_0 M_{1/6} + 2M_{1/3} M_{-1/6} + M_{2/3} M_{-1/2}), \quad (2.152)$$

$$C_1 = 0, \quad (2.153)$$

$$C_2 = 2K_f b (M_1 M_{7/6} + 2M_{4/3} M_{5/6} + M_{5/3} M_{1/2}). \quad (2.154)$$

### 2.5.4.3 Lognormal Plus Power Law Distribution

The same approach that was taken in deriving the lognormal closure can be applied to other distributions, possibly with more parameters, allowing a more accurate PSD representation. The experiments of Zheng et al. [109] and others have shown that soot particle size distributions that include the combined effects of nucleation, growth, and coagulation can be represented by the sum of a power law function and a lognormal distribution. This distribution is given by

$$f(\log m) = \frac{dF(\log m)}{d \log m} = am^{-b} + \frac{c}{\sqrt{2\pi}\sigma} \exp\left(-\frac{\log^2(m/\bar{m})}{2\sigma^2}\right). \quad (2.155)$$

The five parameters ( $a$ ,  $b$ ,  $c$ ,  $\bar{m}$ ,  $\sigma$ ) describe the distribution. The general expression for an arbitrary moment can be easily derived, but it is in terms of the parameters of the size distribution, and an analytic solution for these parameters in terms of the first five moments was not found. Hence, to use the method, a nonlinear solve would be required in order to compute the parameters from the moments in order to close the fractional moments required for closure of the source terms of the first five whole moments. This does not seem worth the effort when there are other methods that make no assumptions about the shape of the size distribution, such as interpolative closure, and quadrature. Interpolative closure is not described here. Quadrature closure is described next.

### 2.5.4.4 Quadrature Method of Moments

It was previously observed that in order to close the moment source equations, fractional moments are required, or, in the case of the general coagulation term, more general integrals over the unknown particle size distribution function are required. This integration can be carried out using numerical quadrature:

$$\int_a^b W(x)f(x)dx \approx \sum_{j=1}^N w_j f(x_j), \quad (2.156)$$

where  $f(x)$  is a general function here and  $W(x)$  is a weighting function. On the RHS of the equation,  $w_j$  are applied weights, and  $x_j$  are evaluation points, or abscissas. The integration is approximated by the sum of products of weights and the function evaluated at abscissas. Generally, more points in the sum give higher accuracy. The book *Numerical Recopies* [110] gives a very good description of quadrature as summarized in this section. For a given weight function, the weights and abscissas can be chosen so that the quadrature in Eq. (2.156) is exact for  $f(x)$  a polynomial of degree  $2N - 1$  or less. The abscissas are chosen to be the roots of the order  $N - 1$  orthogonal polynomial (orthogonal with respect to the weight function). The weights can be found in several ways, such as applying Eq. (2.156) and the definition of orthogonality to the lower-order orthogonal polynomials. To integrate a general function, the idea is to split it into the product of a weight function and a polynomial function. The weights and abscissas are then found for the weight function using orthogonal polynomials, and Eq. (2.156) is applied. The function  $f(x)$  does not have to be a polynomial, but this is ideal. If  $W(x)$  is taken equal to unity and the integration interval scaled to  $-1 < x < 1$ , then the quadrature is the classic Gauss-Legendre, and the weights and abscissas are known and can be looked up in a table. Many other weight functions are also used and tabulated.

In applying quadrature to our case of integration over the unknown particle size distribution, the weight function is taken as the particle size distribution and the weights and abscissas are computed in terms of  $2N$  moments of the distribution. Hence, for a two-point quadrature, four moments are required. For example,

$$\int_0^\infty g(m)f(m)dm \approx \sum_{i=1}^N w_i g(x_i), \quad (2.157)$$

where  $f(m)$  is our particle size distribution. The weights  $w_i$  and abscissas  $x_i$  could be computed using the definition of the moments and the approximate quadrature, which, for  $N = 2$  points (four moments), gives

$$M_0 = w_1 + w_2, \quad (2.158)$$

$$M_1 = x_1 w_1 + x_2 w_2, \quad (2.159)$$

$$M_2 = x_1^2 w_1 + x_2^2 w_2, \quad (2.160)$$

$$M_3 = x_1^3 w_1 + x_2^3 w_2. \quad (2.161)$$

This yields four equations in four unknowns. Once  $w_i$  and  $x_i$  are computed, any integration over the unknown  $f(m)$  can be approximated. The above method is not good numerically as the equation system is ill conditioned, and other algorithms are used. In *Numerical Recipes*, algorithms by Sack and Donovan and others by Wheeler are advocated (see references in [110]). The product difference algorithm of Gordon [111] and also described by McGraw [107] was implemented here with some slight modifications for moment scaling. The inputs to the algorithm are simply the moments, and the outputs are weights and abscissas that are used directly to compute all fractional moments, or other integrations for closure of the moment source terms. Appendix B contains a Matlab program for the product difference algorithm.

#### 2.5.4.5 Verification of Quadrature Implementation

The product difference algorithm implementation is tested simply by feeding in moments and making sure that the resulting abscissas and weights give back the moments under the quadrature definition.

As a validation of the quadrature approach, the first three moments of the particle size distribution are specified through the mean particle size, the standard deviation, and the total number density. The fractional moments of the lognormal size distribution are then computed using the exact analytic expressions Eq. (2.145), and compared to the quadrature approximations. For this analysis, particle size-moments (diameter), not mass-moments, were employed. Results are shown in Fig. 2.14. The six plots correspond to six different fractional moments that approximately span the range appearing in the moment sources up to the sixth moment. On each plot the curves represent one-, two-, three-, and four-point quadratures, requiring two, four, six, and eight moments, respectively. The results are not dependent upon either the total number density or the mean particle size, but only on the standard deviation of the distribution. As the standard deviation increases, the relative error in the moment approximation increases. The error is substantially smaller when more quadrature points are used. The errors also increase as the fractional moments increase, except for the negative moment  $k = -1/2$  whose error is higher than  $k = 1/2$ . However three moments are sufficient to capture a truly lognormal distribution, and the fractional moments higher than about  $k = 3/2$  would

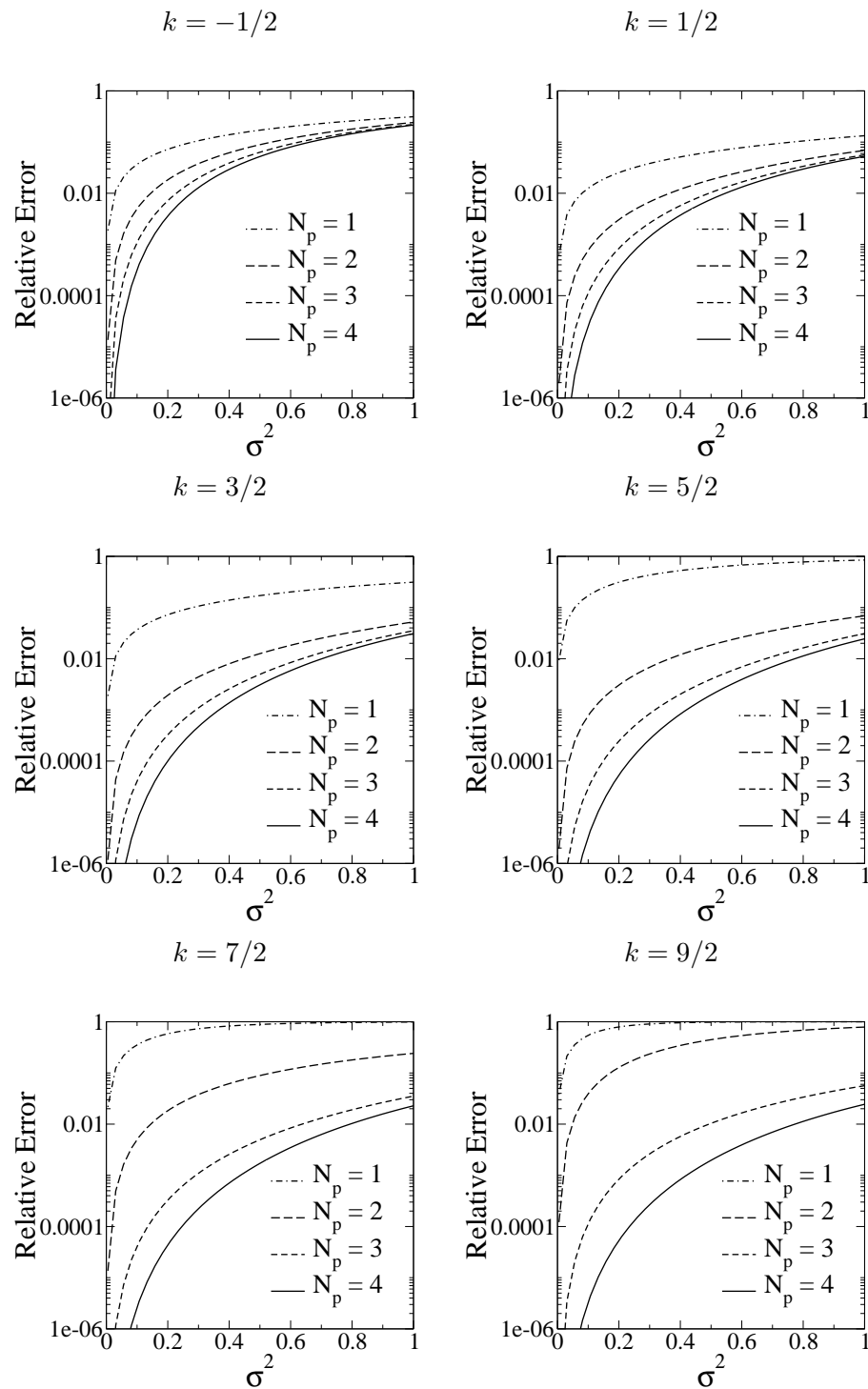


**Figure 2.14.** Validation of quadrature approximation to lognormal fractional moments. Relative error shown as a function of the standard deviation squared of the lognormal distribution for one- to four-point quadratures.  $\sigma^2 = 0.2$  is shown to be a practical upper bound for real systems.

not be needed; or, in other words, the errors at higher fractional moments correspond to the use of a higher number of moments, for which the increases in accuracy are less significant; or, loosely, the errors at higher fractional moments multiply higher order (less significant) terms in the particle size representation.

The errors are actually quite large for high  $\sigma^2$ , especially for the one- and two-point quadratures. One would hope that the errors would be low enough to give confidence in the use of the model. To this end, it is interesting to get a feel for just how large a  $\sigma$  occurs in realistic situations. Particle distributions subject to coagulation are known to develop so-called self-preserving size distributions. That is, the shape and width of the normalized distribution become constant in time during the evolution of the distribution and simply shift as a whole towards higher particle sizes. This is illustrated in Fig. 2.15, which shows results of a simple sectional model that was developed to test the width of the distribution. Section profiles are treated as delta functions, with interpolation for collisions between bins. Plot (a) shows the raw data on a logscale and shows that the number of particles decreases due to coagulation as the mean size grows. Plot (b) is on a linear scale with the data normalized to show the self-preserving form of the distribution.

The developed distribution in Fig. 2.15 at 5 s is well approximated as lognormal with a mean volume of  $5.3 \times 10^{-25} \text{ m}^3$  and a  $\sigma$  of 0.42. As noted above,  $\sigma$  is sometimes replaced with  $\log \sigma_l$ , and the value  $\sigma_l$  reported. In this notation, the above value is  $\sigma_l = 1.52$ , which is very close to the value reported by others. Vemury and Pratsinis found a value of 1.46 [112]. Zhao et al. [109] measured soot distributions in premixed flames including the effects of nucleation and growth and found a values up to 1.6. In Fig. 2.14, a practical upper bound on  $\sigma^2$  is 0.2 for which the two or more point quadratures give less than 1% error for all fractional moments shown except  $k = 9/2$ . It is concluded that quadrature is an accurate method for moment closure.

### 2.5.5 Implementation and Results

The method of moments was implemented in a Fortran 90 module for two, three, four, or six moments. Extension to eight or more moments is straightforward. For three moments, a lognormal closure is used, and for all moments except three, the approximate coagulation expression is optional. In addition, the module is coupled to the DVODE ODE integrator in both constant (gas) property batch (PFR) and perfectly stirred reactor (PSR) configurations. Results for these configurations are shown below.

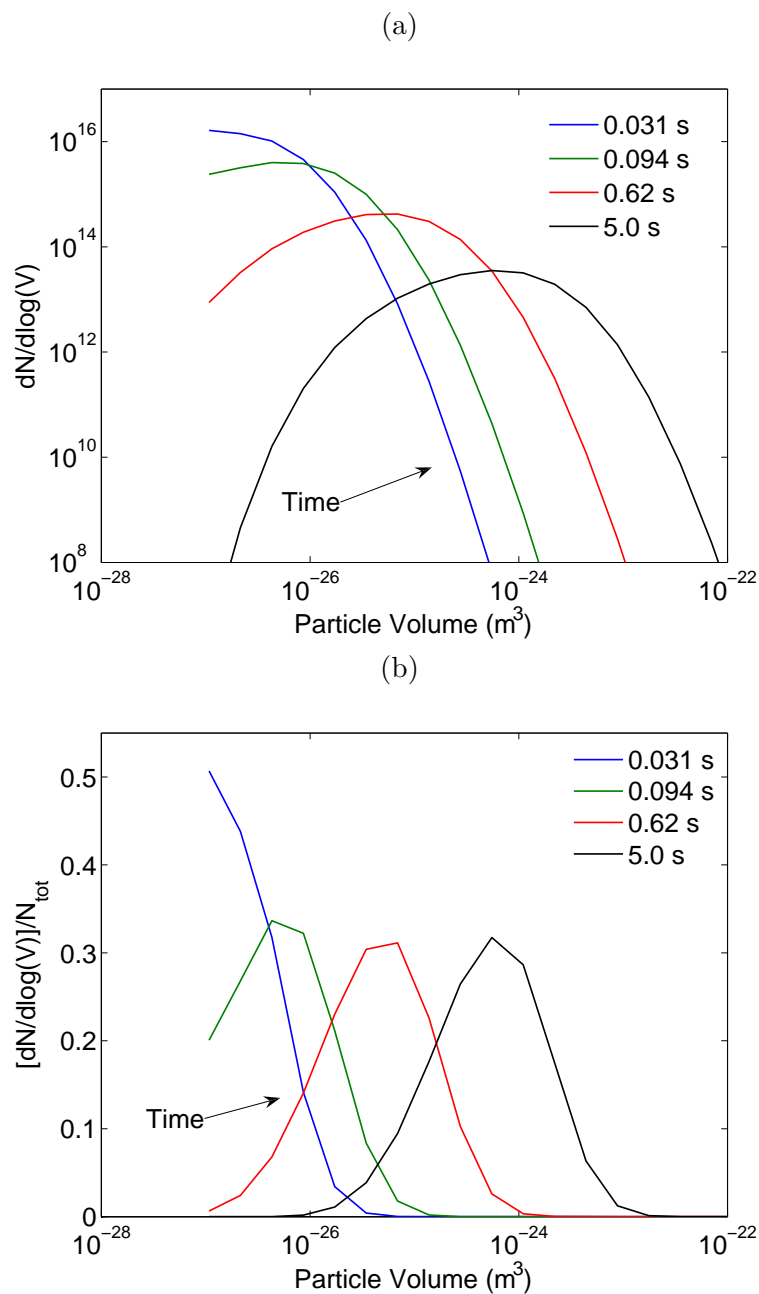


**Figure 2.15.** Sectional coagulation model results. The initial condition is  $1 \times 10^{17}$  particles in the first bin. Bin sizes are spaced geometrically by a factor of 2, and the first bin is  $1 \times 10^{-27} \text{ m}^3$ , which corresponds to a spherical particle with 100 carbons and a density of  $1850 \text{ kg/m}^3$ . Plot (a) shows that the total number of particles decreases as the size grows via coagulation. Plot (b) is normalized and shows the self-preserving distribution that develops in time.

The soot model implemented is from Leung and Lindstedt [5] for nucleation and oxidation and Lindstedt [113] for soot growth. These mechanisms are examples and implementation of other reaction schemes is straightforward. The growth, oxidation, and nucleation rates corresponding to Eqs. (2.57)-(2.58) are

$$k_{s,grw} = 7.5 \times 10^2 \cdot \exp(-12100/T) \cdot [C_2H_2] \cdot 2W_{C_s}, \quad (2.162)$$

$$k_{s,oxid} = 1 \times 10^4 \sqrt{T} \cdot \exp(-19680/T) \cdot [O_2] \cdot 2W_{C_s}, \quad (2.163)$$

$$R_{nuc} = 1 \times 10^4 \cdot \exp(-21100/T) \cdot [C_2H_2], \quad (2.164)$$

where  $W_{C_s}$  is the molecular weight of carbon, and  $[C_2H_2]$  and  $[O_2]$  are concentrations in  $\text{kmol/m}^3$ . The rate units are kilogram per square meter for growth and oxidation and kilomole per cubic meter per second for nucleation.

Unless otherwise noted, the following parameters are used in the calculations. The gas temperature is 1500 K, and the pressure is 1 atm. Acetylene is the nucleation and growth species, with an assumed constant concentration of  $0.000426 \text{ kmol/m}^3$ . The oxygen concentration is fixed at  $1.03 \times 10^{-6} \text{ kmol/m}^3$ . In the following results, oxidation was not allowed, but its effect is very small for the given oxygen concentration. The gas parameters chosen correspond approximately to mean values at the soot peak in the mixture fraction coordinate for nonpremixed ethylene flames computed using DNS.

### 2.5.5.1 Moment Scaling

In implementing the method of moments, the scaling of the moments is important. If mass-moments are used, the moments have widely varying orders of magnitude since each successive moment involves the particle mass to successive powers, and the particle mass is small. Hence the moments must be scaled in order to avoid roundoff error and machine overflow or underflow. For example, with mass-moments in  $\text{kg}$ ,  $\text{m}^3$ , the first three moments are  $O(10^{17})$ ,  $O(10^{-3})$ , and  $O(10^{-23})$ . That is, there are about 20 decimals between the significant range of each moment, but only about 16 decimals of double precision. A remedy is to replace the mass-moments with scaled moments:

$$M_r = \sum_i m_i^r n_i, \quad (2.165)$$

$$\mu_r = \sum_i i^r n_i = \frac{M_r}{m_1^r}, \quad (2.166)$$

$$\eta_r = \sum_i p_i^r n_i = \frac{\mu_r}{\alpha^r} = \frac{M_r}{(m_1 \alpha)^r}, \quad (2.167)$$

where  $\mu_r$  is a monomer-moment, and  $\eta$  is a scaled monomer-moment or just a scaled mass-moment. The parameter  $\alpha$  is a scaling factor.

Figure 2.16 compares time integrated profiles to 20 ms for six moments. These results were computed using QMOM with the general expression for coagulation. Three plots with three separate values of  $\alpha$  are shown. In each case,  $M_0$  is the curve with the least variation, and the other moments are spaced in order. The moment scaling results in a crossover of the curves, whose position shifts to longer times as  $\alpha$  increases. This results in moments being widely spaced in some regions (about 16 orders apart) and nearly the same magnitude in others. The product difference algorithm was slightly modified by scaling by  $M_0$  and  $M_1$ , and no significant numerical errors up to six moments have been observed. The fact that the crossover point changes in time suggests that, if scaling is a problem, the parameter  $\alpha$  could be modified as needed to minimize the span of the moments. Also, higher moments show a lower rate of growth than lower moments, consistent with the fast nucleation of soot and the relatively slow growth and coagulation that tends to spread the size distribution in the internal particle coordinate (i.e., particle mass).

### 2.5.5.2 Comparison of the Number of Moments

Figure 2.17 shows a comparison of two, three, four, and six moments in a batch reactor. In all cases, the above coagulation approximation is used with  $b = 0.73$ . The integration is carried out for 20 ms. The results are in excellent agreement to 20 ms for three, four, and six moments, while the two-moment method is reasonable, but off by about 33% at 20 ms. As the number of moments increases, the differences between the profiles are lessened. There is no visible difference between the four- and six-moment curves and very slight differences between the three-, four-, and six-moment results for  $M_1$ , which is usually the quantity of most interest. At longer times, the  $M_1$  curves continue to diverge with  $M_1$  a little less than a factor of 2 higher for two moments than for four moments ( $M_1 = 1.2 \text{ kg/m}^3$  for four moments) at 100 ms. At the same time,  $M_0$  has declined and levelled to approximately  $1.2 \times 10^{17} \text{ \#/m}^3$  with 18% difference between the two- and four-moment curves. In this calculation, with a fixed gas phase, the results become irrelevant once the soot mass fraction begins to approach that of the original carbon in the system, and

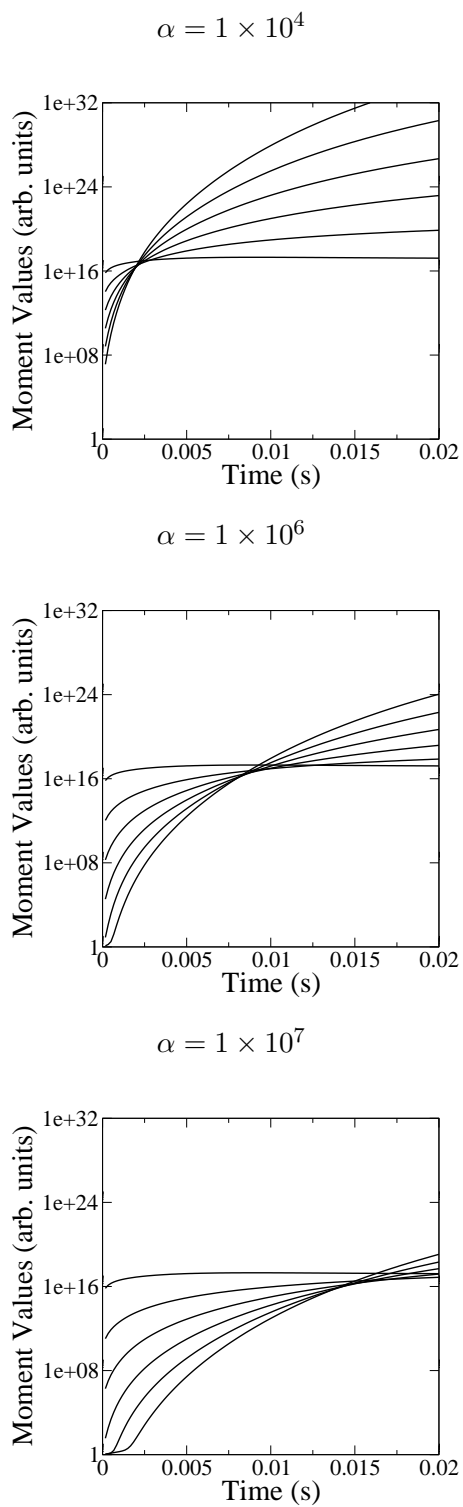


**Figure 2.16.** Comparison of scaling parameters for a six-moment method. In each case,  $M_0$  is the curve with the least variation and higher moments are spaced in order.

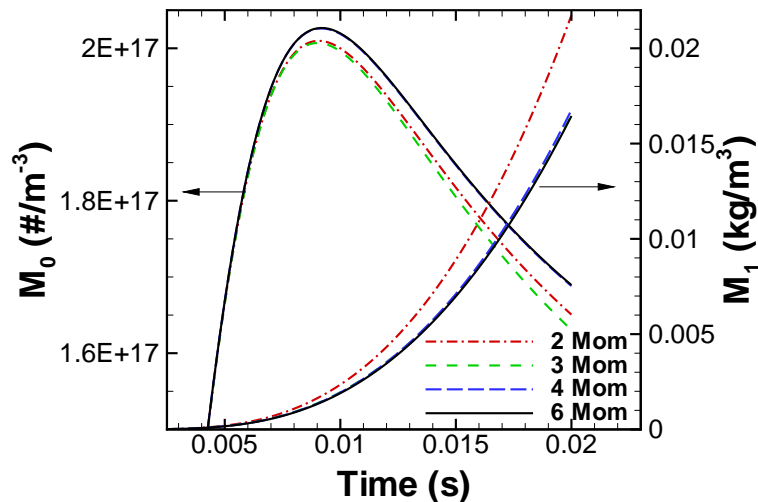


Figure 2.17. Comparison of number of moments in a batch reactor.

consideration of early times is more reasonable.

### 2.5.5.3 Effect of the Approximate Coagulation Source

The approximation for the coagulation source introduced in Eq. (2.84) was used for closure of the lognormal size distribution. As shown in the previous section, three moments are sufficient for approximating the soot distribution, and since transporting three moments is computationally efficient we would like to use the three-moment version whenever possible. Figure 2.18 shows a comparison of  $M_0$  and  $M_1$  using four moments with values of  $b$  spanning the bounds  $\frac{1}{\sqrt{2}} \leq b \leq 1$ . There is substantial variation in the results: about 13% in  $M_1$  and 16% in  $M_0$ . The two solid lines are for  $b = 0.73$  and general coagulation. These two curves are indistinguishable for  $M_1$ , and the  $b = 0.73$  curve is slightly lower for  $M_0$ . These results are encouraging and show that the three-moment model can be used with confidence with  $b = 0.73$ .

This value of  $b = 0.73$  is approximately equal to its mean value over  $m_i$  and  $m_j$  (or  $m$  and  $\mu$  in the continuous form) given the definition, Eq. (2.84). The fact that the optimal  $b$  is close to its lower boundary corresponds to collisions among particles of similar size. The lower boundary corresponds to collision of equal sized particles, and the upper boundary corresponds to collision of particles of very different sizes. It should not be expected that the value of  $b$  be strictly a constant since the integration required for  $C_r$  is dependent upon the particle size distribution and the value of  $r$ . Pratsinis [105] used a lognormal closure

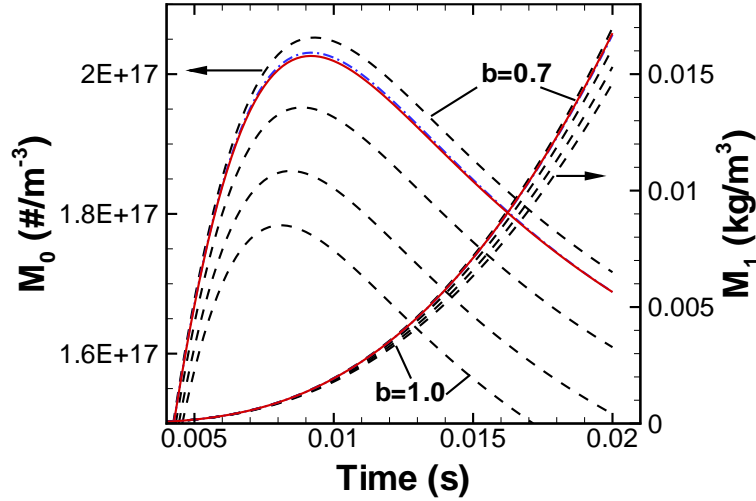


**Figure 2.18.** Comparison of the four-moment model with values of  $b=0.7, 0.8, 0.9, 1.0$  as dashed lines. The dash-dot lines are the general coagulation model, and the solid lines are  $b = 0.73$ , which are indistinguishable for  $M_1$ . For  $M_0$ , the  $b = 0.73$  line is lower.

with the same approximation on collision used here. He correlated values of  $b$  for each moment source as a function of the standard deviation of the particle size distribution. This has been repeated in the present formulation by numerical integration. The results are essentially the same as in [105] and are not repeated. However, it appears that good agreement can be achieved with the constant value given above.

#### 2.5.5.4 Sensitivity to Source Rates

A brief evaluation of the sensitivity of the first and second moments to the rates of nucleation, coagulation, and growth is shown in Fig. 2.19. A set of four simulations were performed with four moments. The four cases correspond to a base case with the parameters used previously, followed by three cases in which each of the rates of nucleation, coagulation, and growth are increased individually by a factor of 2. These increases give rise to substantial differences in both of the first two moments. The increased nucleation rate results in both a higher overall number density ( $M_0$ ) as expected but also increases the total soot mass per volume ( $M_1$ ) since there are more particles for surface growth to act upon. Conversely, increasing the coagulation rate results in fewer particles and a lower overall soot mass. An increase in the soot growth rate results in an increase in the total soot mass in the system, as expected, but the number density is decreased for this case due to higher coagulation rates for larger particle sizes. This

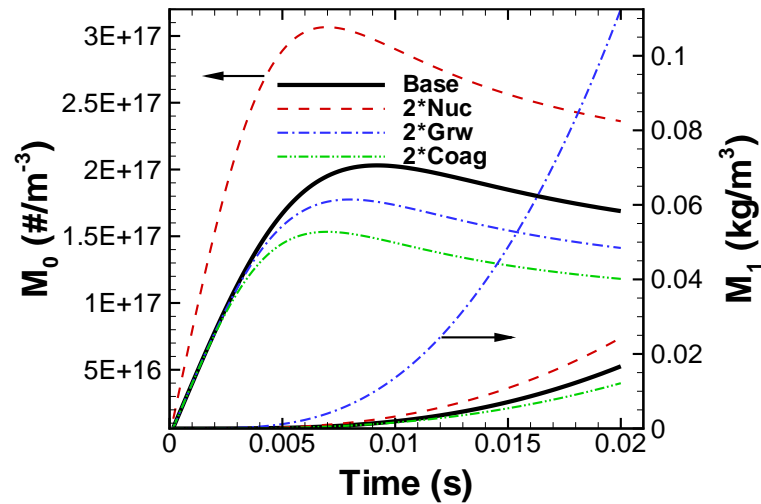


**Figure 2.19.** Sensitivity of  $M_0$  and  $M_1$  to rates of nucleation, growth, and coagulation for the four-moment model.

increase in particle size effectively reduces the particle surface area per unit mass and results in a lower level of growth than would be observed if coagulation rates were constant. As may be expected,  $M_0$ , the total particles per volume, is most sensitive to the nucleation rate, and  $M_1$ , the mass per volume, is most sensitive to the growth rate, the latter by a wide margin. The nucleation, growth, and coagulation curves differ from the base curve for  $M_1$  at 20 ms by 43%, 560%, and 28%, respectively, and by 39%, 16%, and 30%, respectively, for  $M_0$  at the same time. If the total soot mass (proportional to volume fraction) is the most important quantity of interest, the growth rate is important.

#### 2.5.5.5 PSR Tests

To convert the constant gas property batch reactor to a constant gas property PSR, source and sink terms corresponding to the rate at which soot moments enter and leave the reactor are added to the reaction and coagulation source terms. The following equation is solved, assuming no soot mass enters the reactor:

$$\frac{dM_r}{dt} = N_r + G_r + C_r - \frac{M_r}{\tau}, \quad (2.168)$$

where  $\tau$  is the PSR residence time. As  $\tau$  increases, the soot levels decrease due to reduced reaction times available. The PSR equation is written in unsteady form, where there is

no soot at time zero. However, unlike the batch reactor, the PSR reaches a steady state where the source terms sum to zero (primarily due to the exit stream) and the moment profiles reach a steady state. Figure 2.20 shows the unsteady moment profiles for the four-moment model in a PSR with  $\tau = 5$  ms. The characteristic timescale is not that of the PSR but is dominated by the slower soot growth reactions. In the case of the number density, there is a fast transient, then a peak where coagulation begins, followed by a slower descent towards the steady value. Once again, the slower growth of the higher order moments as the particle size distribution develops is observed. The characteristic PSR timescale was verified to equal the imposed residence time by turning off the nucleation rate and observing the rate of decay of the first moment  $M_0$  from an imposed initial condition.

Figure 2.21 shows the steady values of the first two moments as a function of the PSR residence time. The base case is shown as well as results with increased source terms, as in Fig. 2.19. The PSR results appear to be very similar to the PFR results, with the same sensitivity to the moment source terms. The number density shows a smaller variation than the soot mass per volume, as is evident in plot (b), where  $\log(M_1)$  is shown. The  $M_1$  curve spans five orders of magnitude.

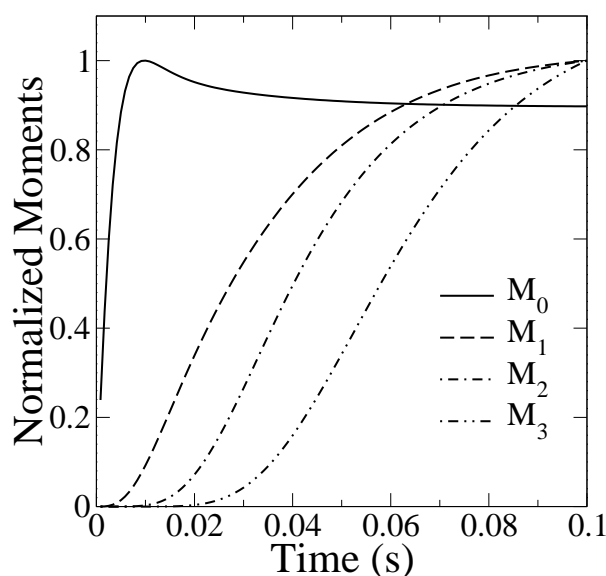


**Figure 2.20.** Normalized moment profiles for the four-moment model in a PSR with a residence time of 5 ms.

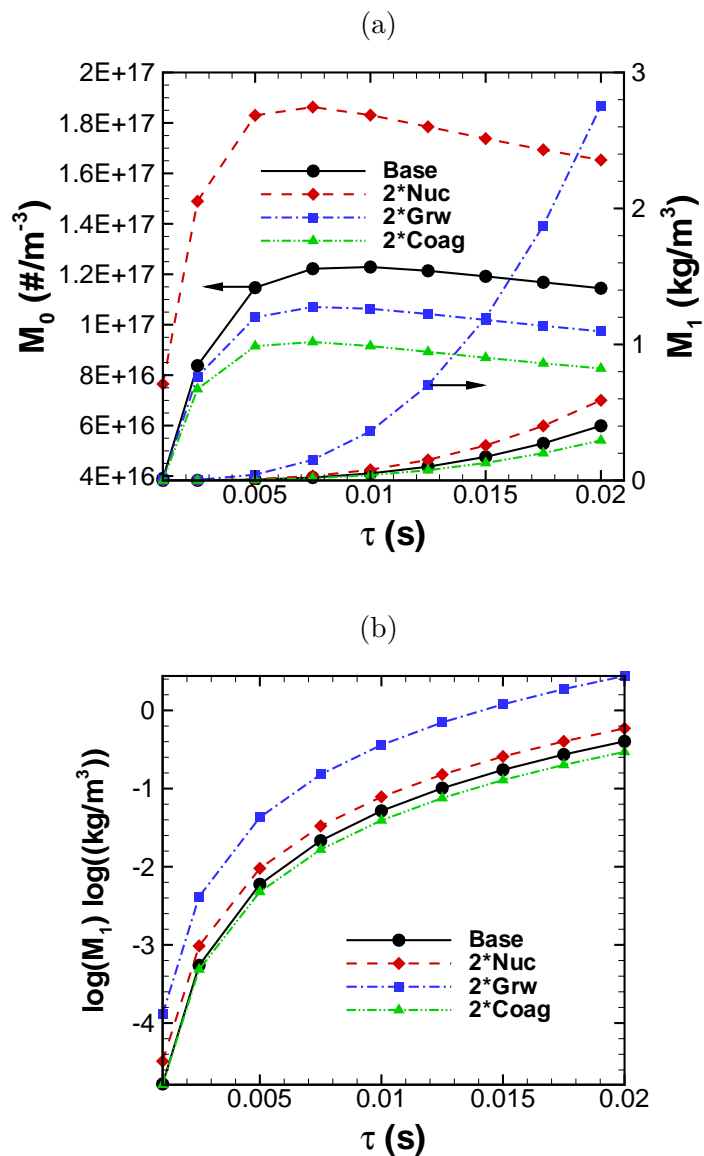


**Figure 2.21.** Steady values of  $M_0$  and  $M_1$  versus PSR residence time for the four-moment model. Plot (a) shows  $M_0$  and  $M_1$ . Plot (b) is  $\log(M_1)$  to show scale. Also shown are the corresponding curves with the indicated increase in reaction and coagulation rates.

## CHAPTER 3

### ONE-DIMENSIONAL SIMULATIONS

A series of four one-dimensional simulations were performed with S3D to complement the multidimensional runs and to gain insight into the effects of soot diffusion and radiation on the temperature and soot fields.

#### 3.1 Configuration

The one-dimensional cases correspond directly to the two-dimensional temporal mixing layer simulations presented in Chapter 4. That is, the initial field is a line of sight in the cross-stream direction through the two-dimensional mixing layer initial field. The cases are nonpremixed with open (nonreflecting) boundary conditions. The flow configuration is simply an unsteady diffusive relaxation of the initial flame, with no imposed strain or flow. This configuration is in contrast to other popular configurations, such as the steady one-dimensional opposed jet, steady laminar flamelets, or steady premixed flames. This particular case is thought to correspond more closely to the unsteady mixing layer cases. The unsteadiness of the case allows us to observe the soot growth, transport, and radiative processes without the complications of added convective fields that are present in two and three dimensions. Because the simulations are one-dimensional, the computational costs are lower, and longer run times are possible (typically by an order of magnitude). In addition, the detailed mechanism upon which the reduced mechanism was based may be applied for direct comparison of the two mechanisms and quantification of the differences.

Although the present cases are not strained, the flame zone of the mixing layer cases are not substantially strained either. In the developed region of turbulent jet flames, strain rates are important in describing the chemical structure of the flames, so these one-dimensional cases should be applied cautiously and in a qualitative way only. However, in fires (e.g., pool fires) flow timescales can be much larger compared to flame timescales. Even turbulent fires may be substantially laminar from the point of view of a flame with

lengthscales of order millimeters, and timescales of order milliseconds. From this point of view, examination of one-dimensional unsteady, unstrained diffusion flames may be quite appropriate, especially considering the level of detail provided in the compressible formulation with expansion, and detailed chemical and transport effects accounted for.

The four cases are as follows:

1. A baseline case.
2. The baseline case with no radiation.
3. The baseline case with no soot diffusion (thermophoresis or otherwise).
4. The baseline case with the detailed chemical mechanism.

The domain size is 3 cm with 500 grid points giving a grid spacing of 60  $\mu\text{m}$  (which is sufficient for full resolution of the expanding flame). The average timestep size for the baseline case is  $5.8 \times 10^{-8}$  s, requiring 1.5 million steps to reach 86.5 ms. The simulation time was 6.33 hours on 10, 2000 MHz AMD Opteron processors.

### 3.1.1 Flame Initialization

The flames in these simulations, and the others presented in subsequent chapters, are initialized from one-dimensional, steady laminar flamelet solutions. This approach is not the only one for initiating a flame. Others include overlaying a hot temperature spike over a stratified fuel-air mixture and allowing auto-ignition to occur. Other possibilities include the addition of regions of hot combustion products to initiate the reactions. The steady flamelet approach is useful since there is no initial transient required to ignite the flame. Also, this approach removes questions regarding unphysical addition of enthalpy, which is a particular problem in temporal simulations in which the flame regions do not exit the domain, in contrast to spatially evolving flows.

Figure 1.2 shows a schematic of a one-dimensional, strained opposed jet diffusion flame. The flamelet model was introduced in Chapter 1. Solutions to the flamelet equations were computed using a program developed by Sutherland [57]. The program was modified to allow formation and transport of soot, incorporation of a heat loss parameter, and calculation of temperature from enthalpy, rather than transport of an energy equation. Additional modifications, described here, were incorporated for use in initializing the DNS simulations. The flamelet code solves the unsteady species flamelet

equations to steady state using the stiff ODE solver DASSL [114]. Thermodynamic quantities and reaction rates are computed using Chemkin [115].

In Eq. (1.11), all information linking the physical space variable to the mixture fraction coordinate is contained in the scalar dissipation rate:

$$\chi = 2D_\xi \left( \frac{\partial \xi}{\partial y} \right)^2. \quad (3.1)$$

Equation (1.11) is an unsteady diffusion, reaction relation that is solved to steady state. The scalar dissipation rate  $\chi$  captures both the effects of diffusion and convection. It is common to specify the scalar dissipation rate profile directly as a function of mixture fraction. A common relation is

$$\chi(\xi) = \chi_{max} \exp[-2(\text{erf}^{-1}(2\xi - 1))^2], \quad (3.2)$$

where  $\chi_{max}$  is the value of  $\chi$  at  $\xi = 0.5$ . Here,  $\text{erf}^{-1}$  is the inverse error function, not  $1/\text{erf}$ . The  $-1$  part of  $2\xi - 1$  is simply to shift the domain to range from 0 to 1 (instead of  $-1/2$  to  $1/2$ ).  $\chi_{max}$  is a parameter.

In specifying the initial composition field, a hyperbolic tangent profile for the mixture fraction in physical space is assumed, and then the corresponding flamelet solution is derived. Equation (3.2) is not used here. The mixture fraction profile is taken to be

$$\xi(y) = \frac{1}{2}(1 + \tanh(\sigma y_c)), \quad (3.3)$$

where  $y_c$  is the centered physical domain, and  $\sigma$  is a scaling factor that determines the sharpness of the profile. The corresponding scalar dissipation rate profile is found by inserting Eq. (3.3) into Eq. (3.1) to give

$$\chi = \frac{D_\xi}{2} \sigma^2 (1 - \tanh^2(\sigma y_c))^2. \quad (3.4)$$

Rearranging Eq. (3.3) yields

$$\tanh^2(\sigma y_c) = (2\xi - 1)^2. \quad (3.5)$$

Inserting Eq. (3.5) into Eq. (3.4) gives

$$\chi = \frac{D_\xi}{2} \sigma^2 (1 - (2\xi - 1)^2)^2. \quad (3.6)$$

This is the equation that is used to solve the flamelet profile when Eq. (3.3) is specified on the physical domain. The diffusivity is assumed to be the thermal diffusivity for  $Le = 1$ , which is a function of composition and temperature. The  $D_\xi(\xi)$  profile is updated directly as part of the solution and yields a  $\chi$  profile that is composition- and temperature-dependent, and not simply a specified function of mixture fraction.

It is interesting to compare Eq. (3.6) with Eq. (3.2). In Eq. (3.6), assume  $D_\xi$  is constant. For a hyperbolic tangent profile, the characteristic width  $\delta$  is defined as

$$\delta = \frac{\Delta\xi}{\left(\frac{\partial\xi}{\partial y}\right)_{max}} = \frac{\Delta\xi}{\sqrt{\frac{\chi_{max}}{2D_\xi}}}, \quad (3.7)$$

where Eq. (3.1) has been used. In addition, the first equality in Eq. (3.7) gives  $\delta = 2/\sigma$ , when Eq. (3.3) is applied. Hence, we obtain (with  $\Delta\xi = 1$ ):

$$\sigma = \sqrt{\frac{2\chi_{max}}{D_\xi}}. \quad (3.8)$$

Applying this expression to Eq. (3.6) gives

$$\chi = \chi_{max} (1 - (2\xi - 1)^2)^2, \quad (3.9)$$

which compares directly with Eq. (3.2). Figure 3.1 compares the two profiles, which are very close to one another. The advantage of the scalar dissipation rate profile derived from the tanh profile is that the expression is simpler to compute, and the profile can more readily be converted from physical space to mixture fraction space. Given the significant assumptions that went into these profiles ( $Le = 1$ , constant diffusivity, etc.) the difference is not that great. On the other hand, the close agreement implies that the tanh profile for mixture fraction is a good representation of the error function mixture fraction solution that was used to derive Eq. (3.2).

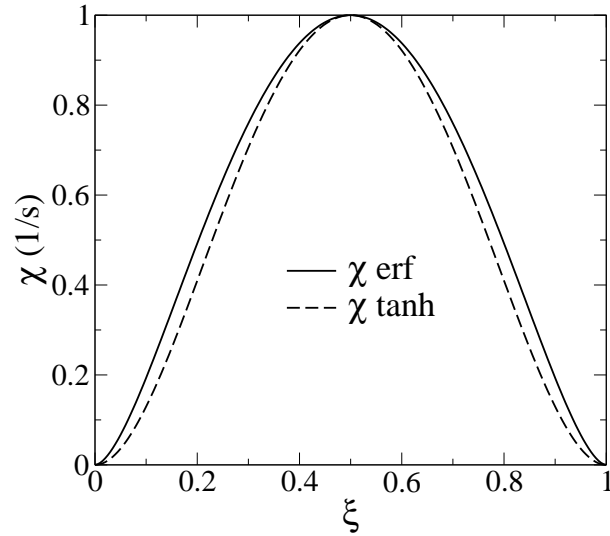


**Figure 3.1.** Comparison of  $\chi$  profiles.

Figure 3.2 shows profiles of mixture fraction versus position for values of  $\sigma$  ranging from 5 to 35 cm in increments of 5 cm. Flamelet profiles were computed for some of the values of  $\sigma$  and are shown in Fig. 3.3. Profiles of temperature and  $O_2$ , OH mass fractions are shown plotted versus mixture fraction on the left side of the figure. Corresponding plots in physical space are shown on the right. As the dissipation rate  $\chi$  (or  $\sigma$ ) increases, the profiles become narrower indicating a more highly strained flame. Figure 3.4 shows the width of the tanh profile and the full width at half maximum (FWHM) of the temperature to be nearly the same. In the mixture fraction ( $\xi$ ) coordinate, the peaks in the profiles tend to occur at the same values of  $\xi$  since the location of the flame in  $\xi$  space is constant. The position of the peaks in physical space is a direct consequence of the mixture stretching in physical space with varying scalar dissipation rate shown in Fig. 3.2. In Fig. 3.3 the temperature versus position curves coincide at position 0, corresponding to a mixture fraction of 0.5, which is where the  $\xi$ - $y$  curves coincide in Fig. 3.2.

As the flame is strained, the intermediate and product profiles decrease, as does temperature. This effect is due to the competition between reaction rates and diffusion rates in  $\xi$  space. As the flame is strained, diffusion rates increase, and the chemical reactions do not proceed to completion as nearly as they do at lower strain. Conversely, as the dissipation rate increases, the oxygen levels are higher (as are CO mass fractions,

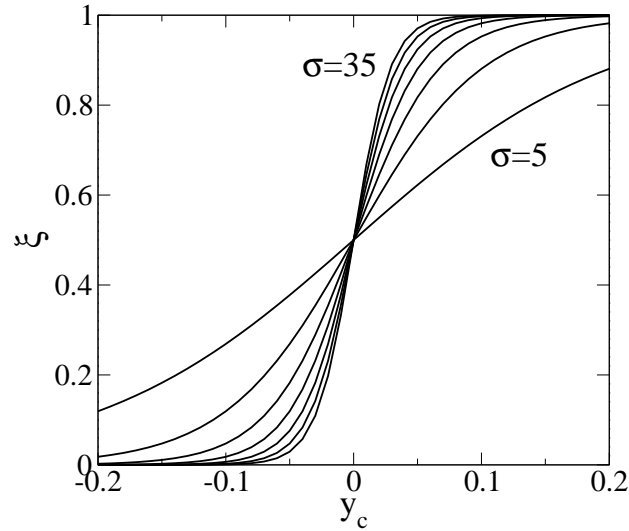


**Figure 3.2.** Hyperbolic tangent profiles of mixture fraction for various  $\sigma$ . Curves are spaced by  $5\sigma$ .

which are not shown). In the higher strained flames, significant amounts of oxygen are able to diffuse unreacted past the reaction zone (indicated by the OH profiles) into very rich regions. With continuing increases of  $\sigma$ , the flame eventually extinguishes.

The composition and temperature dependence of the diffusivity of the mixture fraction used in Eq. (3.6) results in profiles of the scalar dissipation rate not centered on  $\xi = 0.5$  as they are in Fig. 3.1. Figure 3.5 shows the thermal diffusivity as a function of mixture fraction for the  $\sigma = 20$  cm case. The  $\chi$  profile results from the product of the diffusivity and the quadratic functions in Eq. (3.6). The peak in  $\chi$  is intermediate between that in  $D_\xi$  and the quadratic function. If a flamelet profile in physical space is desired at a scalar dissipation rate based on the usual flamelet formulation (not the tanh version), the dissipation rates at the stoichiometric mixture fraction should be equated between Eqs. (3.2) and (3.6) (using  $D_{\xi,st}$ ) and the result solved for  $\sigma$ . The equation is a rearrangement of Eq. (3.6):

$$\sigma = \sqrt{\frac{2 * \chi_{st}}{D_{\xi,st}(1 - (2\xi_{st} - 1)^2)^2}}. \quad (3.10)$$

While the overall  $\chi$  profiles will be different for the two cases, the values at the stoichiometric point are the same. The  $\chi$  profiles between the two approaches are different due

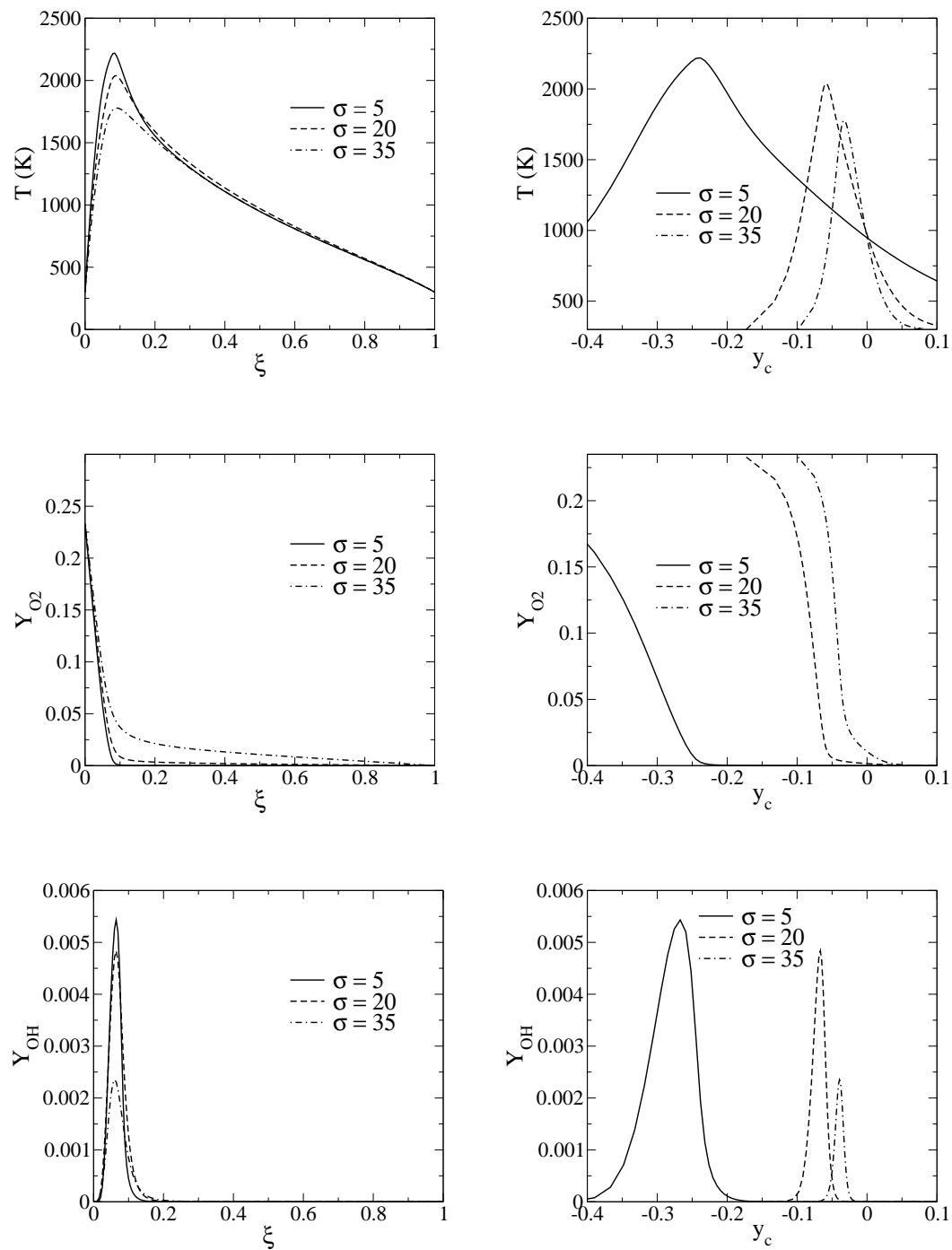


**Figure 3.3.** Flamelet profiles in the physical (right) and mixture fraction (left) domains.

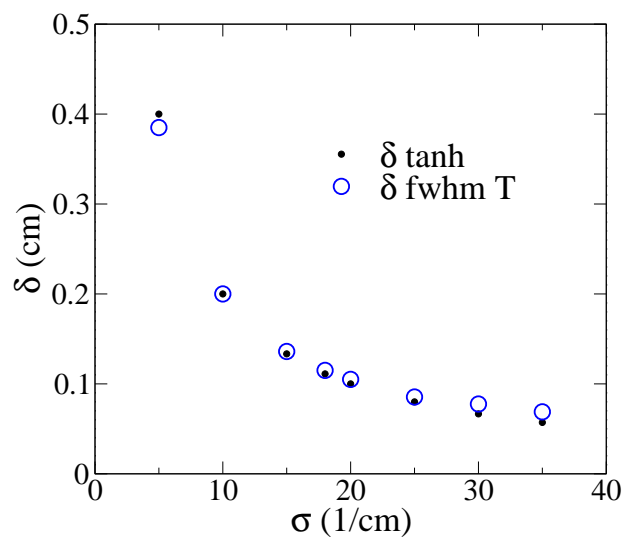


**Figure 3.4.** Comparison of scaling parameter  $\sigma$  and layer thickness  $\delta$  based on tanh and temperature profile at FWHM.

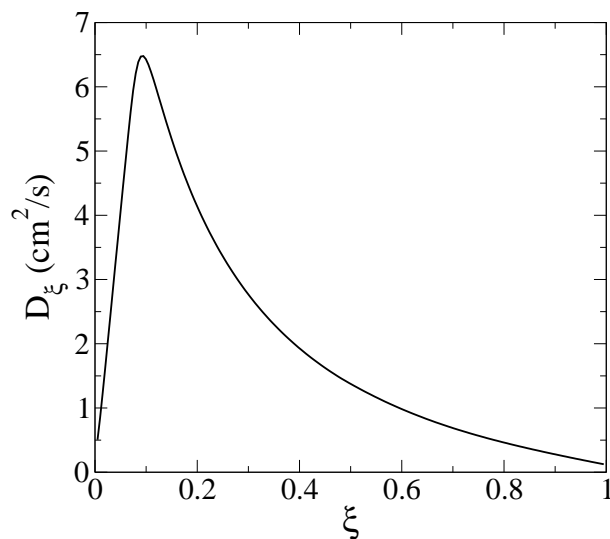


**Figure 3.5.** Mixture fraction diffusivity for  $\sigma = 20 \text{ cm}^{-1}$ .

to the variation of the diffusivity. The  $\chi$  profiles for the usual and tanh versions can be written as

$$\chi = \chi_{st} \frac{g(\xi)}{g(\xi_{st})}, \quad (3.11)$$

$$\chi = \chi_{st} \frac{h(\xi)}{h(\xi_{st})} \frac{D_\xi}{D_{\xi,st}}, \quad (3.12)$$

respectively. Hence, while  $\chi$  may be the same at  $\xi_{st}$ , lower values are obtained for the tanh version at  $\xi$  higher and lower than  $\xi_{st}$  due to the corresponding decrease in  $D_\xi$ . Figure 3.6 shows a sample result for a  $\chi_{max}$  of 800 1/s from Eq. (3.1). The agreement at the stoichiometric point ( $\xi = 0.064$ ) is not perfect since, for this run,  $D_{\xi,st}$  was computed at the equilibrium point, not by iteration within the flamelet code. The strong dependence of the diffusivity on mixture fraction (temperature) highlights the importance of the flame properties on the flame structure.

### 3.2 Results

Figure 3.7 shows the temperature, velocity, mixture fraction, and density of the baseline flame at 10 ms. The pressure is atmospheric, and the fuel and air streams are undiluted. At this time, the velocity ranges from 20 to -20 cm/s. The velocity peaks

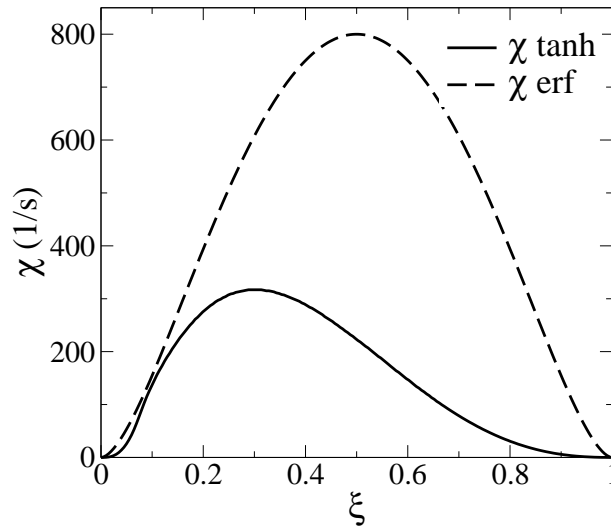


**Figure 3.6.** Comparison of  $\chi$  between the tanh and usual formulations.

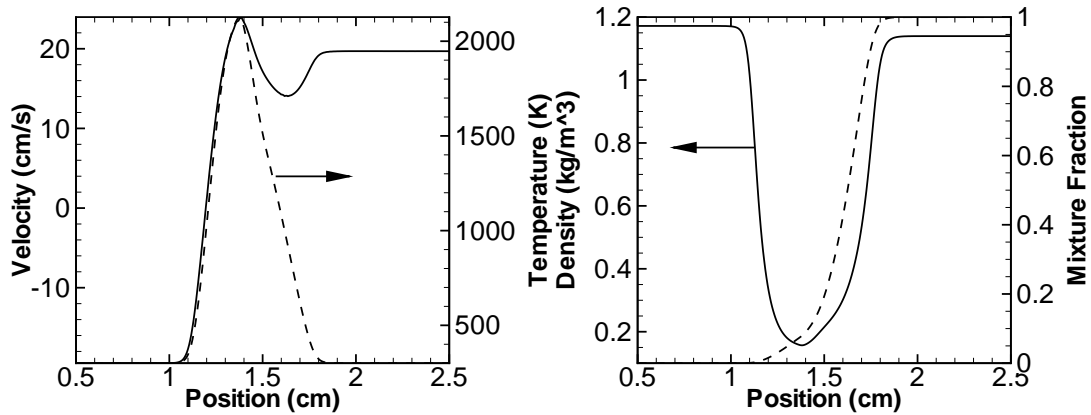


**Figure 3.7.** Flame structure of the base case at 10 ms. Temperature, velocity, density, and mixture fraction profiles are shown.

where the density is a minimum, consistent with mass conservation. This position is also the peak temperature position. The width of all the curves are also consistent. As shown below, the velocity magnitude profile decreases in time as the mixture fraction gradient becomes smaller and the rate of diffusion into the flame zone is reduced. The dip in the velocity profile near 1.5 cm is a commonly observed phenomena in opposed flame simulations. The expansion of the flame zone causes a net outward velocity which passes through zero. The dip is due to the superposition of this velocity profile (negative, through zero, to positive) with the density profile, whose dip tends to *lift* the otherwise monotonic velocity profile correspondingly. Hence, it is not really the dip in the velocity that is interesting; it is the peak in the velocity near 1.5 that is due to the density profile. Near the flame, the mixture fraction profile flattens due to the increased diffusivity of the mixture fraction (taken as the thermal diffusivity,  $Le = 1$ ) at higher temperature.

The influence of the soot on the radiative field and thermal heat loss is of primary interest. Radiative heat losses are due to gas and soot, and the contribution due to soot depends on the soot volume fraction and the temperature. Because the soot is formed and peaks on the rich side of the flame, whereas the temperature is maximum near the stoichiometric point, the peak soot radiation will occur between the peak soot and peak temperature locations. This overlap between soot and temperature is important to the overall radiative heat loss. The position of the soot peak in the flame will depend upon its chemical reaction rates and transport properties. The effects on radiation will depend on the transport and radiative timescales and should be considered in the context of the

turbulent convective scales.

### 3.2.1 Thermophoretic Diffusion Effects

The motion of the soot in the unsteady flame depends on the convective and thermophoretic diffusion velocities, as well as its chemical source term. The soot particles are generally large compared to gaseous species, though still in the free molecular range. Thermophoresis tends to transport soot down the temperature gradient, which is away from the flame, towards the fuel stream. Initially, before any soot is present, the soot peak should overlap with the net soot production peak. However, the soot reaction peak is dominated not only by the local soot loading but also, importantly, by the temperature and  $C_2H_2$  fields. While the soot particles are convected and diffused away from the flame, the soot reaction rate peak is relatively stationary in physical space, at short times. Figure 3.8 shows the soot mass fraction and soot reaction rate peaks at two times. Both the soot and soot rate peaks broaden and increase with time, but the soot peak moves to the right, while the rate peak position is relatively constant.

The mechanism of the motion is examined as follows. The relative position of the soot mass fraction peak in time is extracted from the simulation. In addition, the thermophoretic diffusion velocity and convective gas velocity at the soot mass fraction peak are extracted. The position of the soot peak relative to the reaction rate peak is

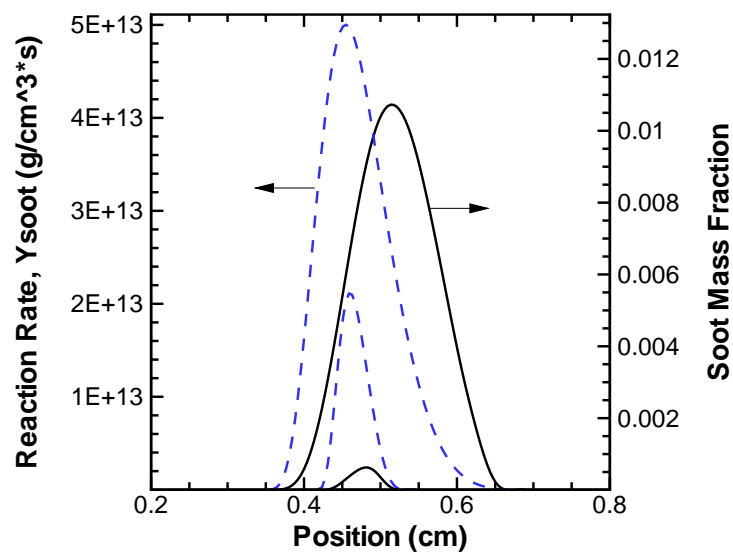


**Figure 3.8.** Soot net reaction rate and mass fraction at 0.9 ms and 8.0 ms for Case 1

predicted by integrating the peak velocity components in time. Figure 3.9 shows the results for Case 1.

The results are somewhat surprising. First, the convective velocity at the soot peak is 4.2 times higher than the thermophoretic velocity with an average deviation of 4% up to 86.5 ms. This results in the predicted peak position due to convection being much higher than by thermophoresis. As previously noted, there is no external flow field in this case. All the convective velocity is due to the flame expansion as it burns. Figure 3.10 shows the convective velocity, thermophoretic diffusion velocity, and the (negative of) diffusion velocity of the mixture fraction at the soot peak as a function of time. The peak soot occurs at a mixture fraction between 0.15 and 0.3, while the stoichiometric mixture fraction is 0.064. Hence, the convective and thermophoretic velocities at peak soot are toward the fuel stream, and the mixture fraction diffusion velocity at peak soot is toward the air stream. This figure provides a feel for the magnitudes of the velocities involved and how they vary in time. The diffusion velocity of the mixture fraction is substantially higher than the convective velocity. This former velocity is defined here as  $V_\xi = \frac{D_\xi}{\xi} \nabla \xi$ , where  $D_\xi$  is taken as the thermal diffusivity. A more rigorous treatment is considered in Chapter 5. The values of the velocities can be roughly compared to a typical

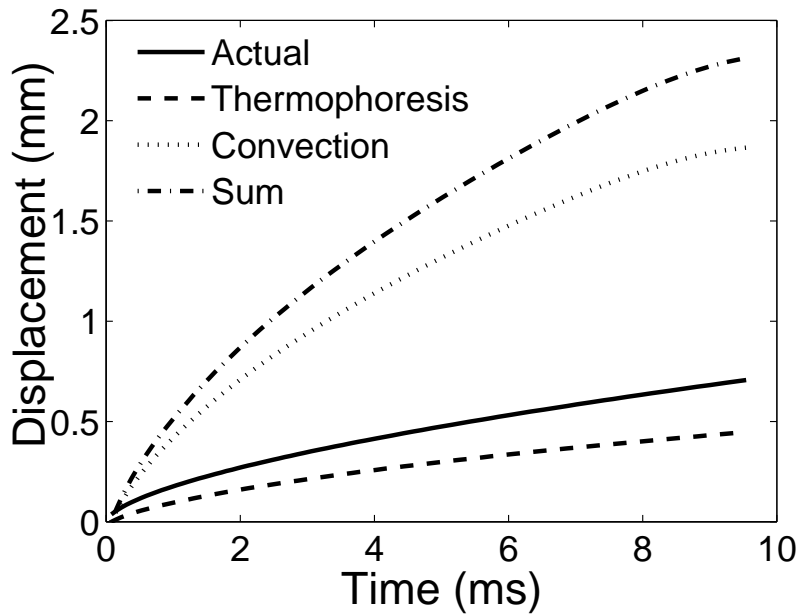


**Figure 3.9.** Actual and predicted soot mass fraction peak position relative to the net soot reaction rate peak versus time.

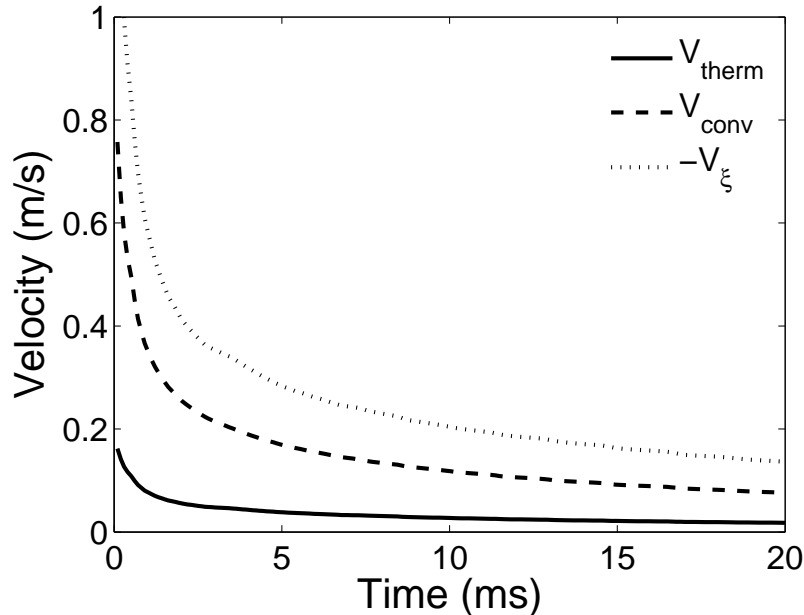


**Figure 3.10.** One-dimensional Case 1 velocities at the soot peak: thermophoretic, convective, and the negative of the mixture fraction diffusive velocity.

turbulent jet. Copalle and Joyeux studied a turbulent flame at an exit Reynolds number of 11,800 with an exit velocity of 29.5 m/s and an exit diameter of 4 mm [14]. The peak soot volume fraction of 1.9 ppmv occurred at 38 cm downstream. Using a simple, cold turbulent jet decay velocity relation [2], the axial velocity at the peak soot is estimated to be  $\approx 2$  m/s. Assuming a turbulent intensity of 10% gives a velocity fluctuation of 0.2 m/s, which is of the same order as the velocities in Figure 3.10.

Another result of Figure 3.9 is the discrepancy between the actual position of the soot peak and the position predicted by integrating the peak velocities. The predicted relative position is about a factor of 3 higher than the actual position. The thermophoretic component alone nearly predicts the position, but the convective component puts it over the top. The discrepancy lies in the fact that the soot peak is continually being modified by the reaction source term. As the thermophoresis and convection move the soot peak to the rich side, the reaction rate peak (which is stationary here) provides a source term that essentially *drags* on the soot and moves the peak, essentially slowing it down. As the reaction proceeds, the mixture fraction profile becomes broader and more diffuse, so the spreading in the soot peak is partly due to the spreading of the reaction rate peak that forms it.

Figure 3.11 shows profiles of soot mass fraction (left) and net soot production rate (right) at times of 2, 10, and 50 ms. The solid lines are those of the base case, while the dashed lines are of the base case with no soot diffusion. As noted earlier, the soot profiles grow and broaden in time and move to the right (away from the flame zone) due to convection and thermophoresis, being modified by chemical reaction. The thermophoretic effect is clear in this figure. Without thermophoresis, the soot peak is slightly greater and less broad due to a steepening of the right side of the peak (the profile is negatively skewed). The left side of the peak is broader than the right side due to the reactive source term that is concentrated on the left and builds up the soot level as the soot is transported to the right via convection and thermophoresis.

The difference between the peaks on the right side in the figure is more directly due to thermophoresis, and the difference corresponds well with the integrated thermophoretic velocity. The effect of thermophoresis, however, is not that significant up to 50 ms. The soot peak mass fractions differ by 20, 17, and 9% at the increasing times of 2, 10, and 50 ms, respectively, shown in the figure. The temperature difference between the case with and without soot diffusion is barely visible when plotted, with a maximum difference of 16 K (less than 1%) at 50 ms. A smaller temperature difference effect exists at earlier times. The case without thermophoresis has a slightly lower temperature profile due to the higher soot level and higher temperature at the soot peak, resulting in slightly greater radiative heat loss. The soot reaction rate profiles are also shown in the figure.

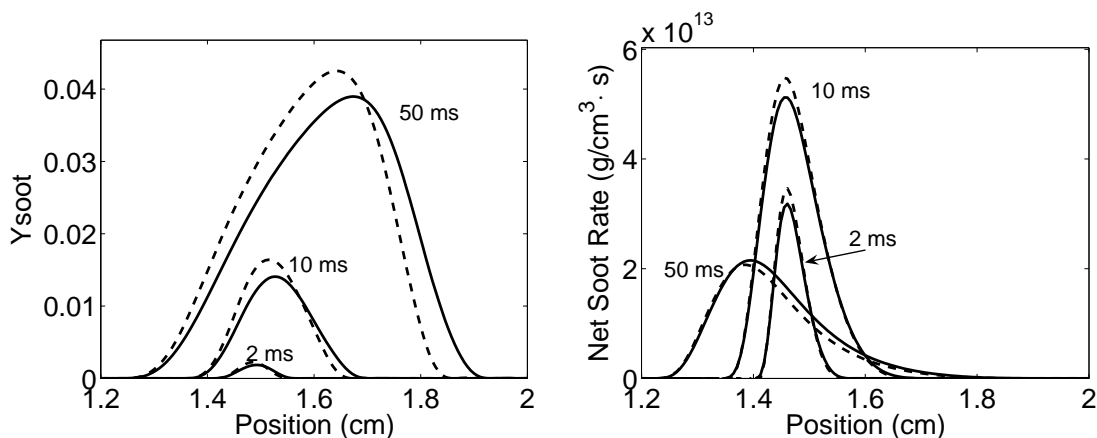


**Figure 3.11.** Soot mass fraction (left) and net soot reaction rate (right) at three times. Solid lines are the baseline case, and dashed lines are the baseline case with no thermophoretic diffusion.

The reaction rate peak is more stationary in time (especially at small times) than the soot peak. The reaction rate peak broadens with time as the mixture fraction broadens. The reaction rate peak, however, is not monotonically increasing with time, but initially increases, then decreases, as a result of the competing dependence of soot concentration, temperature, and acetylene concentration (the latter two tending to decrease with time, while soot increases). At 50 ms, the soot reaction rate with no thermophoresis is actually lower than that with thermophoresis, which is primarily due to the reduced temperature profile of latter. At the other two times, the difference in the reaction rate is due to the difference in the soot levels since the temperature and acetylene concentrations are approximately equal at those times. Thermophoresis alone appears to have a rather marginal effect on the soot and temperature profiles (value and position), which are the most important to the overall flame structure.

### 3.2.2 Radiative Effects

The second parametric case considered is the baseline case with the radiation model turned off. Figure 3.12 shows a comparison of results for the soot mass fraction and temperature profiles at times of 2, 10, and 50 ms. The dashed lines are the adiabatic case. At 2 ms, the temperature profiles are nearly indistinguishable, differing by at most 6 K. At 10 ms the difference of 37 K is still small. At 50 ms, the temperature difference of 261 K is substantial. The fraction of the sensible enthalpy (based on temperature alone) is 0.3, 2, and 14%, at 2, 10, 50 ms, respectively. At the longest time, the characteristic

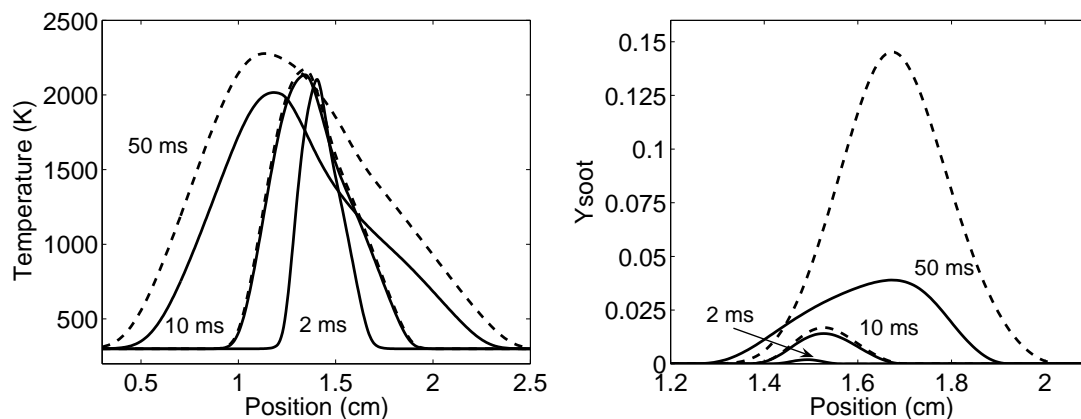


**Figure 3.12.** Temperature profiles (left) and soot mass fraction (right) at three times. Solid lines are the baseline case, and dashed lines are the baseline case with no radiative heat loss.

dip in the temperature profile on the right side of the peak is evident, where the radiative heat loss is maximum. This figure emphasizes the relatively long radiation timescale required for substantial levels of heat loss. The soot profiles are especially indicative of the dependence on temperature through the reaction rate. While the thermophoresis had a relatively small effect on the soot concentration, radiative heat loss affects the soot concentration substantially, but again, only at longer times. The increase of peak soot without radiation is 1.8, 19, and 270% at 2, 10, and 50 ms, respectively. The locations of the soot peaks are virtually the same for each time shown, as is the shape for the first two times, but the shape of the curves at 50 ms is slightly broader on the left of the radiating peak. The peak boundaries are consistent with the acetylene and temperature profiles.

Figure 3.13 shows profiles of the gas and soot components of the radiative source term ( $W/cm^3$ ) at times of 2, 10, and 50 ms. The magnitude of the gas radiation rate is relatively constant in time, as the flame temperature is relatively constant, although the profiles spread significantly as the flame spreads due to diffusion. The position of the peak gas radiation moves with the stoichiometric flame position as the mixture fraction spreads to lower position at the stoichiometric value due to diffusion. The radiative source of the soot peak increases with time since the radiative component is proportional to the soot volume fraction, which grows and spreads with time. The soot radiative peak location is more stationary in time. At 50 ms, the right half of the peak is broader than the left,

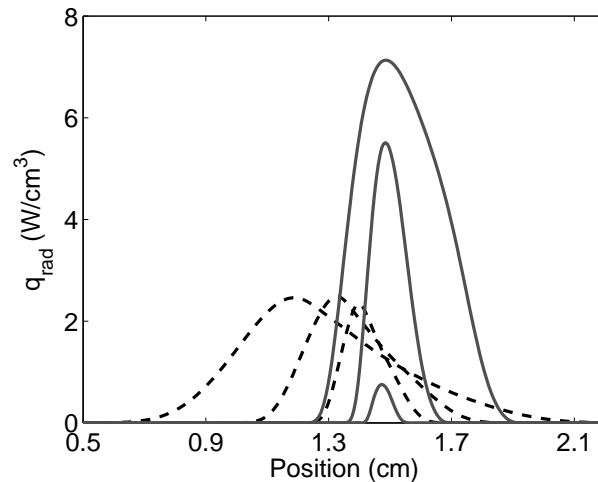


**Figure 3.13.** Optically thin radiative source term at times of 2, 10, and 50 ms. The soot contributions are the solid lines and the gas contributions are the dashed lines. In each case the peaks spread with time.

indicating the tradeoff between the dependence of the radiative source on soot volume fraction (which is higher on the right of the radiative peak) and the temperature (which is higher on the left of the peak). The peaking soot volume fraction counteracts the decreasing temperature, and the peak appears slightly lifted on the right. At any rate, at 10 ms, the soot contribution is twice that of the gas. However, the soot radiation does not increase indefinitely but slows as the soot concentration increase slows (consistent with Figure 3.14).

The peak value of the soot versus time for the radiating case is shown in Figure 3.14. From this figure, the soot formation timescale (for this, unstrained configuration) is estimated to be 25 ms, using the common relation  $\tau = \Delta Y_s / (dY_s/dt)$ . The radiative timescale was estimated in two ways as follows. First, the temperature difference between the radiative and adiabatic cases was plotted versus time and the timescale estimated. This approach does not take into account any chemical reaction effects (internal energy transformations) that may occur at the two different temperatures of the two cases. The second method was to numerically integrate the profile of  $\dot{q}/\rho c_p$  (units of Kelvin per second), at the position of the peak radiation, in time, and compute the timescale as for the soot case. Both methods gave a timescale of 80 ms, indicating that for this configuration, the radiative timescale is about three times greater than the soot formation timescale. This radiative timescale is significantly greater than the soot formation timescale and the relevant transport timescales. The convective (here due to flame

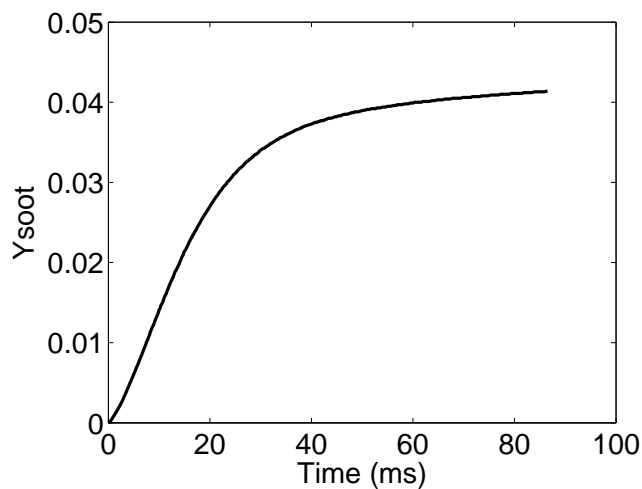


**Figure 3.14.** Peak soot mass fraction versus time for the baseline one-dimensional case.

expansion), thermophoretic diffusion, and mixture fraction diffusion have timescales of 7, 9, and 7 ms, respectively. These values are based on an integration of the data of Figure 3.10 up to 80 ms and are consistent with more crude estimates of the type  $\tau = L^2/D$ . Here, a higher velocity may give a similar timescale if the corresponding lengthscale is higher since  $\tau \sim L/v$ , where  $L$  is the relevant lengthscale.

Figure 3.14 also suggests why laminar diffusion flames often contain substantially more soot than turbulent diffusion flames. Turns lists smoke points in laminar flames for various fuels [2]. Ethylene is listed as having a peak soot volume fraction of 5.9 ppmv. At 50 ms for the baseline case here, the volume fraction is 6.7 ppmv. In many turbulent and opposed flow environments, experimental concentrations of ethylene are about 1 ppmv, consistent with a shorter formation timescale associated with the flow environment. In Fig. 3.14, this concentration corresponds to a soot mass fraction of about 0.01, and a time of 10 ms, which is of the order of many experimental flow times. The point is that soot grows monotonically in time and that the level of soot produced in a given situation may be less than the peak values due to the timescales involved. On the other hand, in order to obtain significant levels of radiative loss, a relatively long residence time is required. The multidimensional DNS simulations are too expensive to be run for more than a few milliseconds. Hence, the radiative heat losses are small, and the optically thin approximation is valid.

### 3.2.3 Comparison of Gas-Phase Chemical Mechanisms

The detailed mechanism that was used to generate the reduced mechanism was run in the same manner as the baseline case in order to further validate the reduced mechanism in the presence of transport. The reduced case was run on a 3 cm domain with 60  $\mu\text{m}$  grid spacing while the detailed mechanism was run on a 1 cm domain with a 20  $\mu\text{m}$  grid spacing. The smaller grid in the detailed case was required due to the high resolution requirements of some short-lived radical species. The smaller domain was used to reduce the computational run time.

The validation of the reduced mechanism has been described but included premixed and nonpremixed flames under varying stoichiometry, strain, and includes extinction. Here the primary interest is to compare the detailed and reduced mechanisms in the current configuration (one-dimensional, S3D) to examine the effects directly applicable to the soot formation. The most important gaseous species considered is acetylene since

this species directly contributes to the soot nucleation and growth steps. Oxygen is the primary oxidation species, and hydrogen and carbon monoxide are products of the soot production/growth and oxidation steps, respectively. The two-dimensional simulations have an upper bound run time of 10 ms, so the detailed case was only run up to 9 ms. The profiles of all major species and temperature were indistinguishable at 9 ms. In addition, radical profiles such as OH, O, H, and HO<sub>2</sub> were virtually the same (so they are not shown) with the exception of HO<sub>2</sub> which has two peaks, the richer one being slightly overpredicted. The reduced mechanism (here and previously) represents the important flame characteristics, and this is not surprising since it was designed that way. However, the reduced mechanism does not include higher hydrocarbon species (although C<sub>3</sub>H<sub>6</sub> is included).

Comparison of the impacts of the detailed and reduced mechanisms on the acetylene and soot mass fractions, along with the soot number density, is performed. Resulting profiles are shown in Fig. 3.15. The acetylene profile for the detailed mechanism is about 30% lower than for the reduced mechanism, resulting in an overprediction of the soot mass fraction. This overprediction of the reduced mechanism is presumably because acetylene is active in the growth of higher hydrocarbon species, the neglect of which results in elevated acetylene concentrations. However, the increase really is not that high, especially considering the level of experimental uncertainty. It is encouraging that the soot profiles are of the same shape, with the same position and width, but with differing magnitudes. Certainly, it can be said that the qualitative behavior of the two mechanisms is the same, and the quantitative agreement is reasonable. The agreement between the soot number density profile is observed to be much closer than soot and acetylene mass fractions. All of these results are essentially unchanged at earlier times in the simulation.

A simple fix to the acetylene overprediction would be to tabulate the acetylene concentration of the detailed mechanism as a function of mixture fraction, heat loss, and scalar dissipation rate and use that value instead of the value computed from the reduced mechanism. This approach would require extensive testing of the parameter space in one-dimensional nonpremixed simulation and would leave open questions associated with multidimensional effects, such as curvature and flame-flame interactions that may be present. Alternatively, the soot reaction rate could be tuned to achieve better agreement with the detailed mechanism. The soot nucleation and growth rates in the Leung and

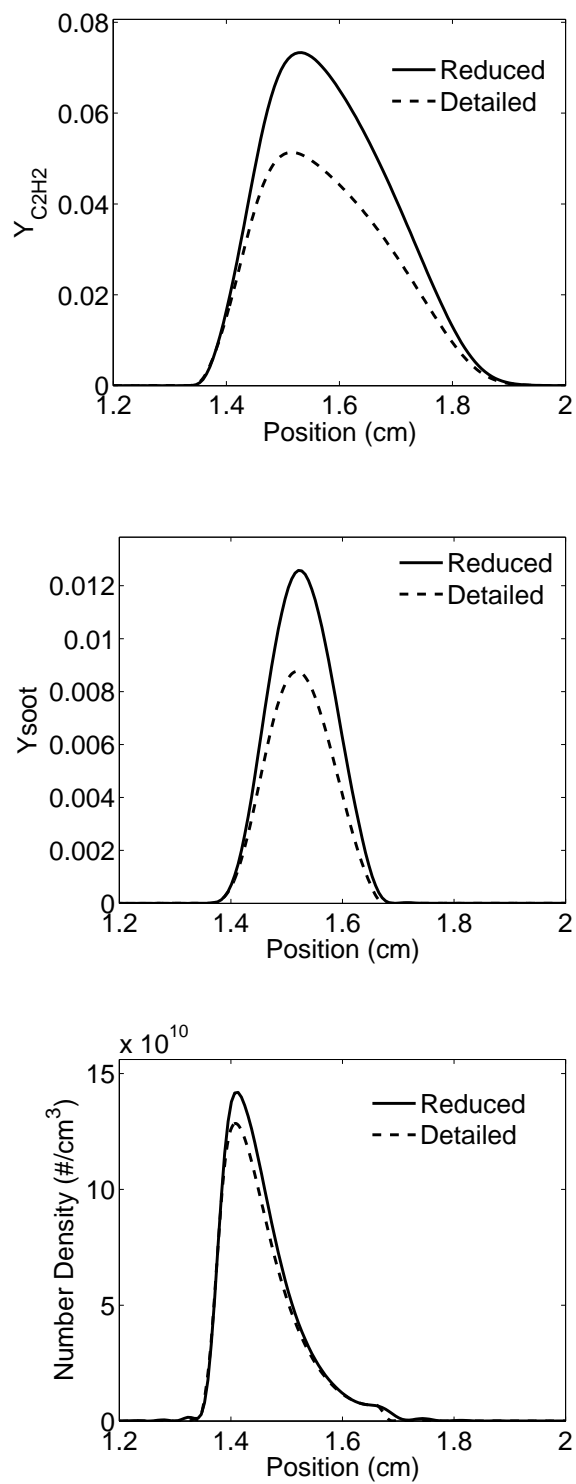


**Figure 3.15.** Comparison of detailed and reduced mechanisms at 9 ms.

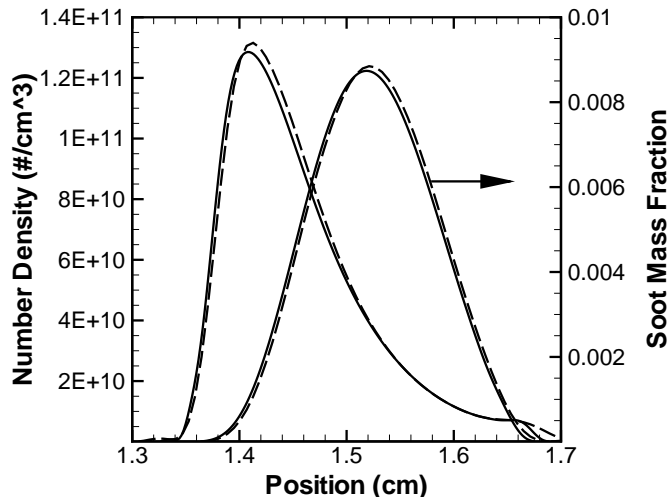


**Figure 3.16.** Soot mass fraction and number density at 9 ms for the detailed case and the base case with soot nucleation and growth rates multiplied by a factor of 0.8. The dashed lines are the reduced chemistry case.

Lindstedt model [5] are proportional to the acetylene concentration, so the discrepancy between the detailed and reduced models suggests a constant multiplicative factor. A series of three tests of the baseline case with tuned soot nucleation and growth rates were attempted using multiplicative factors of 0.7, 0.85, and 0.8. The first two factors were computed by simply taking the fractional overshoot or undershoot in the soot mass fraction between successive cases. This approach tended to overcompensate or undercompensate for the error, so the final value was found by a curve-fit to the relation between the difference between the soot peaks of the reduced and detailed mechanism and the corresponding rate factor. This approach gave a value of 0.8 instead of the value of 0.77 which would have been used if computed as for the first two tries. The factor of 0.8 does a good job of compensating for the increased soot produced by the elevated levels of acetylene in the reduced mechanism. As Fig. 3.16 shows, the soot mass fraction and number density peaks of the reduced and detailed mechanisms are nearly the same with this value. The good agreement was also observed at times of 1 and 4 ms. The proximity to unity of the 0.8 factor emphasizes that the reduced mechanism performs fairly well. In addition, use of this factor would not be expected to do any worse than the current soot mechanism if used under conditions not explicitly considered in determining the rate factor, e.g., conditions of higher strain.

# CHAPTER 4

## TWO-DIMENSIONAL MIXING LAYER SIMULATIONS

A series of two-dimensional temporal mixing layer simulations were performed to study soot formation and flame-flow interactions in a well-characterized and physically relevant configuration. Effects of Reynolds number and radiative heat transfer on soot formation are investigated, as well as the influence of heat release on the flame dynamics.

### 4.1 Introduction

The mixing layer that develops between two parallel streams at different velocities is considered an ideal canonical configuration for the fundamental study of flame-turbulence interactions. Mixing layers are sensitive to flow perturbations which initiate the well-known Kelvin-Helmholtz instabilities present in many flow environments where a parallel shear flow exists. Examples include the region behind a rearward facing step, the developing region of turbulent jets, and the wake region of a bluff body. Figure 4.1 is a schematic of a spatially evolving mixing layer that develops as two streams separated by a thin splitter plate are brought together. The mixing layer thickness increases in the downstream direction as the vortices entrain fluid. The rollup of the eddies strains the interface between the two streams, increasing the surface area and gradients by which diffusive processes result in molecular mixing. In addition, vortex pairing occurs between eddies, resulting in a further increase in the layer thickness and enhanced mixing. Eventually, the flow becomes fully turbulent as the Reynolds number increases. In the self-similar turbulent flow region downstream, the width of the mixing layer has been shown to increase linearly with distance [19]. In the initial developing region, the mixing layer increases steadily until the first eddy forms, after which the layer thickness is relatively constant until vortex pairing occurs, at which point the mixing layer thickness increases again [116], and so on.

Spatially-developing mixing layers are characterized by two velocity scales, the mean

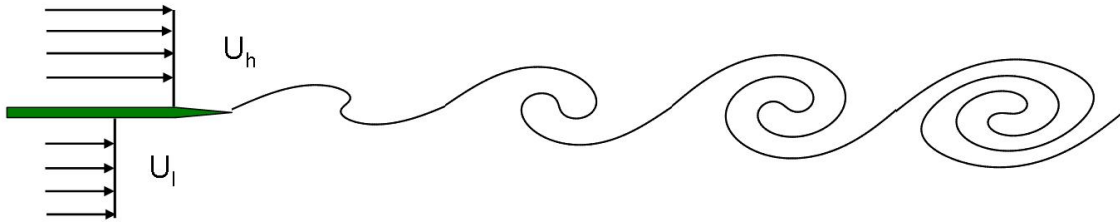


**Figure 4.1.** Typical experimental mixing layer configuration.

stream velocity, and the velocity difference. The primary length scale is taken as the vorticity thickness defined in terms of the maximum velocity gradient, or the momentum thickness, which is an integral property. The Reynolds number increases as the layer thickness increases. Spatial mixing layers are not symmetric about the centerline but spread preferentially into the lower speed fluid [17].

DNS simulations are often performed for temporally evolving mixing layers rather than spatially evolving mixing layers. This is accomplished via a Galilean transformation in which the reference frame follows the evolution of a given eddy and allows many aspects of the spatial configuration to be studied with greater computational efficiency. The Galilean transformation is given by

$$X \rightarrow U_a t, \quad (4.1)$$

where  $U_a$  is the average velocity across the layer [117]. In the temporal mixing layer, the high- and low-speed streams are given equal velocities in opposite directions. This corresponds to the spatial configuration when the velocity difference is much smaller than the average velocity. Nonreactive temporal mixing layers are symmetric about the centerline before turbulence develops. The temporal configuration has the advantage of requiring smaller domain sizes and, hence, reduced computational cost, as well as allowing simpler boundary conditions. In the spatially-developing configuration inflow and outflow boundary conditions are required through which the streamwise flow passes. The specification of these boundary conditions is much more complicated than the periodic boundary conditions that are used in the temporal configuration.

In the developing regions of mixing layers, the primary flow structures are two-

dimensional. Even when the flow transitions to turbulence, two-dimensional structures are observed to persist. In three dimensions, secondary, streamwise vortices develop in the so-called *braid* regions between the main spanwise vortices.

## 4.2 Configuration and Initialization

Here, two-dimensional temporal mixing layer simulations are performed to study soot formation and flame-flow interactions. The configuration consists of periodic boundaries in the streamwise direction and nonreflecting outflow boundaries in the cross-stream direction. The lower portion of the domain consists of the oxidizer stream ( $\xi = 1$ ), and the upper portion of the domain consists of the fuel stream ( $\xi = 0$ ), with the mixing layer between the two streams represented by a hyperbolic tangent transition. A flame is initialized as described previously in Chapter 3 for the reactive shear layer cases. The pressure in all cases is 1 atm and the streams consist of pure ethylene and air at 300 K.

The velocity field is specified as a hyperbolic tangent transition between equal and opposite free-stream velocities:

$$u(y) = \frac{\Delta U}{2} \tanh(\sigma y). \quad (4.2)$$

Here,  $\sigma$  is a scale factor that determines the amplitude of the velocity gradient. Higher values of  $\sigma$  correspond to steeper velocity gradients or a lower vorticity thickness. Figure 4.2 is a schematic of the initial velocity profile. The layer thickness is referred to here as the vorticity thickness and is defined as

$$\delta = \frac{\Delta U}{\left| \frac{dU}{dy} \right|_{max}}. \quad (4.3)$$

Inserting Eq. (4.2) into Eq. (4.3) gives

$$\delta = \frac{\Delta U}{\frac{\Delta U}{2} \sigma (1 - \tanh^2(\sigma x))_{max}} = \frac{2}{\sigma}. \quad (4.4)$$

This velocity profile (which contains an inflection point) is inviscidly unstable to perturbations, and the profile develops a Kelvin-Helmholtz instability. In DNS simulations, it is desirable to develop the initial vortex, or roller, as quickly as possible in order to

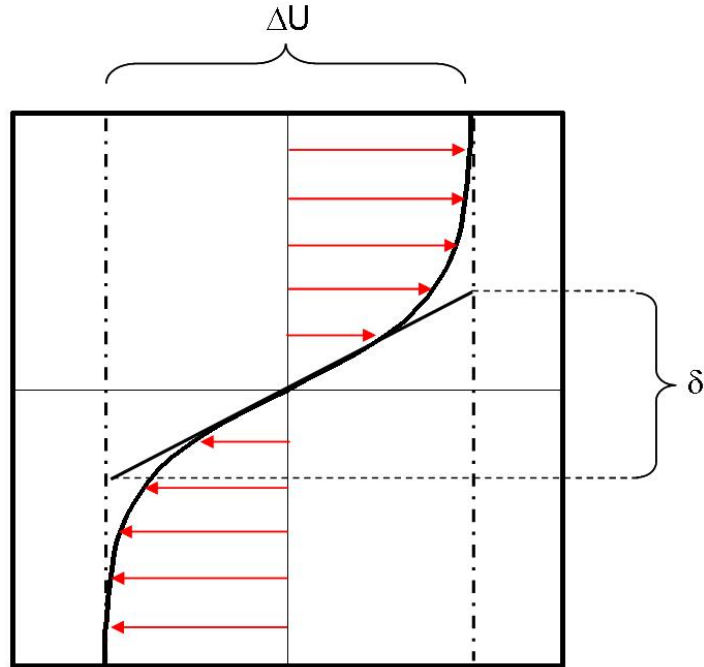


**Figure 4.2.** Initial velocity profile for the temporal mixing layer.

minimize the computational run time. This is done by perturbing the initial velocity profile using linear stability theory applied to the inviscid, incompressible velocity profile. Because the flow is parallel, flow perturbations are decomposed into their normal modes, similar to what is done in a Fourier series. The normal modes are taken to be traveling waves, where the wavelength is in the streamwise direction, and the wave amplitude is taken as a function of the cross stream direction  $y$ . The velocity is decomposed into the sum of the base profile and a perturbation as

$$\vec{u}(x, y, t) = \vec{u}_b(y, t) + \vec{u}_p(x, y, t), \quad (4.5)$$

where  $u_b$  and  $u_p$  denote the base tanh profiles and perturbation profiles, respectively. Appendix C details the specification of the velocity perturbations.

Figure 4.3 shows results of a DNS simulation applying the perturbed velocity profile to a temporal mixing layer. The figure shows the mixing between two streams at five sequential times when the velocity field is perturbed by both the fundamental and subharmonic modes. The upper figures show contours of the vorticity magnitude in the

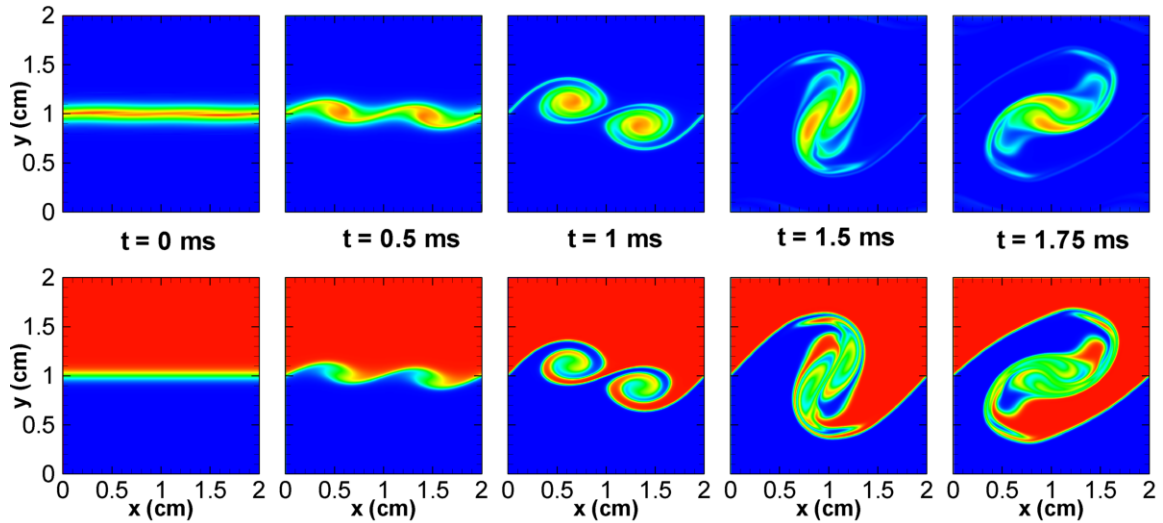


**Figure 4.3.** DNS simulation of a temporal mixing layer with vortex pairing.

range  $0\text{--}33,000\text{ s}^{-1}$ . The lower figures are mixture fraction (with a range of 0-1). The domain is  $2\times 2$  cm, with pure nitrogen at 300 K in both streams, with  $\Delta U = 40$  m/s and  $\delta = 0.14$  cm. The velocity perturbation parameter (see Appendix C) is  $\epsilon = 0.05$ . This figure illustrates both the initial rollup of the eddies, as well as vortex pairing that occurs. The upper figures are the vorticity magnitude, and the lower figures are images of scalar mixing of the two nitrogen streams.

#### 4.2.1 Simulation Parameters

Results of four simulations are discussed below with simulation parameters provided in Table 4.1. The simulations consist of

- Case 1: A baseline case with soot formation.
- Case 2: The baseline case at a higher Reynolds number (the velocity difference is  $\Delta U = 15$  m/s).
- Case 3: A cold flow simulation with no chemical reaction consisting of streams of nitrogen.
- Case 4: The baseline case with no radiation.

Except for Case 4, the optically thin radiation model is used. The velocity perturbation parameter is  $\epsilon = 0.05$  for all cases.

**Table 4.1.** Simulation parameters of mixing layer Case 1.

$L_x$ (cm)	1	$\Delta U$ (m/s)	10	$N_{grid}$	131,072
$L_y$ (cm)	2	$\Delta x, \Delta y$ ( $\mu\text{m}$ )	40	$N_{proc}$	64
$\delta_\xi$ (mm)	1	$\tau_r$ (ms)	10	Cost (CPU-hr)	6,656

### 4.3 Results

The structure of a reacting hydrocarbon mixing layer has been studied experimentally for temporal mixing layers [118, 119]. Here, similar temporal DNS simulations are performed and discussed. While the current cases do not correspond exactly to those of experimental configurations, an effort has been made to make the DNS simulations as relevant as possible, and many similar features are observed.

#### 4.3.1 Mixing Layer Structure

Figure 4.4 shows the evolution of the temperature field for Case 1 at five times: 2, 4, 6, 8, and 10 ms. The first two frames show the structure just prior to and after the initial development of the vortex. The upper half of the figures consists of fuel moving towards the right, and the lower half of the figure consists of air moving towards the left. The velocity profile is dominated in the early stages by the horizontally-dominated velocity. As the velocity perturbations grow, the Kelvin-Helmholtz instability develops and the vortex rolls up, forming a coherent eddy, which entrains fluid into the inner mixing region. These temperature contours illustrate the basic structure of the layer. As

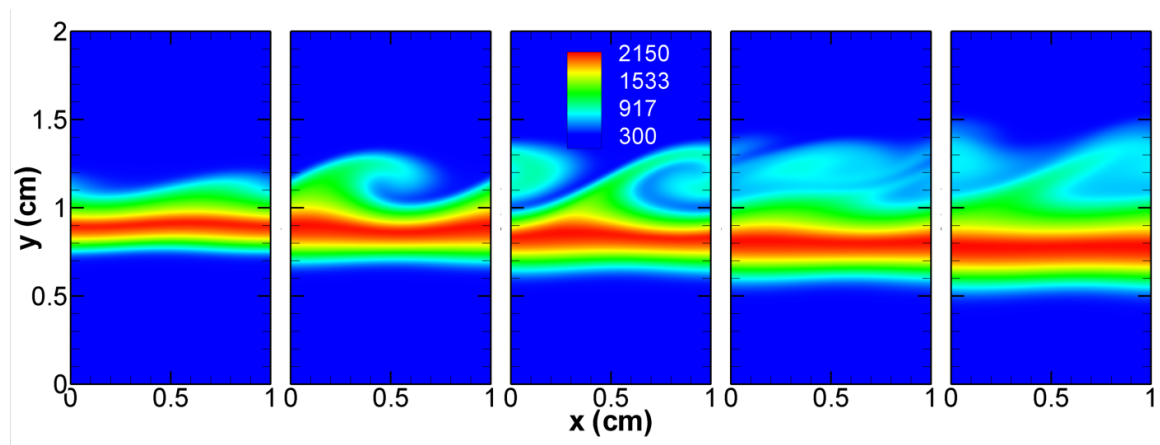


**Figure 4.4.** Progression of temperature (K) contours for Case 1. Frames are at 2, 4, 6, 8, and 10 ms.

has been previously observed, the reaction zone tends to locate entirely outside of the mixing layer [118]. This is clear from the relatively flat band of high temperature located at the base of the mixing layer. At most, the temperature band is slightly curved by the strain imposed by the vortex roll. The vortex forms and develops on the fuel side of the reaction zone. The primary interaction of the vortex with the flame is through convective mixing and straining of the flame. As the combustion products mix with fuel in the vortex, the temperature decreases. The reaction zone broadens with time as the fuel is continually brought into contact with the air stream and the mixing layer grows.

#### 4.3.1.1 Mixture Fraction Profiles

Analyzing the structure of the mixing layers through the mixture fraction is convenient because mixture fraction is a conserved scalar with no reactive source term. The mixture fraction shows the mixing of the material of the two streams and, to first order, is affected by complex chemical composition and temperature gradients only through fluid dynamic effects and the dependence of its diffusivity on temperature and composition. Figure 4.5 shows contours of mixture fraction for Cases 1, 2 and 3. The two isocontour lines shown in the figure are for  $\xi = 0.5$ , and  $\xi = \xi_{st} = 0.064$ . Only the central 1 cm of the transverse distance of the domain is shown. The mixture fraction is nominally the local fluid mass fraction originating in the fuel stream. Any conserved scalar can be used to define the mixture fraction. Here, Bilger's definition of the mixture fraction is used [120], which is a linear combination of elemental mass fractions. In the second and third frames of Cases 1 and 2, the vortex acts to entrain fuel into the core at the trough of the wave on the right side of the eddy. At the same time, combustion products are entrained into the eddy from the base of the vortex. These flame products then mix with the fuel in the vortex core.

Several important differences are observed between the three cases shown in Fig. 4.5. The cold Case 3, representing pure scalar mixing, is highly symmetric, in contrast to the two reacting cases. The differences in the distribution of this quantity between the reacting and cold cases are an indication of the effect of the combustion reactions on the fluid dynamics. The differences between the cases are caused by the effect of heat release, which increases the temperature and decreases the density. The corresponding effects of increased kinematic viscosity tend to lower the local Reynolds number in reactive regions, while the decrease in density of the fluid results in dilatation, which decreases the fluid

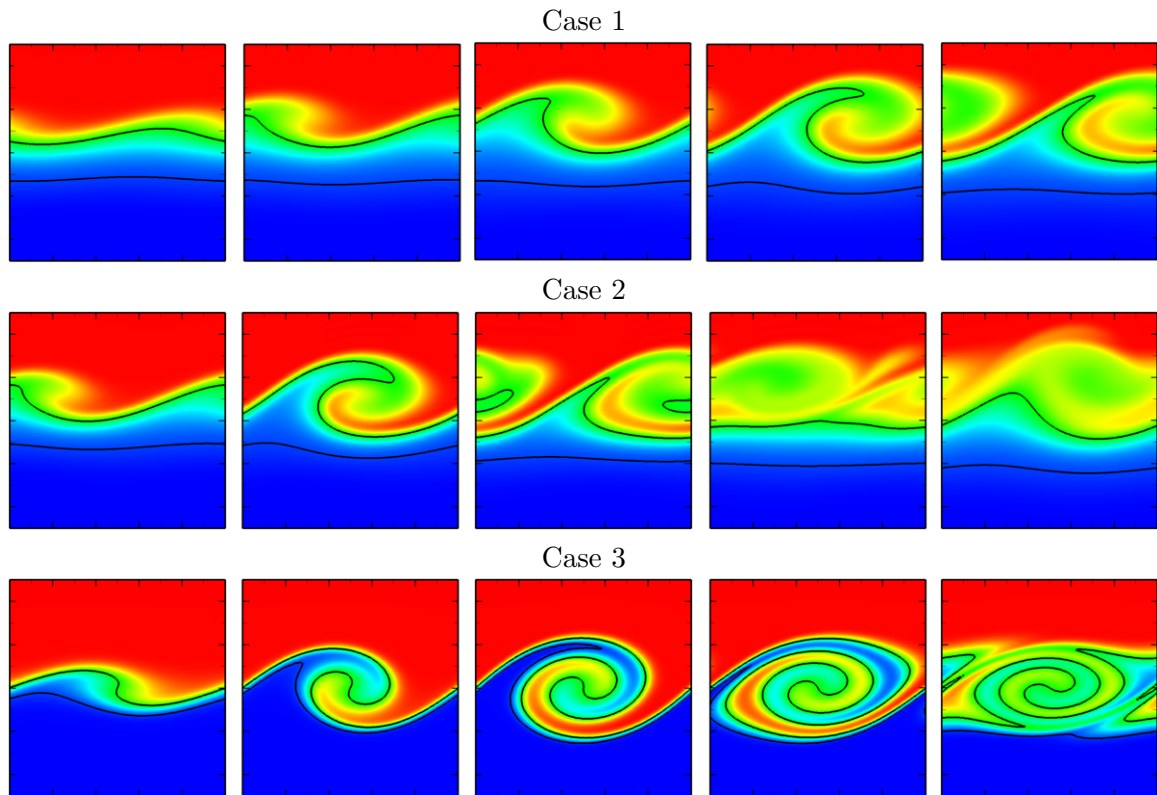


**Figure 4.5.** Progression of mixture fraction for three cases. In each row the frames are at 2, 3, 4, 5, and 6 ms. All frames are  $1 \times 1$  cm. Overlaid are  $\xi_{st} = 0.0637$  and  $\xi = 0.5$  isocontours.

vorticity. The mean molecular weight of the gases is nearly constant for the ethylene-air system chosen, with variations of less than 3%. There is no change of total moles for complete combustion of ethylene, and the molecular weight of ethylene, 28, is close to that of air. Hence, for this constant pressure system, the density change is almost entirely associated with temperature changes.

The position of the vortex-eddy is located in the upper portion of the domain for the reacting cases, in contrast to the cold case, which is centered in the middle of the domain. The fluid expansion, or dilatation, defined as the divergence of the velocity field is positive in the flame band, effectively pushing the vortex upward. In addition to the lack of symmetry in the reacting cases, the cold case has a center of vorticity that is stationary in the computational domain, as expected, while the reacting cases move to the right through the periodic domain. Figure 4.6 compares the cold Case 3 to the reacting Case 1 at 5 ms. The figure is colored by velocity magnitude with vorticity contours overlaid. The velocity at the top of the vortex of Case 1 is clearly greater than that at

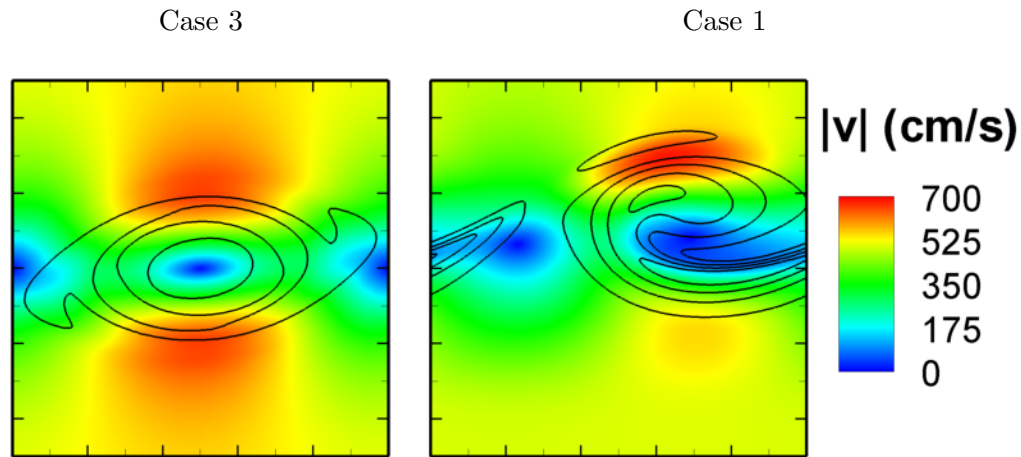


**Figure 4.6.** Velocity magnitude contours (m/s) for Cases 1 and 3 at 5 ms. Overlaid are vorticity contours spaced at  $1400 \text{ s}^{-1}$ .

the bottom, with the result that the vortex moves to the right. The reduced velocity at the bottom is due to the dilatation at the vortex bottom, as well as the increased kinematic viscosity. Perhaps more importantly, the initial burning solution has a reduced density in the lower part of the domain, so that these regions have less momentum than the higher-density upper air stream from the beginning.

In Fig. 4.5, the effect of heat release on the mixing layer development is pronounced. Cases 1 and 3 differ only by the presence of chemical reaction. The 4 ms frame for Case 1 appears to coincide roughly with the 3 ms frame of Case 3, whereas at a later time, the 6 ms and 4 ms frames seem to be in phase for Cases 1 and 3. At the same time, Case 2 seems to be better related to the slower cold Case 3. These effects have been shown to be due to the decreased vorticity in the region of the vortex due to vorticity diffusion via baroclinic torque and dilatation, as well as the decrease in Reynolds number with increasing kinematic viscosity [37].

#### 4.3.1.2 Flame Location

It is well known that flame zones tend to reside outside of shear mixing layers on the air side. Pickett and Ghandhi found this in their experimental mixing layers and summarized similar findings by others [119]. Explanations given include

- an increased diffusion coefficient with temperature in the internal layer, tending to move the flame outside the vortex,
- heat release, causing vorticity decay and relaminarization of the reaction zone, and

- dilatation of the flame pushing the vorticity zone away from the reaction zone.

This flame exclusion is important since mixing layer structures appear in many practical turbulent flows, such as exit regions of burners.

In the cold Case 3,  $\xi_{0.5}$  is rolled up into the core, always located where the two streams meet, as expected. In contrast,  $\xi_{st}$  is initially rolled up into the core but is then *pushed* out of the core at later times and is located below the vortex core. For the reacting cases, the behavior is the same except that  $\xi_{st}$  never makes it into the core at all but lies in a flat band below the vortex at all times. What is most remarkable about Fig. 4.5 is that even  $\xi_{0.5}$  is excluded from the vortex in Cases 1 and 2. This effect is more visible in Case 2 due to the smaller convective timescale. At 5 ms,  $\xi_{0.5}$  lies in a flat band below the vortex. This behavior shows the great difficulty of pulling a flame inside the vortex, even for very high values of the stoichiometric mixture fraction. Clemens and Paul observed this behavior for  $\xi_{st}$  up to 0.44 for diluted hydrogen flames [121]. Here, exclusion of the  $\xi_{0.5}$  isocontour from the vortex is observed when  $\xi_{st} = 0.0637$ .

The motion of isocontours of the mixture fraction is examined in the following chapters. As a given isocontour (e.g.,  $\xi_{st}$ ) is rolled into the eddy, the contour is folded on itself forming a sharp cusp, around which diffusion is geometrically enhanced. Fuel diffuses from the rich side to the lean side of the isocontour, causing it to retreat out of the mixing zone. The exclusion of the  $\xi_{0.5}$  isocontour in the reacting cases, but not the cold case, occurs because the density is lower in the lean portion of the domain where the flame lies. The relatively high density in the fuel-rich upper portion of the domain results in higher momentum there, the density-weighted vorticity is higher there, and the vortex that forms is centered in a region of  $\xi > 0.5$ . In Case 1, the peak vorticity occurs at a mixture fraction of approximately 0.66. Figure 4.7 shows the mixture fraction progression for Case 1 with the isosurface of  $\xi_{0.66}$  shown. This value appears to *ride* the center of the vortex roll in a manner similar to  $\xi_{0.5}$  in Case 3, shown in Fig. 4.6. Clemens and Paul noted that the density ratio had a more significant effect on the interaction of the flame with the mixing layer than the value of the stoichiometric mixture fraction [121].

### 4.3.2 Soot Formation and Transport

Figure 4.8 illustrates the growth of the soot in the mixing layer for Case 1 and is similar to Fig. 4.4 for the temperature contours. Here, the soot clearly is concentrated along the fuel-rich side of the flame band. As the vorticity is organized into a vortex,

the soot follows the streamlines of the flow and is rolled up into the vortex. The gaseous species are transported along as well, but their higher diffusivity results in greater mixing.

Following the soot mass fraction evolution in Fig. 4.8, the soot forms initially via nucleation and surface growth prior to the development of the vortex. Once the vortex forms, soot is swept away from the flame zone, resulting in a decreased level of soot, and hence soot growth at the flame. After the vortex formation, soot growth resumes and the concentration increases with time to its maximum value on the rich side of the flame. At the same time, soot is continuously convected into the mixing layer where it mixes with cold fuel and combustion products. In this mixing zone, the temperature is reduced, and the soot reactions cease. This process, by which soot is loaded into the fuel stream, may have important implications in turbulent flames and fires where the soot may be formed and concentrated in one region, then transported to another where it again may interact with the flame, possibly breaking through the flame. These effects are the subject of the following chapters.

Figure 4.9 shows a comparison of soot mass fraction, number density, net soot production rate, scalar dissipation rate, and temperature for Case 1 at 6 ms. At this time, the number density concentrates near the flame where the nucleation rate is high, while elsewhere the number density drops as coagulation occurs. The soot mass fraction at this time concentrates not at the flame but along the wave crest. This time is near the beginning of the vortex formation, as noted above, where the soot is first entrained. The soot production rate is concentrated at the flame zone. Comparison with the scalar dissipation rate profile shows that the peak soot formation rate is occurring in regions of low scalar dissipation rate. At higher values of scalar dissipation rate, soot formation is known to be slowed as a consequence of the decreased Damköhler number. This is one of the reasons gas turbine combustors operate under highly turbulent, high strain conditions. Also shown is the temperature for comparison. At this time, the peak soot rate is  $0.00048 \text{ g/cm}^3\text{s}$  and occurs at a temperature of 1750 K. At 10 ms, the soot reaction rate is nearly uniform in a band along the flame in the streamwise direction. At that time, the peak soot reaction rate is  $0.00058 \text{ g/cm}^3\text{s}$  and occurs at 1760 K. At 6 ms, the peak soot mass fraction is 0.0045 and occurs at a mixture fraction of 0.54 and a temperature of 880 K. These diluted, low-temperature conditions indicate the extent of mixing and contrast with the expected peak in the soot mass fraction near the flame at much leaner mixture fraction. At 10 ms, the peak soot mass fraction is 0.0064 at

1424 K and a mixture fraction of 0.22, in agreement with the peak from flamelet and one-dimensional simulations. The motion of the peak soot mass fraction in temperature and mixture fraction space will have important consequences on the radiative heat loss, which is proportional to the soot volume fraction, with a strong temperature dependence.

The soot particle size tends to grow with time due to the combined effects of surface growth and particle coagulation. Figure 4.10 shows the spatial distribution of particle size in the mixing layer. In regions of high number density, the soot size is small since this is the region of nucleation and early soot growth. The particle size is larger in regions of higher soot volume fraction as the particles have experienced growth and coagulation. Because the mean particle size involves the ratio of the soot mass fraction and number density (see Eq. (2.111)), regions of little or no soot cause numerical difficulty when computing a particle size. The contours of Fig. 4.10 have been cropped to include only regions where the number density and mass fraction are at least a factor of 0.015 of the maximum values. The particles are at their largest in regions that are relatively cool. The large size results in decreased mobility since the particles are assumed to be transported via soot gradients with a diffusivity that varies inversely as the particle diameter squared.

The overall quantities of interest in this flame, such as the soot volume fraction, number density, and particle size, are compared with those reported for two experimental laboratory flames of similar configuration, i.e., nonpremixed, nondiluted ethylene fuel, at ambient conditions, in laminar or turbulent diffusion flames. Table 4.2 shows the comparison for Case 1. The peak soot volume fraction, number density, and aggregate size at the peak volume fraction are reported. The comparison of the mixing layer case with the laminar opposed flame is expected to be close since the soot model used in the mixing layer case was based upon the experimental result. The mixing layer case is taken at a residence time of 10 ms. The timescale for the laminar flame based on the inverse of the strain rate is 16 ms. For the turbulent case, the axial time-of-flight to the peak soot position using the jet exit velocity is 14 ms.

A comparison of the total soot mass in the domain is shown for Cases 1, 2, and 4 in Fig. 4.11. The soot mass shown in the figure is relative to the final soot mass achieved in Case 4. In this figure, the adiabatic case results in a higher level of soot due to the higher temperature. The difference between Cases 1 and 4 is relatively small, due to the low overall heat loss. The gap between the two curves widens with time since the overall

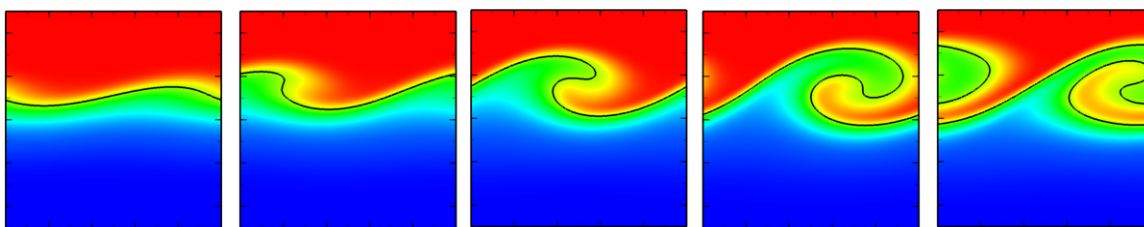


**Figure 4.7.** Mixture fraction progression for Case 1 with isocontour at  $\xi = 0.66$ .

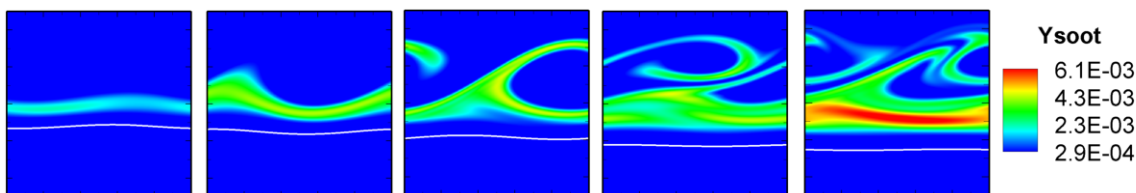


**Figure 4.8.** Soot mass fraction progression for Case 1 at 2, 4, 6, 8, and 10 ms. The stoichiometric mixture fraction isocontour is also shown.

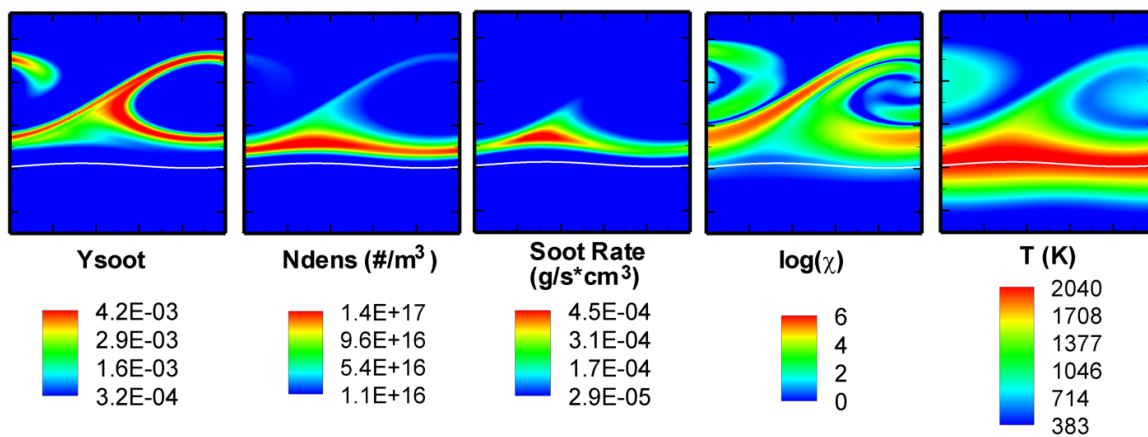


**Figure 4.9.** Soot formation for Case 1 at 6 ms. The stoichiometric mixture fraction isocontour is also shown.

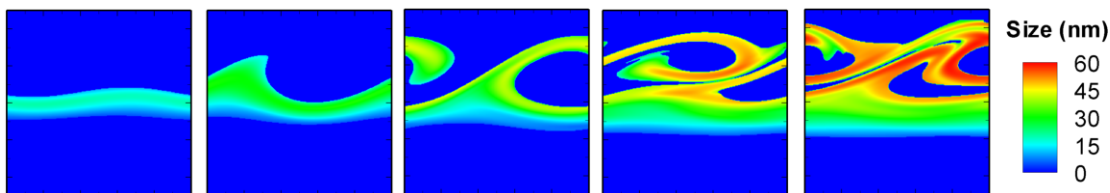


**Figure 4.10.** Soot particle size for Case 1 at 2, 4, 6, 8, and 10 ms.

**Table 4.2.** Comparison of bulk sooting properties of Case 1 with two experimental configurations. Case 1 is at 10 ms.

	Description	$f_v$ (ppm)	$n$ ( $\text{m}^{-3}$ )	Particle Size (nm)
Case 1	Temporal mixing layer	0.9	$1.5 \times 10^{17}$	55
Hu [7]	Turbulent jet: $\text{Re}=13,500$	1.1	$1.1 \times 10^{17}$	35
Vandsburger [122]	Laminar opposed flame strain rate = $63 \text{ s}^{-1}$	1	$0.8 \times 10^{17}$	60

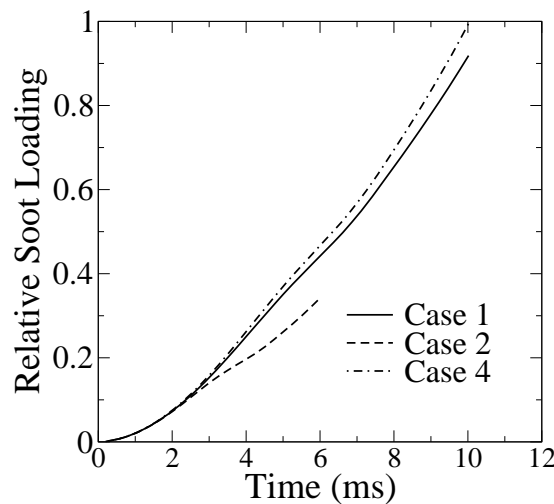


**Figure 4.11.** Relative soot loading on the computational domains for three cases.

heat loss and soot concentration are integral properties. For Case 2, the results deviate strongly from the other two cases. The effect of the higher Reynolds number outweighs the radiative effect. Initially all three cases are identical. The point at which the soot is rolled up into the layer is clearly visible as a *jog* in the curves. This jog occurs at about 3 and 6 ms for Case 2 and Cases 1, 4, respectively, and is consistent with the trend shown in Fig. 4.5. The decrease in the rate of global soot production at the jog (indicated by the decreased slope of the curves) is the result of the soot formed at the flame front being swept into the developing mixing layer as shown previously. Case 2 was run for a shorter length of time because of the higher velocity and faster layer development in the fixed domain size.

The convection of the soot away from the flame zone is highlighted in Fig. 4.12, which

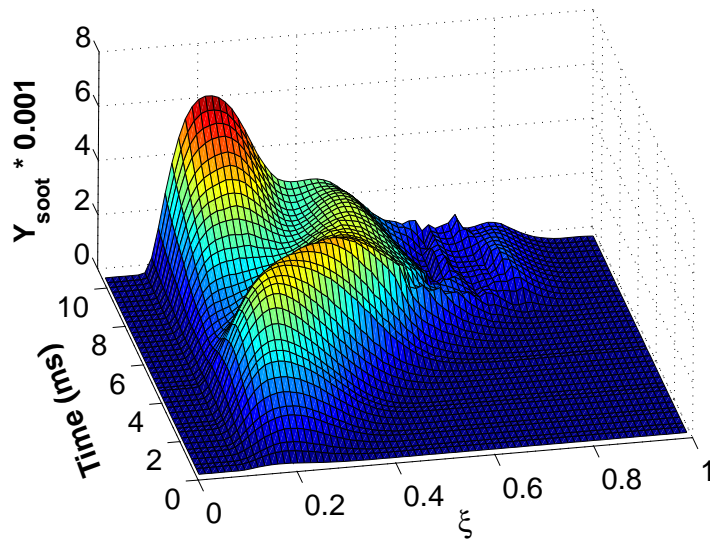


**Figure 4.12.** Conditional mean soot mass fraction for the mixing layer Case 1 at 6 ms.

shows the conditional mean soot mass fraction as a function of mixture fraction and time. Seventy-five mixture fraction bins were used in the conditioning. The figure shows that the soot is initially formed and grows near a mixture fraction of 0.2. At 5 ms, the vortex sweeps the soot into the mixing layer where the soot concentration at  $\xi = 0.2$  drops and the soot migrates to higher  $\xi$  as it is mixed with fuel and combustion products in the vortex-eddy. Once the vortex is formed, the soot again grows in the  $\xi = 0.2$  region, while the soot in the  $\xi = 0.4$  region is diluted, and its concentration falls. The figure shows a continual increase in the mixture fraction at which soot is present, extending to  $\xi = 0.9$  by the end of the simulation. The mixing layer simulations not only highlight the transport of soot into the fuel stream but the extent to which coherent structures, in this case a single vortex, influence the soot concentration and location in the flow.

# CHAPTER 5

## TWO-DIMENSIONAL TURBULENT FLAMES

Soot formation and transport were presented in the previous chapters in simplified configurations consisting of one-dimensional relaxing diffusion flames and a two-dimensional laminar mixing layer with a single eddy. In the latter simulations, soot was shown to be transported away from its region of formation into the mixing layer on the fuel side of the flame where its mixture fraction increased. Differential diffusion effects result in significant transport of soot in the mixture fraction coordinate, affecting the location of soot relative to the flame and, consequently, soot temperature, which dictates reaction rates and radiative emission. Here, the term differential diffusion is used to mean the difference between the Fickian diffusion of gaseous species and the thermophoretic diffusion mechanism of soot transport. In this chapter, soot formation in two-dimensional decaying turbulence is presented to examine the details of soot transport and soot-flame interactions. These results were recently published in [94].

### 5.1 Introduction

Several previous studies have been performed that specifically examined the importance of flame structure and flow configuration on soot formation characteristics. Soot is formed on the fuel-rich side of diffusion flames, and the direction of the fluid convection relative to the flame, as well as flame shape and strain have a strong impact on the soot formation and growth. Smooke et al. [104, 11] have performed detailed experimental and computational studies of steady laminar coflow diffusion flames. Shaddix et al. [12] compared pulsed normal and inverse coflow ethylene diffusion flames. They note that while normal diffusion flames are a more natural configuration, inverse flames may have structures similar to those occurring in large-scale turbulent fires where an eddy may inject a pocket or *tongue* of air into a region of fuel. Kaplan et al. [123] performed simulations of unsteady pulsed methane–air diffusion flames showing large increases in

peak soot concentrations over their steady counterparts due to increased soot residence time at favorable temperatures and stoichiometries in vortex structures.

In counterflow flames, increasing strain rate results in reduced levels of soot, mainly due to reduced residence time in reaction zones [124]. Stream doping/dilution (e.g., O<sub>2</sub>, CO<sub>2</sub>, or N<sub>2</sub> addition) has been shown to affect soot levels both through temperature and chemical changes [125]. Several researchers have evaluated the effect on soot formation of altering the value of the stoichiometric mixture fraction through fuel dilution and oxygen enrichment in the fuel and oxidizer streams, respectively [124, 126, 127, 128, 129, 130]. For example, in ethylene flames the stoichiometric mixture fraction with pure fuel and air is 0.064. By systematically moving nitrogen from the air stream to the fuel stream, a stoichiometric mixture fraction of 0.78 can be obtained, with a constant adiabatic flame temperature [124].

For counterflow diffusion flames, shifting the stoichiometric mixture fraction can move the flame from one side of the stagnation plane to the other, hence changing the direction of the fluid convection through the flame. For flames that reside on the oxidizer side of the stagnation plane, convection transports soot away from the flame zone, minimizing the effects of oxidation and reducing the temperature of the peak soot concentrations. The converse is true for flames that reside on the fuel side of the stagnation plane, where convection transports soot towards the flame to higher temperatures and oxidation regions [129, 130].

Kang et al. [129] compared normal and inverse jet diffusion flames to counterflow opposed jet flames with varying stoichiometric mixture fraction to change the flame structure. They note the similarity of an inverse diffusion flame to the usual counterflow flame with the flame on the oxidizer side of the stagnation plane, and the similarity of a normal jet diffusion flame to a counterflow opposed jet flame with the flame on the fuel side of the stagnation plane. In this comparison, it is particularly interesting that, while counterflow flames require a change in the stream composition (stoichiometric mixture fraction) to change the flame structure, the two-dimensional diffusion flames can achieve similar flame structures through the hydrodynamic configuration. Kang et al. note that, in the normal diffusion flame, convective streamlines cross from the air side to the fuel side near the base of the flame (convecting soot away from the flame), while the opposite occurs at the top of the flame. They found that thermophoresis dominates soot diffusion and acts in the direction of convection near the base and opposite of convection near

the tip. Multidimensional effects of curvature near the flame tip are also present, with thermophoresis tending to focus the soot particles into the fuel core.

In turbulent flames, which are inherently multidimensional and unsteady, we may expect similar behavior. That is, the structure of the soot-flame interaction will depend locally upon the direction of fluid convection relative to the flame, as well as on the flame shape. In this chapter, insights gained from laminar flame structure are used to analyze turbulent soot formation and transport. Specifically, the effects of flame shape obtained from local curvature and fluid velocity normal to the flame are examined. The emphasis of this work is on flame structure and not turbulent mixing statistics. It is found that the differential diffusion of soot allows fluid convection relative to the flame to play a dominant role in the soot formation and growth process. The convection velocity relative to the flame is shown to depend on the flame curvature. These effects determine the location of soot in the mixture fraction coordinate and, hence, the soot temperature, which has a strong impact on soot concentrations and radiative heat transfer.

## 5.2 Configuration and Initial Conditions

The configuration consists of a two-dimensional stripe of fuel surrounded by air, with a two-dimensional isotropic turbulence field superimposed. Periodic boundary conditions are imposed in the direction of the fuel stripe (horizontal), and nonreflecting outflow boundary conditions are imposed in the other direction (vertical), resulting in a constant mean pressure. No mean velocity field is imposed. The intent of this configuration is to obtain a flame that is substantially influenced by a random, unsteady flow field, so that unsteady, multidimensional effects may be investigated. The configuration results in two flame surfaces on either side of the fuel stripe, increasing the amount of flame data, and resulting in a symmetric (except for the turbulent field) profile around the horizontal line splitting the fuel stripe. The case is a temporally evolving simulation as opposed to a statistically stationary case, as might be observed in a nonpremixed turbulent jet flame. This configuration is computationally more efficient because a smaller domain is required to achieve a fully turbulent state. Likewise, the two-dimensional domain saves substantially on computational cost. It is emphasized that the purpose of the simulation is not to gather turbulent mixing statistics, but rather to examine the influence of an unsteady, multidimensional flame on soot formation and transport. To this end, the current simulation is believed to achieve this goal, with the results expected to be

qualitatively similar in more general three-dimensional cases of similar flame structure.

The fuel stripe consists of pure ethylene, 0.5 cm wide, surrounded by air. The stream compositions are given as configuration 1 in Table 2.3. The system pressure is 1 atm, and both stream temperatures are 300 K. The domain size is 2 cm in the direction of the fuel stripe and 3 cm in the transverse direction. The larger vertical extent is chosen to keep the flame away from the boundaries of the domain. The total number of grid points is 960,000. A uniform grid size of 25  $\mu\text{m}$  is used in both directions and is found to adequately resolve all velocity, temperature, and chemical species fields. This was verified by conducting two-dimensional resolution tests in a temporal jet configuration with turbulent straining sufficient to induce extinction (which does not occur in the present simulations). Straining to extinction is conservative in that the smallest chemical species lengthscales (especially radical species) are observed at the point of extinction. No differences in species or velocity profiles were observed on grid sizes of 12 and 24  $\mu\text{m}$ .

The initial, burning composition field is specified as outlined in Chapter 3 by setting the mixture fraction ( $\xi$ ) profile and mapping the temperature and composition of the corresponding steady laminar flamelet solution. The following function for mixture fraction was applied to the domain:

$$\xi(y) = \frac{1}{2} \left( 1 + \tanh \left[ \frac{2}{\delta_\xi} (y - y_1) \right] \right) \cdot \frac{1}{2} \left( 1 + \tanh \left[ \frac{2}{\delta_\xi} (y - y_2) \right] \right), \quad (5.1)$$

where  $y_1$  and  $y_2$  are the centers of the transitions. The transition width,  $\delta_\xi$ , is 0.11 cm and is approximately twice the extinction transition width and gave a scalar dissipation rate about one-third of the stoichiometric extinction dissipation rate of 156  $\text{s}^{-1}$ .

A turbulent velocity field was overlaid on the composition field in order to strain and wrinkle the flame. The turbulence was initialized using an isotropic, homogeneous turbulent kinetic energy spectrum given by [131]

$$E(k) = \frac{32}{3} \sqrt{\frac{2}{\pi}} \frac{u'^2}{k_e} \left( \frac{k}{k_e} \right)^4 \exp \left[ -2 \left( \frac{k}{k_e} \right)^2 \right]. \quad (5.2)$$

Here,  $k_e$  is the most energetic wave-number given by

$$k_e = \sqrt{\frac{4\epsilon}{10\nu u'^2}}. \quad (5.3)$$

The turbulence parameters were set by choosing  $u'$  and  $\epsilon$  such that the desired autocorrelation integral scale ( $L_{11}$ ) was obtained:

$$L_{11} = \frac{8}{3k_e} \sqrt{\frac{2}{\pi}}. \quad (5.4)$$

The turbulence field was filtered to within 1 cm of the open boundaries in order to keep the flow of the expanding flame from recirculating at the boundary. The autocorrelation integral scale and the most energetic lengthscales have values of 0.188, and 0.556 cm, respectively. The Reynolds number of the autocorrelation integral scale is 180, based on the air stream. The initial Kolmogorov lengthscale is 0.0076 cm giving three grid points across the Kolmogorov scale.

Table 5.1 summarizes the initial flame and turbulence parameters of the simulation, as well as estimates of important timescales. The turbulence timescale is defined as the ratio of  $L_{11}$  and  $u'$ ; the flame dissipation timescale is defined as  $2/\chi_{st,ext}$ . The soot diffusion timescale is based on thermophoresis as  $\tau = \delta_\xi^2/0.554\nu$ , using the kinematic viscosity corresponding to products of a mixture at  $\xi = 0.2$  at 1500 K and the initial mixture fraction transition width. The soot reaction timescale corresponds to a nominal value based on global flow and mixing scales in, e.g., jet flames (such as a jet exit velocity and a downstream location of peak soot). As such, this value is not an inherent reaction timescale but includes global, integral mixing effects. The present simulations are conducted to 5 ms, which is sufficient to examine the local soot-flame interactions under reasonable turbulence conditions noted below.

The timescales are of similar magnitudes except for the initial turbulence, which, however, will increase with time. The initial turbulence parameters are of the same order as those exiting a laboratory-scale turbulent jet. For example, Coppalle and Joyeux [14]

**Table 5.1.** Simulation parameters and timescales.

Parameter		Parameter		Timescale (ms)	
$L_x$ (cm)	2	$\delta_\xi$ (cm)	0.11	Turbulence	1.25
$L_y$ (cm)	3	# cells	960,000	Soot reaction	10
$L_{11}$ (cm)	0.188	# timesteps	325,000	Soot diffusion	6
$u'$ (cm/s)	150	Run time (ms)	5	Flame dissipation (ms)	13
$H_\xi$ (cm)	0.5	Sim. Cost. (CPU-hr)	32,500		

studied a turbulent flame with an exit velocity of 30 m/s (a  $u'$  of 5% of the exit is typical) and an initial jet diameter of 4 mm. Hu et al. [7] studied similar flames and cited soot layers down to 1 mm and integral scales of approximately 5 mm, so the values in Table 5.1 are reasonable and should allow the DNS results to be relevant qualitatively to practical situations.

### 5.3 Flame Analysis

The location of peak soot concentration and soot transport, relative to a flame zone, are important since they dictate the soot temperature and, hence, reactivity and radiative properties. This relative motion results from the combined effects of fluid convection, gaseous species diffusion, and thermophoretic diffusion of soot. To quantify these effects, we define the flame location as the position of the stoichiometric iso-surface of mixture fraction. Since soot mainly follows pathlines of the fluid convection (with an additional thermophoretic diffusion component), the motion of the stoichiometric iso-surface of mixture fraction relative to the local fluid convection determines whether soot will be convected into or away from a flame zone. Gibson [132] and Pope [133] derived the expression for the velocity of a constant-property scalar iso-surface relative to the local fluid motion. For variable properties, the relative velocity is

$$\mathbf{v}_\xi = -\frac{\nabla \cdot (\rho D_\xi \nabla \xi)}{\rho |\nabla \xi|} \mathbf{n}. \quad (5.5)$$

In this equation, the surface velocity relative to convection is due to diffusion in the direction of the surface normal, defined by

$$\mathbf{n} = \frac{\nabla \xi}{|\nabla \xi|}, \quad (5.6)$$

where the normal points towards the fuel stream. Henceforth,  $v_\xi$  will be referred to as the flame displacement velocity. For  $v_\xi > 0$  the flame is moving toward the fuel stream and for  $v_\xi < 0$  the flame is moving toward the air stream. The direction of convection across the flame is  $v_{fc} = -v_\xi$ . Thus, for negative  $v_\xi$ , the fluid is convecting across the flame from the air side to the fuel side, and we expect soot to be convected away from the flame zone. This situation is analogous to the canonical fuel-air counterflow configuration.

Equation (5.5) contains multidimensional effects that can be expanded in terms of flame-coordinates as done by Echehki and Chen [134], who applied a similar analysis to

premixed flames. By applying the chain rule of differentiation to  $|\nabla\xi| = \mathbf{n} \cdot \nabla\xi$  in Eq. (5.5) and introducing the operator  $\frac{\partial}{\partial\eta} = \mathbf{n} \cdot \nabla$  and noting that  $|\nabla\xi| = \frac{\partial\xi}{\partial\eta}$ , we obtain

$$v_\xi = -D_\xi \nabla \cdot \mathbf{n} - \frac{1}{\rho|\nabla\xi|} \frac{\partial}{\partial\eta} \left( \rho D_\xi \frac{\partial\xi}{\partial\eta} \right). \quad (5.7)$$

Here,  $\eta$  is the flame-normal coordinate in the direction  $\mathbf{n}$ .

The first term represents the contribution due to iso-surface curvature, where  $\nabla \cdot \mathbf{n}$  is the curvature of the iso-surface. With this definition, curvature is taken to be positive when the center of curvature is on the oxidizer side. The second term in Eq. (5.7) is relative flame motion due to diffusion in the direction normal to the flame. The normal diffusion contribution to the flame displacement velocity can be written in terms of the scalar dissipation rate defined as  $\chi = 2D_\xi|\nabla\xi|^2$ . This is done by rearranging the definition of  $\chi$  to give  $|\nabla\xi| = \sqrt{\chi/2D_\xi}$ , substituting this into  $|\nabla\xi|$  and  $\frac{\partial\xi}{\partial\eta}$  in Eq. (5.7), and simplifying, to give

$$v_\xi = -D_\xi \nabla \cdot \mathbf{n} - \frac{D_\xi}{2} \frac{\partial}{\partial\eta} \ln(\rho^2 D_\xi \chi / 2). \quad (5.8)$$

Hence, the flame displacement velocity is made up of a curvature component and a one-dimensional normal diffusion, or scalar dissipation rate component.

This type of analysis, in which the flame surface motion is studied, has been extensively applied to premixed combustion in the development and use of the G-equation [20]. Application to nonpremixed combustion is less common and has been mainly used in the development of flame surface area models [74, 135].

Figure 5.1 shows the schematic of a hypothetical, strained and curved nonpremixed flame. The solid line represents the flame surface and the dashed line is the location of  $\xi = 0.5$ , nominally the inflection point in the profile normal to the flame. The right half of the figure shows the mixture fraction profile along the bold center normal. The two halves of the figure illustrate the two terms in Eq. (5.7) and show that either term may be positive or negative depending on the direction of curvature and the location of the flame. Generally, we may expect the normal diffusion term to contribute to a negative flame displacement velocity since the flame resides on the lean side of the inflection point (where the second derivative of  $\xi$  is positive with respect to  $\eta$ ). The curvature term competes with, or complements, the normal diffusion term. In the figure, curvature is

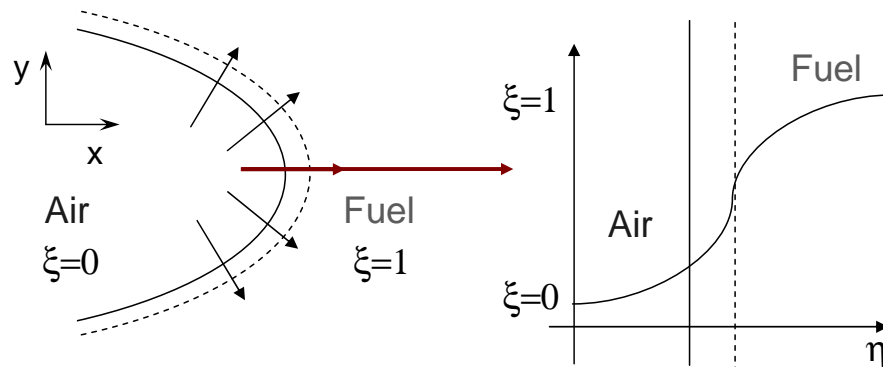


**Figure 5.1.** Schematic of a curved diffusion flame. The solid line represents the stoichiometric surface and the dashed line the  $\xi = 0.5$  surface.

positive and contributes to a negative flame displacement velocity, so that normal diffusion and curvature tend to move the flame to the left toward the air stream. However, if the curvature is reversed, at some point it will be sufficiently negative to overcome the normal diffusion term, and the flame will move to the right toward the fuel stream. Qualitatively, we can consider the rate of change of mixture fraction between the dashed and solid lines as  $j_s A_s - j_d A_d$ . The flux and areas are higher at the dashed line than the solid line (resulting in a net loss of  $\xi$  and motion to the left), but as curvature is reduced, the ratio of the areas of the solid to dashed lines increases so that, for constant fluxes, there can be a net gain of  $\xi$ , with motion of the iso-surfaces to the right.

Flame wrinkling is a clear mechanism by which soot (essentially convected with the flow) is differentially transported towards or away from the flame. Convection through the flame implies motion in the mixture fraction coordinate, to which temperature and species concentrations are primarily tied. Thermophoretic diffusion will transport soot down temperature gradients, away from the flame zone toward the fuel, so that, from the point of view of the soot, the sum of soot convection and diffusion could be considered, rather than just soot convection. The main observation, however, is that turbulent motions themselves can alter the direction of flow through a flame, which can impact soot concentrations.

In the following sections, results are also presented of quantities along directions normal to the flame at a given instant in time. Flame normal directions are defined

as above and computed as follows. Mixture fraction normal vectors are computed at all grid points and interpolated to all intersections of the stoichiometric mixture fraction with the grid lines. Points in the domain are then computed at regular distances (about equal to the grid spacing) along the normal direction, and all field quantities linearly are interpolated to these points. Normals are cropped at any point where the mixture fraction profile becomes nonmonotonic.

## 5.4 Results

### 5.4.1 Overview and Observations

The simulation was computed to a time of 5 ms. Figure 5.2 shows instantaneous snapshots of temperature, acetylene mass fraction, and soot mass fraction at times of 1.25, 2.5, 3.75, and 5 ms. In each series, only the interesting portion of the domain is shown. The soot mass fraction range shown is 0 to 0.003 for clarity, but the peak values are 0.0024, 0.008, 0.013, and 0.022 (or about 0.3, 1.0, 1.7, and 2.9 ppmv) in time. As time progresses, the flame is wrinkled by the turbulence resulting in enhanced mixing of fuel and oxidizer as the flame expands. In each figure, two isocontours of mixture fraction are shown corresponding to the stoichiometric isocontour ( $\xi = 0.064$ ) and the approximate peak in the soot precursor/growth species acetylene ( $\xi = 0.2$ ).

Of particular interest in these progressions is the motion of the stoichiometric contour. In several regions, especially those with positive curvature, the flame is observed to move away from the fuel side, reducing the curvature. In these regions, the curvature and normal diffusion components of the flame displacement velocity in Eq. (5.7) are expected to have the same sign, resulting in enhanced motion. In regions of negative curvature, the curvature contribution results in displacement of the flame towards the fuel, while the effect of normal diffusion is to displace the flame towards the oxidizer. This results in a partial cancellation of flame motion effects and a more stagnant flame surface.

For the range of unsteady strain rates imposed by the initial velocity spectrum, local extinction is negligible, and gaseous combustion timescales are small compared to flow timescales. The temperature peak is concentrated around the stoichiometric mixture fraction isocontour, while the acetylene peak follows the  $\xi = 0.2$  isocontour. The spacing of the mixture fraction isocontours is an indication of the local scalar dissipation rate. Acetylene concentrations tend to be lower in regions of higher scalar dissipation rate. Peak soot concentrations are not as tightly bound to the indicated isocontours as temperature

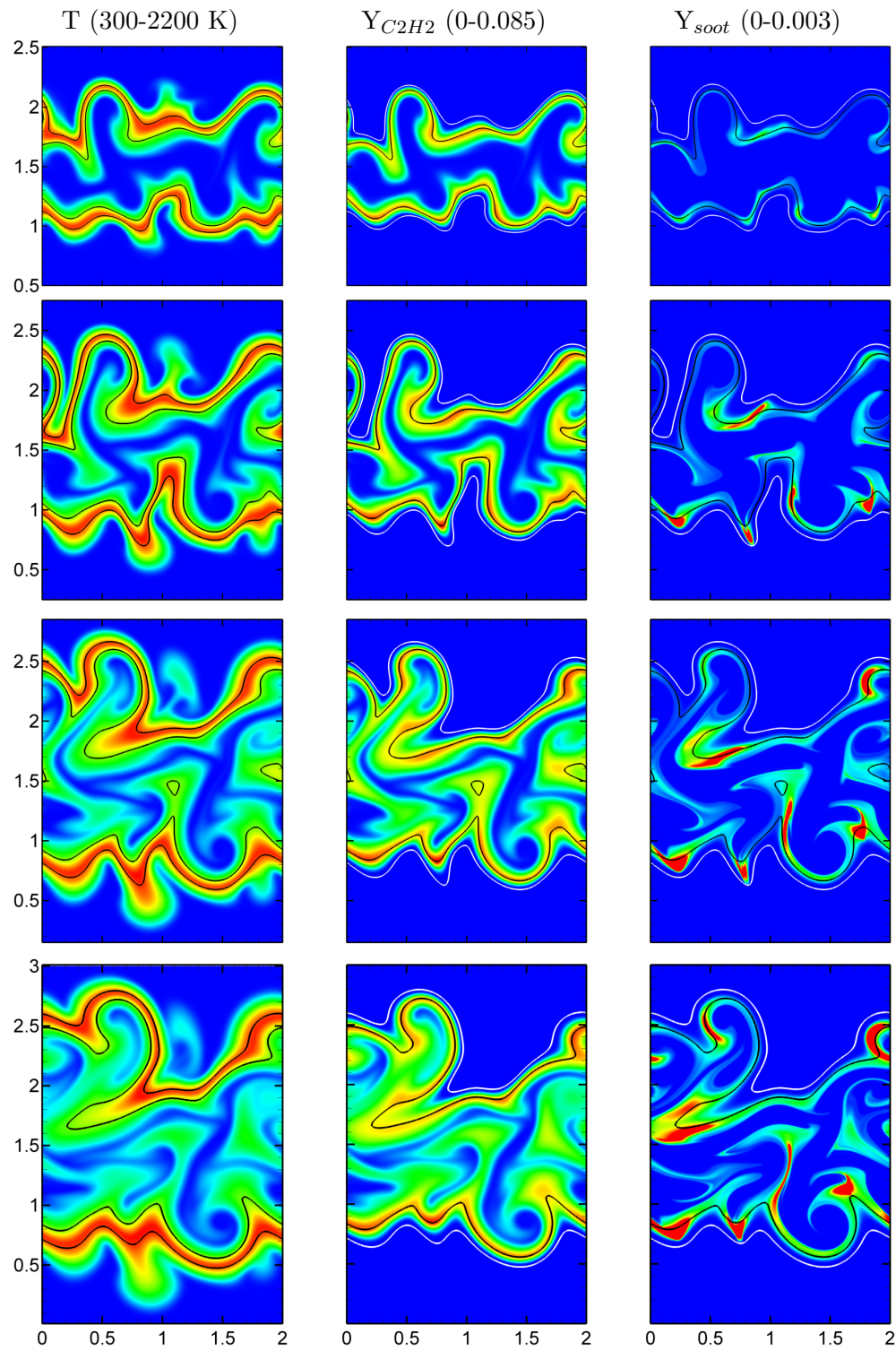


**Figure 5.2.** Vertical time series with indicated ranges (red is high). Times are 1.25, 2.5, 3.75, 5.0 ms. Isocontours are shown at  $\xi = 0.064$ , 0.2. Position units are millimeters.

and acetylene mass fraction are. Initially, soot levels are confined near the  $\xi = 0.2$  mixture fraction isocontour, whereas at later times, high soot levels are observed in richer (and leaner) regions. In particular, regions in Figure 5.2 in which the motion of the positively curved flame essentially leaves the soot behind are observed. Along the flame, it is clear that the soot concentration is not homogeneous but that the peak soot levels tend to occur in regions of large negative flame curvature.

Figure 5.3 shows fields of soot number density, scalar dissipation rate, OH mass fraction, and soot reaction rates of nucleation, growth and oxidation at a time of 2.5 ms. Corresponding temperature, acetylene and soot mass fraction are presented in the second row of Figure 5.2. The number density field is similar to the soot mass fraction

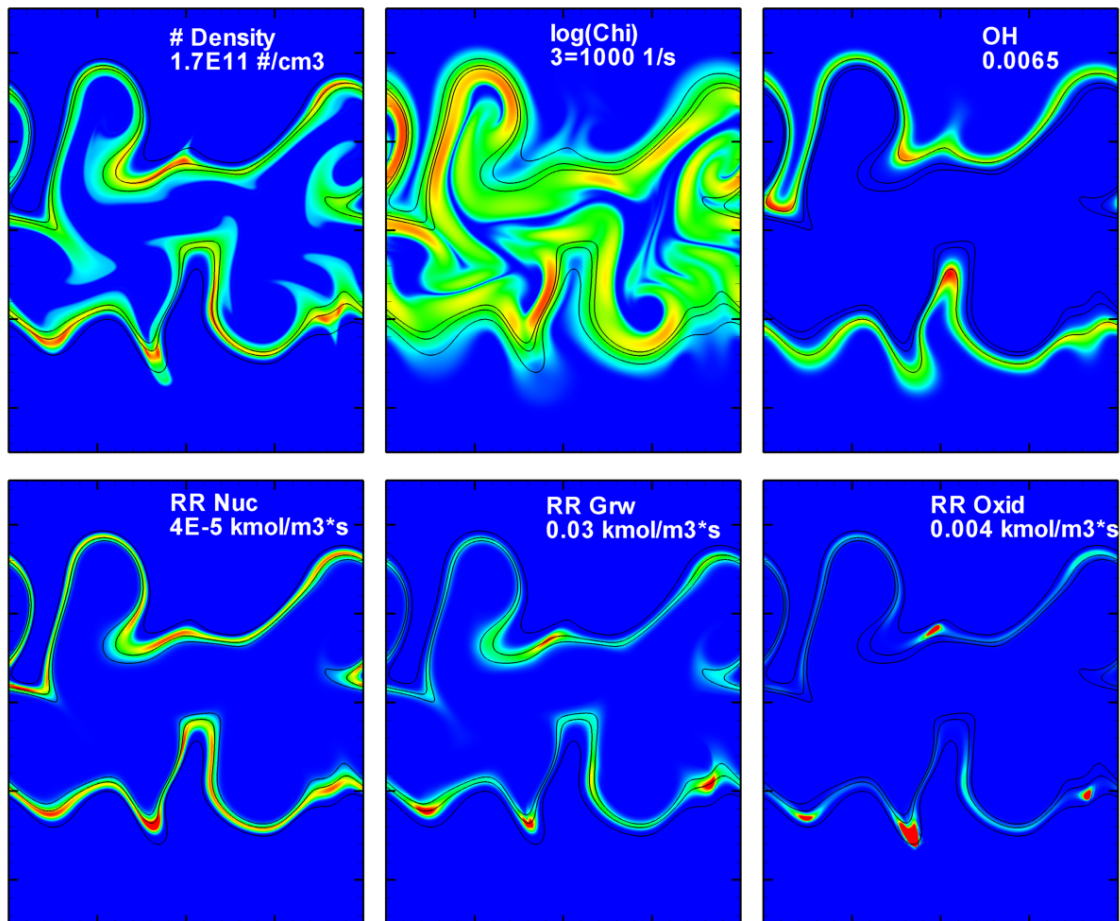


**Figure 5.3.** Scalar fields with indicated peak scale (red) at 2.5 ms with mixture fraction isocontours of 0.064, 0.2 (line color for clarity only). The peak soot nucleation, growth, and oxidation rate peaks are off scale at  $5.1 \times 10^{-5}$ , 0.036, and 0.143 kmol/m<sup>3</sup>s, respectively.

field. The peak levels occur in a similar location both along the flame and in the mixture fraction bands at a given flame location. Number density is more evenly distributed along the flame, however, as particles are generated solely by acetylene for the given soot model. As soot is transported away from reaction zones, particle coagulation occurs, reducing the number density and increasing particle size. Soot mass fraction levels are only affected by number density through the implicit mean particle size, which affects the surface area used in the rate calculation. Unlike number density, which is derived from the gas phase alone, soot mass fraction has the additional source arising from surface growth, which depends on the level of soot in the reaction zone. Thus, depending on soot transport into or out of reaction zones, local soot mass fraction levels can be concentrated or diminished.

This effect is evident by comparing the number density and nucleation rate fields, and the soot mass fraction and growth rate fields. The nucleation occurs all along the flame resulting in a more homogeneous number density field, whereas the soot growth rate field is concentrated along regions of negative flame curvature, just as the soot mass fraction is. It is interesting to note that the soot oxidation rate also shows a high degree of variation along the flame, with peaks in the same locations as the growth rate, indicating that high levels of soot growth occur with high levels of soot oxidation. However, the location of the rates in the mixture fraction coordinate are different, as expected, with oxidation occurring at leaner mixture fractions than growth, though both are on the rich side of the flame where soot is present. The peak soot oxidation zones occur where the soot levels are at leaner mixture fractions. In these regions, the soot concentration is higher, and the oxygen concentration at the location of soot is higher. Both of these effects enhance the soot oxidation rate. Contours of oxygen concentration are not shown in the figure since they are negligible at the stoichiometric surface. OH mass fraction contours are shown to indicate the flame surface and reaction zone, and because OH is known to contribute to soot oxidation.

In Figure 5.3, there appears (visually) to be a strong correlation between the soot levels and rates and the flame curvature as well as scalar dissipation rate. These relations are discussed further by considering global statistics and quantities along the flame.

### 5.4.2 Global Statistics

Figure 5.4 shows scatter plots of soot mass fraction at times of 1.75 and 5 ms and temperature, acetylene, soot growth rate, and nucleation rate at times of 1.75 ms, all

versus mixture fraction. The mean stoichiometric scalar dissipation rates at the two times are 14.2 and 5.5 s<sup>-1</sup>, respectively (the steady extinction value is 148 s<sup>-1</sup>). The low degree of scatter in temperature indicates that this flame is not highly strained and combustion reactions are mixing limited. The soot mass fraction plots reveal two important effects. First, the relatively slow soot growth and nucleation rates result in widely varying soot mass fractions at any given mixture fraction so that the scatter plot appears dense below its upper range. The soot mass fraction figure on the left at 1.75 ms has a scale five times less than the same plot on the right at 5 ms. At 1.75 ms, the profile is rather smooth, with a peak at approximately  $\xi = 0.15$ , which corresponds to the locations of the maximum growth and nucleation rates. At 1500 K a soot mass fraction of 0.02, 0.01 and 0.002 corresponds to volume fractions of 2.6, 1.3 and 0.26 ppmv, respectively, with the conversion given by  $f_v = \rho Y_s / \rho_s = 191030 Y_s / T$  ppmv, assuming a soot density of 1850 kg/m<sup>3</sup> and a gas molecular weight of 29 kg/kmol at 1 atm pressure.

Second, the soot mass fraction is transported in the mixture fraction coordinate. In time, the soot clearly migrates toward richer mixtures. The peak soot level is still at approximately  $\xi = 0.15$ , but substantial levels of soot are present at mixture fractions as high as 0.8. The scatter profile is also seen not to be smooth, but evidence of the transport of soot to large values of mixture fraction along coherent structures is observed as eddies convect soot away from flame zones into the fuel core where mixture fraction diffusion increases the richness of the soot-gas mixture. The temperature, acetylene, and rate profiles are shown at only one time since they are essentially the same at 5 ms, with the exception that the acetylene mass fraction and soot growth rate peaks are nearly twice as high, while the nucleation rate peaks at about  $5 \times 10^{-5}$  kmol/m<sup>3</sup>s. Unlike soot mass fraction, the soot growth and nucleation rate profiles are localized in the mixture fraction coordinate. This localization of the soot rates is well known and is due to the strong temperature dependence and locality of the gaseous species with respect to mixture fraction.

### 5.4.3 Flame Displacement Velocity

Figures 5.2 and 5.3 clearly demonstrate the correlation between soot concentrations and flame shape. The correlation is better understood by examining the displacement velocity of the flame relative to the fluid motion given by Eq. (5.5). Figure 5.5 plot (a) shows the stoichiometric flame displacement velocity relative to the fluid convective

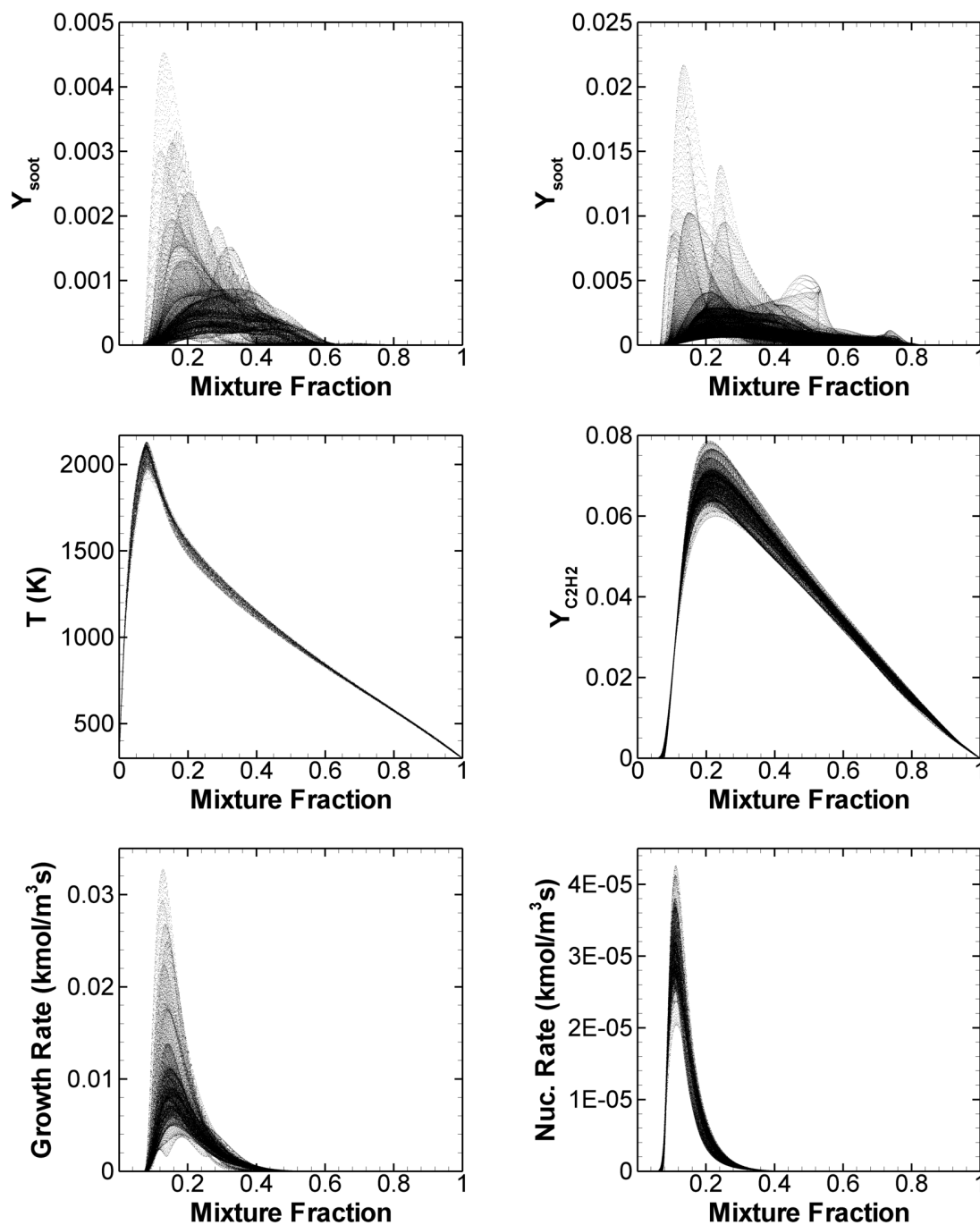


**Figure 5.4.** Scatter plots at 1.75 ms with soot mass fraction at 1.75 (left) and 5 ms (right). The temperature plot shows one in three indices in the  $x$  and  $y$  directions.

velocity as the two solid lines at 1.75 ms. Soot mass fraction is shown as grayscale contours, with a peak value colored at 0.002 (dark). The peak soot mass fraction is 0.0045 (or 0.46 ppmv) and occurs along the lower flame at the far right of the figure. Along the stoichiometric surface, fluid velocity vectors are shown. As discussed earlier, positive values of the flame displacement velocity correspond to the flame moving towards the fuel stream, while negative values denote flame motion towards the air stream. The convective velocity through the flame is opposite the flame displacement velocity, and for positive values soot will be convected into the flame. This figure shows that high soot levels occur with flame motion towards the soot. Clearly the highest levels of soot occur in positive regions of flame displacement velocity. History effects of transported soot are also evident in the figure, though minimized by the early time chosen here.

This figure generally confirms the behavior that was described and predicted in Section 5.3. In relatively flat regions of the flame, the flame displacement velocity is negative (towards air) since this is the direction (sign) of the normal diffusion term of the flame displacement velocity shown in Eq. (5.7). Flame regions that are positively curved result in even higher negative flame velocities, whereas flame regions that are negatively curved are those with more positive flame displacement velocity. Figure 5.5 shows that fluid vectors are not strictly tied to the direction of the flame displacement velocity. For example, there are regions of opposite flame displacement velocity with the fluid normal component pointing toward the air stream. This emphasizes the importance of the flame motion relative to the local fluid velocity.

Plot (b) of Fig. 5.5 is the same as plot (a) but with the stoichiometric surface colored by the scalar dissipation rate. As expected, the peak soot levels tend to occur in regions of low  $\chi$ . However, low levels of soot also occur in regions of low  $\chi$ , especially where the flame surface is positively curved, such as along the lower flame near the center and along the upper flame at the left. In plot (a), for  $v_\xi$ , in the same regions, there appear to be high concentrations of soot with negative values of  $v_\xi$ , contrary to the main correlation of soot and  $v_\xi$ . The analysis is somewhat complicated by the history effects of the soot evolution and the flame dynamics, which can change the magnitude of  $\chi$ , and the sign of  $\kappa$ . For example, the upper flame at the left shows a soot peak in a downward arch. The flame curvature at this position changes sign as the flow evolves, with the initial curvature centered in the fuel stream. This also occurs at the soot peak on the lower flame at the right, which can be seen in the time progression in Fig. 5.2. As the flame displacement

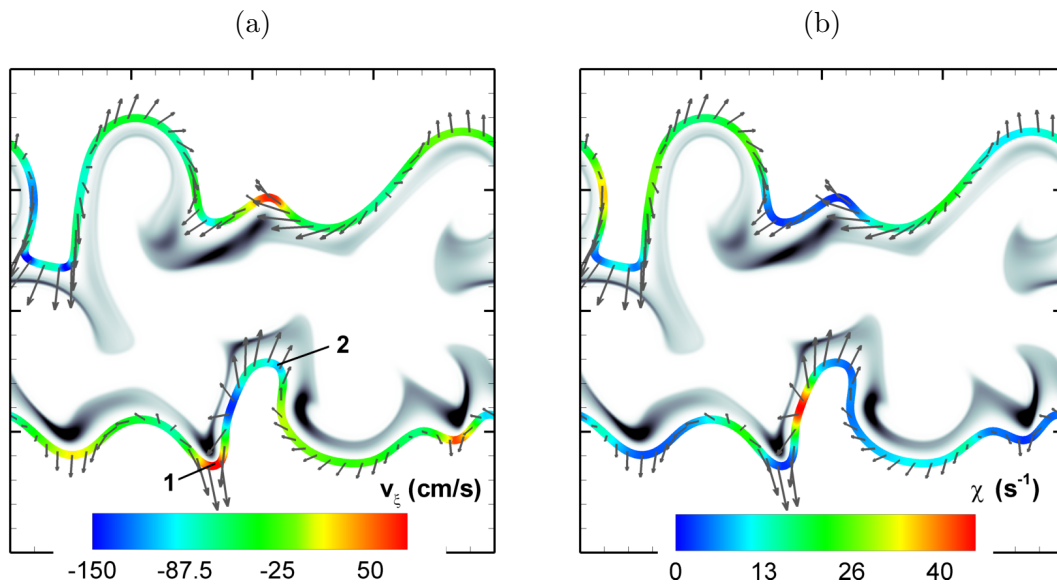


**Figure 5.5.** Soot field at 1.75 ms with stoichiometric surface colored by flame displacement velocity (a), and scalar dissipation rate (b). Vectors are fluid velocity. The soot mass fraction is shown in grayscale where the maximum value shown (dark) is 0.002.

velocity accounts for the effects of both flame curvature and scalar dissipation rate (as discussed previously and shown in Eq. (5.8)), it seems to be a better indicator of high soot regions.

At the 1.75 ms time shown in Fig. 5.5, there appears to be relatively little flame-flame interaction, with the flame structure varying from pure fuel to pure air across a given location of the flame. This allows analyzing the flame in the context of more traditional one-dimensional and flamelet models, to examine the importance of multidimensional effects.

#### 5.4.4 Flame Normals

The soot-flame interaction is examined in more detail by considering scalar profiles of temperature, composition, and reaction rates along flame normals. Representative individual results are presented at two spatial locations of opposite flame displacement velocity at 1.75 ms in Fig. 5.6. Statistics considering all flame normals are presented later. The positions of the two normals considered are labelled in Fig. 5.5. Positions 1 and 2 have flame displacement velocities of 90 and -100 cm/s, respectively. The stoichiometric scalar dissipation rate values are approximately  $3.5 \text{ s}^{-1}$  and were chosen to be close in magnitude. The peak temperatures for these two cases differ by only 25 K. Plots of

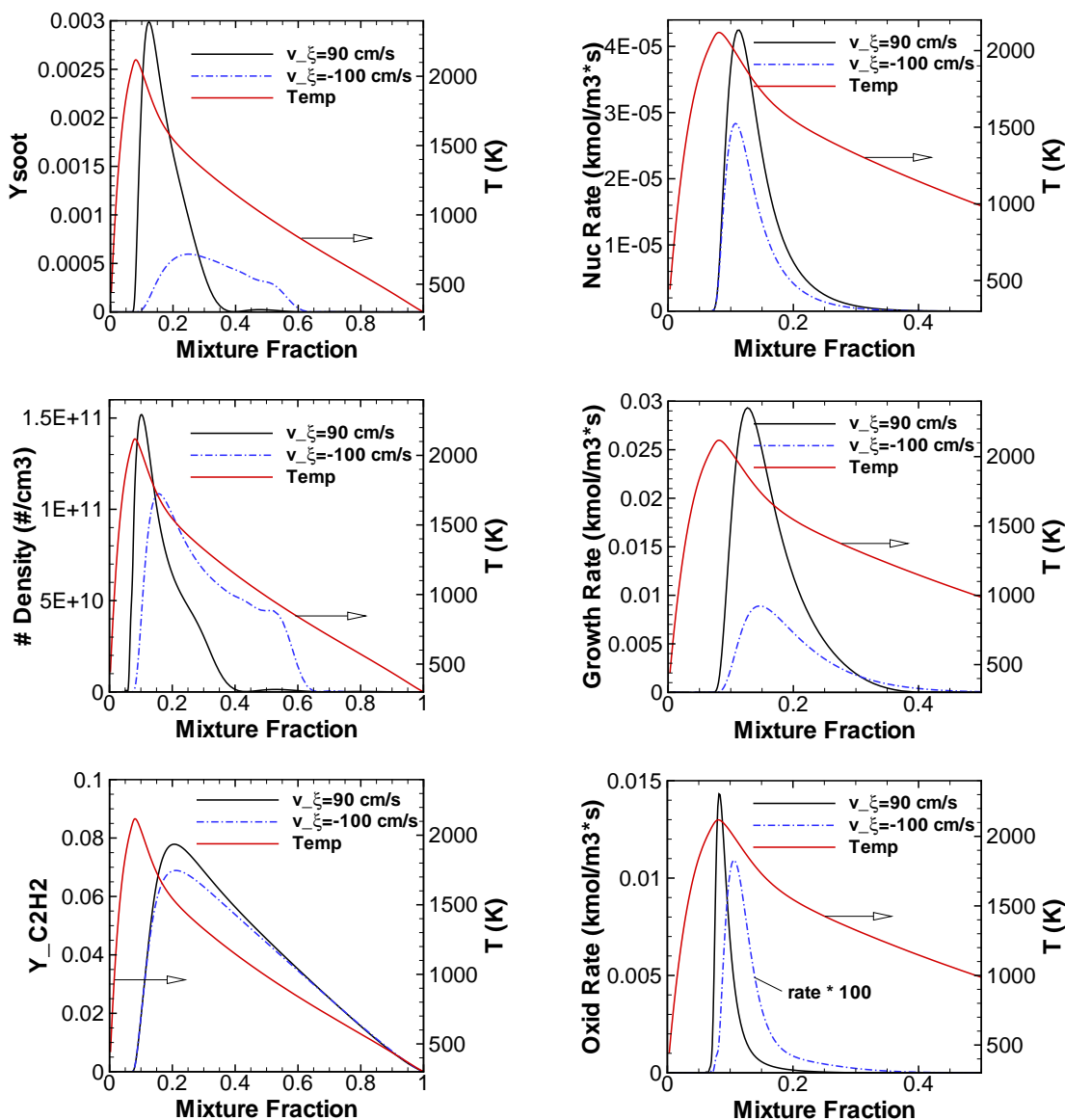


**Figure 5.6.** Plots along two flame normals shown in Fig. 5.5. at 1.75 ms.

soot mass fraction, number density, acetylene mass fraction and soot rates of nucleation, growth, and oxidation are shown versus mixture fraction in the figure.

The soot mass fraction profile is particularly interesting. At position 1, the flame displacement velocity is positive, resulting in the flame moving toward the convected soot particles. The opposite occurs at position 2, where the flame displacement velocity is negative. The soot peak of position 1 has a value of 0.003, at a mixture fraction of 0.121 ( $\phi = 2.0$ ). At position 2, the soot mass fraction peak is 0.0006, at a mixture

fraction of 0.254 ( $\phi = 5.0$ ). The soot level at position 1 is a factor of 5 higher than at position 2 and peaks much leaner as well. The temperatures at the soot peaks for positions 1 and 2 are 1898 and 1358 K, respectively, a difference of 540 K. This difference in temperature, as well as soot level, strongly affects the soot contribution to the radiative source term. Figure 5.7 shows the optically thin gas and soot radiative source terms at the two positions. These terms are given by

$$Q_{rad} = 4\sigma K(T^4 - T_{\infty}^4), \quad (5.9)$$

where  $\sigma$  is the Steffan-Boltzmann constant, and  $K$  is the gas or soot absorption coefficient. The ratio of the soot contribution to the optically thin radiative heat flux of position 1 to position 2 is 15 using values at the soot peaks. The gas radiation sources are similar while the soot radiation is substantially higher at position 1, even exceeding the gas source term. The total peak radiative transfer rate at position 1 is more than twice the total peak rate at position 2.

The width of the soot peak at position 2 is also much wider than at position 1. As the flame moves away from the soot, the soot peak is drawn out in mixture fraction, resulting in the profile spanning  $\xi = 0.1 - 0.6$ . Presumably, the soot peak at position 1 is also stretched as the flame moves into the soot, but the soot is oxidized as it approaches

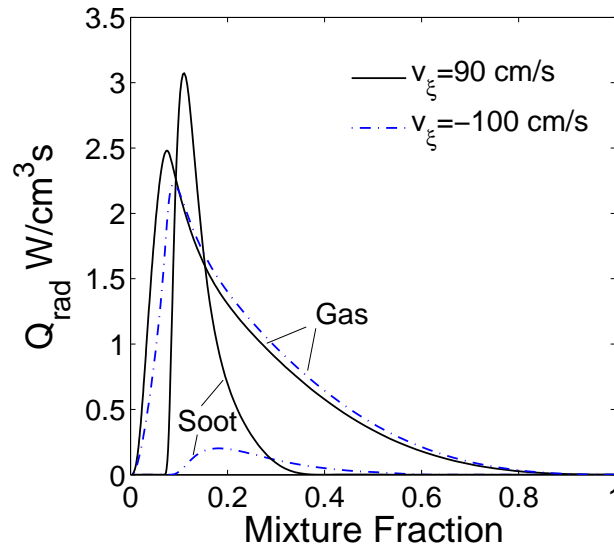


**Figure 5.7.** Gas and soot optically thin radiative source terms along flame normals at positions indicated in Fig. 5.5.

the flame; hence the profile is limited. This motion in the mixture fraction coordinate can only be explained by differential diffusion of the soot relative to the gaseous species comprising the flame. A close look at the soot mass fraction and number density profiles at position 2 shows a bimodal profile, consistent with production at lower mixture fractions coupled with transport toward higher mixture fractions. The number density profile is qualitatively similar to the soot mass fraction profile in its width and location. The difference in magnitude of the two positions is not as severe for the number density as for the soot mass fraction. This difference is similar to the difference in the nucleation rate peaks, the values of which are dependent upon differences in the acetylene concentration and temperature profiles. The shift in number density toward lower mixture fraction at position 1 is contrasted with the similarity in the locations of the nucleation rate peaks, which depend only on the gaseous environment, and further indicate the motion of the flame towards the soot at position 1.

In contrast to the soot profiles at both locations, the locations and widths of the profiles of the soot precursor, acetylene, as well as the soot nucleation and growth rate profiles, are nearly constant. The soot oxidation rate is a factor of 100 higher at position 1 than at position 2 as the soot is convected toward the flame zone into regions of higher oxidizer concentration.

Figure 5.6 shows profiles through two flame positions at a single point in time and emphasizes the fact that the flame motion can result in peak soot levels very close to the flame. Figure 5.2 shows the position of the soot peak relative to the mixture fraction contours at four times. At position 1 in Fig. 5.6, values at the peak level of soot are shown at times from 1 to 2.5 ms in Fig. 5.8. At later times the soot is oxidized by the flame, and as the flame folds together, two vertical soot zones appear, making further comparison difficult. As time progresses, the mixture fraction of peak soot decreases from 0.18 to 0.09, the temperature at peak soot increases from 1592 to 2139 K, and the soot volume fraction increases from 0.1 to 0.44 ppmv. The corresponding mass fraction varies from 0.00087 to 0.0049. These results clearly show the unsteady motion of the stoichiometric surface towards the soot peak as the flames evolve.

#### 5.4.5 Soot-Flame Breakthrough

Soot-flame breakthrough is an important phenomenon and one that is not well understood. In fires, for example, large quantities of soot are commonly emitted, that can

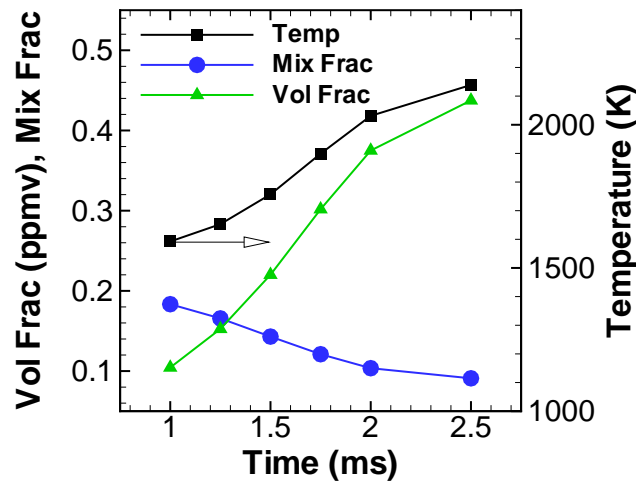


**Figure 5.8.** Soot concentration, temperature, and mixture fraction at the peak soot level at times from 1 to 2.5 ms at the location corresponding to position 1 in Fig. 5.5.

absorb radiation and shield the surroundings from radiative heat transfer. Although the flow timescales of direct numerical simulation are small compared to fires, DNS allows detailed examination of soot-flame interactions. In the present simulation, soot was not observed to penetrate the burning flame zone. However, in another simulation, similar to the base case, but with a more vigorous turbulence field imposed, soot was found to break through the flame. Figure 5.9 shows the soot and temperature profiles of this alternate case at 1.14 ms. This case had a mean fluctuating velocity  $u' = 300$  cm/s, a turbulent integral scale of  $L_{11} = 0.133$  cm, and half the domain width at  $1 \times 3$  cm. The parameters of the baseline case are in Table 5.1. In the upper-right side of plot (a) the soot clearly breaks through the flame. Plot (b) shows the temperature field, clearly indicating that the flame is burning. There are regions in this flow for which the flame is quenched, as evident along the central region of the upper flame. The soot mass fraction at the top of the stream is  $8.8 \times 10^{-5}$ , with a corresponding volume fraction of 0.015 ppmv. The peak soot mass fraction in the domain is 0.002 (0.2 ppmv) and occurs in the *ball* of soot at the lower right of the figure. Soot also breaks through to the lean side of stoichiometric at the central red cusp along the lower flame, but to a lesser extent at the time shown.

Consideration of soot-flame breakthrough calls into question the validity of the soot oxidation model used. Figure 5.10 compares profiles of soot oxidation rate for three oxidation reactions presented in reference [136]:

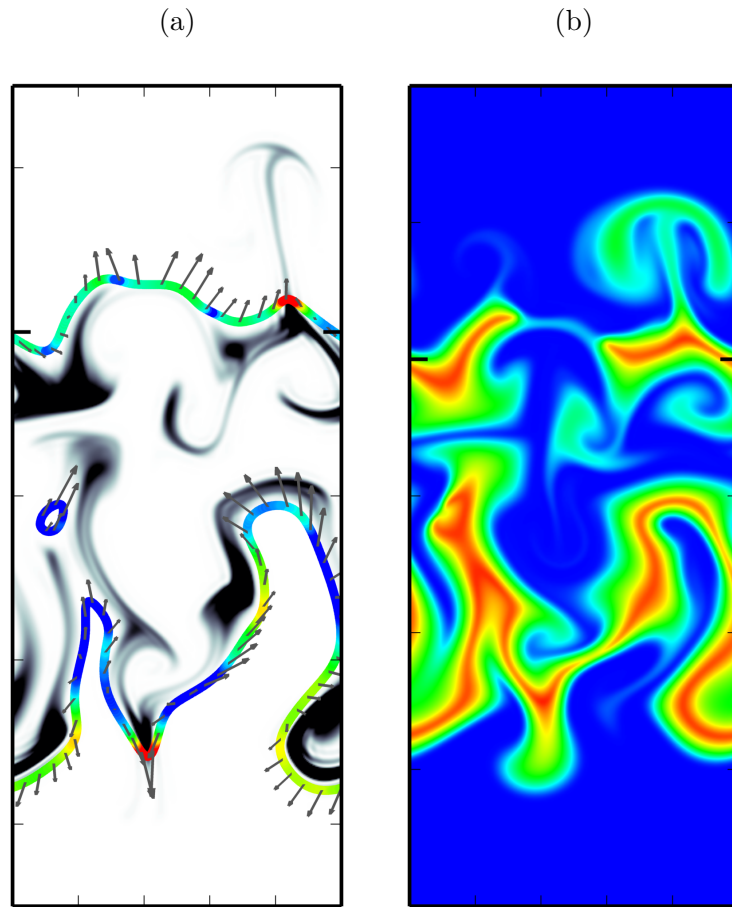


**Figure 5.9.** Alternate simulation results showing temperature (b) colored from 300 to 2200 K. Plot (a) corresponds to Fig. 5.5 showing the stoichiometric surface colored by the flame displacement velocity, with a grayscale soot mass fraction field (black is 0.0002 or greater). The time is 1.14 ms. Note soot breakthrough at top left.



Rates for the reactions as given in [136]; taken from [5, 137, 138] are

$$R_{O_2} = 10000e^{-19640/T}T^{1/2}[O_2]A_s, \quad (5.13)$$

$$R_{OH} = 106\phi_{OH}T^{-1/2}X_{OH}A_s, \quad (5.14)$$

$$R_O = 55.4\phi_O T^{-1/2}X_O A_s, \quad (5.15)$$

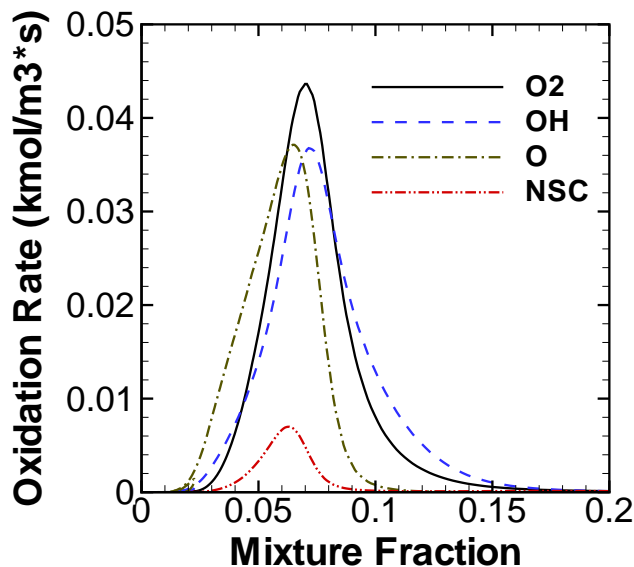


**Figure 5.10.** Plots of soot oxidation rates versus mixture fraction along a streamline through the flame at the point of soot breakthrough in Fig. 5.9.

where  $\phi_{OH}$  and  $\phi_O$  are 0.13 and 0.5,  $X$  is mole fraction, and units are kilomole, meters, seconds, Kelvin, giving rates in units of kilomole per cubic meter.  $A_s$  is the particle surface area per volume given in Eq. (2.37). Figure 5.10 also shows the original Nagle–Strickland–Constable  $O_2$  oxidation rate [139] by way of comparison, which is smaller than the other rates.

The profiles in Fig. 5.10 are along a streamline through the point of soot breakthrough at the upper right of Fig. 5.9 at 1.14 ms. In this case, the OH and the Leung and Lindstedt (L&L)  $O_2$  oxidation rates are very similar in magnitude, shape, and position. The O oxidation rate is similar in magnitude and width but occurs at a somewhat lower mixture fraction, which is consistent with its mass fraction profile. The rate given for the L&L  $O_2$  oxidation was used alone in the present DNS simulations. In [5] it was noted that the oxidation rate constant for  $O_2$  oxidation was adjusted to match the maximum surface oxidation rate for laminar, coflowing methane–air flames. Thus, effects of O and OH oxidation would be partially built into the oxygen rate. If the L&L  $O_2$  rate is taken as the sum of  $O_2$ , O, and OH reactions, then there is a discrepancy of about a factor of 2: either the L&L rate is too low, or the other rates (together) are too high. No attempt is made here to provide a comprehensive treatment of soot oxidation, which is the subject of ongoing research. Rather, the phenomenon of soot–flame breakthrough observed in

the DNS calculations highlights an interesting, and potentially important mechanism for soot emission from flames. The quantitative results of the soot breakthrough in the DNS are subject to uncertainties in the soot growth and oxidation model, as noted, and also the representation of the particle size distribution, which, while common, is limited in the present, two-moment (i.e., monodispersed) approach. This model will tend to underestimate soot surface area and, hence, soot reactivity.

It is worth emphasizing that the soot breakthrough computed here is different from what would be expected in larger-scale flames and fires. In those situations, increased flow residence times result in higher soot concentrations, hence increased radiative heat losses and flame-chemistry interactions. In the present simulations, while the soot is fully coupled to the gaseous composition and energy flow fields, the soot concentration and residence times are too small to have a substantial impact on the temperature and composition of the flames. A soot concentration of 1 ppmv corresponds to about 5% of the local fuel carbon. Soot breakthrough was shown here to be possible in a configuration for which soot breakthrough is not favorable. In real situations, as soot passes through a flame, the flame temperature will decrease due to radiative losses, and be further weakened, possibly to the point of extinction (allowing substantial soot emission), as flame radicals are consumed by oxidation of soot. Furthermore, higher soot concentrations occur with larger particle sizes, so the soot area-to-mass ratio will be lower, reducing soot reactivity per unit mass and tending to increase the amount of soot breakthrough.

#### 5.4.6 Normal Statistics

Figure 5.6 showed scalar profiles along two selected normals. To further clarify the flame-soot interaction and structure, flame normal profiles were computed all along the stoichiometric mixture fraction surface. Along a flame normal, the point of intersection of the normal with the flame and the point of peak soot mass fraction,  $Y_{soot}^*$  are of particular interest. Figure 5.11 shows values of the mixture fraction and temperature at peak soot (denoted  $\xi^*$  and  $T^*$ , respectively) along the normal versus the stoichiometric flame displacement velocity  $v_\xi$ . These plots show a clear correlation between the location of the peak soot in the mixture fraction coordinate and the flame displacement velocity. Where  $v_\xi$  is shifted towards positive values through negative flame curvature, the peak soot occurs at lower mixture fraction, closer to the flame, hence at a higher temperature where reaction and radiative rates are higher. Higher values of  $v_\xi$  tend to occur in regions of

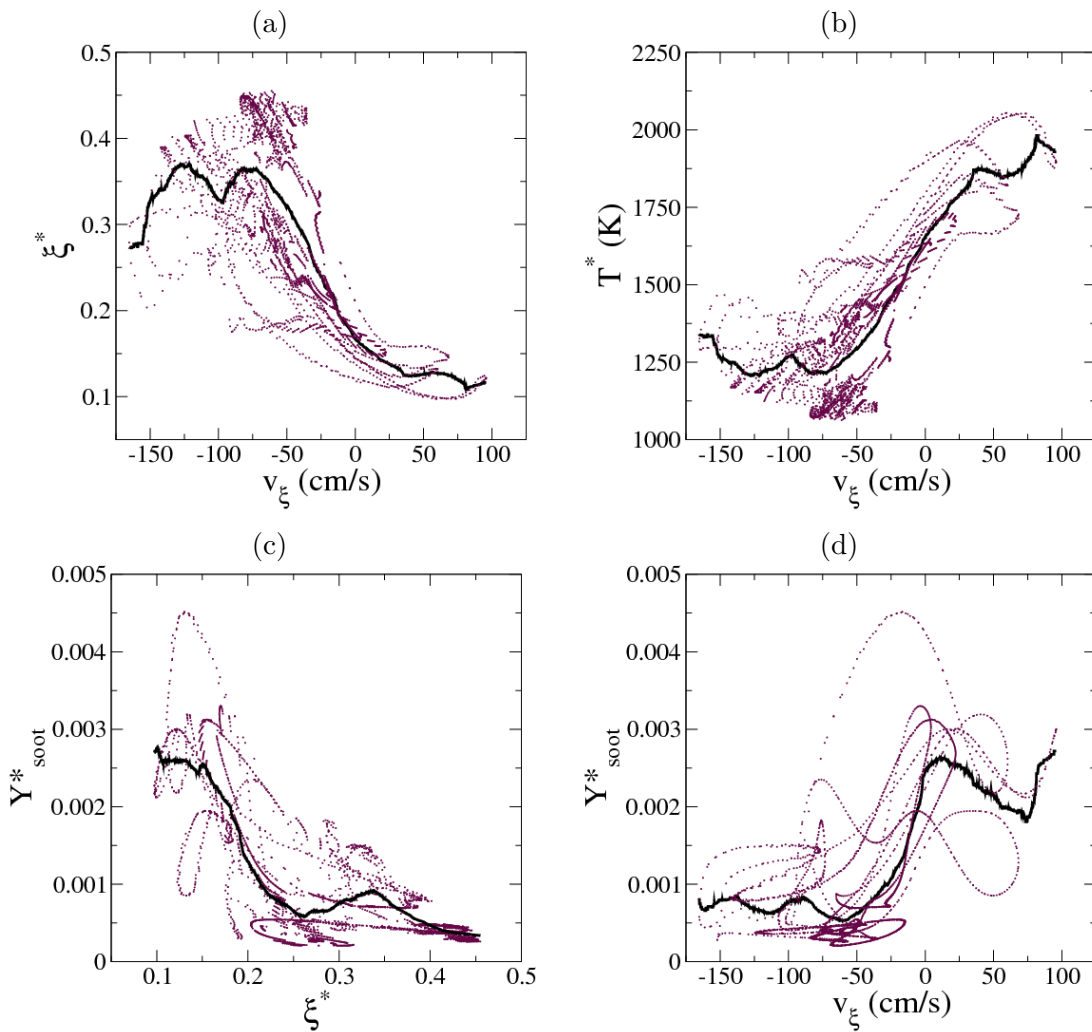


**Figure 5.11.** Scatter plots along flame normals at 1.75 ms. Starred symbols correspond to values at peak soot mass fraction along flame normals. Solid lines are a moving average of the data with a window size  $1/10^{th}$  the domain of the data.

negative flame curvature. In these regions, the effect of thermophoresis is to focus the soot, increasing soot concentrations. However, it is shown below that thermophoretic effects are relatively small, and elevated soot concentrations are dominated by the proximity of the soot and flame.

While there are not a lot of data points at the highest levels of the flame velocity, the  $\xi^*$  data appear to be levelling off there. This is consistent with the soot reaching an oxidation barrier near the flame surface. The presence of soot breakthrough would show up in the presence of soot at mixture fractions below stoichiometric (0.064).

The plot of peak soot mass fraction versus  $\xi^*$  in the figure shows a strong correlation

between the level of soot and the location of the soot in the mixture fraction coordinate, with a spread of a factor of 22 in soot mass fraction with peak levels ranging from mixture fractions of 0.1 to 0.45. Hence, at higher  $v_\xi$ , plots (a) and (b) show that the peak soot is closer to the flame and at a higher temperature, while plot (c) shows that the soot concentration is higher when the peak mixture fraction is lower. In plot (d), the  $Y_{soot}^*$  is shown versus  $v_\xi$ , which is essentially a combination of plots (a) and (c). Here, the data show more scatter, and the correlation of peak soot concentration along a flame normal with the flame displacement velocity is not as obvious, although the soot concentration is higher at higher flame velocity. However, plot (d) is also correlating two spatially segregated points along a flame normal, where the soot concentration grows in time. Regions of positive and negative  $v_\xi$  are conceptually similar to normal and inverse coflow diffusion flames, respectively. These results are consistent with experimental observations of lower soot concentrations in inverse diffusion flames than normal diffusion flames [12].

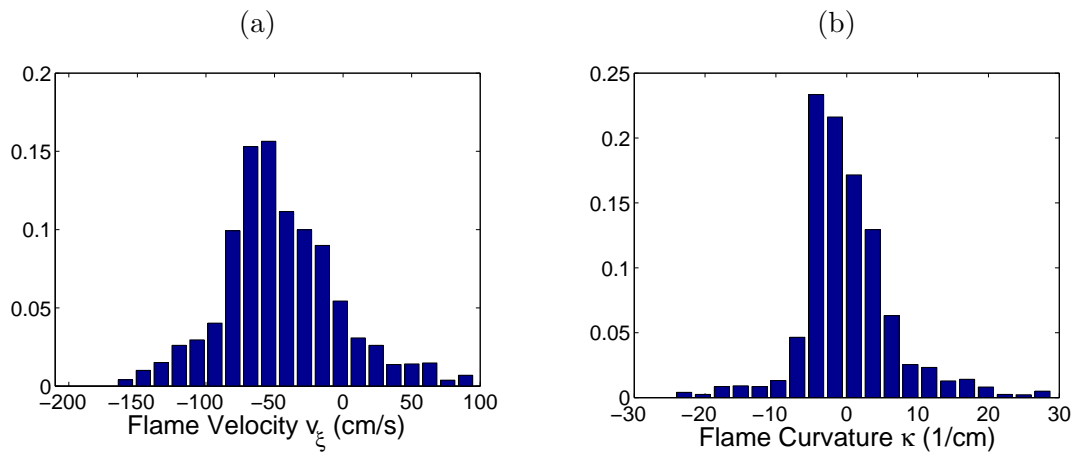
Although not shown here, the peak soot mass fraction is observed to be correlated as expected with the two terms of the flame displacement velocity equation, and not just their sum. That is,  $Y_{soot}^*$  is highest in regions of low scalar dissipation rate and more negative flame curvature. Low scalar dissipation rates, alone, imply higher flame temperatures and longer residence times for soot nucleation and growth reactions. Negative flame curvatures, in addition to shifting the relative flame motion towards the fuel (resulting in soot at lower mixture fractions with higher temperatures), will increase the temperature in the fuel-rich soot growth area through thermal focusing, further promoting soot growth. The low degree of scatter in the temperature-mixture fraction plot of Fig. 5.4 (about 100 K), compared with the strong dependence of temperature at peak soot in Fig. 5.11, shows that any thermal focusing effects are secondary to curvature-induced flame motion. The relatively low degree of scatter in the temperature plot of Fig. 5.4 includes the relatively strong effects of the full range of scalar dissipation rates. A similar plot of temperature versus mixture fraction conditional on scalar dissipation rate would show a smaller temperature variation associated with effects such as thermal focusing.

Figure 5.11 also indicates the distribution of the flame displacement velocity, with most of the data having negative values of velocity. Figure 5.12 plot (a) shows the PDF of  $v_\xi$  at 1.75 ms. The mean  $v_\xi$  is -45.7 cm/s and the standard deviation is 42.9 cm/s, and 13% of the velocity data are at positive velocity. The mean  $v_\xi$  is negative since the normal diffusion component is negative (see Eq. (5.7)) while the mean of the flame curvature is

nearly zero, as shown in Fig. 5.12 plot (b). The standard deviation of the flame curvature PDF is  $6.6 \text{ cm}^{-1}$ .

The flame displacement velocity  $v_\xi$  has been used to correlate the flame-soot interaction. This quantity is made up of curvature and normal diffusion terms as shown in Eq. (5.7). The relative importance of these terms is shown in Fig. 5.13. In the figure, a scatter plot of the curvature (first) term in Eq. (5.7), plot (a), is compared to the normal diffusion term, plot (b), versus  $v_\xi$ . The strong relation between the flame curvature term and  $v_\xi$  indicates the importance of this term, especially near the extrema of the range of  $v_\xi$ . The highest and lowest values of flame displacement velocity occur with low and high values of flame curvature. The normal diffusion term is restricted in magnitude to smaller values than the range of the curvature term for this flame, but in general we can see that both terms are of similar magnitude, which has been previously observed [74]. The normal diffusion term is negative over nearly all of the flame, consistent with the stoichiometric mixture fraction being on the lean side of the inflection point in Fig. 5.1.

It is well known from one-dimensional studies that soot levels are reduced as strain rate increases due to lower formation times and reduced flame temperatures, e.g., [124]. The scalar dissipation rate is related to the flame displacement velocity through the normal diffusion term since higher mixture fraction gradients give rise to both higher normal diffusion and higher dissipation rate. The lower two images of Fig. 5.13 show the two terms of  $v_\xi$  versus the scalar dissipation rate. The mean curvature is defined above as the divergence of the mixture fraction iso-surface normal vector field, so as a normal with



**Figure 5.12.** PDFs of relative flame displacement velocity  $v_\xi$  and flame curvature at 1.75 ms.

unity magnitude, we would not expect much relation to the scalar dissipation rate. Figure 5.13, however, shows that the magnitude of the curvature term is small at high scalar dissipation rates, consistent with the known fluid mechanical effect of mixture fraction iso-contours aligning with the strain field, which should reduce flame curvature in regions of high strain. The correlation of the normal diffusion term with the scalar dissipation rate is strong, with higher dissipation rate resulting in more negative flame displacement velocity.

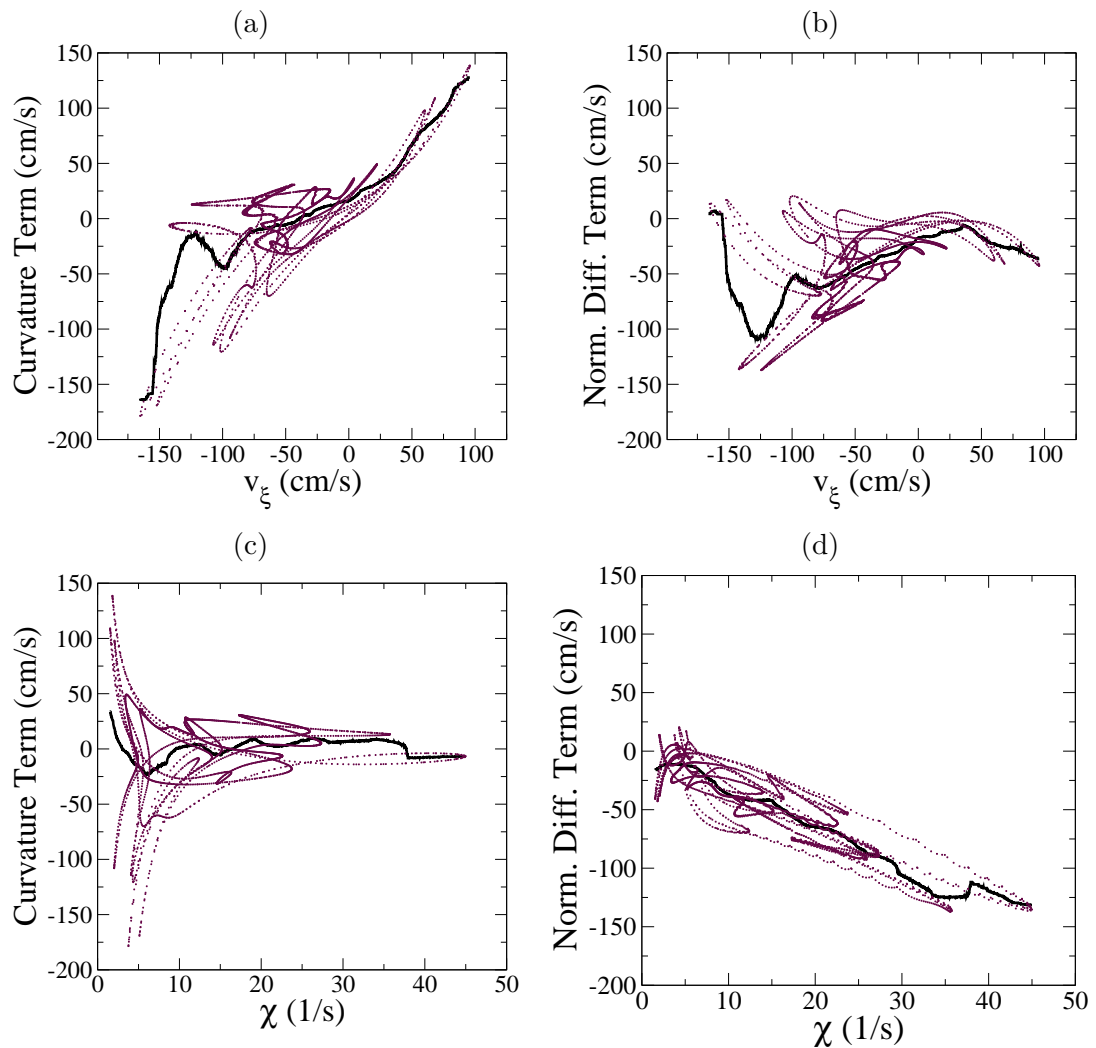


**Figure 5.13.** Scatter plots of curvature and normal diffusion components of  $v_\xi$  versus  $v_\xi$  and  $\chi$  at 1.75 ms. Solid lines are moving average of data with a window size  $1/10^{th}$  the domain of the data.

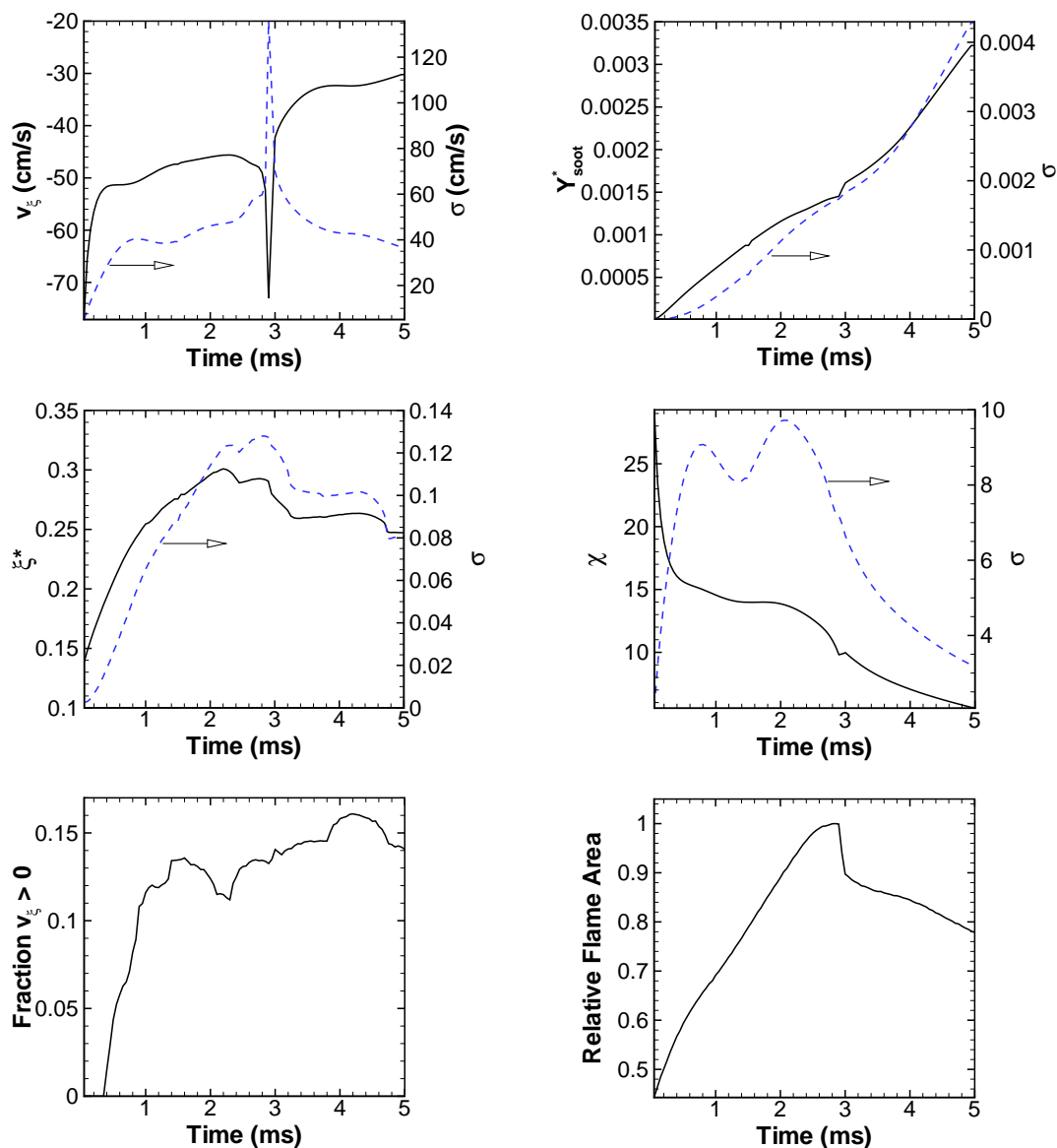
### 5.4.7 Temporal Evolution of Mean Flame Quantities

Figure 5.14 shows the flame surface area-weighted mean and standard deviation of flame quantities as a function of time. The flame displacement velocity, soot mass fraction and mixture fraction at peak soot along normals, and stoichiometric scalar dissipation rate are shown, as well as the relative flame surface area and the fraction of flame area with positive flame displacement velocity. The maximum number of flame normals considered was 3789. The initial transient, as evident in the  $v_\xi$  and  $\chi$  profiles, is observed at times less than about 0.4 ms in which the strained flame relaxes and turbulence begins to wrinkle the flame.

An obvious anomaly is observed in the flame displacement velocity profile at a time just under 3 ms in which the flame displacement velocity spikes downwards. This is observed in part because of the limited size of the simulation providing a limited amount of flame area. This negative spike occurs as two flame sheets merge and quickly propagate under the influence of a strong positive curvature, leaving a faint trail of soot in its wake. In Fig. 5.2, this flame motion occurs at the flame cusp along the upper flame sheet at the far left of the domain and corresponds to the sharp drop in the relative flame surface area profile shown in Fig. 5.14.

The mean flame displacement velocity, shown in the upper left plot of Fig. 5.14, is negative at all times but decays in magnitude as the turbulence field decays and scalar gradients relax diffusively. A mean velocity away from the fuel core (in the mixture fraction coordinate) is expected initially, but for a finite fuel core surrounded by air, eventually the stoichiometric flame surface will move inward toward the center and disappear as the air stream diffuses into the fuel stream. So eventually, the mean flame displacement velocity has to become positive. The fraction (based on flame points) of flame displacement velocity greater than zero increases in time, as does the flame displacement velocity, and varies from 0-15% but is in the range of 10-15% for most of the simulation.

The mean stoichiometric scalar dissipation rate decays continuously from a value of 29 to  $5.5 \text{ s}^{-1}$ , with the initial transient rapidly reducing the dissipation rate to  $16 \text{ s}^{-1}$  at 0.4 ms. The mean of  $Y_{soot}^*$  along flame normals increases continuously from zero to 0.0033 ( $f_v \approx 0.35 \text{ ppmv}$ ). The mean of  $\xi^*$  along flame normals is initially quite lean—at the location of peak production. As time passes, soot thermophoretically diffuses towards higher mixture fractions and the flame on average is moving away from the soot, resulting



**Figure 5.14.** Time average quantities and standard deviations along the flame or along flame normals in the case of soot mass fraction and mixture fraction at peak soot.

in the mean peak soot mixture fraction initially increasing with time. A peak is reached near the middle of the simulation after which the mean peak mixture fraction appears to level off and decrease slightly. So, soot is produced at low  $\xi$ , moves toward higher  $\xi$  under thermophoresis and negative flame displacement velocity, and levels off/decreases as the flame displacement velocity magnitude and flame gradients (e.g., temperature) are reduced while the soot formation region is relatively constant (as shown below) at  $\xi \approx 0.15$ .

The standard deviation of the flame and flame normal data are given along with means in Fig. 5.14 and are of similar magnitude as the mean quantity, though plotted on a separate scale for clarity. The mean flame curvature is approximately zero throughout the simulation, but the mean curvature magnitude increases from zero to a maximum of  $4.9 \text{ cm}^{-1}$  at about 1 ms, and decays to values between 3.5 and 4 at times above 2.5 ms. The standard deviation of flame curvature rises to a fairly constant value of about  $6 \text{ cm}^{-1}$  at 1 ms.

The relative flame surface area varies over a range of about a factor of 2 in the simulation. Initially the flame area increases, reaches a maximum at 2.85 ms, and then decays as turbulence decays and flame curvature is reduced. This is about the same point as the mean peak in  $\xi^*$  in time.

#### 5.4.8 Temporal Evolution of Total Soot and Radiation

Of interest in the present discussion of the interaction between flame and soot is the overall amount of soot that resides in regions of negative curvature and positive flame displacement velocity. Weighted PDFs of curvature and mixture fraction isocontour displacement velocities were computed throughout the flow field (not just at the flame surface or along flame normals). The PDFs were weighted by  $\rho Y_s$ , soot growth rate, and the soot radiative source term. For example, the PDF of  $v_\xi$ , weighting with  $\rho Y_s$ , is

$$P_{\rho Y_s}(v_\xi) = \frac{\langle \rho Y_s | v_\xi \rangle P(v_\xi)}{\langle \rho Y_s \rangle}. \quad (5.16)$$

This expression would be a Favre (density) average if  $\rho$  were used in place of  $\rho Y_s$ . Physically,  $P_{\rho Y_s}(v_\xi) dv_\xi$  is the fraction of soot mass in the domain that is in the range  $v_\xi$  to  $v_\xi + dv_\xi$ , where, in this section,  $v_\xi$  is at any mixture fraction, not just stoichiometric.

Figure 5.15 shows  $P_{\rho Y_s}$  at 1.75 ms in plot (a). The shaded region is one minus the cumulative PDF and represents the total fraction of soot that has positive  $v_\xi$ . This quantity is shown as a function of time in plot (b) for the cumulative PDFs of  $v_\xi$ , and also curvature  $\kappa$  (again, for any  $\xi$  surface), weighted by  $\rho Y_s$ , volumetric soot growth rate, and soot radiative source term. Here  $F$  denotes a cumulative weighted PDF. From plot (b), we see that up to 30% of the radiative source term occurs at positive  $v_\xi$ , while nearly 70% resides in regions of negative  $\kappa$ . We expect a significant portion of the radiative source term to reside in positive  $v_\xi$  and negative  $\kappa$ , since the soot temperature is higher there and the radiative source is nonlinear with temperature. A significant fraction (up

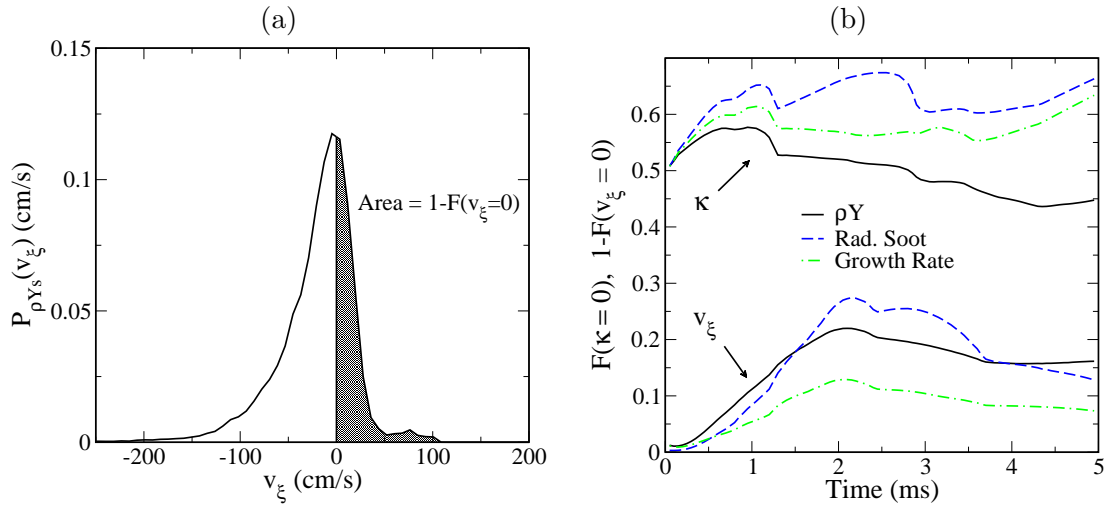


**Figure 5.15.** PDF of  $v_\xi$  weighted by  $\rho Y_s$  (a) with one minus the cumulative PDF shown shaded, at 1.75 ms. Plot (b) is the temporal evolution of the cumulative weighted PDF. The upper curves are PDFs of  $\kappa$  and the lower curves are PDFs of  $v_\xi$ . Individual curves are PDFs weighted by the indicated quantities.

to 20%) of the total soot resides in regions of positive  $v_\xi$ . As noted previously,  $v_\xi$  is initially negative in the domain, as reflected by the lower set of curves. That we do not have higher fractions of radiation and soot mass in regions of positive  $v_\xi$  is a reflection of the relatively small portion of the domain with positive  $v_\xi$ . However, the critical value of  $v_\xi = 0$  used here is somewhat arbitrary since  $v_\xi$  can be positive or negative depending on the competition between the curvature and normal diffusion components, and soot is shifted towards the flame for all negative curvature. Even though the fraction of soot mass and radiative source in positive  $v_\xi$  and negative  $\kappa$  are not overwhelming, they are still significant and occur through multidimensional effects that are not captured in most standard models that neglect these effects.

#### 5.4.9 Soot Transport

Soot transport is due to thermophoretic diffusion and fluid convection. The importance of these terms in relation to the flame motion is depicted in Fig. 5.16. The upper two plots show profiles through the two normals listed in Fig. 5.5, similar to Fig. 5.6. Each plot contains the flame displacement velocity, the normal component of the thermophoretic diffusion velocity,  $V_{thm}$ , and normal,  $V_{c,n}$ , and in-plane,  $V_{c,t}$ , components of the convective velocity. The in-plane convection is always positive since there is no directionality associated with it. The normal velocities are components in the direction of

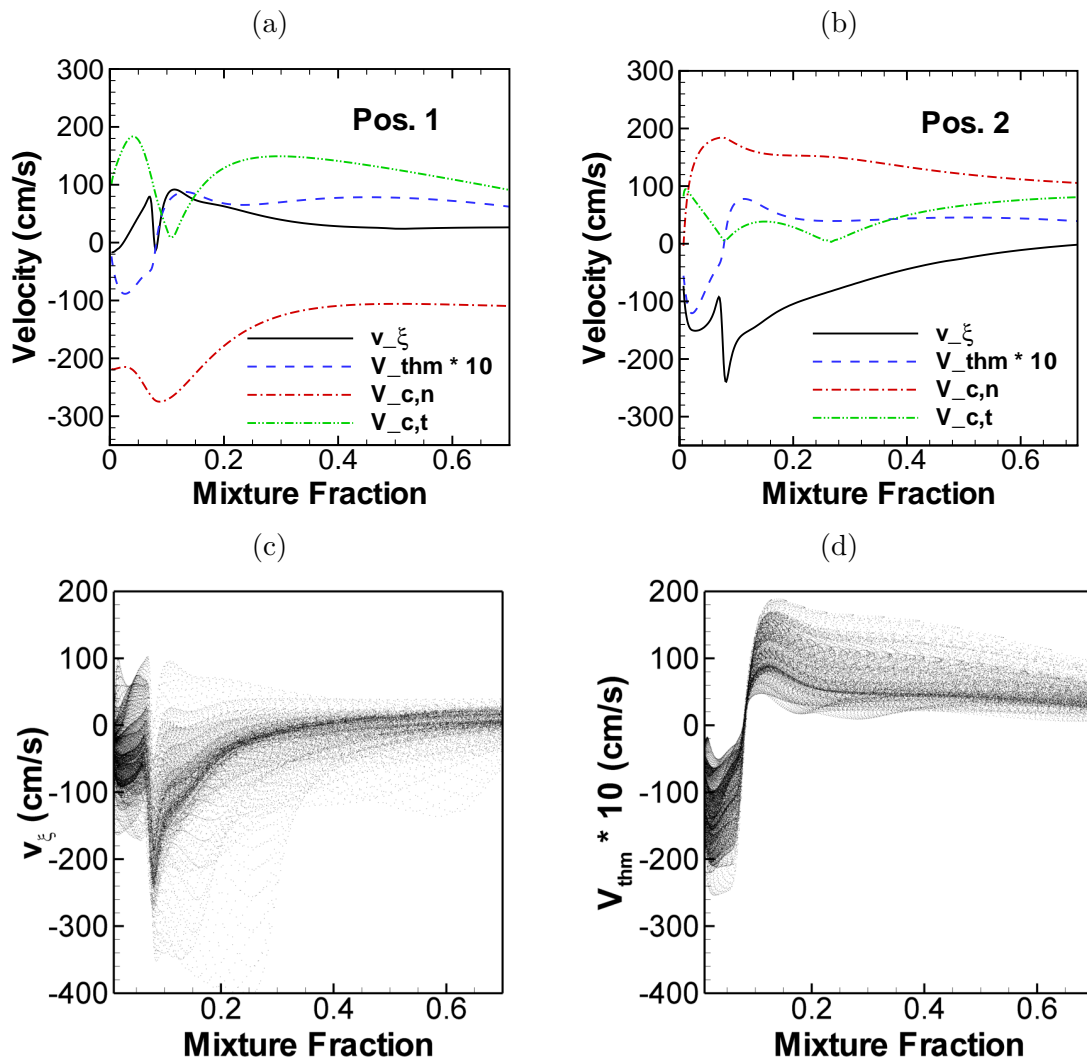


**Figure 5.16.** Profiles of flame displacement velocity, the normal component of thermophoretic diffusion velocity, and normal and in-plane components of convective velocity through two flame normals at the positions in Fig. 5.5 (a) and (b). Figures (c) and (d) show scatter plots of normal thermophoretic diffusion and flame displacement velocity versus mixture fraction (skipping over other point in the x and y directions for clarity). The simulation time is 1.75 ms.

the local mixture fraction gradient. The thermophoretic velocity is multiplied by a factor of 10, which, on the current plots shows that its value is about an order of magnitude below both the fluid convection and flame velocities. For this reason, the soot has been considered to be largely convected with the fluid. The thermophoretic velocity is similar at both positions and has values ranging from -10 to 10 cm/s over the whole mixture fraction range (the velocity is defined even where there is no soot) but has values of 6.8

and 4.5 cm/s at  $\xi = 0.2$  at positions 1 and 2, respectively. These values are in agreement with those found by Kang et al. [129]. The in-plane component of the thermophoretic diffusion velocity is less than 5% of the normal component and is ignored.

The normal and in-plane components of flow velocity are of similar magnitude at these two positions. This is important because (ignoring the flame displacement velocity), soot is convected as much toward or away from a flame as along a flame. If the curvature scales are of similar magnitude relative to the mixture fraction gradients, multidimensional effects will affect the soot history as the soot passes through the flow field. Also observe that in this flame, the flame displacement velocity is of a similar magnitude as the convective velocities, with values ranging from 0 to 100 and 0 to -200 cm/s at positions 1 and 2, respectively.

The lower two images of Fig. 5.16 show scatter plots of the flame displacement velocity and thermophoretic velocity versus the mixture fraction. Here again the flame displacement velocity tends to dominate the thermophoretic velocity for the interesting mixture fraction range from 0.1 to 0.4, above which the two velocities are comparable.

## 5.5 Discussion

The previous results have concentrated on the location of soot in the mixture fraction coordinate and the dependence of this locality on the dynamics of the soot-flame interaction. As noted previously, the location of soot determines its temperature and quantity, both of which impact soot yield and radiative heat transfer. A practical importance of understanding soot-flame interactions, which DNS alone can provide, arises through the need for turbulence-chemistry closures for RANS and LES models. Soot modeling in these contexts has been a challenge because of its complex chemistry, particle size distribution, optically thick radiative heat transfer, and long reaction timescales implying long history effects that must somehow be tracked through a flame.

Transporting detailed chemistry in CFD is usually too expensive and subgrid reaction models are often used to simplify the chemical description. Fox provides a good review of models for turbulent reacting flow [23]. A common approach that is illustrative of important modeling issues and that has been widely applied to modeling sooting turbulent flames is the steady laminar flamelet model and its variations [26], which was introduced in Chapter 1.

Soot modeling has provided a challenge since, as shown in Fig. 5.4, soot does not have

a clean one-to-one state relationship with mixture fraction that is often observed in other quantities such as temperature. This has been shown here to be due to both the unsteady reaction of soot and the differential transport. These effects must be properly accounted for in order to obtain an accurate representation of soot. Differential diffusion of soot is usually handled by assigning a large Lewis number to the soot species or by accounting for the thermophoretic diffusion, which, for flamelets solved in mixture fraction space, requires a treatment such as that given in [140]. The unsteady effects have been accounted for by transporting one or more soot moments at the grid level and computing the soot rates normalized by the soot quantity in the subgrid model [28]. Pitsch et al. used an unsteady flamelet model to capture the soot timescale and correlated the flamelet time to the spatial location in a turbulent jet flame to account for the unsteady soot growth [30].

Flamelet models as well as stochastic models such as the Linear Eddy Model rely on a one-dimensional description of the flame zone. In this chapter, it is shown that multidimensional effects can significantly impact the interaction between the soot and the flame, through flame shape and displacement velocity. Consequently, one-dimensional descriptions are not adequate for flames with significant multidimensional effects. To properly account for variable flame velocity effects in one-dimensional models, a correction would have to be applied for the differential soot transport. To this end, Van Kalmthout and Veynante have modeled the mean flame displacement velocity in nonsooting turbulent nonpremixed flames in terms of the mean flame curvature and the normal diffusion component written in terms of the solution of an unsteady unstrained flame solution [74].

It has been shown here that soot breakthrough in a flame is possible, though only small concentrations are observed in the DNS simulation due to the relatively short simulation time. Soot-flame breakthrough is an important problem in large-scale fires where large amounts of soot can be present on the outside (air side) of a flame, resulting in shielding of radiative heat transfer to the surroundings. Modeling this process is important if simulations are to yield correct heat transfer rates. However, the fundamental mechanisms for how soot can be formed in fuel-rich regions and end up on the outside of a fire without first being oxidized are not fully understood. Although the time and length scales of DNS cannot approach those of fires, DNS is currently the only tool available for detailed examination of soot-flame interactions and may lend insight into soot breakthrough and other phenomena. For example, we have here observed the motion of soot towards higher and higher mixture fractions as time progresses. In flames with

long timescales, downstream flames will likely exist between air and soot-loaded fuel that may increase the possibility of soot breaking through a burning flame and may result in flame quenching through a combination of strain and radiative heat loss, allowing soot to escape to colder fuel-lean regions.

The semiempirical soot mechanism employed in this work was chosen as a reasonable compromise between complexity, computational cost, and existing uncertainty in soot modeling, as discussed above. The mechanism does not include detailed soot chemistry involving combustion intermediates such as OH and H radicals. Soot growth and reaction steps are written in terms of acetylene, whereas soot nucleation is known to occur where PAH concentrations are high. Physical phenomena such as these will affect the location of the soot reactivity and may be expected to alter the soot concentrations and locations within the flame zone. However, the primary result of this chapter is that differential diffusion between soot and the mixture fraction directly shifts the soot into or out of the *bulk* flame zone. The soot reactivity depends not only on gaseous species concentrations, which are largely tied to the reactive flame zone, but also on the soot concentration in those reaction zones. In this chapter, it was shown that differential diffusion of soot results in soot transport over nearly the full span of mixture fraction. Hence, while the details of the soot mechanism will have an impact on soot concentrations, one would still expect to see higher soot concentrations in regions of more positive  $v_\xi$ .

Computational costs have dictated the DNS run time of 5 ms used. However, the soot-flame interaction results of this work should be similar under turbulent conditions at longer times. We have noted that soot growth timescales are longer than those typical of combustion reactions but that local (to single flame sheets) turbulent soot-flame interactions occur over shorter timescales than those based on global flow quantities (like timescales derived from jet exit velocities and location of peak mean soot concentrations). At longer times, one would expect higher levels of soot due to slower mixing rates of the decaying turbulence, as well as history effects as soot grows almost indefinitely given a hot, rich environment. However, the important velocities discussed (convection, thermophoretic, and flame displacement) depend on the soot concentration only indirectly through the temperature, density, and gas composition fields, so similar behavior under similar turbulent conditions at higher soot levels may be expected.

The simulations presented here are two-dimensional, and attention is focused on soot-flame interactions in flames wrinkled by turbulence, rather than on turbulent statistics,

which are not available in the present simulation. However, as the primary interest is in real turbulent flames, from which DNS can lend insight, the degree to which the results of this work will carry over to three-dimensional turbulence is important. The flame displacement velocity has been used to quantify the soot-flame interaction. This velocity arises from flame curvature and normal diffusion (i.e., flame strain). Qualitatively, three-dimensional turbulence will curve and strain a flame sheet as has been shown in the present simulation. Quantitatively, the relative importance of the curvature and strain terms in Eq. (5.7) may vary. However, it was shown in the present simulation that both terms are important, and examination of Eq. (5.7) shows that the curvature and normal diffusion terms both scale inversely with the lengthscale associated with mixture fraction gradients and so should stay in proportion as Reynolds number changes. Of course, the analysis is conditioned on the extent to which combustion is fast enough to maintain a coherent flame sheet. The behavior of soot transport and flame dynamics in three dimensions is studied in Chapter 6.

# CHAPTER 6

## THREE-DIMENSIONAL ETHYLENE JET SIMULATION

Chapter 5 presented results of a detailed study of flame dynamics and soot-flame interactions in two-dimensional decaying turbulence. The results highlighted the importance of multidimensional effects of flame curvature and differential diffusion of the flames. In this chapter, the flame dynamics analysis is extended to three dimensions. These results represent the first extension of DNS to turbulent, sooting, nonpremixed flames with realistic combustion chemistry, in three dimensions. The transport of soot in the mixture fraction coordinate is of primary interest. The flame displacement velocity, discussed in Chapter 5, is considered here, and statistics of this velocity as well as its component terms are presented. The results presented here support those found in the two-dimensional simulations. However, unlike the two-dimensional decaying turbulence simulation, significant bulk mixing of the fuel and oxidizer streams occurs, which impacts soot transport in the mixture fraction coordinate.

As in the two-dimensional DNS, the soot model is based on that of Leung and Lindstedt [5], which has been used extensively in simulations of turbulent sooting flames. The model is semiempirical and consists of four steps: nucleation, growth, oxidation, and coagulation. Acetylene is the gaseous species through which soot nucleation and surface growth occurs. Soot oxidation occurs in a global reaction with  $O_2$ , with effects of oxidation via species such as OH and O partially built into the rate. Although more complex soot chemistry models are available, such as the HACA mechanism [9], the present mechanism has been widely and successfully used in nonpremixed combustion and is considered adequate for the present purposes in which soot is introduced to three-dimensional DNS.

The soot particle size distribution (PSD) is modeled using the method of moments, in which the first three mass-moments of the PSD are transported. The derivation of the moment transport equations results in fractional moments in the chemical source terms that are closed using an assumed-shape lognormal distribution [105]. This assumption

was compared with quadrature closures [107] using four and six moments in Chapter 2 with good agreement between the models for the first two moments. The soot model is fully integrated into the gas phase mechanism by accounting for mass and energy transfer between the gas and soot phases. Soot particles are small enough that they do not impact the fluid momentum (the Stokes number is much less than unity) and are convected with the flow. Soot diffusion occurs primarily via thermophoresis as given by

$$j_{Mr} = -0.554M_r \frac{\nu}{T} \nabla T, \quad (6.1)$$

where  $M_r$  is the  $r^{\text{th}}$  soot moment,  $T$  is temperature,  $\nu$  is kinematic viscosity, and  $j$  is the diffusion flux. Soot particles have a high molecular weight, and Brownian diffusion, while implemented [94], is insignificant [103, 30].

Soot and gaseous radiation is accounted for using an optically thin model as before. However, radiative effects are negligible for the domain size, run time, and soot concentrations of the simulation.

## 6.1 Initial Conditions and Configuration

The simulation consists of a temporally evolving, nonpremixed, planar ethylene jet flame. In the temporally evolving jet configuration, the domain is periodic in the streamwise direction, and fluid exits the domain only through the cross-stream boundaries due to flame expansion. Time in a temporal jet is the analog of axial position in a typical jet flame. A major difference between these two cases is that, whereas a spatial jet continually spreads in the axial direction the temporal jet is statistically homogeneous in the streamwise direction and spreads in time.

The initial configuration is very similar to the two-dimensional decaying turbulence configuration of Chapter 5, except for the addition of a periodic spanwise direction, and a mean velocity field. A layer of fuel in the domain center is surrounded by oxidizer. The fuel slab extends to the full range of the streamwise and spanwise directions, which are periodic. The cross-stream boundaries are open, with nonreflecting outflow boundary conditions [85]. The mean flow is one-dimensional in the cross-stream direction, and pressure is constant at 1 atm. The fuel and oxidizer streams are given equal and opposite velocities. This configuration is optimal for model development because it is representative of shear-driven turbulent flows, maximizes the residence time of the

fluid in the domain (for soot growth), and provides two homogeneous flow directions for turbulence statistics.

Physical parameters characterizing the simulation are presented in Table 6.1. The configuration was designed to balance competing computational costs associated with grid resolution (number of grid cells), total computational run time (which dictates the number of time steps and the soot reaction time), domain size (maximize Reynolds number and turbulence-flame interactions), and flame extinction (to be minimized). The fuel core width,  $H$ , is 1.8 mm, and the difference in velocity streams,  $\Delta U$  is 82 m/s, giving a jet Reynolds number of 3700, based on the kinematic viscosity of the fuel stream. While the Reynolds number of the present flow is moderate, it is in the range of values studied in nonreacting, turbulent slot-jet experiments [141]. The simulation was run for 50 jet times,  $\tau_j$ , defined by  $H$  and  $\Delta U$ . The size of the domain is  $16H \times 11H \times 6H$  in the streamwise, cross-stream, and spanwise directions, respectively. A grid size of  $30 \mu\text{m}$  is used in each direction, giving 228 million computational grid cells. The simulation is well resolved for the mass, momentum, energy, and chemical species fields, with a minimum of 10 grid points across the thinnest radical species structures (i.e., a peak in the profile of a cross-stream cut). The soot moment fields are less well resolved with most of the thin structures containing at least five points.

The fuel core velocity is perturbed with three-dimensional isotropic, homogeneous turbulence intended to trip instabilities in the shear layers between the fuel and the oxidizer streams. The turbulence was initialized with  $u'/\Delta U = 4\%$ , and  $H/L_{11} = 3$ , where  $u'/\Delta U$  is the turbulence intensity and  $L_{11}$  is the integral lengthscale. These parameters are used to define the velocity field satisfying the Passot-Pouquet turbulence kinetic energy spectrum presented in Chapter 5. In three dimensions, the factor  $32/3$  in Eq. (5.2) is replaced with 16, the factor 10 in Eq. (5.3) is replaced with 15, and the factor  $8/3$  is removed from Eq. (5.4).

**Table 6.1.** Temporal ethylene jet simulation parameters.

$H$ (mm)	1.8	$L_x/H$	16	$\tau_{jet}$	0.022
$\Delta U$ (m/s)	82	$L_y/H$	11	$\tau_{run}/\tau_{jet}$	50
$Re_{jet}$	3700	$L_z/H$	6	# Cells (millions)	228
$u'/\Delta U$ (init)	4%	$\Delta x$ ( $\mu\text{m}$ )	30	Sim. Cost (million CPU-hr)	1.5
$H/L_{11}$ (init)	3	$\delta_\xi$ (mm)	0.8		

The chemical composition of the flowfield was initialized as described in Chapter 3. The pure stream composition is given as composition 3 in Table 2.3. The stoichiometric mixture fraction is 0.25. The increased  $\xi_{st}$  of 0.25, compared to 0.064 for pure fuel and air streams, increases the steady, stoichiometric, extinction scalar dissipation rate from 311 to 2554  $\text{s}^{-1}$  and moves the flame location closer to the turbulent shear layer. The stream temperatures were both preheated to 550 K. Preheating serves to make the flame more robust towards extinction and reduces the density ratio between the burned and unburnt mixtures from 8.0 (with streams at 300 K) to 4.6. The lower density ratio and more robust flame provide a greater degree of flame-turbulence interaction than would otherwise be possible under the time and spatial resolution constraints of the DNS.

The simulation was performed on the Redstorm supercomputer at Sandia National Laboratories using 7,920 processors at a computational cost of 1.5 million CPU-hours.

## 6.2 Results

The DNS results are presented in terms of

1. conditional statistics of gaseous combustion and soot scalars,
2. transport of soot relative to the flame in terms of the flame displacement velocity relative to convection, where the component terms of this velocity are quantified,
3. the relative importance of the thermophoretic diffusion velocity.

### 6.2.1 Overview

Figure 6.1 presents contour plots of temperature and soot mass fraction at  $t = 50\tau_j$  for which significant development and mixing of the jet have occurred. At this time, the soot concentration is at its maximum and has undergone substantial flame and turbulence interactions. On the right are spanwise cuts corresponding to a plane in the streamwise and cross-stream directions with the initial fuel velocity moving towards the right and the surrounding counterflowing oxidizer streams moving towards the left. On the left are axial cuts showing the cross-stream and spanwise directions. As the simulation progresses in time, the turbulent shear layers develop and the jet spreads outwards in the cross-stream direction. The flame location also spreads outwards, as expansion associated with combustion pushes fluid out of the domain. This figure illustrates the flow configuration and global flame characteristics. There is very little flame extinction occurring, although

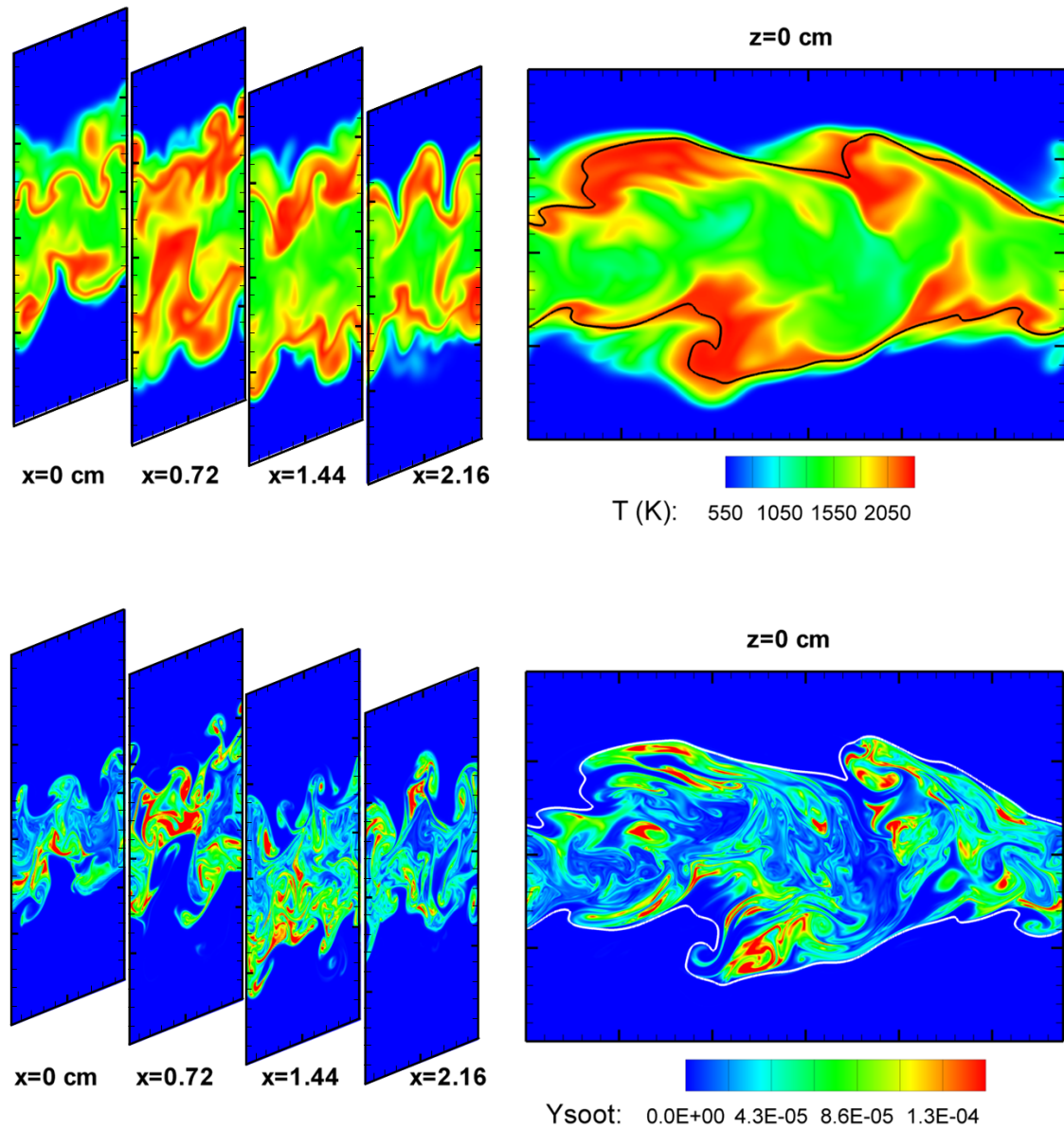


**Figure 6.1.** Isocontours of temperature (top) and  $Y_{soot}$  (bottom) at  $t = 50\tau_j$  for streamwise and spanwise cutting planes. The stoichiometric mixture fraction isocontour is shown in the spanwise cut. The peak  $Y_{soot}$  is off scale at  $4.5 \times 10^{-4}$ , located at  $x=0.72$  cm in the central region.

the flame is highly strained in the braid regions between large-scale vortex structures. A key observation is the difference in the small-scale structure of the temperature field and the soot field. The temperature field is much more diffuse than the soot mass fraction field. All of the soot moments are qualitatively similar in appearance to the soot mass fraction ( $M_1 = \rho Y_{soot}$ ). The soot diffusivity occurs primarily via thermophoresis and results in very thin structures. Soot is formed and grows on the fuel-rich side of the flame surface. Turbulent eddies strain the soot and convect it into the jet core where it mixes with combustion products and fuel. As discussed below, in the jet core region, the local mixture fraction surrounding the soot increases, while soot temperature and reaction rates are reduced.

### 6.2.2 Conditional Means and Scatter

The combustion and flow characteristics of the ethylene jet are quantified in Figure 6.2. This figure presents scatter data from the DNS at  $t = 50\tau_j$ , as well as the conditional (on mixture fraction) mean and conditional standard deviation as a function of mixture fraction. The soot mass is not included in the calculation of the mixture fraction as the soot concentration is small compared to local elemental carbon concentrations. The figure presents temperature, scalar dissipation rate, OH mass fraction (indicative of the flame zone and reactivity), and acetylene (the soot precursor) mass fraction.

At earlier times, the results are qualitatively similar to those at  $t = 50\tau_j$ , with the exception that some flame extinction appears in the scatter plots of temperature and OH mass fraction at points significantly below the conditional mean. The conditional mean is not significantly affected by extinction, however, as the extent of the flame extinction is small. The peak flame extinction is 12% at  $25\tau_j$ . The level of extinction is computed as the fraction of the stoichiometric mixture fraction iso-surface with  $Y_{OH} < 0.0015$ , which is half the steady laminar extinction value.

At  $t = 50\tau_j$ , the fuel core has mixed out somewhat and the data extend to mixture fractions just below 0.8. The temperature peak occurs rich of the stoichiometric mixture fraction, at  $\xi_{st} = 0.3$ , whereas the  $Y_{OH}$  peak is at a location slightly lean of stoichiometric. This behavior is consistent with the one-dimensional laminar flame structures. The acetylene concentration peaks at  $\xi = 0.5$ , which approximately coincides with the peak in  $\chi$ . This peak will reduce the concentration of soot obtained in the simulation as a higher  $\chi$  corresponds to a lower residence time for reaction.

The temperature and mass fraction plots in Fig. 6.2 show a strong state relationship

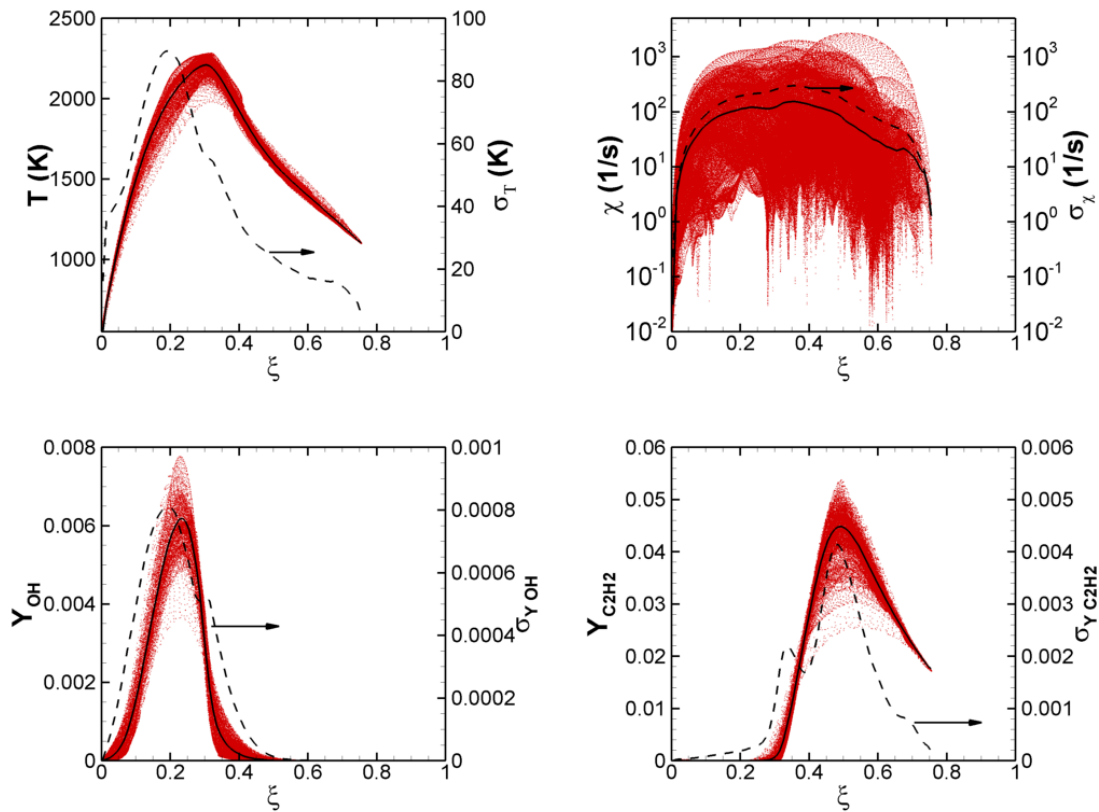


**Figure 6.2.** Scatter plots of combustion and flow quantities with conditional means and conditional standard deviations at  $t = 50\tau_j$ .

between a given variable and the mixture fraction. This relationship is indicated by values of the standard deviation about an order of magnitude lower than corresponding values of the conditional means.

Figure 6.3 presents scatter data, conditional means, and conditional standard deviations of the soot moments, and the net chemical source terms of the soot moments. The soot species exhibit distinct behavior from the gaseous species. The conditional scatter in the soot moments is much broader. Hence, the standard deviations of the moments are of the same order of magnitude as the conditional mean. This is in contrast with the gaseous species concentrations, where the conditional standard deviations are an order of magnitude lower than the conditional means. It is widely known that soot moments do not have a simple state relationship with mixture fraction [13]. Here, the same result is observed, which is the source of great difficulty in modeling turbulent sooting flames. In the previous, two-dimensional DNS, this was shown to be due to the combined effects of

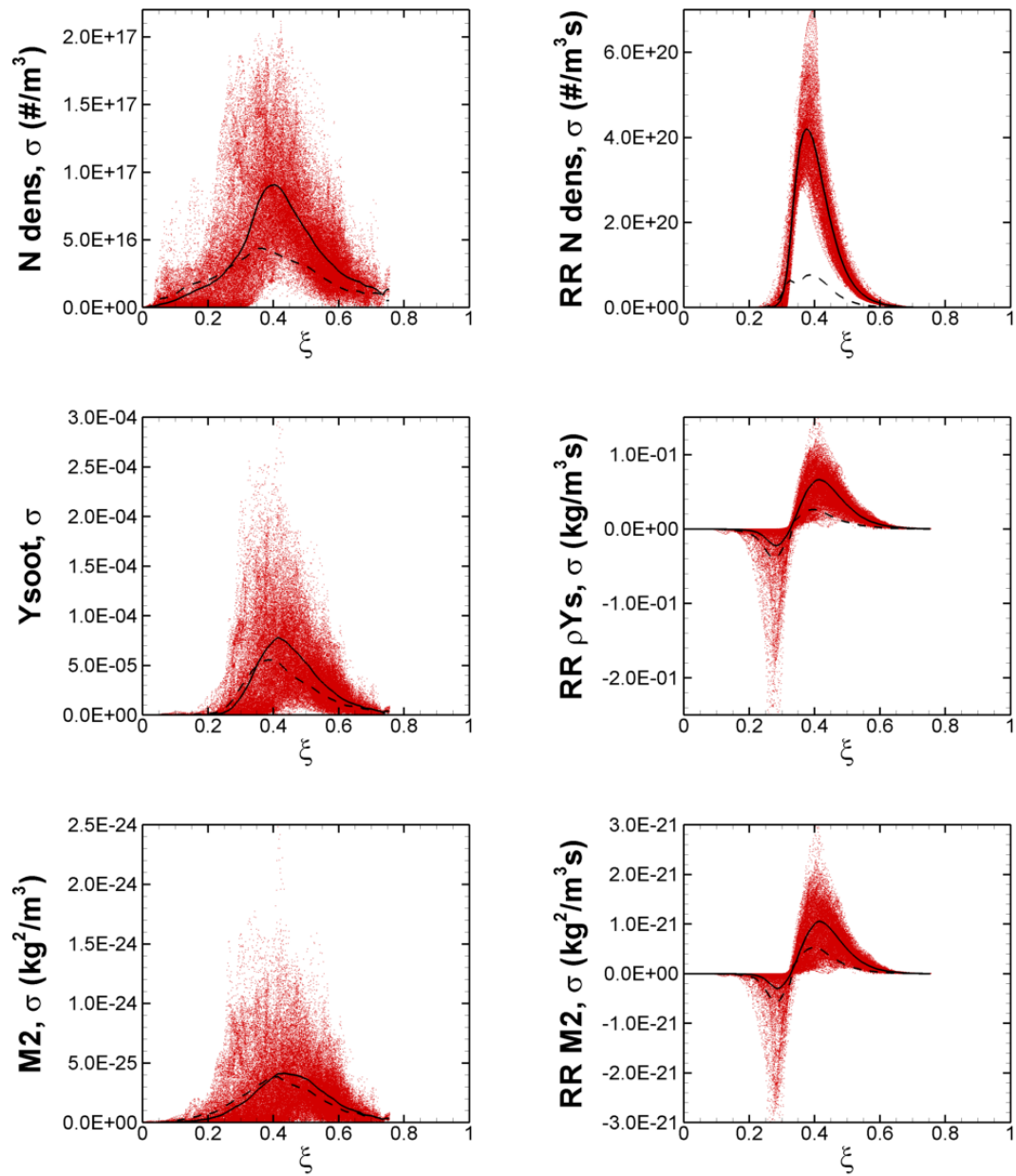


**Figure 6.3.** Scatter plots of soot quantities with conditional means (solid lines) and signed conditional standard deviations (dashed lines) at  $t = 50\tau_j$ .

unsteady soot growth and strong differential diffusion in the mixture fraction coordinate. Evidence for this is shown by comparing the soot moments to their respective reaction rates. The nucleation rate depends only on gaseous species and has similar characteristics, e.g., a relatively low  $\sigma$ . The rates for the second and third moments, while fixed in the mixture fraction coordinate, show much greater scatter, consistent with their dependence upon the soot moments. The crossover from negative to positive reaction rate occurs fuel-rich of  $\xi_{st}$  at  $\xi = 0.33$  as the soot transitions from being consumed in oxidizing regions to being formed in growth regions as the mixture fraction is increased. This position is the approximate upper limit in  $\xi$  of  $O_2$ .

The soot moments span the full range of the mixture fraction domain at mixture fraction values fuel-rich of  $\xi_{st}$ , whereas the soot rates vanish at approximately  $\xi = 0.6$ . The only possible mechanism for this is differential diffusion between soot and mixture fraction. This behavior is somewhat masked at  $t = 50\tau_j$  since the maximum mixture fraction is below unity. Moreover, due to nitrogen dilution in the fuel core,  $\xi_{st} = 0.25$  is much higher than in systems with combustion between pure ethylene and air  $\xi_{st} = 0.064$ . These two effects render the relative motion between the soot and mixture fraction somewhat obscured as indicated by scatter plots. The relative motion was more readily observed in the earlier two-dimensional simulation where there was less mixing of the fuel and oxidizer streams. In the present simulation, at  $t = 25\tau_j$ , the peak mixture fraction is near unity and the soot moments extend to this upper bound, whereas the soot rates are limited to the regions of mixture fraction shown in Fig. 6.3.

On the lean side of  $\xi_{st}$ , the second two moments are observed to be very small due to the oxidation barrier presented by the flame. The number density ( $M_0$ ) experiences no such barrier since its only sink is coagulation. For  $M_0$ , the extent to which differential diffusion between soot and mixture fraction results in soot transported to lean regions is seen. It is possible that, were the soot mass fraction high enough that oxidation could not fully consume the soot as it is transported past a reactive flame region, substantial quantities of soot could appear at mixture fraction values fuel-lean of  $\xi_{st}$ . This process of soot-flame breakthrough or, at least, soot- $\xi_{st}$  breakthrough in the event of flame quenching may be important in describing soot emissions as previously discussed. In large-scale fires, a substantial quantity of soot is observed to escape the flames where smoke emission occurs along with radiative shielding [142]. Modeling this process is important for performing predictive simulations of heat transfer in and around fires.

### 6.2.2.1 Scalar Dissipation Rate

The scalar dissipation rate is an important quantity in turbulent nonpremixed flames as it determines the rate of mixing between fuel and oxidizer and the combustion heat release rate. The inverse of the scalar dissipation rate is a mixing timescale. In the following presentation, the scalar dissipation rate is directly related to the component of the flame displacement velocity representing diffusion of isosurfaces of mixture fraction in the isosurface-normal direction, relative to convection. Here, statistics of the scalar dissipation rate are first presented.

Figure 6.4 shows the PDF of  $\log_{10} \chi$  at  $t = 50\tau_j$ . The data are shown on linear and log scales and have been centered and normalized to give a mean and standard deviation of zero and unity, respectively. The values of  $\langle \log_{10} \chi \rangle$  and  $\sigma_{\log_{10} \chi}$  are 1.41, and 0.744, respectively. The data are conditioned on mixture fraction between 0.02 and 0.98 to minimize possible bias associated with the pure streams. The DNS data are shown as symbols and a Gaussian distribution (in  $\log_{10} \chi$ ) is shown as the solid line. The Gaussian distribution has the same first two moments as the DNS data. The DNS data are observed to be very nearly lognormal, with a slight negative skewness. These results

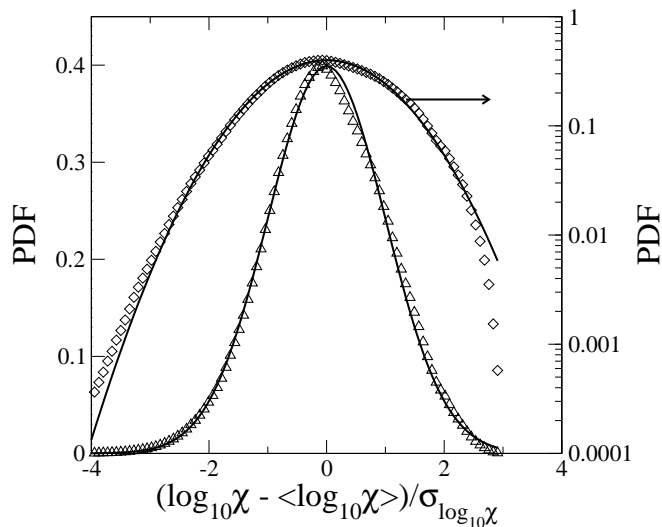


**Figure 6.4.** Centered and normalized PDF of  $\log_{10} \chi$  at  $t = 50\tau_j$  on linear and log scales. Symbols are data conditioned on  $0.02 < \xi < 0.98$ . Solid lines are a Gaussian distribution with the same first two moments as the DNS data.

are in agreement with those previously reported experimentally [141] and in DNS of a similar configuration in an extinction-reignition study of CO-H<sub>2</sub> fuel [81]. Although the jet Reynolds number of the present simulation is not large, the turbulence is sufficient to yield a lognormal PDF of the scalar dissipation rate with a wide range of values.

The conditional mean and standard deviation, along with instantaneous scatter data, are shown in Fig. 6.2 for the scalar dissipation rate at  $t = 50\tau_j$ . Consistent with experimental observations, the standard deviation of the scalar dissipation rate is observed to be higher than the conditional mean value [27]. Though partially obscured by the logarithmic scale, the conditional mean  $\chi$  has a dip in the vicinity of the stoichiometric point. This has been previously observed experimentally [143] and in DNS [79] and is consistent with effects of flow divergence through gas expansion from the flame and increased kinematic viscosity (reduced local  $Re$ ) in the flame zone.

The evolution of the conditional mean scalar dissipation rate is shown in Fig. 6.5. As the jet evolves, the peak scalar dissipation rate decreases continuously. In addition, as fuel and oxidizer mix, the peak mixture fraction in the fuel core decreases. The mixture fraction value of the peak scalar dissipation rate is indicated in the figure by the vertical lines. The mixture fraction of peak  $\langle\chi|\xi\rangle$  becomes progressively lower as the jet evolves.

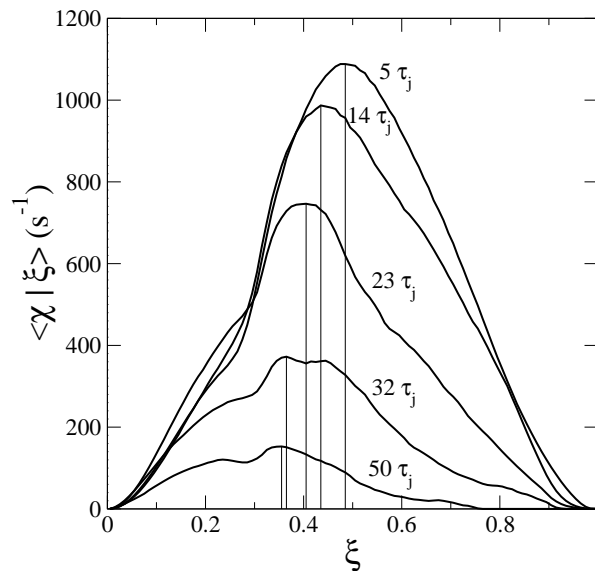


**Figure 6.5.** Conditional mean scalar dissipation rate versus mixture fraction at five times. Vertical lines indicate the location of peak conditional scalar dissipation rate.

At  $t = 23\tau_j$  the peak  $\langle\chi|\xi\rangle$  occurs at a mixture fraction of approximately 0.4, which coincides with the peak soot mass concentration and reaction rate shown in Fig. 6.3. At earlier times, the mixture fraction of peak  $\langle\chi|\xi\rangle$  is rich of  $\xi = 0.4$ , and at later times, the peak is lean of this value. In a turbulent flow, on average, fluid elements that are rich of the peak  $\langle\chi|\xi\rangle$  will become leaner, and fluid elements that are lean of the peak  $\langle\chi|\xi\rangle$  will become richer. Hence, as the mixture fraction of peak  $\langle\chi|\xi\rangle$  crosses  $\xi = 0.4$  (where soot production peaks), we expect transport in the mixture fraction coordinate to be nonmonotonic, with soot transported to higher then lower mixture fractions as the jet evolves. This behavior is shown in the following section.

### 6.2.3 Mixture Fraction PDF and Soot Transport

The transport of soot in the mixture fraction coordinate is important since this affects the soot concentrations through chemical reactivity, as well as the temperature of the soot, which directly affects radiative emission rates. Figure 6.6 presents density-weighted (Favre) and soot mass density-weighted, probability density functions of mixture fraction. In Fig. 6.6 plots (a) and (b), respectively,  $P_\rho$  is the fraction of mass per unit mixture fraction at a given mixture fraction, while  $P_{\rho Y_s}$  is the fraction of the total soot mass per unit mixture fraction, at a given mixture fraction. These weighted PDFs are defined in Eq. (5.16):

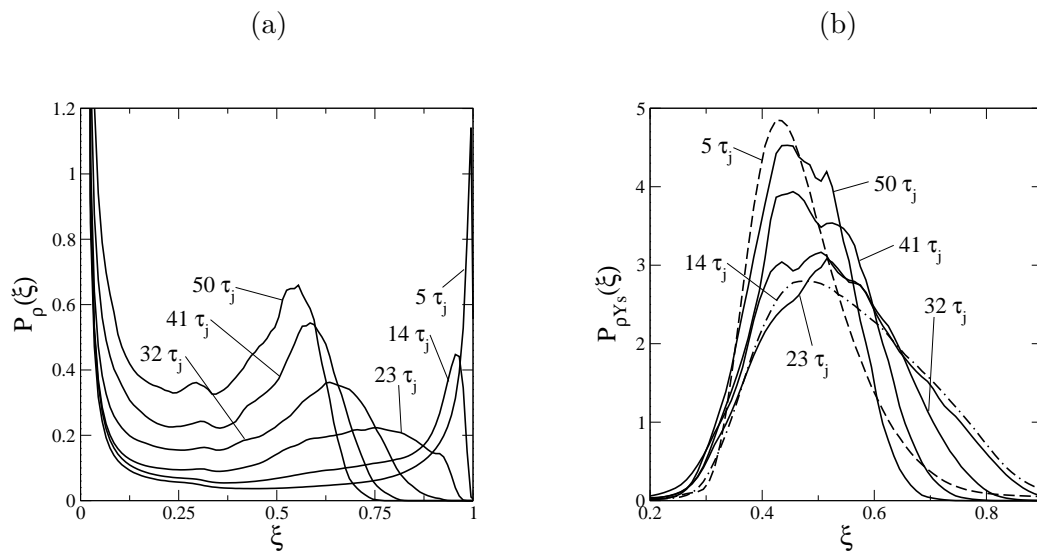


**Figure 6.6.** Density-weighted (a) and soot mass density-weighted (b) PDFs of mixture fraction at evenly spaced times.

$$P_\phi = \frac{\langle \phi | \xi \rangle P(\xi)}{\langle \phi \rangle}, \quad (6.2)$$

where  $\phi$  is the weighting variable ( $\rho$ , or  $\rho Y_s$ ). Figure 6.6 plot (a) has the general shape of a  $\beta$ -PDF. At early times, the mixture fraction is partitioned mainly between pure fuel and oxidizer (mostly oxidizer). As the jet evolves, the fuel stream mixes out and the upper bound migrates towards leaner mixture fraction. At  $t = 50\tau_j$ , the peak mixture fraction is just below 0.8, and the peak in the PDF is just above 0.5, which corresponds with the location of the peak acetylene mass fraction, shown in Fig. 6.2.

Figure 6.6 plot (b) is more interesting. The plot has an approximate Gaussian shape, but with a noticeable positive skewness, i.e., a tail towards the fuel stream. As the jet evolves, the PDF first widens and subsequently contracts. This is a consequence of two competing effects:

1. Differential diffusion between soot and mixture fraction, as evidenced by the soot locality outside of the mixture fraction bounds of the soot reaction rates (see Fig. 6.3). This differential diffusion occurs due to the dynamics between mixing of soot and isocontours of mixture fraction.
2. As fuel and oxidizer mix together, the fuel core is diluted and the upper bound of mixture fraction decreases in time.

Hence, while differential diffusion of soot and mixture fraction tends to spread soot in the mixture fraction coordinate, the upper bound on the mixture fraction is becoming smaller as gas mixing occurs. Time in the present simulation is the analogue of axial position in a nonpremixed jet flame. If the present simulation were continued to longer time, one would expect the peak in the mixture fraction PDF to approach the stoichiometric value and eventually mix to the oxidizer free-stream composition. The soot would be squeezed towards the flame zone until soot oxidation (and possibly some emission) occurs.

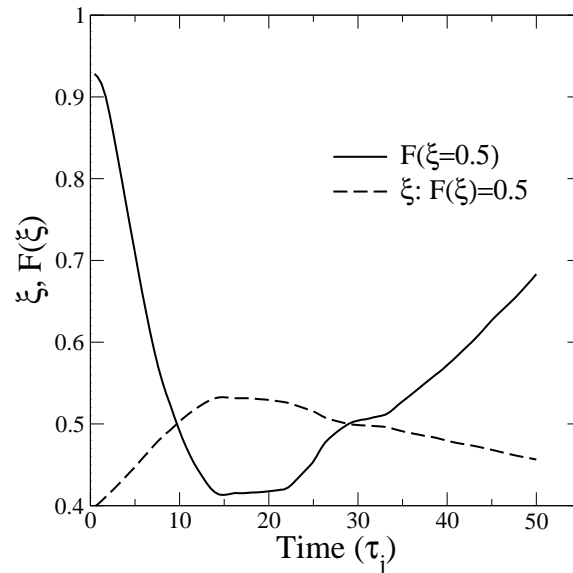
Soot is essentially convected with the fluid, and the rate of motion of isocontours of mixture fraction relative to fluid convection gives the motion of soot with respect to mixture fraction. This motion can be of either positive or negative sign, as was previously demonstrated in Chapter 5 by examining the so-called flame displacement velocity  $v_\xi$ . This quantity is elaborated on below for the present three-dimensional simulation. Unlike the present case, in the two-dimensional DNS, the peak mixture fraction did not decrease substantially below unity, and bulk mixing of the fuel zone was not observed.

Figure 6.7 highlights the location and width of  $P_{\rho Y_s}$  in  $\xi$  that was presented in Fig. 6.6. Here, the cumulative soot mass-weighted PDF of mixture fraction is considered:

$$F(\xi) = \int_0^\xi P_{\rho Y_s}(\eta) d\eta, \quad (6.3)$$

where  $\eta$  is an integration variable for  $\xi$ . The solid line in Fig. 6.7 is the value of  $F(\xi = 0.5)$  and is the fraction of the total soot mass below a mixture fraction of 0.5. This value starts at over 90% and decreases to below 50% as the soot is transported towards richer  $\xi$ . The curve then reaches its minimum point just above 40% at  $14\tau_j$ . At approximately  $23\tau_j$ , the curve rises sharply and increases to approximately 70% at  $50\tau_j$  as the fuel stream is mixed out and the peak mixture fraction decreases. In Fig. 6.5  $23\tau_j$  corresponds to the time at which the peak  $\langle \chi | \xi \rangle$  crosses  $\xi = 0.4$ , which is where the conditional mean soot mass and soot mass rate exhibit maxima.

The dashed curve in Fig. 6.7 indicates the motion of  $P_{\rho Y_s}$ . This curve represents the location in the mixture fraction coordinate of the median soot mass. The dashed curve is qualitatively the inverse of  $F(\xi = 0.5)$  and shows that the location of the median soot



**Figure 6.7.** Plot of the cumulative soot mass density-weighted PDF of mixture fraction evaluated at  $\xi = 0.5$  (solid line). The dashed line shows the mixture fraction location where the same cumulative PDF has a value of 0.5.

mass starts out lean at a mixture fraction of about  $\xi = 0.4$ . The mixture fraction at  $F(\xi) = 0.5$  then increases in time to  $\xi = 0.53$ , where it peaks at about the same time as the minimum in  $F(\xi = 0.5)$ , after which it decreases monotonically to  $\xi = 0.45$ .

#### 6.2.4 Mixture Fraction Dynamics and Soot-Flame Diffusion

The soot transport in the mixture fraction coordinate via differential diffusion between soot and the gaseous species is examined as in Chapter 5 by consideration of the flame displacement velocity  $v_\xi$ , given in Eqs. (5.7) and (5.8) and repeated here:

$$v_\xi = -D_\xi \nabla \cdot \mathbf{n} - \frac{1}{\rho |\nabla \xi|} \frac{\partial}{\partial \eta} \left( \rho D_\xi \frac{\partial \xi}{\partial \eta} \right), \quad (6.4)$$

$$= -D_\xi \nabla \cdot \mathbf{n} - \frac{D_\xi}{2} \frac{\partial}{\partial \eta} \ln(\rho^2 D_\xi \chi / 2). \quad (6.5)$$

In the two-dimensional analysis, it was found that the curvature term is either positive or negative with a mean near zero, while the normal diffusion term is primarily negative since the flame exists between pure streams at a low value of the mixture fraction, such that a diffusive relaxation of the flame tends to move the flame towards the oxidizer stream. In other words, the second derivative of the mixture fraction profile in the  $\eta$  coordinate was almost exclusively positive. Here,  $\xi_{st}$  is much higher, hence closer to the inflection point in the  $\xi$  profile. This, together with the decreasing upper bound on  $\xi$ , through bulk fuel-oxidizer mixing, results in the normal diffusion term taking on both positive and negative values, as shown below.

The terms in Eq. (6.4) dictate the sign, magnitude, and origin of  $v_\xi$ , which determine whether soot is locally convected into or away from the flame zone. In the two-dimensional analysis, it was found that both terms are of similar magnitude. Here, we extend the analysis to three dimensions.

Figure 6.8 presents the stoichiometric isosurface colored by  $v_\xi$  at six times along with grayscale isocontours of the soot mass fraction. The scales in the figure vary with time. At early times, there is a strong positive correlation between the soot concentration and the magnitude and sign of  $v_\xi$ . Regions of positive  $v_\xi$  correspond to the flame moving towards the fuel stream relative to convection. In these regions, the soot is locally convected towards the flame zone where its temperature is higher and the soot is more reactive, as observed in Chapter 5. There the turbulence was decaying, the Reynolds number was

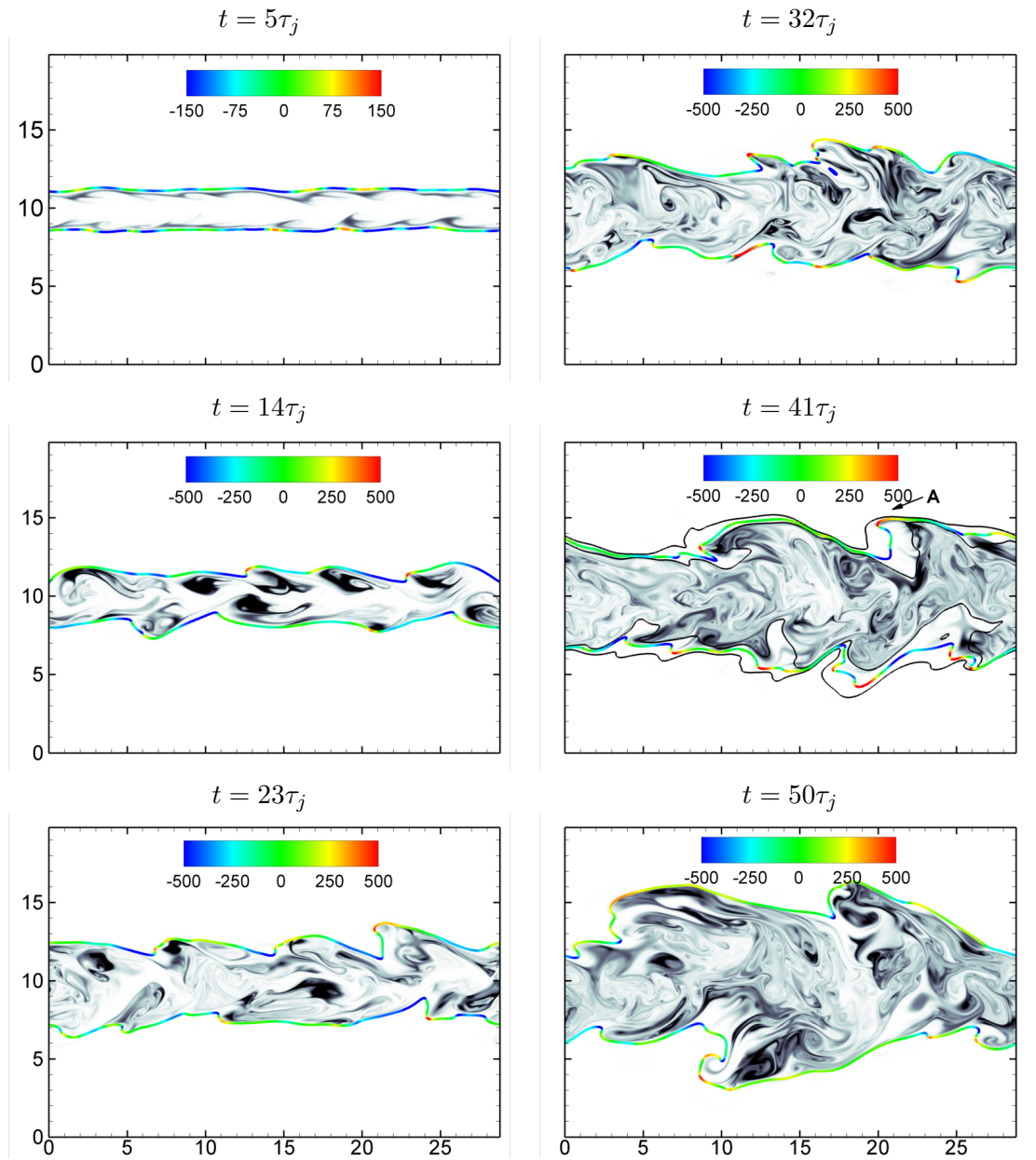


**Figure 6.8.**  $Y_{soot}$  (grayscale, black is high value) and stoichiometric isosurface colored by  $v_\xi$ . The scales vary: with increasing time the peak  $Y_{soot}$  scale is  $1 \times 10^{-5}$ ,  $1 \times 10^{-5}$ ,  $4 \times 10^{-5}$ ,  $5 \times 10^{-5}$ ,  $10 \times 10^{-5}$ , and  $15 \times 10^{-5}$ . The length dimension is millimeters. At  $41\tau_j$  two additional mixture fraction isocontours, 0.15 and 0.35, are shown.

smaller, and the soot was not strongly convected away from the flame zone. Here at  $14\tau_j$ , spanwise coherent structures associated with the Kelvin-Helmholtz shear instability are evident, which convectively transport soot away from the flame zone, as was discussed in Chapter 4. These strong transport and history effects complicate the analysis. Ideally, a Lagrangian description of the soot would record the full history, especially the reactive history, of the soot. As it is, soot is formed and grows in reactive zones near the flame. Subsequently, turbulence transports the soot away from the flame where mixing increases the local mixture fraction surrounding the soot, hence reducing the soot temperature and growth rate, but soot remains to be strained and diluted by the flow. The soot structures persist even as the turbulent energy decays, serving as an example of Gibson’s so-called fossil turbulence [144].

At later times, e.g.,  $t = 41\tau_j$ , there are regions of high  $v_\xi$  for which the soot concentration appears to be very small. There are two possible reasons for this. One is simply that the thickness of the colored stoichiometric surface obscures a high concentration of soot beneath it. This occurs, for example, at  $t = 41\tau_j$  on the right of the upper flame sheet at point “A”. More importantly, the flame sheet is wrinkled with a curvature that changes sign and, hence, can change the sign of  $v_\xi$ . Therefore, soot may be formed preferentially in a region of positive  $v_\xi$ , which subsequently changes sign through flame curvature, but leaves a higher concentration of soot in its wake.

At  $t = 41\tau_j$ , mixture fraction isocontours at 0.15 and 0.35 are also shown. In some regions, soot appears to be absent “far” from the flame but these regions, in fact, coincide with the spacing of the mixture fraction contours. That is, the soot is not “far” from the flame in the mixture fraction coordinate, since extensive strain rate in the upstream portions of the spanwise rollers separates the mixture fraction isocontours. From Fig. 6.3, the crossover between production and destruction of  $M_1 = \rho Y_s$  occurs at  $\xi = 0.33$ , which accounts for the low soot mass between these isocontours.

### 6.2.5 The Flame Displacement Velocity and Its Terms

The stoichiometric mixture fraction probability density functions of  $v_\xi$  and its constituent terms at three times corresponding to  $5\tau_j$ ,  $23\tau_j$ , and  $41\tau_j$  are presented in Fig. 6.9. In the figure, CRV and ND denote the curvature and normal diffusion terms, respectively, on the right-hand side of Eq. (6.4). These PDFs are area-weighted on the stoichiometric surface extracted from the mixture fraction field. The scale of the

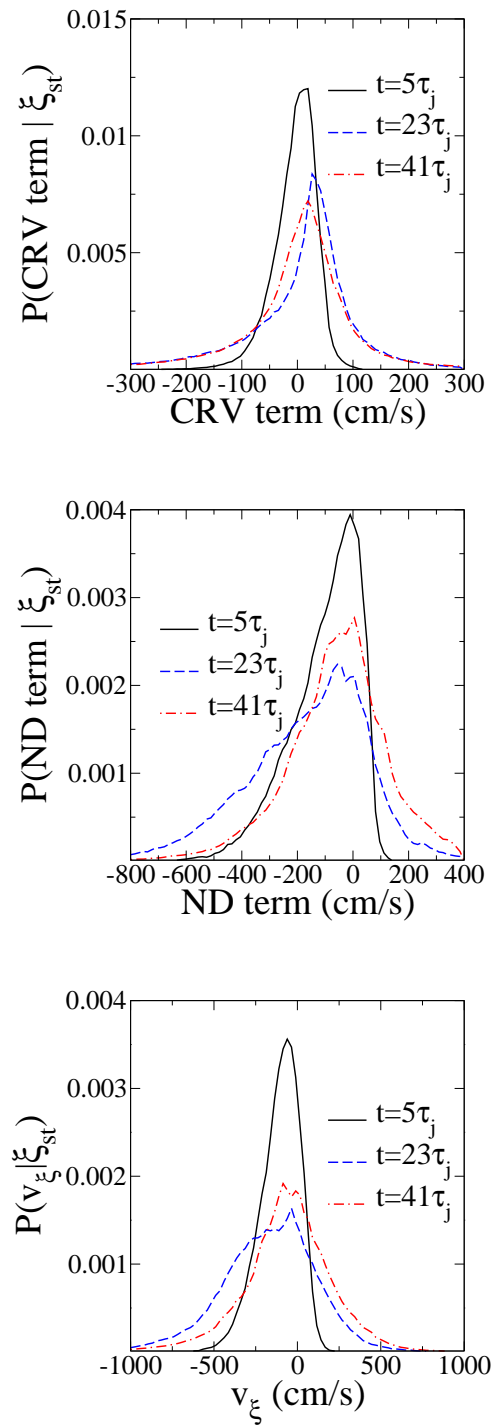


**Figure 6.9.** Probability density functions of  $v_\xi$  and its two terms in Eq. (6.4), conditioned on  $\xi_{st}$  at three times.

terms in the figure indicates that both terms of  $v_\xi$  are of similar magnitudes. These terms are of either positive or negative sign, although the normal diffusion term and  $v_\xi$  are negatively biased. Positive values of the curvature term, normal diffusion term, and  $v_\xi$  correspond to convection through the flame from the fuel side to the oxidizer side or, relative to convection, positive values of these terms correspond to diffusion of the  $\xi_{st}$  isosurface towards the fuel stream. The converse is true for negative values of these quantities.

The normal diffusion term is observed from Fig. 6.9 to have a negative skewness. As noted previously, in the absence of curvature, in an ideal diffusion flame with  $\xi_{st} \lesssim 0.5$ , the mixture fraction profile through the flame will have a positive second derivative for which diffusive relaxation will move the flame towards the oxidizer. This effect is less strong as  $\xi_{st}$  increases towards the inflection point (at which point the sign changes and the diffusive relaxation causes flame motion towards the fuel side). Conversely, as the jet evolves, the maximum mixture fraction decays due to mixing, and the inflection point in the mixture fraction profile moves towards the stoichiometric surface. This results in an increased portion of the flame existing with a positive normal diffusion term, hence a more positive  $v_\xi$ . The effect of the terms on the stoichiometric probability density function of  $v_\xi$  is also shown in Fig. 6.9.  $v_\xi$  is always biased to negative values, as expected, due to the small mean of the curvature term and the negative bias of the normal diffusion term. As the jet evolves, however, this bias is reduced and the fraction of positive  $v_\xi$  increases from 22.8% at  $5\tau_j$  to 49.1% at  $50\tau_j$ . Table 6.2 shows the fraction of the stoichiometric surface for which the curvature term, normal diffusion term, and  $v_\xi$  are positive at six times in the simulation. The fraction of positive curvature term shows little variation, while the fraction of positive normal diffusion term and  $v_\xi$  have similar values and steadily increase in time.

The fact that  $v_\xi$  is significantly positive is important from a modeling perspective because it means that multidimensional effects associated with flame curvature and mixing effects associated with normal diffusion can result in a diffusion flame that moves (relative to convection) in both the fuel and oxidizer directions with nearly equal frequency. Positive  $v_\xi$  is the opposite of what occurs in canonical opposed jet diffusion flames of similar stream compositions. Although these effects may play a small role in the combustion gas dynamics, they are shown to play a strong role in soot formation and radiative processes in the two-dimensional simulations in Chapter 5. Here, it is demonstrated that similar

**Table 6.2.** Positive fraction of stoichiometric surface quantities.

Time ( $\tau_j$ )	$v_\xi$	Curvature Term	Normal Diffusion Term
5	0.228	0.558	0.254
14	0.235	0.632	0.228
23	0.291	0.636	0.248
32	0.412	0.594	0.395
41	0.427	0.588	0.402
50	0.491	0.580	0.492

flame dynamics are observed in both two- and three-dimensional turbulence.

Figure 6.10 presents the area-weighted stoichiometric mean and standard deviation of  $v_\xi$ , and the curvature and normal diffusion terms, as a function of time. The mean curvature term is nearly zero, but its standard deviation is significant. The difference between the mean  $v_\xi$  and mean normal diffusion term is the mean curvature term, which is small. Hence, the mean  $v_\xi$  closely follows the mean normal diffusion term. The mean  $v_\xi$  and normal diffusion terms are negative for the extent of the simulation, up to  $50\tau_j$ . However, the mean normal diffusion term at first decreases to a minimum of -200 cm/s

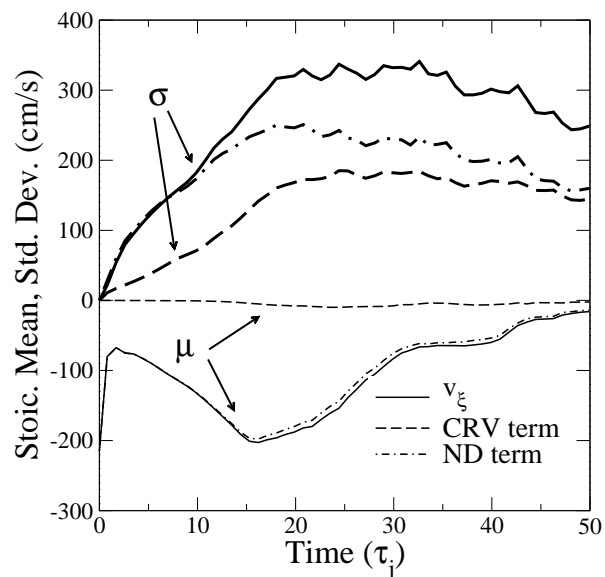


**Figure 6.10.** Stoichiometric conditional means,  $\mu$ , (thin lines) and conditional standard deviations,  $\sigma$ , (bold lines) of  $v_\xi$  and its constituent terms.

at  $16\tau_j$  but then increases steadily to  $-14$  cm/s at  $50\tau_j$ . The minimum curvature term is  $-10$  cm/s at  $23\tau_j$ .

The standard deviation of the normal diffusion term is approximately twice that of the curvature term in the first quarter of the simulation, after which the discrepancy in the standard deviations becomes smaller. The standard deviation of the normal diffusion term is comparable to its mean value over the first half of the simulation. The combination of the location of the mean and the magnitude of the standard deviation indicates the extent to which the curvature and normal diffusion terms contribute to positive and negative  $v_\xi$ .

More detailed insight into the relationship between the various terms considered is obtained from the correlation coefficient. The stoichiometric correlation coefficient between pairs of terms is shown in Fig. 6.11. The correlation coefficient is defined as

$$\rho_{X,Y} = \frac{\langle XY \rangle - \langle X \rangle \langle Y \rangle}{\sigma_X \sigma_Y}, \quad (6.6)$$

where  $X$  and  $Y$  denote the variables of the correlation. The correlation between  $v_\xi$  and the normal diffusion term is strongly positive, having a value above 0.83 throughout the simulation, as the diffusive velocity of the stoichiometric mixture fraction iso-surface is

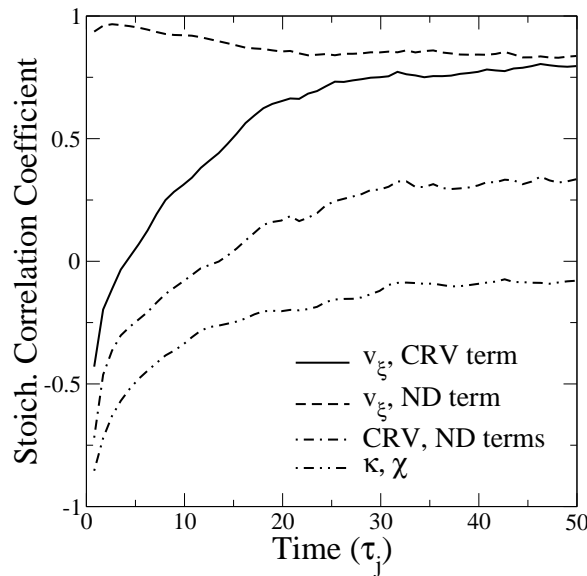


**Figure 6.11.** Stoichiometric correlation coefficient between various terms as a function of time.

directly influenced by turbulent straining in the flame-normal direction. The correlation coefficient of  $v_\xi$  and the curvature term is not as large as for  $v_\xi$  and the normal diffusion term. A positive correlation for  $v_\xi$  and the curvature corresponds to the flame moving (relative to convection) towards the fuel stream when the center of curvature is in the fuel stream. The correlation is initially negative as the jet develops, then increases continuously throughout the simulation. This rise in  $\rho_{v_\xi, CRV}$  is consistent with the increasing importance of the curvature term to  $v_\xi$ , compared with the normal diffusion term, indicated by comparing their means and standard deviations in Fig. 6.10. Except for an initial transient, the magnitude of the correlation coefficient between the curvature and normal diffusion terms directly is less than 0.33 throughout the simulation. The values of  $\rho_{v_\xi, CRV}$  and  $\rho_{v_\xi, ND}$  are higher than  $\rho_{CRV, ND}$  because the former two quantities include the correlation of the curvature and normal diffusion terms with themselves.

As noted, the mean curvature term in  $v_\xi$  is slightly negative throughout the simulation. However, the mean curvature,  $\kappa$ , of the stoichiometric surface is nearly zero. This difference is due to the temperature dependence of  $D_\xi$  and the location of  $\xi_{st}$ . When the flame has a negative curvature,  $\chi_{st}$  tends to be higher than when the flame has a positive curvature. These higher  $\chi_{st}$  with negative curvature result in a lower flame temperature and a lower  $D_\xi$ . The  $\chi$ - $\kappa$  relation at  $\xi_{st}$  results from the bias towards extensive strain of  $\xi \lesssim 0.5\xi_{max}$  with negative curvature. The correlation coefficient between  $\kappa$  and  $\chi$  on the stoichiometric mixture fraction surface increases from -0.5 at  $5\tau_j$ , to -0.08 at  $50\tau_j$ . Initially, the stoichiometric mixture fraction is 0.25, and the peak mixture fraction is unity. At  $50\tau_j$ , the peak in the mixture fraction PDF occurs at  $\xi = 0.5$ . The peak in  $\langle\chi|\xi\rangle$  occurs at  $\xi = 0.5$  and  $\xi = 0.35$  at  $t = 0$  and  $t = 50\tau_j$ , respectively. Hence, the magnitude of the correlation coefficient between curvature and scalar dissipation rate decreases as the position of the peak of  $\langle\chi|\xi\rangle$  approaches the stoichiometric mixture fraction.

### 6.2.6 Thermophoretic Diffusion Velocity

The conditional mean thermophoretic diffusion velocity  $\langle v_T|\xi\rangle$  and flame displacement velocity  $\langle v_\xi|\xi\rangle$  at four times are presented in Fig. 6.12. Here,  $v_\xi$  refers to the velocity at a given mixture fraction and not the stoichiometric surface. The scale of  $\langle v_T|\xi\rangle$  is a factor of 10 lower than the scale of  $\langle v_\xi|\xi\rangle$ , while the curves are of similar magnitude on the scale given. Hence, the thermophoretic velocity is much smaller than the differential diffusion velocity between the gas and the soot fields. The relatively low thermophoretic

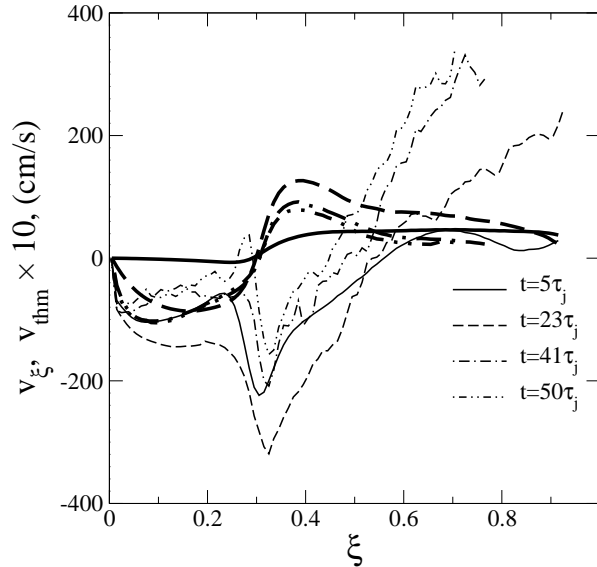


**Figure 6.12.** Conditional mean thermophoretic velocity (bold lines), and mixture fraction displacement velocity (thin lines) at four times.

diffusion velocity reinforces the presumption that soot is essentially convected with the flow field and that soot-mixture fraction transport may be quantified using  $v_\xi$ .

The curves of conditional mean  $v_\xi$  cross from negative to positive value close to  $\xi = 0.5$  at the times shown. Hence, isocontours of mixture fraction above  $\xi \approx 0.5$  are moving towards the fuel stream or, in other words, towards the jet center, and isocontours of mixture fraction below  $\xi \approx 0.5$  are moving towards the oxidizer stream as the jet spreads. As the jet evolves and mixing occurs, the crossover mixture fraction shifts towards smaller mixture fraction. In the negative  $v_\xi$  regions, the magnitude of  $v_\xi$  first increases, then decreases in time, whereas the magnitude of the positive regions increases with time. The value of  $v_\xi$  approaches zero as  $\xi$  approaches zero, that is, as the free oxidizer stream is approached. At the upper bound of  $\xi$ , the velocity is positive as the highest  $\xi$  isocontours move towards the jet center region, then merge, and are annihilated as oxidizer mixes into the core.

### 6.3 Discussion

The present simulation provides not only insight into soot formation and transport processes, but a database by which models of turbulent soot formation may be developed

and quantitatively validated.

The unsteady growth of soot that overlaps convective and diffusive timescales and the transport of soot in the mixture fraction coordinate are difficult problems in modeling soot formation in turbulent flames. The conditional moment closure (CMC) model solves unsteady transport equations for reactive scalars conditionally averaged on the mixture fraction [31]. CMC formulations have been developed that allow for differential diffusion of reactive scalars [145, 31, 146], and CMC modeling of turbulent sooting flames has been successfully applied [32]. In CMC, accurate modeling of transport of conditionally averaged scalars in the mixture fraction coordinate is important. In the conservation-form of the CMC formulation of Hewson et al. [146], the quantity  $|\nabla\xi|v_\xi$  appears directly in the differential diffusion term of the conditional mean transport equation for the soot moments. Here,  $|\nabla\xi|v_\xi$  has units of inverse seconds, or *mixture fraction* per second, and represents a diffusion velocity in the mixture fraction coordinate. Hence, the relative mixture fraction displacement velocity  $v_\xi$  has direct relevance to practical models of turbulent soot formation. An a-priori study of a CMC model is presented in Chapter 7.

This simulation represents a first step towards providing a detailed view of soot formation and transport in a turbulent flow, and as such, several concessions were made to limit computational costs. In order to resolve the time and lengthscales of the simulation with a fixed computational cost, the simulation time was limited to 1.1 ms. This relatively short duration, combined with the relatively high velocity of the jet and the increased stoichiometric mixture fraction, results in lower soot concentrations. The peak soot concentration observed in the present simulation is  $f_{v,peak} = 0.03$ , which is comparable to experimental values in methane flames [147]. In larger-scale configurations (e.g., fires), longer residence times occur for soot growth and radiative heat transfer, with significantly stronger soot-flame interactions expected. However, the basic interactions between soot and the flame due to differential transport influenced by the flame dynamics are expected to remain.

The present simulation describes the early-to-intermediate stages of the jet development and mixing. Near the end of the simulation, the (rich) peak of the mixture fraction PDF has mixed towards lower  $\xi$  and overlaps with the peak of the conditional mean soot mass fraction. In the process, the soot is being forced towards leaner mixture fraction, where oxidation will eventually occur. An important extension to the present work is the simulation of the latter portion of the jet mixing in which soot is transported fully into

the flame and burned out. Computational costs to reach this state from a developing jet as performed here are currently prohibitive. However, an initial condition could be constructed such that the entirety of the resultant jet development proceeds in the desired regime of jet mixing (e.g., from the desired intermediate jet composition and Reynolds number).

## CHAPTER 7

### FLAMELET AND CMC MODELING

Approaches for modeling turbulent combustion were presented previously in Chapter 1. When considering soot formation in modeling, care must be taken to account for features unique to the soot formation process, specifically, the longer soot formation timescales and the differential transport between soot and gaseous species. In this chapter, two models are considered: (1) the laminar flamelet model, and (2) the conditional moment closure model (CMC). Soot formation is introduced into the laminar flamelet model, and solutions and properties of the model are explored. The CMC model is evaluated using the DNS data in an a-priori fashion. That is, the DNS data are used to evaluate terms in the CMC equations. Here, the focus for both models considered is the transport of soot in the mixture fraction coordinate.

#### 7.1 Laminar Flamelets with Soot

The laminar flamelet model has been introduced in Chapter 1 and was used to initialize the DNS simulations. Discussion has been made on the limitations of the model, namely, that multidimensional effects are not accounted for. An important assumption in the derivation of the classic flamelet equations is that of unity Lewis numbers for all species. That is, all species are assumed to have the same diffusivity, equal to the thermal diffusivity.

The unity Lewis number constraint may be relaxed by dividing the diffusivity appearing in Eq. (1.11) by the species Lewis number. However, doing this does not conserve mass, as is readily evident by summing the equation over all species. Pitsch and Peters [140] have developed a flamelet formulation that treats differential species diffusion consistently and accurately. In their derivation, rather than define the mixture fraction as the local mass fraction of material that originated in the fuel stream (or in terms of centered and scaled linear combinations of conserved scalars), they define the mixture fraction in terms of a transport equation (here in one dimension):

$$\rho \frac{\partial \xi}{\partial t} + \rho v \frac{\partial \xi}{\partial y} - \frac{\partial}{\partial y} \left( \rho D_\xi \frac{\partial \xi}{\partial y} \right) = 0. \quad (7.1)$$

This mixture fraction loses its strict physical interpretation as defined in terms of linear combinations of conserved scalars (e.g., elemental mass fractions) in the absence of unity Lewis numbers and becomes simply a parameterizing variable.

Allowance for general transport in the flamelet coordinate is important for soot formation since soot has a very small (if not negligible) gradient-based diffusivity due to its large molecular weight, along with a substantial thermophoretic diffusion mechanism.

### 7.1.1 Soot Flamelet Formulation

The flamelet implementation of soot is as follows. Gaseous species are assumed to have unity Lewis numbers for convenience and the one-dimensional transport equation for soot is converted to a flamelet equation in mixture fraction space. The one-dimensional soot moment transport equation is given by

$$\rho \frac{\partial m_r}{\partial t} + \rho v \frac{\partial m_r}{\partial y} - \frac{\partial}{\partial y} \left( \rho D_p \frac{\partial m_r}{\partial y} \right) - \frac{\partial}{\partial y} \left( \frac{0.554\mu}{T} m_r \frac{\partial T}{\partial y} \right) - \dot{M}_r = 0. \quad (7.2)$$

Here,  $m_r$  is the  $r^{\text{th}}$  soot mass-moment divided by total (gas+soot) density,  $D_p$  is the soot particle diffusivity (assumed constant),  $\mu$  is viscosity, and  $\dot{M}_r$  is the moment source term. The soot diffusion term (term 3) is neglected from the outset. This equation is converted to mixture fraction space using the coordinate transformation rules

$$\frac{\partial}{\partial t} \rightarrow \frac{\partial}{\partial t} + \frac{\partial \xi}{\partial t} \frac{\partial}{\partial \xi}, \quad (7.3)$$

$$\frac{\partial}{\partial y} \rightarrow \frac{\partial \xi}{\partial y} \frac{\partial}{\partial \xi}. \quad (7.4)$$

This transformation follows from taking derivatives of  $\phi = \phi(t, \xi(t, y))$ . Applying the transformation to (7.2) gives

$$\rho \frac{\partial m_r}{\partial t} + \rho \frac{\partial \xi}{\partial t} \frac{\partial m_r}{\partial \xi} + \rho v \frac{\partial \xi}{\partial y} \frac{\partial m_r}{\partial \xi} - \frac{\partial \xi}{\partial y} \frac{\partial}{\partial \xi} \left( \frac{0.554\mu}{T} m_r \frac{\partial \xi}{\partial y} \frac{\partial T}{\partial \xi} \right) - \dot{M}_r = 0. \quad (7.5)$$

Now, the following term is added and subtracted:  $\frac{\partial m_r}{\partial \xi} \frac{\partial}{\partial y} \left( \rho D_\xi \frac{\partial \xi}{\partial y} \right)$ . Regrouping yields

$$\begin{aligned} & \frac{\partial m_r}{\partial \xi} \left[ \rho \frac{\partial \xi}{\partial t} + \rho v \frac{\partial \xi}{\partial y} - \frac{\partial}{\partial y} \left( \rho D_\xi \frac{\partial \xi}{\partial y} \right) \right] + \\ & \rho \frac{\partial m_r}{\partial t} + \frac{\partial m}{\partial \xi} \frac{\partial}{\partial y} \left( \rho D_\xi \frac{\partial \xi}{\partial y} \right) - \frac{\partial \xi}{\partial y} \frac{\partial}{\partial \xi} \left( \frac{0.554\mu}{T} m_r \frac{\partial \xi}{\partial y} \frac{\partial T}{\partial \xi} \right) - \dot{M}_r = 0. \end{aligned} \quad (7.6)$$

Using Eq. (7.1), the term in brackets cancels (note the cancellation of the convective term). Applying the transformation rules again to the physical space derivatives and rearranging gives

$$\rho \frac{\partial m_r}{\partial t} = - \frac{\partial m}{\partial \xi} \frac{\partial \xi}{\partial y} \frac{\partial}{\partial \xi} \left( \rho D_\xi \frac{\partial \xi}{\partial y} \right) + \frac{\partial \xi}{\partial y} \frac{\partial}{\partial \xi} \left( \frac{0.554\mu}{T} m_r \frac{\partial \xi}{\partial y} \frac{\partial T}{\partial \xi} \right) + \dot{M}_r. \quad (7.7)$$

In this equation, the definition of  $\chi$  in Eq. (1.12) is used to close the  $\frac{\partial \xi}{\partial y}$  terms:

$$\frac{\partial \xi}{\partial y} = \sqrt{\frac{\chi}{2D_\xi}}, \quad (7.8)$$

which is denoted  $\beta$ . Equation (7.7) can be massaged into the following form convenient for numerical solution:

$$\begin{aligned} \frac{\partial m_r}{\partial t} &= C \frac{\partial m_r}{\partial \xi} + S; \\ C &= \left[ \frac{0.554\mu}{\rho T} \beta^2 \frac{\partial T}{\partial \xi} - \frac{\beta}{\rho} \frac{\partial(\rho D_\xi \beta)}{\partial \xi} \right], \\ S &= \frac{m_r}{\rho} \left[ \beta \frac{\partial T}{\partial \xi} \frac{\partial}{\partial \xi} \left( \frac{0.554\mu\beta}{T} \right) + \beta^2 \frac{0.554\mu}{T} \frac{\partial^2 T}{\partial \xi^2} \right] + \frac{\dot{M}_r}{\rho}. \end{aligned} \quad (7.9)$$

This equation emphasizes that the soot moment flamelet equation is hyperbolic, with  $C$  taking the place of a velocity and  $S$  a source term. Casting the equations in this form allows proper (stable) discretization for numerical solution. The present approach is to use central differences on all derivatives appearing in brackets and upwind differencing on the convective derivative, using the sign of the coefficient  $C$  to determine whether to use and upwind or downwind derivative. If it is desired to keep the gaseous diffusion term in Eq. (7.2), it can be incorporated as follows. First, apply the transformation  $\frac{\partial}{\partial y} = \beta \frac{\partial}{\partial \xi}$  to the spatial derivatives and then apply the chain rule to obtain

$$\frac{1}{\rho} \frac{\partial}{\partial y} \left( \frac{\rho D_\xi}{Le_s} \frac{\partial m_r}{\partial y} \right) = \frac{\chi}{2Le_s} \frac{\partial^2 m_r}{\partial \xi^2} + \frac{\beta}{\rho Le_s} \frac{\partial m_r}{\partial \xi} \frac{\partial(\rho D_\xi \beta)}{\partial \xi}, \quad (7.10)$$

where, in the first term, Eq. (7.8) has been used, as well as assuming  $D_p = D_\xi/Le_s$ . This term can be added directly to Eq. (7.9) as term  $D$ , recognizing that the second term will contribute to the convective term in Eq. (7.9) and be small compared to the other convective terms, so it is neglected and a diffusion term would be given by

$$D = \frac{\chi}{2Le_s} \frac{\partial^2 m_r}{\partial \xi^2}. \quad (7.11)$$

Soot Lewis numbers are large as noted in Chapter 5 and the diffusion term can be safely neglected.

### 7.1.2 Results and Discussion

Figure 7.1 shows results of a flamelet calculation with soot. The soot model is that of Leung and Lindstedt [5], with two transported soot moments (soot mass fraction and number density). The results are at steady state using a detailed ethylene mechanism with 70 species and 463 reactions [95]. The flamelet equations represent an opposed jet flow with air and fuel at mixture fractions of zero and one, respectively. The scalar dissipation rate profile is given by Eq. (3.2), and plotted in Fig. 3.1. This dissipation profile corresponds to a cold opposed jet with the stagnation plane at the center. Thus, in the flamelet solution, the flame is located on the air side of the stagnation plane, and fluid streamlines are directed towards the stagnation plane through the flame. Soot is formed

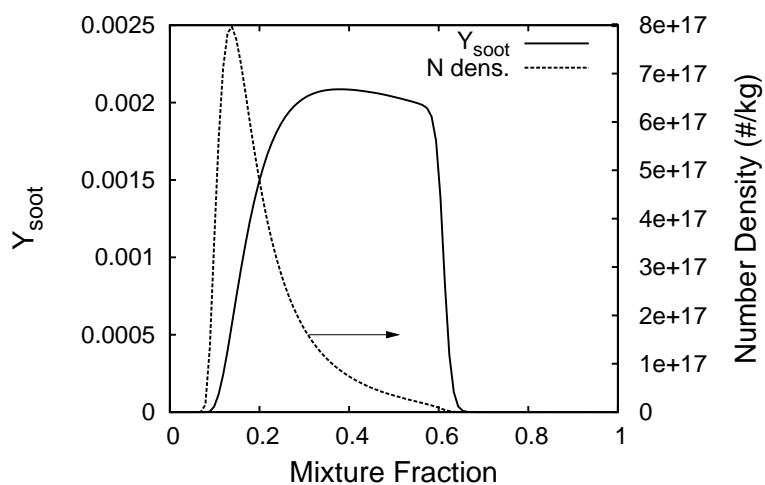


**Figure 7.1.** Steady flamelet soot mass fraction and number density profiles for a maximum  $\chi$  of  $100 \text{ s}^{-1}$  using the Leung and Lindstedt soot model and detailed ethylene chemistry.

on the rich side of the flame sheet and is primarily convected towards the stagnation plane. The thermophoretic diffusion velocity transports soot down the temperature gradient, in the direction of the stagnation plane at  $\xi = 0.5$ . However, since the negative temperature gradient persists past the fluid stagnation plane, soot is able to be transported beyond the stagnation plane where the particles stagnate at the so-called *particle stagnation plane*. Physically, this position occurs where the convective velocity or *wind*, coefficient  $C$  in Eq. (7.9), becomes zero. Figure 7.2 shows the velocity profiles  $C$ , with and without the thermophoretic velocity. Without the thermophoretic velocity,  $C$  crosses zero at  $\xi = 0.5$ , as expected.

The peak in the number density curve in Fig. 7.1 shows the location in the mixture fraction coordinate of the soot nucleation. As the soot diffuses and convects to higher mixture fractions, the number density decreases due to coagulation and a reduced nucleation rate corresponding to low temperatures away from the flame. The soot mass fraction begins low near the point of nucleation and rises to a broad plateau as soot growth occurs along with transport. At the particle stagnation plane, both profiles drop abruptly to zero.

Figure 7.3 compares the soot mass fraction at  $\chi_{max} = 100 \text{ s}^{-1}$  with diffusion via thermophoresis and with Brownian diffusion with a unity Lewis number given as in Eq. (1.11). Flamelet approaches that treat soot without thermophoretic diffusion but with the

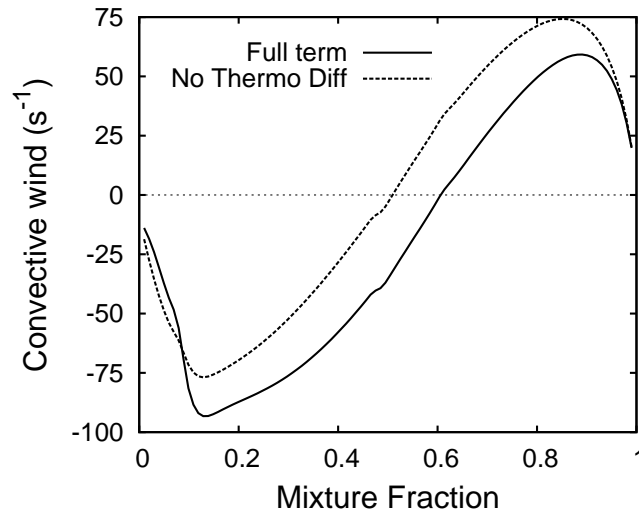


**Figure 7.2.** Soot flamelet equation convective wind with and without thermophoretic diffusion for  $\chi_{max} = 100 \text{ s}^{-1}$ .

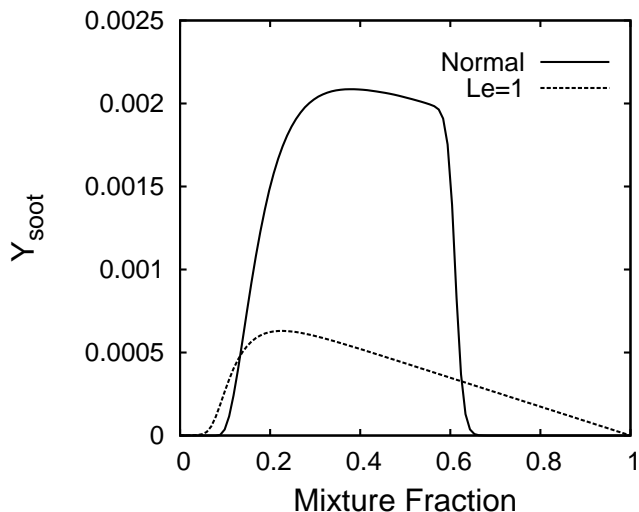


**Figure 7.3.** Comparison of soot profiles for unity Lewis number and thermophoretic diffusion for  $\chi_{max} = 100 \text{ s}^{-1}$ .

usual transport are qualitatively different. Most notably, no particle stagnation plane is observed and the soot mass fraction profile peaks near  $\xi = 0.2$  and decays approximately linearly to zero at the fuel stream. Oxidation prevents the soot from similar uniform decay from the peak toward the air stream at  $f = 0$ , and the soot is confined to the rich side of the flame where the oxidizer concentration (in this case oxygen) decays to zero. The  $Le = 1$  case allows soot at much leaner mixture fractions than the normal case. The soot level is also lower for the  $Le = 1$  case since formation rates compete with higher diffusion rates. At higher Lewis numbers, the soot profile is qualitatively the same but with a larger magnitude.

At higher scalar dissipation rates, the soot levels are reduced as higher dissipation rate implies higher transport of soot (convection) away from the flame zone, hence lower residence times for the relatively slow soot growth rate to form soot. This effect is shown in Figure 7.4, where the peak soot drops by three orders of magnitude for  $\chi_{max}$  ranging from 50 to  $1500 \text{ s}^{-1}$ , the latter being the limit of flame extinction.

Remarkably, the particle stagnation plane does not shift noticeably in the mixture fraction coordinate with increasing maximum scalar dissipation rate. This was unexpected since a higher dissipation rate implies a higher convection velocity. However, it also implies higher temperature gradients for soot diffusion. In the convection term in Eq. (7.9), the maximum scalar dissipation rate in the  $\beta$  factor multiplies both terms, so it cancels where the convective coefficient is zero. The dependence of the convective

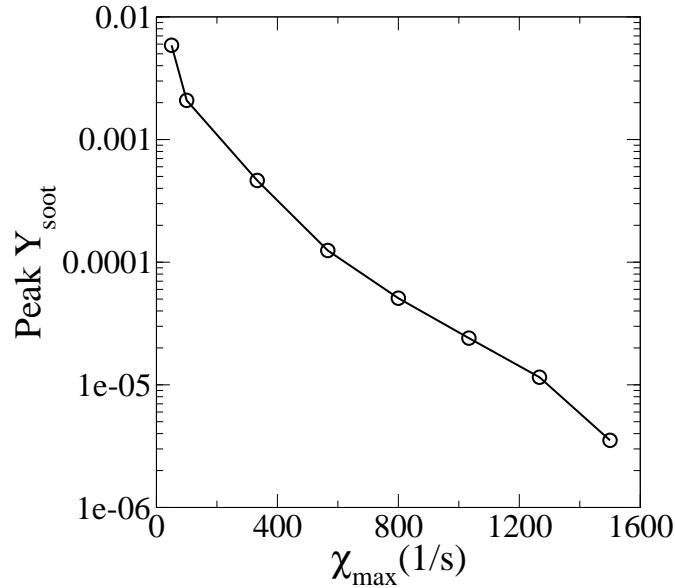


**Figure 7.4.** Effect of scalar dissipation rate on peak soot mass fraction.

coefficient on the peak dissipation rate is then through the dependence of temperature and composition profiles on the peak dissipation rate. In the convection coefficient, considering only temperature dependencies of viscosity, density, and diffusivity, the variation of the location of  $C = 0$  with  $\chi_{\max}$  should be small. Viscosity, density and diffusivity are approximately proportional to  $T^{0.5}$ ,  $T^{-1}$ , and  $T^{1.5}$ , respectively. Then, at  $C = 0$

$$\frac{1}{T} \frac{\partial T}{\partial \xi} (a + bT^{-0.25}) + c = 0 \quad (7.12)$$

is the criterion for locating the particle stagnation point. Here,  $a$ ,  $b$ , and  $c$  are composition-dependent constants. As the maximum dissipation rate is varied from zero to extinction, the peak temperature decreases from 2400 to 1800 K. The ratio of peak and minimum temperatures is 1.33. The corresponding ratio to the 0.25 power is 1.07, showing the small effect of the second term in the above equation. The temperature gradient coefficient variation is also small since it is normalized by the temperature. Figure 7.5 shows the convection coefficient for maximum scalar dissipation rates varying from 100 to 1500  $s^{-1}$ . The profiles are nearly identical except near the flame zone. The jog in the curves at  $\xi = 0.47$  is due to differentiating the mixture fraction diffusivity defined as  $\lambda/\rho C_p$ .

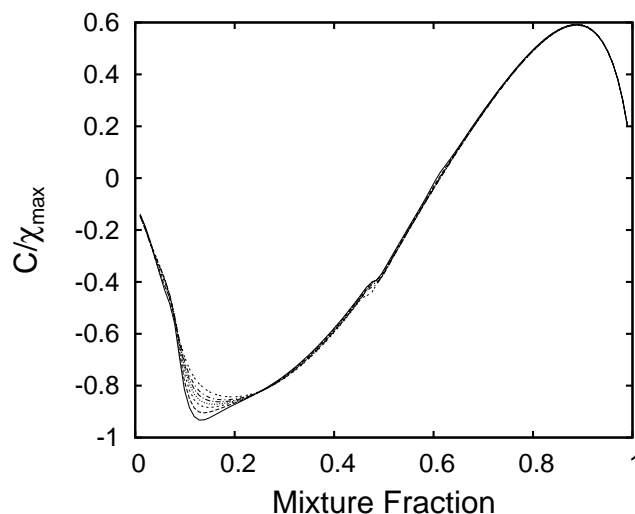


**Figure 7.5.** Variation of convective coefficient normalized by  $\chi_{max}$  versus mixture fraction for  $\chi_{max}$  ranging from 100 to 1500  $s^{-1}$ .

The tabulated heat capacity data from the Chemkin thermodynamic database have a discontinuous derivative of temperature at 1000 K which separates the high and low temperature curve fits.

These results show that the position of the particle stagnation plane in the mixture fraction coordinate is largely independent of the dissipation rate field. In flamelet models with soot, the soot cannot penetrate to mixture fractions larger than the position of the particle stagnation plane (PSP). Since soot is oxidized at the flame zone and always convected away from the flame zone for usual stream compositions, soot can also not exist lean of the soot production zone in the laminar flamelet model. Hence soot is effectively pinned to a specific band of mixture fraction. This is clearly in opposition to the DNS results presented in Chapters 5 and 6. In the presence of turbulent mixing, convolution over a PDF to obtain mean values would allow soot to occur at regions with mean mixture fractions greater than  $\xi_{PSP}$ , but this occurs at the turbulent mixing scale and not at the fine scales where chemical reaction occurs. Of course, it is possible to allow soot to be present in the pure streams or to set the boundaries of the flamelet to nonpure conditions, such as partially burned products. For example, in a real flame, a blob of sooty gas at  $\xi = 0.3$  could be surrounded by pure fuel; diffusion would result in a nearly  $\xi = 1$  mixture with soot.

It is well known in gas combustion that the boundary conditions of pure fuel and air are not always appropriate in real flames since flames may exist between air and

partially burned products or fuel and partially diluted air. The latter case implies partial premixing, which would occur in flames with extinction phenomena and the present arguments concern those in the flamelet regimes. This argument is valid only in as much as the maximum scalar dissipation rate affects the flow at a given mixture fraction. For example, consider a flow for which the peak scalar dissipation rate is constant, and the mixture fraction dependence of the scalar dissipation rate is given by Eq. (3.2). In this case, flames existing between, e.g., air and partially burned fuel are identical to those between pure air and fuel. Just take a given pure stream flamelet solution and draw a line at the mixture fraction of the partially burned fuel stream  $\xi_{pb}$ . The new flame between  $\xi = 0$  and  $\xi = \xi_{pb}$  is the same as for the pure streams. The assumption is that the partially burned boundary arises from a flamelet with pure streams, with the same maximum scalar dissipation rate and scalar dissipation rate profile. With soot formation, this scenario is complicated by the physical barrier of soot at the PSP in contrast to the realistic scenario in which soot may be present in more rich streams through non-flamelet-like mixing alluded to above.

## 7.2 Quantification of the Temperature Flamelet Equation

The classic flamelet equations described by Peters [25] and given by

$$\rho \frac{\partial Y_i}{\partial \tau} = \frac{\rho \chi}{2} \frac{\partial^2 Y_i}{\partial \xi^2} + \dot{m}_i''', \quad (7.13)$$

$$\rho \frac{\partial T}{\partial \tau} = \frac{\rho \chi}{2} \frac{\partial^2 T}{\partial \xi^2} - \sum_i \frac{h_i}{c_p} \dot{m}_i''', \quad (7.14)$$

have been applied extensively in turbulent combustion modeling. The temperature flamelet equation given above is approximate within the assumptions of the flamelet concept. Assuming constant pressure, no heat losses, and ignoring viscous dissipation and kinetic energy, the energy equation in physical space written in terms of the temperature is given by

$$\begin{aligned} \rho \frac{\partial T}{\partial t} + \rho v_i \frac{\partial T}{\partial x_i} - \frac{\partial}{\partial x_i} \left( \rho D \frac{\partial T}{\partial x_i} \right) = & - \sum_k \frac{h_k \dot{m}_k'''}{C_p} \\ & + \left[ \frac{\rho D}{C_p} \frac{\partial T}{\partial x_i} \frac{\partial c_p}{\partial x_i} + \frac{\rho D}{C_p} \sum_k \frac{\partial Y_k}{\partial x_i} \frac{\partial h_k}{\partial x_i} \right]. \end{aligned} \quad (7.15)$$

Before this equation is transformed to the mixture fraction coordinate to yield Eq. (7.13), the terms in brackets in Eq. (7.15) are often ignored. These terms arise from the heat flux term in the energy equation, specifically from the thermal conduction term. To quote Peters [25, p. 322]: “For approximate solutions, the last two terms in [Eq. (7.15)] are in general neglected as being small compared to the source term.” If the bracketed terms are not ignored, the following *exact* temperature flamelet equation is obtained:

$$\rho \frac{\partial T}{\partial \tau} = \rho \frac{\chi}{2} \frac{\partial^2 T}{\partial \xi^2} - \sum_k \frac{h_k}{c_p} \dot{m}_k''' + \left[ \frac{\chi \rho}{2c_p} \frac{\partial T}{\partial \xi} \frac{\partial c_p}{\partial \xi} + \frac{\chi \rho}{2c_p} \sum_k \frac{\partial Y_k}{\partial \xi} \frac{\partial h_k}{\partial \xi} \right]. \quad (7.16)$$

In the literature, several forms of the energy equation are used including

- the exact form of the temperature equation, e.g., [29],
- the approximate form of the temperature equation, e.g., [148],
- and enthalpy formulations, e.g., [41, 149].

In this section the neglect of the bracketed terms in Eq. (7.15) is quantified by comparing the results of the steady temperature flamelet equation given above with the exact energy equation, written in terms of enthalpy. With a unity Lewis number assumption and no heat losses, enthalpy is a known function of the mixture fraction given simply as

$$h(\xi) = h_{\xi=1}\xi + (1 - \xi)h_{\xi=0}. \quad (7.17)$$

With enthalpy known and composition computed, temperature may be inverted from  $h = h(T, Y_i)$ , as given in Chapter 1. It is found that the neglect of the bracketed terms in Eq. (7.15) is reasonable in the reaction zone, but that large errors occur outside of the main combustion zone, resulting in substantial error in the temperature-mixture fraction profile and failure to conserve energy.

The flamelet equations are solved as described in Chapter 3 by integration of the unsteady equations to steady state. Spatial derivatives are approximated with second-order central differences on uniform grids of 1000 points in the mixture fraction coordinate. The scalar dissipation rate is computed from Eq. (3.2). Two versions of the flamelet code

are used: the first solves the temperature flamelet equation given above, Eq. (7.14), and the second computes temperature from the known enthalpy profile. The solutions from both formulations were shown to satisfy their respective forms of the steady temperature flamelet equations, given above, in a separate postprocessing step.

A flamelet with streams of pure air ( $\xi = 0$ ) and pure hydrogen ( $\xi = 1$ ) at 1 atm pressure and 298.15 K was computed with a stoichiometric scalar dissipation rate ( $\chi_{st}$ ) of  $1 \text{ s}^{-1}$ . Figure 7.6 shows profiles of the resulting temperature for the approximate and exact energy equations. The temperature error at the stoichiometric point of  $\xi = 0.0281$  is 66 K, while the peak error at  $\xi = 0.29$  is 916 K. The shapes of the temperature profiles are significantly different and the maximum error is very large. However, the error at the stoichiometric point is only 3%. Similar results are obtained for hydrogen at other scalar dissipation rates. At  $\chi_{st} = 45.2 \text{ s}^{-1}$  the stoichiometric temperature for the exact formulation is 1583 K with the stoichiometric temperature for the approximate equation 44 K less. The peak temperature difference is 685 K at  $\xi = 0.31$ . The temperature maximum and mixture fraction for the exact case are at 1607 K and  $\xi = 0.039$ , with the approximate case higher in both values by 90 K and  $\Delta\xi = 0.024$ , respectively. The stoichiometric extinction dissipation rates of  $100 \text{ s}^{-1}$  differed by 3% for the two formulations.

In addition to the hydrogen case, a methane-air case at  $\chi_{st} = 1 \text{ s}^{-1}$  was performed. The temperature difference at the stoichiometric point ( $\xi = 0.0552$ ) was 78 K, while the

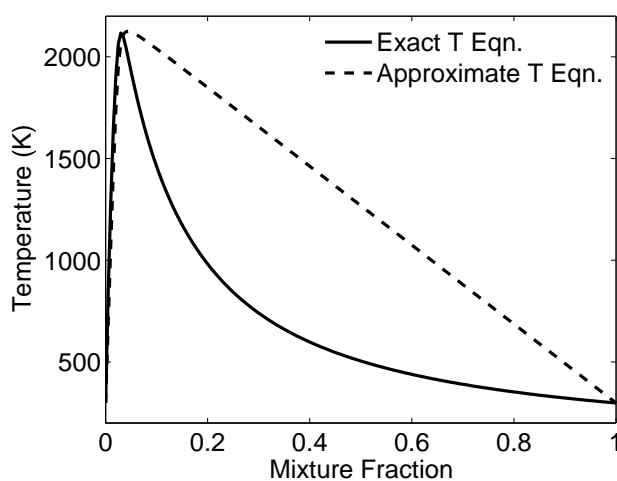


**Figure 7.6.** Flamelet temperature profiles at a stoichiometric scalar dissipation rate of  $1 \text{ s}^{-1}$  for hydrogen combustion.

peak temperature difference was 271 K at  $\xi = 0.39$ .

Figure 7.7 shows a comparison of the four terms in the exact temperature flamelet equation over a part of the mixture fraction domain. At larger mixture fractions the profiles decay smoothly to zero. In the region of the stoichiometric point, the dissipation rate term is nearly balanced by the reaction rate term with the extra terms contributing little. This explains the similarity in the temperature profiles of the exact and approximate equations in that region. However, at a mixture fraction of about 0.05, the reaction term has decayed nearly to zero, while the other terms remain. The temperature dissipation term is balanced nearly equally by the other two terms which each account for 50% of the dissipation term. The linearity of the temperature profile in Fig. 7.6 for the approximate temperature equation is a result of the reaction term being zero, hence at steady state, requiring the dissipation term to be zero, which occurs when the curvature of the temperature profile is zero.

While temperature errors are relatively small near the stoichiometric point using the approximate formulation, the errors away from stoichiometric are significant. Several applications of flamelets will suffer from the approximate energy formulation, such as environments with significant chemical kinetics in the rich region. Soot rates peak around a mixture fraction of 0.2 and are very sensitive to temperature. Convolution of flamelet tables over a mixture fraction and possibly scalar dissipation rate and/or the heat loss

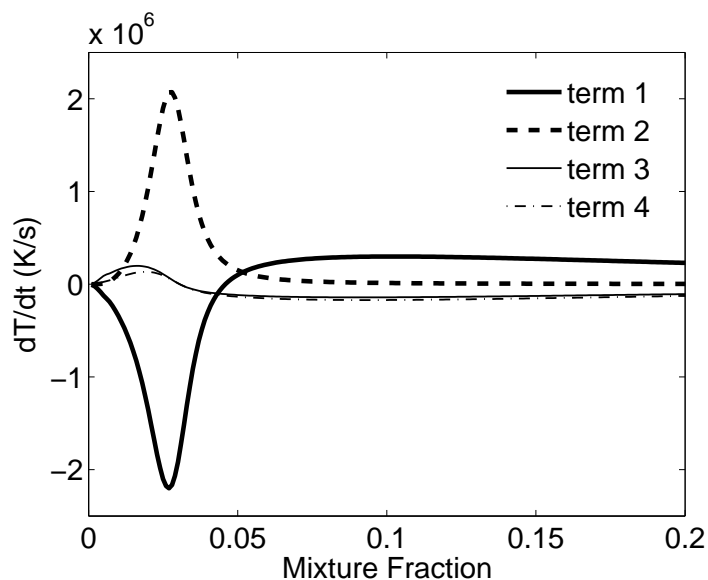


**Figure 7.7.** Budget of terms in the temperature flamelet equation given in Eq. (7.16).

joint PDF in turbulence modeling will result in the effects of the temperature profile throughout the flamelet being felt by a mean quantity dependent upon the mixture fraction. For example, considering only mixture fraction dependence,

$$\bar{\phi} = \int_0^1 \phi(\xi)P(\xi)d\xi, \quad (7.18)$$

where  $\phi$  is some scalar quantity dependent on mixture fraction, such as temperature, and  $P(\xi)$  is the mixture fraction PDF. Even for a stoichiometric mean mixture fraction, the temperature error may be large if the variance of the PDF is wide enough to access mixture fractions of high temperature error. In addition, the deviation of the enthalpy from the exact linear profile that occurs when using the approximate temperature flamelet equation is a significant fraction of the sensible enthalpy and will have adverse effects on subgrid heat losses, which may be incorporated into a flamelet model for use in an LES or RANS simulation. For these reasons, the flamelet model should only be implemented with the exact temperature equation or with an equivalent enthalpy equation.

### 7.3 A-Priori Analysis of CMC Modeling

In Chapters 5 and 6, soot transport was investigated using DNS. Differential soot diffusion was shown to result in strong transport in the mixture fraction coordinate. The relatively long formation timescale of soot and the well-known lack of a simple state relationship with the mixture fraction complicate modeling of turbulent sooting flames.

The conditional moment closure model was introduced in Chapter 1 and is a promising model for simulation of soot formation and transport in turbulent flames. CMC is an elegant and general model that solves unsteady transport equations for reactive scalars that are conditionally averaged on given values of mixture fraction [31, 150]. The conditional mean scalars, along with a description of the mixture fraction PDF, allows a solution of the mean flow. This conditioning allows more accurate closure of nonlinear reactive source terms since conditional fluctuations are smaller than unconditional ones. Since CMC deals directly with transport in physical space and the mixture fraction coordinate, turbulent transport of soot in this coordinate may be treated directly. The success of the CMC model depends on closure models for terms in the derived CMC equations. DNS data are ideal for model development and evaluation since detailed flow structure is available, and CMC terms can be evaluated a-priori in their unclosed and closed forms.

One of the major challenges of CMC modeling is the accurate treatment of differentially diffusing species. This is an inherent difficulty since the mixture fraction itself, which is the conditioning variable, relies on the absence of strong differential diffusion for its definition. This inconsistency is generally ignored, however, and corrections for differential diffusion are incorporated into the species and enthalpy transport equations. Kronenburg and Bilger [145] have developed a CMC formulation allowing for differential diffusion of chemical species, but the formulation requires solution of additional transport equations to solve for restorative terms associated with the differential diffusion. CMC accounting for differential diffusion has been applied to the problem of soot formation in nonpremixed flames [32]. Hewson et al. [146] have recently presented a new CMC formulation for soot formation accounting for differential diffusion that does not require the solution of additional transport equations, which significantly reduces the computational costs of the model. Their model was developed for application to fires with large quantities of soot formation. The model was tested a-priori using the one-dimensional turbulence model. Since differential diffusion of soot is much stronger than that of other gaseous species, only differential diffusion of soot is considered. In applications with high levels of soot formation, significant conversion of gaseous carbon to soot can result. This complicates the definition of the mixture fraction as noted above. To minimize this effect, all scalars are conditioned on a gas-only mixture fraction. This mixture fraction is no longer a conserved scalar, but by conditioning on the gas-only mixture fraction, the difference is only the addition of a reactive source term accounting for conversion of gaseous carbon to soot mass. Details of this model can be found in [146].

In this section, the three-dimensional DNS simulation presented in Chapter 6 is used to study the CMC formulation developed by Hewson et al. A budget of selected terms in the CMC equations is presented for soot species and also gaseous species. Closure models for the considered terms are compared to the unclosed terms in the equations. Here, the gas-only mixture fraction formulation is not required since soot concentrations are low and represent a small fraction of the gaseous carbon in the system.

### 7.3.1 CMC Formulation

The CMC equations considered in this paper are derived from the joint species PDF equation following Klimenko [31]. The dependence of conditional quantities on the nonhomogeneous cross-stream direction is neglected here, so that all spatial derivatives

of conditional quantities are neglected. This is a common assumption in CMC modeling of jet diffusion flames [32, 151].

A brief description of the CMC model derivation is presented below. A more detailed derivation is given in Appendix D. One begins by taking the average of the transport equation for the multidimensional fine-grain PDF by integrating over the multidimensional sample space to obtain the joint PDF transport equation. The transport equation for the fine grain PDF is given by

$$\begin{aligned} \frac{\partial \rho \psi}{\partial t} + \nabla \cdot (\rho \vec{v} \psi) + \frac{\partial}{\partial Z_i} (\psi \nabla \cdot (\rho D_i \nabla Y_i)) = \\ - \frac{\partial}{\partial Z_i} (\psi \omega_i) - \frac{\partial}{\partial Z_i} (\psi \nabla \cdot (\rho^{-1} D_{T,i} Y_i \nabla \ln T)). \end{aligned} \quad (7.19)$$

Here,  $\psi$  is the fine grain PDF,  $w_i$  is a reaction source term,  $\rho$  is density,  $\mathbf{v}$  is velocity,  $T$  is temperature,  $D$  is a diffusivity,  $Y_i$  is a species random variable (including mixture fraction and soot mass-moments divided by density), and  $Z_i$  is its sample space variable. Index notation is used (but  $D_i$  refers directly to  $Y_i$  with no implied summation). The last term is the thermophoretic term and is assumed zero for all species except soot moments. The third term is the diffusion term and is rearranged significantly in the derivation.

The diffusive term is split into two terms: (1) a term with all diffusivities equal, and (2) a correction to this:

$$\begin{aligned} \frac{\partial}{\partial Z_i} (\psi \nabla \cdot (\rho D_i \nabla Y_i)) = \frac{\partial}{\partial Z_i} (\psi \nabla \cdot (\rho D \nabla Y_i)) + \\ \frac{\partial}{\partial Z_i} (\psi \nabla \cdot (\rho (D_i - D) \nabla Y_i)). \end{aligned} \quad (7.20)$$

The derivation then proceeds as in the constant diffusivity case, and the correction term is brought along directly, with no additional rearrangement. The first term on the right-hand side (RHS) is replaced according to the identity

$$\frac{\partial}{\partial Z_i} (\psi \nabla \cdot (\rho D \nabla Y_i)) = \frac{\partial}{\partial Z_i} \frac{\partial}{\partial Z_j} (\psi \rho D \nabla Y_i \cdot \nabla Y_j) - \nabla \cdot (\rho D \nabla \psi). \quad (7.21)$$

The term on the far RHS of this equation is replaced with the identity

$$\nabla \cdot (\rho D \nabla \psi) = \nabla^2 (\rho D \psi) - \nabla \cdot (\psi \nabla (\rho D)). \quad (7.22)$$

The resulting equation is averaged over the sample space to obtain the joint PDF transport equation:

$$\begin{aligned}
\frac{\partial \langle \rho | \mathbf{Z} \rangle P}{\partial t} + \nabla \cdot (\langle \rho \vec{v} | \mathbf{Z} \rangle P) &= - \frac{\partial}{\partial Z_i} (\langle \omega_i | \mathbf{Z} \rangle P) \\
&- \frac{\partial}{\partial Z_i} (\langle \nabla \cdot (\rho^{-1} D_{T,i} Y_i \nabla \ln T) \rangle P) \\
&- \frac{\partial}{\partial Z_i} (\langle \nabla \cdot (\rho (D_i - D) \nabla Y_i) | \mathbf{Z} \rangle P) \\
&- \frac{\partial}{\partial Z_i} \frac{\partial}{\partial Z_j} (\langle \rho D \nabla Y_i \cdot \nabla Y_j | \mathbf{Z} \rangle P) \\
&+ \nabla^2 (\langle \rho D | \mathbf{Z} \rangle P) - \nabla \cdot (\langle \nabla (\rho D) | \mathbf{Z} \rangle P).
\end{aligned} \tag{7.23}$$

The terms on the RHS are a reaction term, a thermophoretic diffusion term, a differential diffusion term, a diffusion term and two terms arising from the diffusion term (which are normally neglected at high Reynolds number [31]).

The joint PDF equation is multiplied by one of the  $Z_i$  (say  $Z_k$ ) and integrated over all  $Z_i$  except for  $\eta$ , where  $\eta$  is the sample space variable for mixture fraction,  $\xi$ . This results in the transport equation for conditionally averaged scalars, the CMC equation. Here, the identity of the diffusivity  $D$  must be determined, and different results are obtained with different choices. Setting  $D$  equal to the thermal diffusivity is a popular choice. Hewson et al. [146] set  $D$  equal to the species under consideration (that is,  $D = D_i$  corresponding to  $Z_k$ ). The resulting equation for soot mass fraction is

$$\begin{aligned}
\frac{\partial \langle \rho Y_s | \eta \rangle P_\eta}{\partial t} + \nabla \cdot (\langle \rho Y_s \vec{v} | \eta \rangle P_\eta) &= \langle \omega_{Y_s} | \eta \rangle P_\eta \\
&+ \langle \nabla \cdot (\rho Y_s D_{T,i} \nabla \ln T) | \eta \rangle P_\eta \\
&- \frac{\partial}{\partial \eta} (\langle \nabla \cdot [\rho (D_\xi - D_s) \nabla \xi] Y_s | \eta \rangle P_\eta) \\
&- \frac{\partial^2}{\partial \eta^2} (\langle \rho D_s (\nabla \xi)^2 Y_s | \eta \rangle P_\eta) \\
&+ \frac{\partial}{\partial \eta} (\langle 2 \rho D_s (\nabla Y_s \nabla \xi) | \eta \rangle P_\eta) \\
&+ \nabla^2 (\langle \rho D_s Y_s | \eta \rangle P_\eta) - \nabla \cdot (\langle \nabla (\rho D_s Y_s) | \eta \rangle P_\eta).
\end{aligned} \tag{7.24}$$

This equation can be rewritten in terms of other chemical species mass fractions instead of soot by a simple change of notation and by ignoring the thermophoretic term. When

soot is considered, its diffusivity is so small that terms multiplying  $D_s$  can be neglected. In that case, the differential diffusion term has the form

$$\frac{\partial}{\partial \eta} (\langle \nabla \cdot [\rho D_\xi \nabla \xi] Y_s | \eta \rangle P_\eta) = - \frac{\partial}{\partial \eta} (\langle Y_s \rho | \nabla \xi | v_\xi | \eta \rangle P_\eta). \quad (7.25)$$

Here, the quantity  $|\nabla \xi| v_\xi$  is a diffusion velocity with units of inverse seconds or, rather, with units of *mixture fraction* per second. The differential diffusion term is physically the divergence of soot mass flux in the mixture fraction coordinate. The form of Eq. (7.25) is exactly analogous to the more common diffusion term in physical space. The analogy is shown here as

$$j_x = \frac{\partial}{\partial x} (\rho Y_k V_x), \quad (7.26)$$

$$j_\eta = \frac{\partial}{\partial \eta} (\langle \rho Y_k \hat{v}_\xi | \eta \rangle P_\eta), \quad (7.27)$$

where  $\hat{v}_\xi$  is  $|\nabla \xi| v_\xi$ . In the first equation, the divergence is in physical space of the product of a mass density of species  $Y_k$  and a diffusion velocity in the physical space. In the second equation (ignoring the cross-correlations in the conditional variables),  $\langle \rho | \eta \rangle P_\eta \langle Y_k | \eta \rangle$  is a mass density in the physical and mixture fraction space (that is, mass per meter cubed per unit mixture fraction), and  $\hat{v}_\xi$  is a velocity in the mixture fraction coordinate.

Most of the terms in Eq. (7.24) are unclosed. In this section, comparison of the magnitudes of the transport terms on the RHS of Eq. (7.24) is made, along with closure models for three of these terms. Following the primary closure hypothesis of Klimenko and Bilger [31], closures of the differential diffusion (DD) term, the dissipation-scalar (DS) term, and the cross-dissipation (CD) term (which are terms 3, 4, and 5, respectively, on the RHS of Eq. (7.24)), are obtained [146]:

$$DD: \quad - \frac{\partial}{\partial \eta} (\langle \nabla \cdot [\rho (D_\xi - D_s) \nabla \xi] Y_s | \eta \rangle P_\eta) \approx - \frac{\partial}{\partial \eta} \left( \frac{(D_\xi - D_s)_\eta \rho_\eta M_\eta Q_s}{(D_\xi)_\eta} P_\eta \right), \quad (7.28)$$

$$DS: \quad - \frac{\partial^2}{\partial \eta^2} (\langle \rho D_s (\nabla \xi)^2 Y_s | \eta \rangle P_\eta) \approx - \frac{\partial^2}{\partial \eta^2} \left( \frac{\rho_\eta \chi_\eta (D_s)_\eta Q_s}{2 D_\xi} P_\eta \right), \quad (7.29)$$

$$CD: \quad \frac{\partial}{\partial \eta} (\langle 2 \rho D_s (\nabla Y_s \nabla \xi) | \eta \rangle P_\eta) \approx \frac{\partial}{\partial \eta} \left( \frac{\rho_\eta \chi_\eta (D_s)_\eta}{(D_\xi)_\eta} \frac{\partial Q_s}{\partial \eta} P_\eta \right). \quad (7.30)$$

In this equation, a subscript  $\eta$  is short for  $\langle \cdot | \eta \rangle$ ,  $Q_s$  denotes the conditional mass fraction of soot (or other species), and  $M_\eta$  is defined as

$$M_\eta = \frac{1}{\rho_\eta} \langle \nabla \cdot (\rho D_\xi \nabla \xi) | \eta \rangle. \quad (7.31)$$

These closures arise chiefly from the neglect of cross-correlations among conditional quantities, that is, by assuming  $\langle ab | \eta \rangle \approx \langle a | \eta \rangle \langle b | \eta \rangle$ .

### 7.3.2 Results

The CMC terms, unclosed in Eq. (7.24) and closed in Eqs. (7.28)-(7.30), are evaluated from the raw DNS data by conditionally averaging using 100 bins in the mixture fraction coordinate. The conditional data are relatively smooth, but derivatives, especially second derivatives, are very noisy. A filter that removes high wavenumber content containing little energy was applied to the raw conditional data for which derivatives in the mixture fraction coordinate were taken.

#### 7.3.2.1 Soot Mass Fraction Equation

Figure 7.8 shows a comparison of three key terms on the RHS of Eq. (7.24) for the soot mass fraction at times of  $t = 25\tau_j$  and  $t = 50\tau_j$ . The terms shown are the reaction source term, the differential diffusion term, and the thermophoretic diffusion term. Spatial derivatives of conditional mean quantities are not considered, and the soot diffusivity is equal to zero. The magnitude of the terms at the later time is higher because the PDF of the mixture fraction is higher in the reactive regions as the combustion products expand and fuel and oxidizer mix. In addition, the peak  $\langle Y_s | \eta \rangle$  at  $t = 50\tau_j$  is approximately five times the value at  $t = 25\tau_j$ . At a given time, the reaction and differential diffusion terms are of similar magnitudes, showing the importance of both terms. The thermophoretic term, however, has a much smaller magnitude and this term does not contribute significantly to the conditional soot transport equation. These results are consistent with comparisons between the diffusive velocity of the mixture fraction and thermophoretic diffusion velocity shown in Chapters 5 and 6.

The dual peaks in the differential diffusion term near the stoichiometric point arise from a small peak in the mixture fraction PDF at this point. Near this location, flow dilatation and temperature (hence, kinematic viscosity) are high and the local Reynolds number is lower, reducing mixing rates. This peak coincides with a depression in the

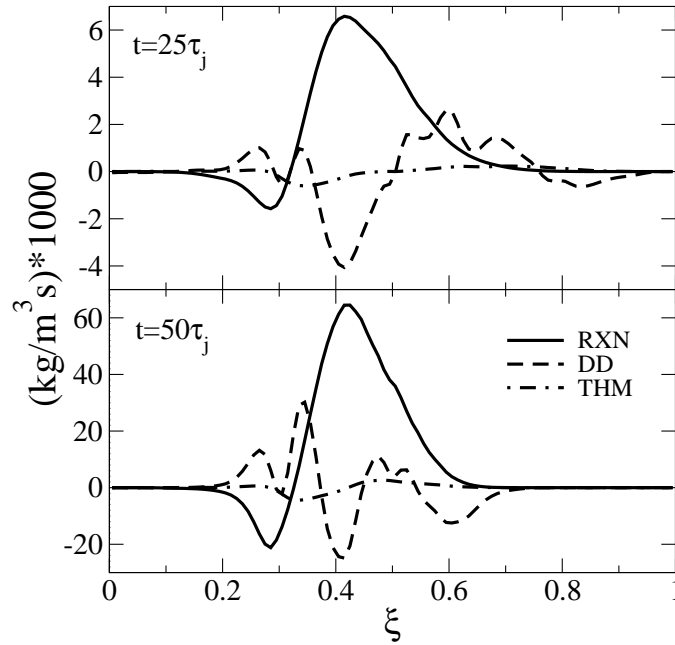


**Figure 7.8.** CMC terms for conditional soot mass fraction equation at two times.

conditional mean scalar dissipation rate. The mixture fraction PDF and conditional mean scalar dissipation rate are shown in Fig. 7.9.

Figure 7.10 shows the differential diffusion term for soot mass fraction, as well as the model approximation for this term, given in Eq. (7.28). The DD term and its model are of similar magnitudes overall. The agreement between the two terms is good at very rich mixture fractions. However, at intermediate mixture fractions and near the flame zone, large differences exist. Hewson et al. [146] noted this discrepancy and proposed a model for the residual DD term, representing the error between the exact term and its modeled approximation. The model is based on a turbulent diffusion process in mixture fraction space and is given by

$$RDDM \approx \frac{\rho_\eta \chi_\eta P_\eta}{2Le_{DD,t}} \frac{\partial^2 Q_s}{\partial \eta^2}, \quad (7.32)$$

where  $Le_{DD,t}$  is an effective turbulent Lewis number. The  $RDD$  term is also plotted in Fig. 7.10 plot (a), as the dash-dot line. In Fig. 7.10 plot (b), the DD term is plotted along with the sum of the modeled DD term and modeled residual DD term. Here  $Le_{DD,t}$  was set to a value of 3.0 to give reasonable agreement between the curves. The sum of the model and residual terms is observed to reproduce the qualitative shape of the exact

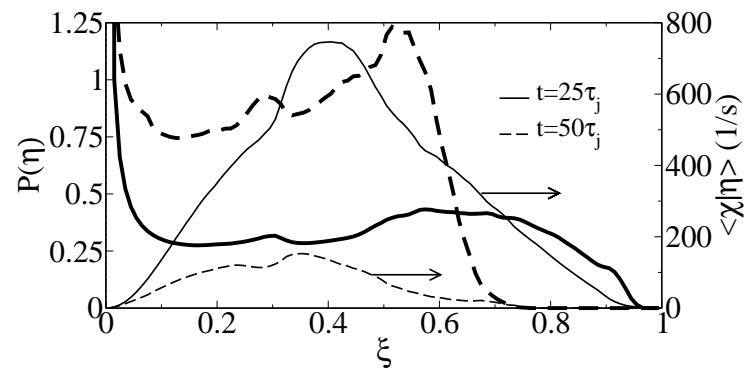


**Figure 7.9.** PDF of mixture fraction (bold lines) and conditional mean scalar dissipation rate (thin lines) at two times.

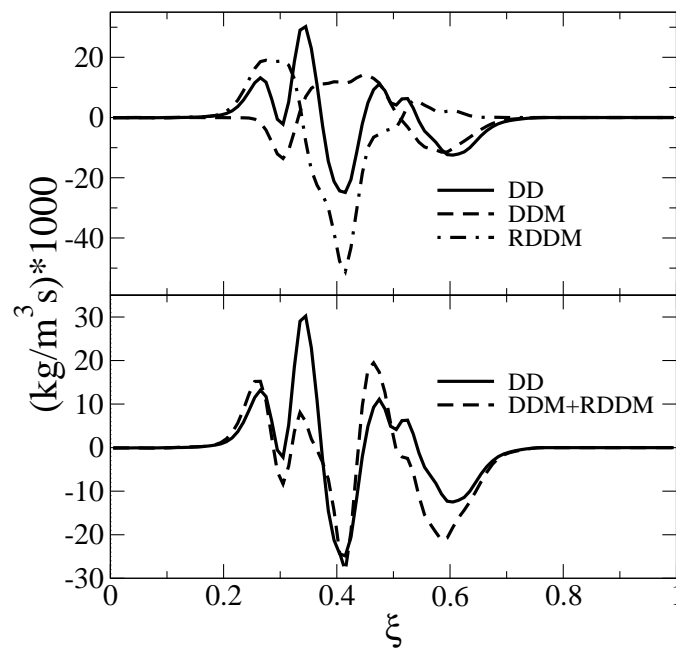


**Figure 7.10.** Plots of differential diffusion term and its models for the soot mass fraction CMC equation at  $t = 50\tau_j$ .

DD term throughout the whole mixture fraction domain. The quantitative agreement is also remarkably good, consistent with previous results [146].

### 7.3.2.2 Gaseous Species

The CMC transport equation is applicable to gaseous species as well as soot, with a change of notation:  $D_s$  and  $Y_s$  refer now to the species mass fractions instead of soot mass fractions. Whereas the soot diffusivity is practically zero, the species diffusivities are significant, and the fourth and fifth terms on the RHS of Eq. (7.24) are present in the balance equation. The thermophoretic term is neglected for gaseous species, however. It is noted that the model for species diffusion fluxes used in S3D is not exactly the same as the model used in the CMC transport equations, and a slight discrepancy arises. In an a-priori simulation, the composition fields can be analyzed without regard to the physical mechanism in which the fields were obtained, but absolute consistency between the model and the DNS data is not obtained. The mixture averaged transport model used in S3D is given by

$$\begin{aligned} \mathbf{j}_i &= -\frac{\rho Y_i}{X_i} D_i \nabla X_i, \\ &= -\rho D_i \left( \nabla Y_i + \frac{Y_i}{W_t} \nabla W_t \right), \end{aligned} \quad (7.33)$$

where  $X_i$  is the mole fraction, and  $W_t$  is the mean molecular weight. For the ethylene fuel, however, the fuel and oxidizer streams have nearly the same mean molecular weight, and there is no change in the number of moles for complete combustion of the fuel. Hence, the  $W_t$  field is approximately constant, and the gradient of  $W_t$  is neglected here.

The upper plots of Fig. 7.11 show the exact CMC terms of Eq. (7.24) for reactive scalars  $\text{CO}_2$ , OH, and H, at  $t = 50\tau_j$ . For each gaseous species, the four terms shown are of similar magnitudes in all regions of the mixture fraction coordinate; hence all terms are important to the CMC transport equation of the given species. The differential diffusion term is quite small for OH but significant for  $\text{CO}_2$  and H. The cross-dissipation and dissipation-scalar terms tend to oppose and balance one another for each of the species throughout most of the mixture fraction domain, as previously observed [146].

A comparison of the exact and modeled CMC terms is given in the middle and lower plots of Fig. 7.11 for species  $\text{CO}_2$ , OH, and H. For each species, the center plot contains the dissipation-scalar and cross-dissipation terms, along with their modeling closures.

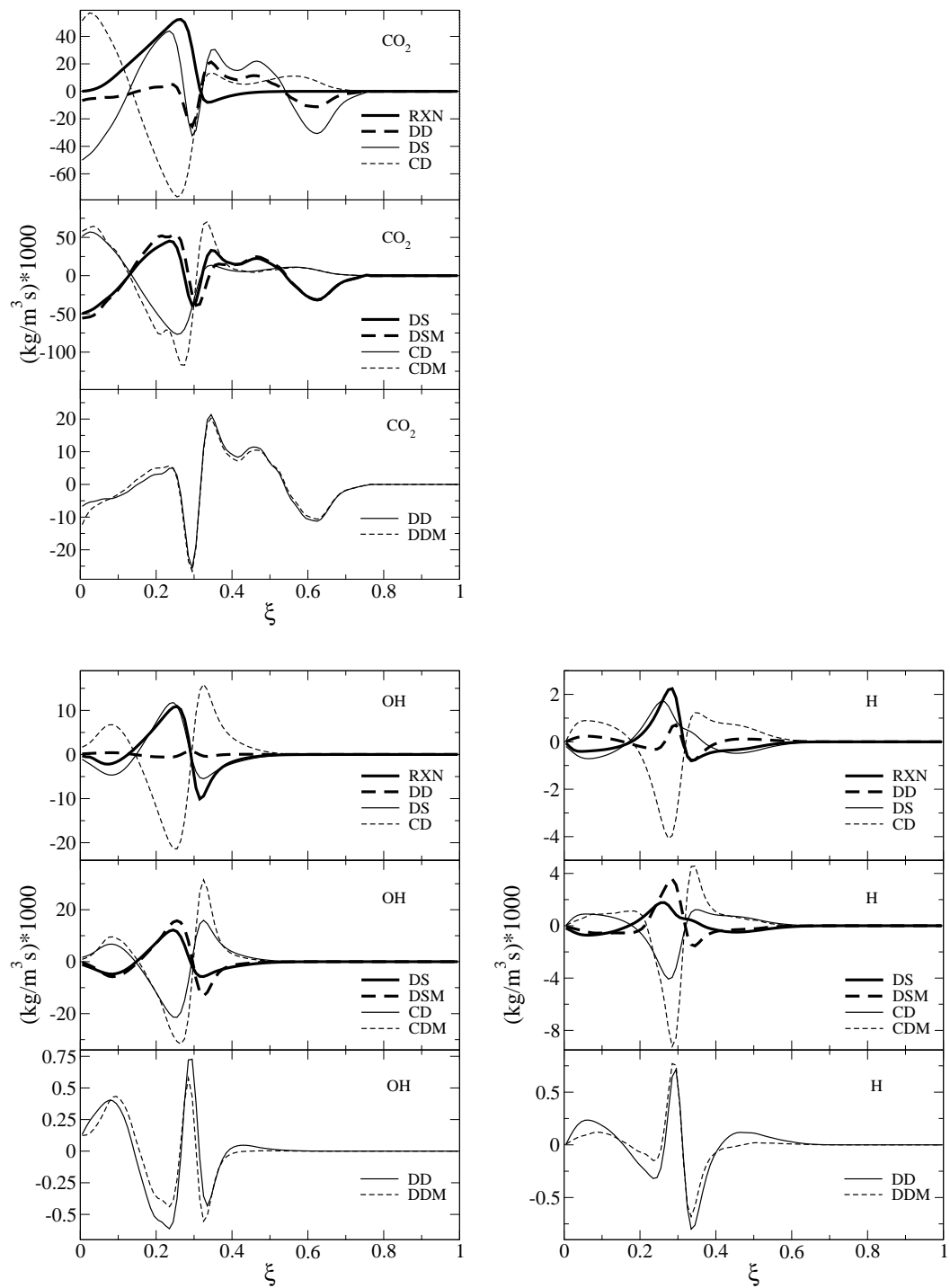


**Figure 7.11.** Plots of exact and modeled CMC terms for  $\text{CO}_2$ , OH, and H.

The lower plots show the differential diffusion term and its model. The DS and CD models show the right trend for each of the species and reasonably good quantitative agreement for species  $\text{CO}_2$  and OH. The modeled CS and DS terms do not agree as well for H, however.

The DD term and its model similarly show a good qualitative trend over the mixture fraction domain for each of the species and the two curves are reasonably close in magnitude. The discrepancies between the modeled and exact terms are due to the neglect of cross-correlations between the products of quantities making up the terms since this assumption is made in deriving the modeled terms. The model for the differential diffusion term of gaseous species, DDM in Eq. (7.28), is remarkably accurate, in contrast to the soot mass fraction, and the model for the residual of the differential diffusion model of the gaseous species is not required. This is likely a direct consequence of the relatively fast chemistry of the gaseous reactions. These species have relatively low conditional standard deviations, as previously shown. The fast chemistry allows these species to relax to new conditional values quickly as they are transported in the mixture fraction coordinate, precluding the need for the additional residual model.

## CHAPTER 8

### CONCLUSIONS AND FUTURE WORK

In this chapter, a summary of major results and conclusions drawn from the DNS studies presented previously is given. Direct numerical simulation of combustion with soot formation is a new contribution to the field of numerical simulation and opportunities for future studies are presented.

#### 8.1 DNS of Soot Formation and Transport

A series of DNS simulations of nonpremixed ethylene flames were conducted in configurations of increasing complexity. These included one-dimensional simulations of a relaxing diffusion flame, two-dimensional simulations of a laminar mixing layer and decaying isotropic turbulence, and a three-dimensional simulation of a temporally evolving jet flame. The simulations represent the first extension of DNS to soot formation in configurations with realistic combustion chemistry and a complex fuel: ethylene. The focus of the work has been on fundamental mechanisms of soot transport in turbulent flames.

##### 8.1.1 One-Dimensional Simulations

The one-dimensional simulations provided insight into soot formation in a trivial configuration. The simulations allowed comparison of convective and mixture fraction velocities in an unstrained configuration. The convective velocity arising from flame expansion alone was found to be significant. The simulation showed that the effect of radiation on soot concentration and temperature is important, but only at timescales greater than approximately 10 ms. For this reason, the optically thin radiation model is adequate for DNS simulations restricted to small simulation times.

##### 8.1.2 Two-Dimensional Mixing Layer Simulations

The two-dimensional mixing layer simulations showed the importance of soot transport in the mixture fraction coordinate as soot was convected away from its formation

region into the vortex structures. These results showed how soot transport, and hence soot concentrations are influenced directly by coherent turbulent structures. The simulations also showed the importance of flame expansion and heat release on the mixing characteristics of the flames. Specifically, the inability of the flame to penetrate the small-scale vortex was highlighted. The exclusion of the flame from the eddy prompted investigation of flame dynamic effects that were used to understand soot formation in the turbulent simulations that followed.

### 8.1.3 Two-Dimensional Decaying Turbulence Simulations

The two-dimensional decaying turbulence simulations provided great insight into the importance of soot transport in the mixture fraction coordinate. The analysis made use of the diffusion velocity of isocontours of the mixture fraction relative to convection. The expression for this velocity was decomposed into a multidimensional curvature term and a one-dimensional normal diffusion term. It was shown that the normal diffusion term could be written in terms of the scalar dissipation rate, providing a link between the scalar dissipation rate and the flame displacement velocity. Several important results are summarized below:

- The location of soot relative to a flame, as measured by the mixture fraction, has a strong impact on the local concentrations of soot, the rates of soot reaction, and the soot temperatures.
- Soot spreads over mixture fractions from 0.1-0.8, with mass fractions ranging from 0-0.22 (approximately 2 ppmv). This broad spread of soot was shown to result from its differential diffusion with respect to the gaseous species.
- Soot transport is primarily governed by fluid convection and thermophoresis. In the turbulent simulations, fluid convection dominates soot thermophoresis (by a factor of about 10) and soot is mainly convected with the flow. The flame displacement velocity and fluid convective velocity is of the same order of magnitude. The soot-flame position is given by the relative motion between the flame surface and the fluid motion.
- The flame displacement velocity was computed and the soot concentrations were found to peak where the flame displacement velocity is zero or positive—i.e., where

the flame moves towards the soot.

- The flame displacement velocity was derived from two terms: a normal diffusion term, present in all flames, and a curvature term, present only in multidimensional flames. Both terms were shown to be important. Since the stoichiometric mixture fraction is low ( $\xi_{st} = 0.064$ ) in the two-dimensional simulation, normal diffusion generally moved the flame toward the air stream, away from soot. The curvature term augments the flame displacement velocity so that flames curved towards the fuel stream have a flame displacement velocity shifted towards the fuel stream, while the converse occurs for flames curved toward the air stream.
- Low levels of soot-flame breakthrough were also observed in regions of high flame curvature.
- While soot mass fraction showed a high degree of scatter in magnitude and mixture fraction, temperature showed very little scatter, and soot reaction rates were sharply located in the mixture fraction coordinate. These observations have been known and used by others in modeling turbulent sooting flames, but the influence of differential soot transport due to multidimensional flame effects should be accounted for to accurately predict flame radiation and soot emission.

#### 8.1.4 Three-Dimensional Temporal Jet Simulation

The analysis of the two-dimensional simulation was also applied in the three-dimensional simulation. Furthermore, the three-dimensional simulation is physically more realistic than two-dimensional turbulence and allowed the gathering of turbulence statistics to quantify the importance of the flame dynamic analysis. The temporal jet configuration is also a more realistic configuration that is more relevant to turbulent combustion in realistic environments.

The major conclusions of the two-dimensional simulations remain unchanged in going to three dimensions. An important effect not observed in the two-dimensional simulations is the competition between turbulent soot transport towards higher mixture fractions and the reduction in peak mixture fraction through bulk mixing of the fuel and oxidizer streams. This is due, in part, to the relatively shorter turbulence timescales imposed in the three-dimensional DNS, as well as the greater mixing rates in three-dimensional turbulence. In addition, as the jet evolves, the normal diffusion component of the flame

displacement velocity, which is almost exclusively negative in the two-dimensional case, is substantially positive in the jet configuration. Several key findings are reported below:

- The turbulent flame yields a lognormal probability density function of scalar dissipation rate with a negative skewness in agreement with nonreacting experimental data and reacting DNS results.
- Motion of soot in the mixture fraction coordinate arises from differential diffusion between soot and mixture fraction, as well as the bulk effect of mixing of the fuel jet core.
- The curvature and normal diffusion terms of  $v_\xi$  were computed and found to be of similar magnitude and of either sign. As the jet evolved, the curvature PDF remained centered at zero, while the positive fraction of the normal diffusion term progressively increased, resulting in an increase in the fraction of positive  $v_\xi$ .
- A substantial portion of the  $\xi_{st}$  surface (nearly 50% towards the end of the simulation) had  $v_\xi > 0$ . In these regions soot is convected towards the flame, which is the opposite of what occurs in canonical opposed jet or flamelet configurations commonly used in modeling.
- The thermophoretic velocity was again found to be lower than  $v_\xi$  by an order of magnitude over the range of  $\xi$ , indicating that thermophoretic effects are small compared to differential diffusion effects between gaseous species and soot.

## 8.2 Flamelet and CMC Modeling

Soot formation and transport were implemented in a laminar flamelet model, which can (and has) been used in RANS and LES modeling of nonpremixed combustion. The flamelet formulation incorporated the thermophoretic diffusion of soot, with numerical behavior distinct from the usual flamelet equations with unity Lewis numbers. The soot transport equation that results is an unsteady, convection (in mixture fraction-space) and reaction equation. Thermophoresis was found to move the particle stagnation plane away from the intrinsic stagnation plane at  $\xi = 0.5$ , which is built into the imposed scalar dissipation rate profile. In the flamelet model, soot is convected away from the flame zone and is effectively pinned to a zone of mixture fraction between the location of soot formation and the particle stagnation plane. The location of the particle stagnation plane was shown to be insensitive to the scalar dissipation rate.

The three-dimensional DNS were used to conduct an a-priori study of a new CMC model for soot transport. A comparison of important terms in the CMC equations was made. The flame displacement velocity  $v_\xi$  was shown to arise naturally in the formulation and appeared, as expected, in the differential diffusion term between soot and the mixture fraction. For soot transport, the reaction and differential diffusion terms were of similar magnitudes while the thermophoretic term was much smaller. The analysis was also applied to gaseous species, of which three were considered. The balance of the unclosed terms for the gaseous species showed that the dissipation-scalar, cross-dissipation, differential diffusion, and chemical reaction terms all were important. In each case, the cross-dissipation and dissipation-scalar terms opposed and partially cancelled one another. This behavior highlights the importance of considering not just individual terms but collections of terms when applying closure models. For instance, it may be difficult to find accurate closures for individual terms, but these closures may not be needed if collections of terms are small. This is an area in which DNS analysis can be invaluable.

Closure models for transport terms were applied that neglect cross-correlations of conditional products of terms. The model for the differential diffusion term of the gaseous species was quite accurate, whereas the models for the cross-dissipation terms, while qualitatively correct, tended to overshoot the unclosed terms. In contrast, the differential diffusion model for soot was rather poor, but when augmented by a model for the residual, the results were quite accurate. This result is very encouraging for the prospects of modeling turbulent soot formation using CMC.

### 8.3 Future Work

The DNS simulations presented in this work are the first of their kind. They were developed with two goals: (1) to provide fundamental insight into turbulent soot formation and transport, and (2) to provide a database by which models can be tested and developed. Because of the high computational cost of the simulations, the number and complexity of the simulations were limited. Future simulations would benefit by several extensions and additions:

- The incorporation of more complex gas and soot chemistry. Gas chemistry that included PAH formation, even if only with semiempirical or global steps, would lend confidence to the soot nucleation processes. More complex soot models could

be applied. These would include detailed growth mechanisms, such as the HACA mechanism, in which the influence of H atoms, with strong differential diffusion of its own, may play a role. An oxidation mechanism directly including the effects of OH oxidation, rather than implicitly including its effects, would be useful.

- Longer simulation run times would better accommodate the slower soot formation processes, but at a higher computational cost. For low-Mach environments with acoustic, rather than chemical restrictions on timestep size, the DNS would benefit from the use of acoustic scaling to increase the possible timestep size for accurate and stable solution.
- The configurations investigated consist of the early to intermediate stages of burnout of the fuel stream. Additional simulations that explore the later, burnout portion of the flame in which the peak mixture fractions are lower and soot is forced towards the flame zone where it oxidizes would be of great interest. Computational costs for this situation could be minimized by initializing a domain with stream compositions and turbulence that correspond to an intermediate stage of development of a turbulent flame.
- Presently, no experimental results are available in the parameter space accessible to DNS. This is unfortunate since it precludes direct comparison with experimental data. Generally, DNS simulations are well resolved and solve transport equations and chemistry that are reliable and accurate. Soot chemistry and the modeling of the particle size distribution is less precise, but a long-term goal would be to do turbulent simulations that could be compared directly with experiment, preferably with both simulation and experiment progressing together to a region of good overlap in the parameter space (domain size, Reynolds number, etc.).
- The importance of flames and fires requires accurate combustion models that can accurately capture known physics (such as soot-flame breakthrough). The development of cost-effective turbulence models that can incorporate relevant physics and a willingness to fund research to achieve these goals are important for progress of the science and its potential benefits for real-world applications.

## APPENDIX A

### FINITE DIFFERENCE PROGRAM

```
%%%%%%%%%%%%%%%%%%%%%%%%%%%%%%%%%%%%%%%%%%%%%%%%%%%%%%%%%%%%%%%%%%%%%%%%%
% Finite difference approximations to arbitrary order derivatives %
% using arbitrary stencils. %
% %
%  $d^n u = \frac{1}{\Delta x^n} \sum_k a_k u_k$  %
% ----- * sum_k( a_k * u_k ) %
%  $d x^n \quad \Delta x^n$  %
% %
% As an example, a second order central second difference: %
%  $d^2 u/dx^2 = 1/dx^2 * (a_{(j-1)}u_{(j-1)} +$  %
%  $a_{(j)}u_{(j)}+a_{(j+1)}u_{(j+1)})$  %
% with a_u's are 1 -2 1 %
% I assume here that j=0 is the base point. %
% %
% INPUT: nder -- is order of the derivative to be approximated. %
% npts -- is number of points in the stencil %
% (at least nder+1). %
% jb -- is the position of the base point in the stencil %
% OUPUT: a_u -- are the coefficients of the grid points %
% order -- is the order of the method %
% (Note a hardwired max order and tolerance) %
%%%%%%%%%%%%%%%%%%%%%%%%%%%%%%%%%%%%%%%%%%%%%%%%%%%%%%%%%%%%%%%%%%%%%%%%%

clc; clear;

nder = input('Enter order of derivative to approximate: ');
npts = input('Enter # of points in stencil (min is nder+1): ');
jb = input('Enter position of the base point in stencil: ');

jp = 1-jb:npts-jb; % indx of grd pnts of u (eg j-1, j, j+1)

j=1:npts; % compute the FD approximation
for k=1:npts
    a_kj(k,j) = (jp(j).^(k-1))./factorial(k-1);
end
b = zeros(npts,1);
b(nder+1) = 1;
a_u = inv(a_kj)*b;
a_u = a_u';
```

```
                                % check the order
for k=nder+2:100
    aa(j) = (jp(j).^(k-1))./factorial(k-1);
    if(abs(sum(aa.*a_u)) > 1.0E-10)
        break;
    end
end

                                % output the results
disp(' ');
disp('grid_position, coefficient');
disp([jp' a_u']);
order = k-nder-1
```

## APPENDIX B

### PRODUCT DIFFERENCE ALGORITHM

```
% Product Difference Algorithm for use with the quadrature  
% method of moments (QMOM)
```

```
function absc_wts = pd( M )  
n = size(M); n = n(1,1);  
N = n/2;  
mu = M;  
mu = mu/mu(1);  
ms = mu(2);  
i=[2:n]';  
mu(i) = mu(i)./ms.^(i-1);  
P = zeros(n+1,n+1);  
P(1,1) = 1;  
i=[1:n]';  
P(i,2) = mu.*(-1).^(i-1);  
for j=3:n+1  
    for i=1:n-j+3-1  
        P(i,j) = P(1,j-1)*P(i+1,j-2) - P(1,j-2)*P(i+1,j-1);  
    end  
end  
alph =zeros(n,1);  
alph(1) = 0;  
i=[2:n]';  
alph(i) = P(1,i+1)./(P(1,i).*P(1,i-1));  
i=[1:N]';  
a=zeros(N,1);  
b=a;  
a(i) = alph(2*i) + alph(2*i-1);  
i=[1:N-1]';  
b(i) = sqrt(alph(2*i+1).*alph(2*i));  
J=diag(a,0) + diag(b(1:N-1),1) + diag(b(1:N-1),-1);  
[V, x] = eig(J);  
absc_wts = [diag(x) [V(1,:).^2]'*M(1)];  
absc_wts(:,1) = absc_wts(:,1)*ms;
```

## APPENDIX C

### MIXING LAYER INSTABILITY

This appendix details the specification of the velocity perturbations applied to the two-dimensional mixing layer simulations to trip the Kelvin-Helmholtz instability. Linear stability theory is applied to the initial tanh velocity profile assuming incompressible, inviscid flow. The treatment follows that given by Michalke [152]. The initial velocity profile is given by

$$u(y) = \frac{\Delta U}{2} \tanh(\sigma y), \quad (\text{C.1})$$

where  $\sigma = 2/\delta$ , and  $\delta$  is the characteristic width of the tanh transition.

The velocity field is cast in terms of a stream function  $\psi$ , where

$$u = \frac{d\psi}{dy}, \quad (\text{C.2})$$

$$v = -\frac{d\psi}{dx}. \quad (\text{C.3})$$

Here, take  $\psi_1$  to be the stream function of the velocity perturbation mode. Then  $\psi_1$  is assumed to be of the form

$$\psi_1(x, y, t) = \Re[\phi(y)e^{i\alpha(x-ct)}], \quad (\text{C.4})$$

where  $c$  and  $\phi$  are complex, and  $\alpha$  is real. Here,  $\alpha$  is the wavenumber of the disturbance, and the real and imaginary parts of  $c$ :  $c_r$ , and  $c_i$ , are the phase velocity and an amplification factor, respectively. This can be observed by partially expanding Eq. (C.4) to

$$\psi_1(x, y, t) = \Re[\phi(y)e^{-i\alpha(x-c_r t)}e^{\alpha c_i t}]. \quad (\text{C.5})$$

Clearly,  $c_i$  acts as an amplification factor to the travelling wave given by the oscillatory term. For temporally evolving mixing layers, the phase velocity  $c_r$  is zero; otherwise it is equal to the mean velocity. The goal is to find the complex function  $\phi(y)$  and to maximize the product  $\alpha c_i$ . Also, since we are looking for the initial velocity perturbation, the results are applied at  $t = 0$ . In Michalke's derivation,  $\Delta U$  and  $\sigma$  were not explicitly considered (i.e., they would have been implicitly taken as unity).

First, Eqs. (C.2)-(C.4) are substituted into the Euler equation of motion to give the so-called Rayleigh stability equation:

$$[u_b - c][\phi'' - \alpha^2\phi] - u_b''\phi = 0. \quad (\text{C.6})$$

In this equation, second-order terms involving the disturbance have been ignored (hence the *linear* stability theory). Also,  $\phi$  is seen to be an eigenfunction of the differential operator, with  $c = c(\alpha)$  the eigenvalue. This eigenvalue is solved as follows. First, set

$$\phi = \exp\left(\int \Phi dy\right), \quad (\text{C.7})$$

which, on substitution into Eq. (C.6) gives the so-called Riccati equation in  $\Phi(y)$ :

$$\Phi' = \alpha^2 - \Phi^2 + \frac{u_b''}{u_b - c}. \quad (\text{C.8})$$

The boundary conditions for this equation are given as  $\Phi(+\infty) = -\alpha$ , and  $\Phi(-\infty) = +\alpha$ , which follow from  $\phi$  decaying to zero as  $y \rightarrow \pm\infty$ . This equation is simplified by changing variables from  $y$  to  $z$  as

$$z = \tanh(y), \quad (\text{C.9})$$

so that the integration interval changes from  $y = \pm\infty$  to  $z = \pm 1$ . Equation (C.8) becomes

$$\frac{d\Phi}{dz} = \frac{\alpha^2 - \Phi^2}{1 - z^2} - \frac{2z}{z - 2ic_i}. \quad (\text{C.10})$$

The real and imaginary components are separated to yield

$$\frac{d\Phi_r}{dz} = \frac{\alpha^2 - \Phi_r^2 + \Phi_i^2}{1 - z^2} - \frac{2z^2}{z^2 + (2c_i)^2}, \quad (\text{C.11})$$

$$\frac{d\Phi_i}{dz} = \frac{2\Phi_r\Phi_i}{1 - z^2} - \frac{4c_i z}{z^2 + (2c_i)^2}, \quad (\text{C.12})$$

with boundary conditions given by

$$\Phi_r(1) = -\alpha, \quad (\text{C.13})$$

$$\Phi_r(-1) = +\alpha, \quad (\text{C.14})$$

$$\Phi_i(1) = 0, \quad (\text{C.15})$$

$$\Phi_i(-1) = 0. \quad (\text{C.16})$$

In Eqs. (C.11)-(C.12), the derivatives are undefined at the boundaries, so L'Hospital's rule is applied to give

$$\left. \frac{d\Phi_r}{dz} \right|_{z=+1} = -\frac{2}{(\alpha + 1)(1 + (2c_i)^2)}, \quad (\text{C.17})$$

$$\left. \frac{d\Phi_r}{dz} \right|_{z=-1} = -\frac{2}{(\alpha + 1)(1 + (2c_i)^2)}, \quad (\text{C.18})$$

$$\left. \frac{d\Phi_i}{dz} \right|_{z=+1} = -\frac{4c_i}{(\alpha + 1)(1 + (2c_i)^2)}, \quad (\text{C.19})$$

$$\left. \frac{d\Phi_i}{dz} \right|_{z=-1} = \frac{4c_i}{(\alpha + 1)(1 + (2c_i)^2)}. \quad (\text{C.20})$$

Here,  $\Phi_r$  and  $\Phi_i$  are antisymmetric and symmetric functions, respectively, so the integration interval is taken from -1 to 0, and  $c_i$  is found by iterating on its value until the boundary conditions

$$\Phi_r(0) = 0, \quad (\text{C.21})$$

$$\left. \frac{d\Phi_i}{dz} \right|_{z=0} = 0, \quad (\text{C.22})$$

are satisfied. Here, satisfying one of these conditions satisfies the other. Equations (C.11)-(C.12) were integrated with Matlab, where  $c_i$  was converged in an outer loop implementing linear extrapolation.

The solution of the Ricatti Eq. (C.8) was solved to obtain  $c_i$  for various values of  $\alpha$ , and the maximum value of  $c_i\alpha$  was obtained, hence  $\alpha$ . Figure C.1 is a plot of  $c_i\alpha$  versus  $\alpha$ .

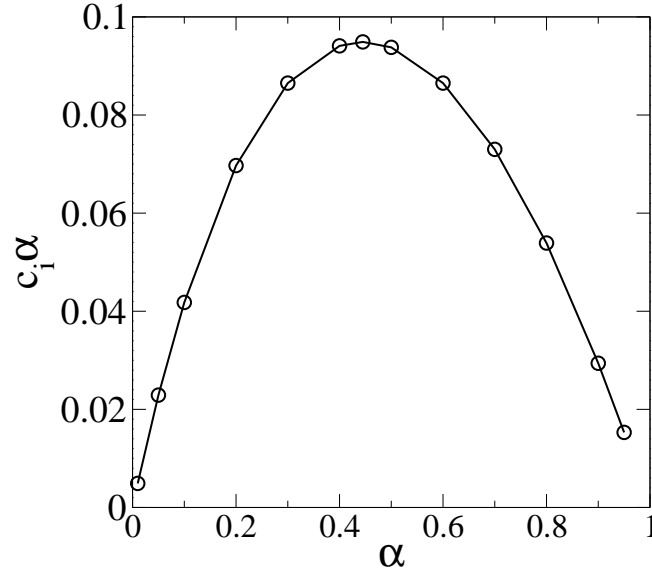


**Figure C.1.** Plot showing the most unstable mode (peak) of the inviscid tanh velocity profile.

The peak occurs at  $\alpha = 0.444918$ , which is the most unstable mode. The corresponding period is  $P = 2\pi/\alpha$ . Figure C.2 shows the real and imaginary functions  $\Phi_r$  and  $\Phi_i$  for the most unstable mode.

With  $c_i$  and  $\alpha$  known, the solution of the Rayleigh equation is computed. Again Eq. (C.6) is

$$\frac{d^2\phi}{dy^2} = \frac{u_b''\phi}{u_b - c} + \alpha^2\phi. \quad (\text{C.23})$$

To solve this equation, it is first converted into two first-order equations using  $\gamma = d\phi/dy$  to yield

$$\frac{d\phi}{dy} = \gamma, \quad (\text{C.24})$$

$$\frac{d\gamma}{dy} = \frac{u_b''\phi}{u_b - c} + \alpha^2\phi. \quad (\text{C.25})$$

These are expanded into their real and imaginary parts with  $c_r = 0$  to give

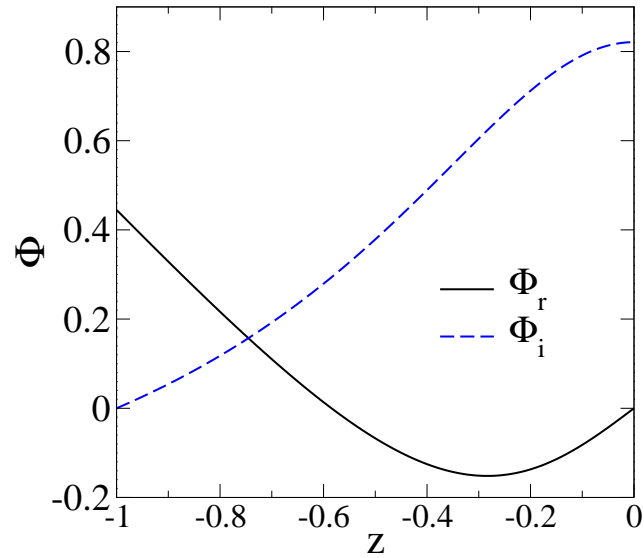


**Figure C.2.** Solution to the Riccati equation  $\Phi(z)$  for the most unstable mode.

$$\frac{d\phi_r}{dy} = \gamma_r, \quad (\text{C.26})$$

$$\frac{d\phi_i}{dy} = \gamma_i, \quad (\text{C.27})$$

$$\frac{d\gamma_r}{dy} = \frac{u_b''(u_b\phi_r - c_i\phi_i)}{u_b^2 + c_i^2} + \alpha^2\phi_r, \quad (\text{C.28})$$

$$\frac{d\gamma_i}{dy} = \frac{u_b''(u_b\phi_i - c_i\phi_r)}{u_b^2 + c_i^2} + \alpha^2\phi_i. \quad (\text{C.29})$$

The boundary conditions for these equations are

$$\phi_r(0) = 1, \quad \gamma_r(0) = 0, \quad (\text{C.30})$$

$$\phi_i(0) = 1, \quad \gamma_i(0) = \Phi_i(0), \quad (\text{C.31})$$

and the integration is carried out to some large  $y$ . The boundary conditions for  $\gamma$  here follow from Eq. (C.7), so the solution to the Riccati equation is needed for the boundary condition  $\gamma_i(0) = \Phi_i(0)$  in the Rayleigh equation. Figure C.3 shows the resulting solutions for  $\phi_r$ , and  $\phi_i$ . Since  $\phi_r$  is symmetric about zero and  $\phi_i$  is antisymmetric, the solution on the half-domain is sufficient. These two functions were curve fit in the regions above and below  $y = 3$  using the relations:

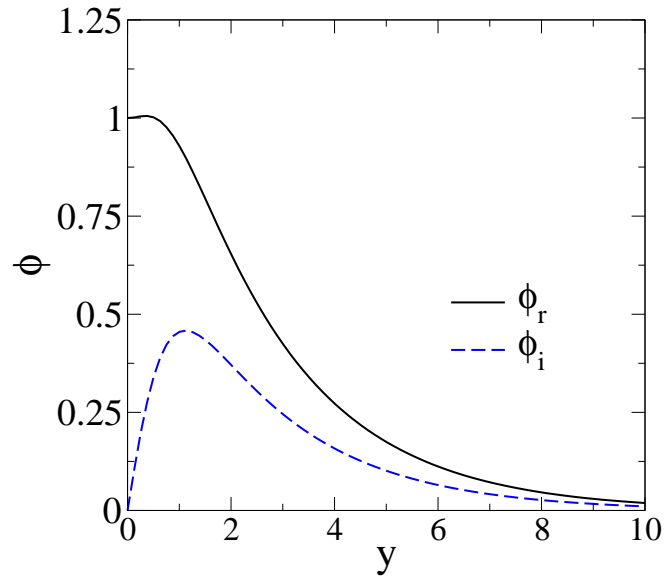


**Figure C.3.** Solution to the Rayleigh equation for the instability amplitude function.

$y < 3$  :

$$\begin{aligned} \phi_r(y) = & -0.005470y^4 + 0.073828y^3 - 0.285178y^2 \\ & + 0.151226y + 0.990538, \end{aligned} \quad (\text{C.32})$$

$$\begin{aligned} \phi_i(y) = & -0.020165y^4 + 0.203970y^3 - 0.741852y^2 \\ & + 1.019843y - 0.009734, \end{aligned} \quad (\text{C.33})$$

$y > 3$  :

$$\phi_r(y) = 1.597986 \exp(-0.442692y), \quad (\text{C.34})$$

$$\phi_i(y) = 0.981717 \exp(-0.453942y). \quad (\text{C.35})$$

The development above follows that of Michalke; however, all of Michalke's relations were rederived for the general case involving  $\Delta U$  and  $\sigma$ , when the solutions were computed. As expected, the results scale in a predictable way. That is,  $\alpha$  does not depend on  $\Delta U$  since this is just a scaling factor applied to the velocity. Also, the value of the eigenvalue  $c_i$  appears as  $c_i/\Delta U$  (when  $\Delta U$  is included), which does not depend on  $\Delta U$ . This is interesting because it shows that the amplification factor (which determines the

rate of growth of the instability) is proportional to  $\Delta U$ . Also, when  $\sigma$  is included,  $\alpha$  appears as  $\alpha/\sigma$ , which is constant for the most unstable mode. This just shows that the period of the waves are scaled as the initial vorticity thickness is scaled. When  $x$  and  $y$  are replaced by  $\sigma y$  and  $\sigma x$  and  $\Delta U$  is inserted instead of using  $\Delta U = 1$ , the total perturbed stream function becomes

$$\psi = \frac{\Delta U}{2\sigma} \ln(\cosh(\sigma y)) + \frac{\Delta U}{2\sigma} \epsilon [\phi_r(\sigma y) \cos(\eta \sigma x) - \phi_i(\sigma y) \sin(\eta \sigma x)]. \quad (\text{C.36})$$

Here, the first term is the base velocity stream function and the second term is the stream function of the perturbation. In this equation,  $\eta = 0.444918$  is the most unstable mode the period is  $P = 2\pi/\eta\sigma$ , and  $\epsilon$  is a small number representing the fraction of the base velocity to add as a perturbation. The velocity components are computed using Eqs. (C.2)-(C.3). In the above equations,  $y$  is centered about zero, and  $x$  begins at zero, so, for general domains, the  $x$  and  $y$  are first centered in applying the relations.

In the DNS simulations, the streamwise domain is equal to the period of the most unstable mode, which then sets the vorticity thickness scaling parameter  $\sigma$ . In this case, only a single vortex will fit in the domain. If the domain is set to be twice the period of the most unstable mode and the above equations used, then two vorticities will form. Experimentally it is known that these vorticities pair up as the flow progresses due to amplification of, primarily, the first subharmonic of the most unstable mode. The pairing process will occur naturally in an experiment or simulation due to the amplification of noise, or numerical error. To speed this process, the first subharmonic of the most unstable mode can be added to the stream function in Eq. (C.36) as a term identical to the second term, but with  $\eta$  becoming  $\eta/2$  and with correspondingly different eigenfunctions  $\phi_r$  and  $\phi_i$ . These functions have similar shapes to those corresponding to  $\eta$  but are stretched along the  $y$ -axis. The curve fits to these functions were also computed and are given by the relations

$y < 3$  :

$$\begin{aligned} \phi_r(y) = & -0.002505y^4 + 0.032325y^3 - 0.138069y^2 \\ & + 0.079256y + 0.993696, \end{aligned} \quad (\text{C.37})$$

$$\begin{aligned} \phi_i(y) = & -0.012930y^4 + 0.155110y^3 - 0.677865y^2 \\ & + 1.166394y - 0.014376, \end{aligned} \quad (\text{C.38})$$

$y > 3$ :

$$\phi_r(y) = 1.231697 \exp(-0.217780y), \quad (\text{C.39})$$

$$\phi_i(y) = 1.061436 \exp(-0.226491y). \quad (\text{C.40})$$

Figures C.4 and C.5 show the resulting velocity profiles and stream functions for the case of  $\sigma = \Delta U = 1$ ,  $\epsilon = 0.1$ , with and without the subharmonic, respectively. In Fig. C.5, the period is twice that of the most unstable mode. The contours of  $\psi$  show that essentially two waves have been overlaid on the initial tanh profile. The two shorter waves will evolve into two vortices, and the longer wave essentially perturbs the left vortex up and the right vortex down, which will result in vortex pairing. The  $v$  velocity contours also illustrate this.

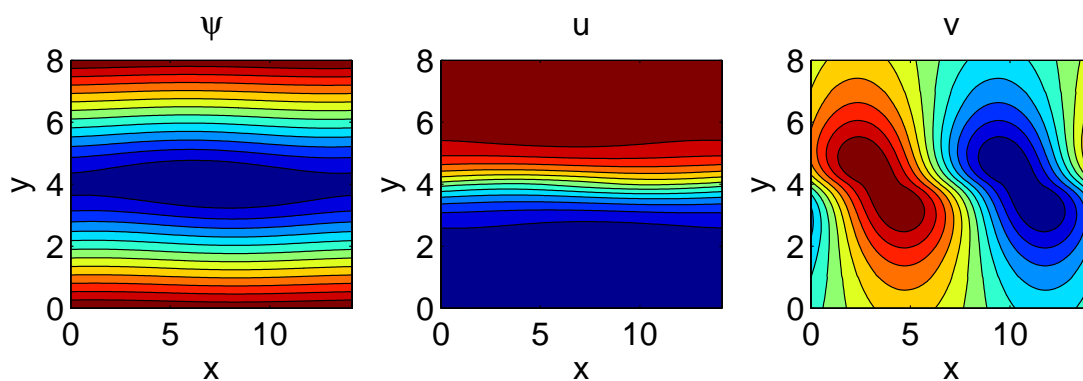


**Figure C.4.** Contour plots of  $\psi$ ,  $u$ , and  $v$ , from left to right, for the case of  $\sigma = 1$ ,  $\Delta U = 1$ ,  $\epsilon = 0.1$ , no subharmonic.

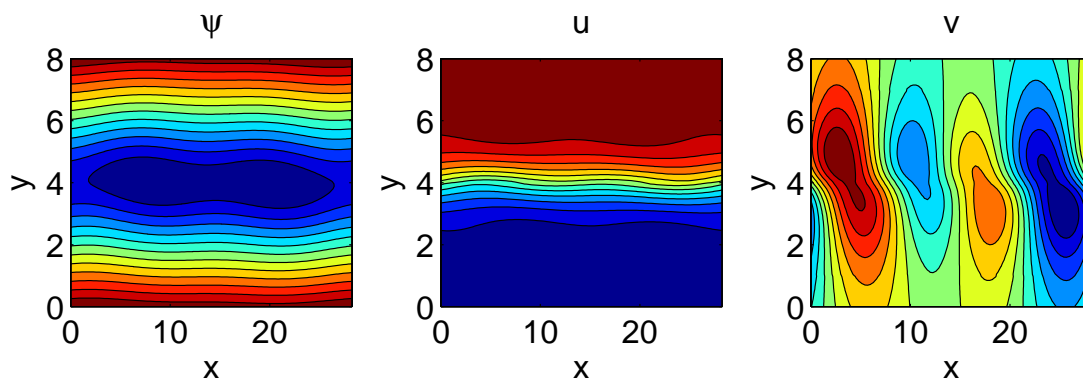


**Figure C.5.** Contour plots of  $\psi$ ,  $u$ , and  $v$ , from left to right, for the case of  $\sigma = 1$ ,  $\Delta U = 1$ ,  $\epsilon = 0.1$ , with the subharmonic.

## APPENDIX D

### DERIVATION OF THE CMC EQUATIONS

There are two approaches to deriving the CMC transport equations. The first is the decomposition method in which scalars are decomposed into a conditional mean and fluctuation [150]. The second method proceeds through the joint PDF transport equation. Here, the latter method is used to derive the CMC equations for soot. The derivation follows the approach given by Klimenko and Bilger [31].

We begin with the fine grain PDF  $\delta(Z - Y(x, t))$ , where  $\delta$  is the Dirac delta function,  $Y(x, t)$  is a random variable, such as a species mass fraction, and  $Z$  is the corresponding sample space variable, which is an independent variable. The derivative of the fine grain PDF is given by

$$\frac{\partial \delta}{\partial t} = -\frac{\partial}{\partial Z} \left( \delta \frac{\partial Y}{\partial t} \right). \quad (\text{D.1})$$

This identity is derived with the following progression (with  $u = Z - Y(x, t)$ ):

$$\begin{aligned} d\delta &= \frac{d\delta}{du} du = \frac{d\delta}{du} \left( \frac{\partial u}{\partial Z} dZ + \frac{\partial u}{\partial Y} dY \right), \\ &= \frac{d\delta}{du} du = \frac{d\delta}{du} \left( \frac{\partial u}{\partial Z} dZ + \frac{\partial u}{\partial Y} \left( \frac{\partial Y}{\partial t} dt + \frac{\partial Y}{\partial x} dx \right) \right), \\ \frac{\partial \delta}{\partial t} &= \frac{d\delta}{du} \left( -\frac{\partial Y}{\partial t} \right). \end{aligned} \quad (\text{D.2})$$

In the last step, the independence of  $t$  and  $Z$  is used. Now, using  $\frac{d\delta}{du} = \frac{\partial \delta}{\partial Z}$  and noting that  $\frac{\partial Y}{\partial t}$  is independent of the derivative with respect to  $Z$  recovers Eq. (D.1) when  $\frac{\partial Y}{\partial t}$  is brought inside the derivative with respect to  $Z$ . The multidimensional fine grain PDF is given by

$$\psi = \prod_i \delta(Z_i - Y_i(x, t)). \quad (\text{D.3})$$

The derivative of  $\psi$  is a straightforward extension of the scalar case:

$$\frac{\partial \psi}{\partial t} = \frac{\partial}{\partial Z_i} \left( \psi \frac{\partial Y_i}{\partial t} \right), \quad (\text{D.4})$$

where index notation is used to imply summation.

The transport equation for species  $Y_i$  is given by

$$\frac{\partial Y_i}{\partial t} = -\mathbf{v} \cdot \nabla Y_i + \frac{1}{\rho} \nabla \cdot (\rho D_i \nabla Y_i) + \frac{1}{\rho} \nabla \cdot (\rho^{-1} D_{T,i} Y_i \nabla \ln T) + \frac{\omega_i}{\rho}. \quad (\text{D.5})$$

In this equation  $D_{T,i}$  is the thermophoretic diffusion coefficient corresponding to species  $i$ , with no implied summation on that term. This equation is good for gaseous species and soot moments with  $Y_i$  a generic notation ( $Y_i$  would be a soot mass-moment divided by density) and  $D_{T,i}$  set to zero to turn off thermophoresis. Equation (D.5) is inserted into Eq. (D.4) to give

$$\frac{\partial \psi}{\partial t} = \frac{\partial}{\partial Z_i} \left( \psi \mathbf{v} \cdot \nabla Y_i - \frac{\psi}{\rho} \nabla \cdot (\rho D_i \nabla Y_i) - \frac{\psi}{\rho} \nabla \cdot (\rho^{-1} D_{T,i} Y_i \nabla \ln T) - \psi \frac{\omega_i}{\rho} \right). \quad (\text{D.6})$$

The divergence of  $\psi$  is defined similarly to Eq. (D.4):

$$\nabla \psi = -\frac{\partial}{\partial Z_i} (\psi \nabla Y_i). \quad (\text{D.7})$$

Also,

$$\mathbf{v} \cdot \nabla \psi = -\frac{\partial}{\partial Z_i} (\psi \mathbf{v} \cdot \nabla Y_i), \quad (\text{D.8})$$

where  $\mathbf{v}$  is independent of  $Z_i$  and is brought inside the derivative. Applying this expression to Eq. (D.6), multiplying by density (which is independent of  $Z_i$ ), and applying continuity give

$$\begin{aligned} \frac{\partial \rho \psi}{\partial t} + \nabla \cdot (\rho \mathbf{v} \psi) &= -\frac{\partial}{\partial Z_i} (\psi \nabla \cdot (\rho D_i \nabla Y_i)) \\ &\quad - \frac{\partial}{\partial Z_i} (\psi \nabla \cdot (\rho^{-1} D_{T,i} Y_i \nabla \ln T)) \end{aligned} \quad (\text{D.9})$$

$$- \frac{\partial}{\partial Z_i} (\psi \omega_i).$$

The first term on the right-hand side (RHS) of this equation, the diffusion term, is reworked into an alternative form. First, in order to apply an identity to the term, the diffusivity needs to be the same for all species. To maintain generality, however, in the present derivation, the diffusivity is assumed to be

$$D_i = D + (D_i - D), \quad (\text{D.10})$$

where  $D$  is the uniform diffusivity. Applying this to Eq. (D.9) amounts to adding and subtracting a term with constant diffusivity. The following substitution is made for the diffusion term in Eq. (D.9):

$$\frac{\partial}{\partial Z_i} (\psi \nabla \cdot (\rho D_i \nabla Y_i)) = \frac{\partial}{\partial Z_i} (\psi \nabla \cdot (\rho D \nabla Y_i)) + \frac{\partial}{\partial Z_i} (\psi \nabla \cdot (\rho (D_i - D) \nabla Y_i)). \quad (\text{D.11})$$

The following identity is applied:

$$\begin{aligned} -\nabla \cdot (\rho D \nabla \psi) &= \frac{\partial}{\partial Z_i} (\nabla \cdot (\psi \rho D \nabla Y_i)), \\ &= \frac{\partial}{\partial Z_i} (\psi \nabla \cdot (\rho D \nabla Y_i)) + \frac{\partial}{\partial Z_i} (\rho D \nabla Y_i \cdot \nabla \psi), \\ &= \frac{\partial}{\partial Z_i} (\psi \nabla \cdot (\rho D \nabla Y_i)) - \frac{\partial}{\partial Z_i} \frac{\partial}{\partial Z_j} (\psi \rho D \nabla Y_i \cdot \nabla Y_j). \end{aligned} \quad (\text{D.12})$$

The first term on the RHS of the last expression matches the first term on the RHS of Eq. (D.11). Substituting the last expression in Eq. (D.12) into Eq. (D.11) and the result into Eq. (D.9) yields

$$\begin{aligned} \frac{\partial \rho \psi}{\partial t} + \nabla \cdot (\rho \mathbf{v} \psi) &= - \frac{\partial}{\partial Z_i} (\psi \omega_i) \\ &\quad - \frac{\partial}{\partial Z_i} (\psi \nabla \cdot (\rho^{-1} D_{T,i} Y_i \nabla \ln T)) \\ &\quad - \frac{\partial}{\partial Z_i} (\psi \nabla \cdot (\rho (D_i - D) \nabla Y_i)) \\ &\quad - \frac{\partial}{\partial Z_i} \frac{\partial}{\partial Z_j} (\psi \rho D \nabla Y_i \cdot \nabla Y_j) \\ &\quad + \nabla \cdot (\rho D \nabla \psi). \end{aligned} \quad (\text{D.13})$$

The last term in this equation is replaced using the identity

$$\nabla \cdot (\nabla(\rho D\psi)) = \nabla \cdot (\rho D\nabla\psi) + \nabla \cdot (\psi\nabla(\rho D)), \quad (\text{D.14})$$

to give

$$\begin{aligned} \frac{\partial \rho\psi}{\partial t} + \nabla \cdot (\rho\mathbf{v}\psi) &= -\frac{\partial}{\partial Z_i}(\psi\omega_i) \\ &\quad - \frac{\partial}{\partial Z_i}(\psi\nabla \cdot (\rho^{-1}D_{T,i}Y_i\nabla \ln T)) \\ &\quad - \frac{\partial}{\partial Z_i}(\psi\nabla \cdot (\rho(D_i - D)\nabla Y_i)) \\ &\quad - \frac{\partial}{\partial Z_i} \frac{\partial}{\partial Z_j}(\psi\rho D\nabla Y_i \cdot \nabla Y_j) \\ &\quad + \nabla \cdot (\nabla(\rho D\psi)) - \nabla \cdot (\psi\nabla(\rho D)). \end{aligned} \quad (\text{D.15})$$

The last line in this equation is considered to be small at high Reynolds number in [31]. The last four terms on the RHS of this equation arise from the diffusion term in Eq. (D.9). Equation (D.15) is convolved over the joint PDF (averaged) to give the joint PDF transport equation. This is done by multiplying by the joint PDF and integrating over the sample space. Use is made of the independence of the sample space variables and commutivity of differentiation and integration. The averaging operation is done as follows:

$$\begin{aligned} \langle \rho\psi \rangle &= \int_{\mathbf{Y}} \int_{\mathbf{\Pi}} \rho\psi(\mathbf{Z} - \mathbf{Y})P(\mathbf{Y}, \mathbf{\Pi})d\mathbf{Y}d\mathbf{\Pi}, \\ &= \int_{\mathbf{Y}} \int_{\mathbf{\Pi}} \rho\psi(\mathbf{Z} - \mathbf{Y})P(\mathbf{\Pi}|\mathbf{Y} = \mathbf{Z})P(\mathbf{Y})d\mathbf{Y}d\mathbf{\Pi}, \\ &= \int_{\mathbf{Y}} \psi(\mathbf{Z} - \mathbf{Y})P(\mathbf{Y}) \left( \int_{\mathbf{\Pi}} \rho P(\mathbf{\Pi}|\mathbf{Y} = \mathbf{Z})d\mathbf{\Pi} \right) d\mathbf{Y}, \\ &= \int_{\mathbf{Y}} \psi(\mathbf{Z} - \mathbf{Y})P(\mathbf{Y})\langle \rho|\mathbf{Y} = \mathbf{Z} \rangle d\mathbf{Y}, \\ &= \langle \rho|\mathbf{Y} = \mathbf{Z} \rangle \int_{\mathbf{Y}} \psi(\mathbf{Z} - \mathbf{Y})P(\mathbf{Y})d\mathbf{Y}, \\ &= \langle \rho|\mathbf{Y} = \mathbf{Z} \rangle P(\mathbf{Z}), \end{aligned} \quad (\text{D.16})$$

where  $\mathbf{\Pi}$  represents the sample space of all dependencies not included in  $\mathbf{Z}$ , and  $\mathbf{Y}$ ,  $\mathbf{Z}$ , and  $\mathbf{\Pi}$  are vector quantities. Averaging Eq. (D.15) gives the joint PDF transport equation:

$$\begin{aligned}
\frac{\partial \langle \rho | \mathbf{Z} \rangle P}{\partial t} + \nabla \cdot (\langle \rho \mathbf{v} | \mathbf{Z} \rangle P) &= - \frac{\partial}{\partial Z_i} (\langle \omega_i | \mathbf{Z} \rangle P) \\
&- \frac{\partial}{\partial Z_i} (\langle \nabla \cdot (\rho^{-1} D_{T,i} Y_i \nabla \ln T) | \mathbf{Z} \rangle P) \\
&- \frac{\partial}{\partial Z_i} (\langle \nabla \cdot (\rho (D_i - D) \nabla Y_i) | \mathbf{Z} \rangle P) \\
&- \frac{\partial}{\partial Z_i} \frac{\partial}{\partial Z_j} (\langle \rho D \nabla Y_i \cdot \nabla Y_j | \mathbf{Z} \rangle P) \\
&+ \nabla^2 (\langle \rho D | \mathbf{Z} \rangle P) - \nabla \cdot (\langle \nabla (\rho D) | \mathbf{Z} \rangle P).
\end{aligned} \tag{D.17}$$

The CMC equation is derived by multiplying Eq. (D.17) by one of the  $Z_i$ , say  $Z_{Y_s}$ , and integrating overall all  $Z_i$  except the mixture fraction sample space variable  $\eta$ , where  $\eta$  is included in  $\mathbf{Z}$ . This is illustrated below for the first term in Eq. (D.17):

$$\begin{aligned}
\int Z_{Y_s} \frac{\partial \langle \rho | \mathbf{Z} \rangle P(\mathbf{Z}', \eta)}{\partial t} d\mathbf{Z}' &= \frac{\partial}{\partial t} \int Z_{Y_s} \langle \rho | \mathbf{Z} \rangle P(\mathbf{Z}', \eta) d\mathbf{Z}', \\
&= \frac{\partial}{\partial t} \int Z_{Y_s} \langle \rho | \mathbf{Z} \rangle P(\mathbf{Z}' | \eta) P(\eta) d\mathbf{Z}', \\
&= \frac{\partial}{\partial t} \left( P(\eta) \int Z_{Y_s} \langle \rho | \mathbf{Z} \rangle P(\mathbf{Z}' | \eta) d\mathbf{Z}' \right), \\
&= \frac{\partial}{\partial t} (\langle \rho Y_s | \eta \rangle P(\eta)).
\end{aligned} \tag{D.18}$$

Here,  $\mathbf{Z}'$  denotes the sample space not including  $\eta$ . There are eight terms in Eq. (D.17). A similar operation as just shown is applied to terms 2, 7, and 8 in Eq. (D.17). Term 3 in the same equation, the reaction source term, is treated as

$$\begin{aligned}
- \int Z_{Y_s} \frac{\partial}{\partial Z_i} (\langle \omega_i | \mathbf{Z} \rangle P) d\mathbf{Z}' &= - \int_{\hat{\mathbf{Z}}} \int_{Z_{Y_s}} Z_{Y_s} \frac{\partial}{\partial \hat{Z}_i} (\langle \omega_i | \mathbf{Z} \rangle P) dZ_{Y_s} d\hat{\mathbf{Z}} \\
&- \int_{\hat{\mathbf{Z}}} \int_{Z_{Y_s}} Z_{Y_s} \frac{\partial}{\partial Z_{Y_s}} (\langle \omega_{Y_s} | \mathbf{Z} \rangle P) dZ_{Y_s} d\hat{\mathbf{Z}} \\
&- \int_{\hat{\mathbf{Z}}} \int_{Z_{Y_s}} Z_{Y_s} \frac{\partial}{\partial \eta} (\langle \omega_\xi | \mathbf{Z} \rangle P) dZ_{Y_s} d\hat{\mathbf{Z}},
\end{aligned} \tag{D.19}$$

where  $\hat{\mathbf{Z}}$  is everything in  $\mathbf{Z}'$  except  $Z_{Y_s}$ . On the left-hand side, integration by parts shows that the first term is zero since  $Z_{Y_s}$  is independent of  $\hat{Z}_i$ . The third term is zero since the

mixture fraction reaction source term is neglected. If the reaction source is not neglected, then the term remains, and the derivative with respect to mixture fraction is moved outside the integration to yield  $\frac{\partial}{\partial \eta}(\langle Y_s \omega_\xi | \eta \rangle P(\eta))$ . Integration by parts is performed on the second term to give

$$- \int Z_{Y_s} \frac{\partial}{\partial Z_i} (\langle \omega_i | \mathbf{Z} \rangle P) d\mathbf{Z}' = \langle \rho \omega_{Y_s} | \eta \rangle P(\eta), \quad (\text{D.20})$$

where a progression similar to Eq. (D.18) has been used. Terms 4 and 5 in Eq. (D.17) are computed similarly to term 3 in Eq. (D.17). In term 5 in Eq. (D.17), if the uniform  $D$  is taken to be  $D_\xi$ , the term becomes

$$\langle \nabla \cdot (\rho(D_s - D_\xi) \nabla Y_s) | \eta \rangle P(\eta). \quad (\text{D.21})$$

If the uniform  $D$  is taken to be  $D_s$ , the term becomes

$$- \frac{\partial}{\partial \eta} (\langle \nabla \cdot (\rho(D_\xi - D_s) \nabla \xi) Y_s | \eta \rangle P(\eta)). \quad (\text{D.22})$$

Equations (D.21) and (D.22) are the analog of the last two terms on the RHS of Eq. (D.19), respectively.

Term 6 in Eq. (D.17) is the most complicated of the terms. The averaging of the term gives

$$- \int Z_{Y_s} \frac{\partial}{\partial Z_i} \frac{\partial}{\partial Z_j} (\langle \rho D \nabla Y_i \cdot \nabla Y_j | \mathbf{Z} \rangle P) d\mathbf{Z}'. \quad (\text{D.23})$$

There are four interesting types of terms that arise from expansion of the summation implied by the index notation. These terms are given by

$$\begin{aligned} & - \int Z_{Y_s} \frac{\partial}{\partial Z_i} \frac{\partial}{\partial Z_j} (\langle \rho D \nabla Y_i \cdot \nabla Y_j | \mathbf{Z} \rangle P) d\mathbf{Z}' = \\ & \quad - \int_{\hat{\mathbf{Z}}} \int_{Z_{Y_s}} Z_{Y_s} \frac{\partial}{\partial \eta} \frac{\partial}{\partial \eta} (\langle \rho D \nabla \xi \cdot \nabla \xi | \mathbf{Z} \rangle P) dZ_{Y_s} d\hat{\mathbf{Z}} \\ & \quad - \int_{\hat{\mathbf{Z}}} \int_{Z_{Y_s}} Z_{Y_s} \frac{\partial}{\partial Z_{Y_s}} \frac{\partial}{\partial Z_{Y_s}} (\langle \rho D \nabla Y_s \cdot \nabla Y_s | \mathbf{Z} \rangle P) dZ_{Y_s} d\hat{\mathbf{Z}} \\ & \quad - \int_{\hat{\mathbf{Z}}} \int_{Z_{Y_s}} Z_{Y_s} \frac{\partial}{\partial Z_{Y_s}} \frac{\partial}{\partial \eta} (\langle 2\rho D \nabla Y_s \cdot \nabla \xi | \mathbf{Z} \rangle P) dZ_{Y_s} d\hat{\mathbf{Z}} \dots \end{aligned} \quad (\text{D.24})$$

$$- \int_{\hat{\mathbf{Z}}} \int_{Z_{Y_s}} Z_{Y_s} \frac{\partial}{\partial \hat{Z}_i} \frac{\partial}{\partial Z_j} (\langle \rho D \nabla Y_i \cdot \nabla Y_j | \mathbf{Z} \rangle P) dZ_{Y_s} d\hat{\mathbf{Z}}.$$

Integrations are carried out over the bounds  $-\infty$  to  $\infty$ , and the PDF is zero at these bounds. The second term on the RHS is zero because of the bounds of integration after integrating by parts. The fourth term is also zero when integrating by parts since  $Z_{Y_s}$  is independent of  $\hat{\mathbf{Z}}$ . In the first term, the derivatives with respect to  $\eta$  are moved outside the integral, and the integration is performed to yield

$$\begin{aligned} - \int_{\hat{\mathbf{Z}}} \int_{Z_{Y_s}} Z_{Y_s} \frac{\partial}{\partial \eta} \frac{\partial}{\partial \eta} (\langle \rho D \nabla Y_i \cdot \nabla Y_j | \mathbf{Z} \rangle P) dZ_{Y_s} d\hat{\mathbf{Z}} = & \quad (D.25) \\ - \frac{\partial^2}{\partial \eta^2} (\langle \rho D (\nabla \xi)^2 Y_s | \eta \rangle P(\eta)). & \end{aligned}$$

In the third term in Eq. (D.24), the derivative with respect to eta is brought outside the integral, and the result is integrated by parts to yield

$$\begin{aligned} - \int_{\hat{\mathbf{Z}}} \int_{Z_{Y_s}} Z_{Y_s} \frac{\partial}{\partial Z_{Y_s}} \frac{\partial}{\partial \eta} (\langle \rho D \nabla Y_i \cdot \nabla Y_j | \mathbf{Z} \rangle P) dZ_{Y_s} d\hat{\mathbf{Z}} = & \quad (D.26) \\ - \frac{\partial}{\partial \eta} (\langle 2\rho D \nabla Y_s \cdot \nabla \xi | \eta \rangle P(\eta)). & \end{aligned}$$

In this equation and Eq. (D.24), the factor of 2 arises from symmetry.

The final result of multiplication of Eq. (D.17) and integrating over  $\mathbf{Z}'$  is given below, when each of the terms are collected (here, the uniform  $D$  is taken as  $D_s$ ):

$$\begin{aligned} \frac{\partial \langle \rho Y_s | \eta \rangle P(\eta)}{\partial t} + \nabla \cdot (\langle \rho Y_s \mathbf{v} | \eta \rangle P(\eta)) = \langle \omega_{Y_s} | \eta \rangle P(\eta) & \quad (D.27) \\ + \langle \nabla \cdot (\rho Y_s D_{T,i} \nabla \ln T) | \eta \rangle P(\eta) & \\ - \frac{\partial}{\partial \eta} (\langle \nabla \cdot [\rho (D_\xi - D_s) \nabla \xi] Y_s | \eta \rangle P(\eta)) & \\ - \frac{\partial^2}{\partial \eta^2} (\langle \rho D_s (\nabla \xi)^2 Y_s | \eta \rangle P(\eta)) & \\ + \frac{\partial}{\partial \eta} (\langle 2\rho D_s (\nabla Y_s \nabla \xi) | \eta \rangle P(\eta)) & \\ + \nabla^2 (\langle \rho D_s Y_s | \eta \rangle P(\eta)) - \nabla \cdot (\langle \nabla (\rho D_s Y_s) | \eta \rangle P(\eta)), & \end{aligned}$$

which is the CMC soot transport equation examined in Chapter 7.

## REFERENCES

- [1] U.S. Department of Energy, Annual Energy Review 2006, DOE/EIA-0384 2006, URL: <http://www.eia.doe.gov/emeu/aer/contents.html>, Posted June 27, 2007.
- [2] S. R. Turns, An Introduction to Combustion, 2nd Edition, McGraw-Hill, New York, 2000.
- [3] H. Bockhorn, Soot Formation in Combustion, Springer-Verlag, Heidelberg, Germany, 1994.
- [4] U.S. Environmental Protection Agency, Air quality criteria for particulate matter, EPA/600/P-99/002aF, October 2004.
- [5] K. M. Leung, R. P. Lindstedt, A simplified reaction mechanism for soot formation in nonpremixed flames, *Combustion and Flame* 87 (1991) 289–305.
- [6] J. H. Kent, A quantitative relationship between soot yield and smoke point measurements, *Combustion and Flame* 63 (1986) 349–358.
- [7] B. Hu, B. Yang, U. O. Koylu, Soot measurements at the axis of an ethylene/air non-premixed turbulent jet flame, *Combustion and Flame* 134 (2003) 93–106.
- [8] N. J. Brown, K. L. Revzan, M. Frenklach, Detailed kinetic modelling of soot formation in ethylene-air mixtures reacting in a perfectly stirred reactor, *Proceedings of the Combustion Institute* 27 (1962) 1573–1580.
- [9] J. Appel, H. Bockhorn, M. Frenklach, Kinetic modelling of soot formation with detailed chemistry and physics: laminar premixed flames of C<sub>2</sub> hydrocarbons, *Combustion and Flame* 121 (2000) 122–136.
- [10] H. Wang, D. X. Du, C. J. Sung, C. K. Law, Experiments and numerical simulation on soot formation in opposed-jet ethylene diffusion flames, *Proceedings of the Combustion Institute* 26 (1996) 2359–2368.
- [11] M. D. Smooke, R. J. Hall, M. B. Colket, J. Fielding, M. B. Long, C. S. McEnally, L. D. Pfefferle, Investigation of the transition from lightly sooting towards heavily sooting co-flow ethylene diffusion flames, *Combustion Theory and Modelling* 8 (2004) 593–606.
- [12] C. R. Shaddix, T. C. Williams, L. G. Blevins, R. W. Schefer, Flame structure of steady and pulsed sooting inverse jet diffusion flames, *Proceedings of the Combustion Institute* 30 (2005) 1501–1508.
- [13] J. H. Kent, D. Honnery, Soot and mixture fraction in turbulent diffusion flames, *Combustion Science and Technology* 54 (1987) 383–397.

- [14] A. Coppalle, D. Joyeux, Temperature and soot volume fraction in turbulent diffusion flames: measurements of mean and fluctuating values, *Combustion and Flame* 96 (1994) 275–285.
- [15] S. J. Brookes, J. B. Moss, Predictions of soot and thermal radiation properties in confined turbulent jet diffusion flames, *Combustion and Flame* 116 (1999) 486–503.
- [16] U. Piomelli, E. Balaras, Wall-layer models for large-eddy simulations, *Annual Review of Fluid Mechanics* 34 (2002) 349–374.
- [17] S. B. Pope, *Turbulent Flows*, Cambridge University Press, New York, 2000.
- [18] U. Piomelli, Large-eddy simulation: achievements and challenges, *Progress in Aerospace Sciences* 35 (1999) 335–362.
- [19] R. L. Panton, *Incompressible Flow*, 2nd Edition, Wiley-Interscience, New York, 1997.
- [20] N. Peters, *Turbulent Combustion*, Cambridge University Press, Cambridge, United Kingdom, 2000.
- [21] L. D. Smoot, P. J. Smith, *Coal Combustion and Gasification*, Plenum Publishing Corp., New York, 1985.
- [22] S. B. Pope, PDF methods for turbulent reactive flows, *Progress in Energy and Combustion Science* 11 (1985) 119–192.
- [23] R. O. Fox, *Computational Models for Turbulent Reacting Flows*, Cambridge University Press, Cambridge, United Kingdom, 2003.
- [24] N. Peters, Local quenching due to flame stretch and non-premixed turbulent combustion, *Combustion Science and Technology* 30 (1983) 1–17.
- [25] N. Peters, Laminar diffusion flamelet models in non-premixed turbulent combustion, *Progress in Energy and Combustion Science* 10 (1984) 319–339.
- [26] A. W. Cook, J. J. Riley, G. Kosaly, A laminar flamelet approach to subgrid-scale chemistry in turbulent flows, *Combustion and Flame* 109 (1997) 332–341.
- [27] E. Effelsberg, N. Peters, Scalar dissipation rates in turbulent jets and jet diffusion flames, *Proceedings of the Combustion Institute* 22 (1988) 693–700.
- [28] X. S. Bai, M. Balthasar, F. Mauss, L. Fuchs, Detailed soot modeling in turbulent jet diffusion flames, *Proceedings of the Combustion Institute* 27 (1998) 1623–1630.
- [29] H. Pitsch, M. Chen, N. Peters, Unsteady flamelet modelling of turbulent hydrogen-air diffusion flames, *Proceedings of the Combustion Institute* 27 (1998) 1057–1064.
- [30] H. Pitsch, E. Riesmeier, N. Peters, Unsteady flamelet modelling of soot formation in turbulent diffusion flames, *Combustion Science and Technology* 158 (2000) 389–406.
- [31] A. Y. Klimenko, R. W. Bilger, Conditional moment closure for turbulent combustion, *Progress in Energy and Combustion Science* 25 (1999) 595–687.

- [32] A. Kronenburg, R. W. Bilger, J. H. Kent, Modeling soot formation in turbulent methane-air jet diffusion flames, *Combustion and Flame* 121 (2000) 24–40.
- [33] P. Bushan, P. Smith, A systematic evaluation of nox formation pathways and subgrid scale models in turbulent nonpremixed CO/H<sub>2</sub>/N<sub>2</sub> jet flame predictions, Proceedings of IMECE04, ASME International Mechanical Engineering Congress and Expo.
- [34] C. D. Pierce, P. Moin, Progress-variable approach for large-eddy simulation of non-premixed turbulent combustion, *Journal of Fluid Mechanics* 504 (2004) 73–97.
- [35] D. P. N. Nguyen, Lower dimensional manifold (LDM) reaction modelling applied to turbulent combustion simulations, Ph.D. thesis, University of Utah (2003).
- [36] U. Maas, S. B. Pope, Simplifying chemical kinetics: intrinsic low-dimensional manifolds in composition space, *Combustion and Flame* 88 (1992) 239–264.
- [37] P. A. McMurtry, W. H. Jou, J. J. Riley, R. W. Metcalfe, Direct numerical simulations of a reacting mixing layer with chemical heat release, *AIAA Journal* 24 (1985) 962–970.
- [38] T. Echekki, A. R. Kerstein, T. D. Dreeben, One-dimensional turbulence simulation of turbulent jet diffusion flames: model formulation and illustrative applications, *Combustion and Flame* 125 (2001) 1083–1105.
- [39] S. M. Jeng, L. D. Chen, G. M. Faeth, The structure of bouyant methane and propane diffusion flames, *Proceedings of the Combustion Institute* 19 (1982) 349–358.
- [40] J. P. Gore, U. S. IP, Y. R. Sivathanu, Coupled structure and radiation analysis of acetylene/air flames, *Journal of Heat Transfer-Transactions of the ASME* 114 (1992) 487–493.
- [41] K. J. Young, J. B. Moss, Modelling sooting turbulent jet flames using an extended flamelet technique, *Combustion Science and Technology* 105 (1995) 33–53.
- [42] N. W. Bressloff, J. B. Moss, P. A. Rubini, CFD prediction of coupled radiation heat transfer and soot production in turbulent flames, *Proceedings of the Combustion Institute* 26 (1996) 2379–2386.
- [43] Z. Yan, G. Holmstedt, Three-dimensional computation of heat transfer from flames between vertical parallel walls, *Combustion and Flame* 117 (1999) 574–588.
- [44] D. Morvan, B. Porterie, J. C. Loraud, M. Larini, A numerical investigation of cross wind effects on a turbulent buoyant diffusion flame, *Combustion Science and Technology* 164 (2001) 1–35.
- [45] T. M. Gruenberger, M. Moghiman, P. J. Bowen, N. Syred, Dynamics of soot formation by turbulent combustion and thermal decomposition of natural gas, *Combustion Science and Technology* 174 (2002) 67–86.
- [46] A. S. Dederichs, M. Balthasar, F. Mauss, Modelling of NO<sub>x</sub> and soot formation in diesel combustion, *Oil and Gas Science and Technology* 54 (1999) 245–249.

- [47] M. Balthasar, A. Heyl, F. Mauß, F. Schmitt, H. Bockhorn, Flamelet modelling of soot formation in laminar ethyne/air diffusion flames, *Proceedings of the Combustion Institute* 26 (1996) 2369–2377.
- [48] L. Wang, D. C. Haworth, S. R. Turns, M. F. Modest, Interactions among soot, thermal radiation, and  $\text{NO}_x$  emissions in oxygen-enriched turbulent nonpremixed flames: a computational fluid dynamics modelling study, *Combustion and Flame* 141 (2005) 170–179.
- [49] P. E. Desjardin, S. H. Frankel, Two-dimensional large eddy simulation of soot formation in the near-field of a strongly radiating nonpremixed acetylene-air turbulent jet flame, *Combustion and Flame* 119 (1999) 121–132.
- [50] R. P. Lindstedt, S. A. Louloudi, Joint-scalar transported PDF modeling of soot formation and oxidation, *Proceedings of the Combustion Institute* 30 (2005) 775–783.
- [51] C. S. Yoo, H. G. Im, Transient soot dynamics in turbulent nonpremixed ethylene-air counterflow flames, *Proceedings of the Combustion Institute* 31 (2007) 701–708.
- [52] J. H. Ferziger, *Computational Methods for Fluid Dynamics*, 3rd Edition, Springer Verlag, Heidelberg, Germany, 2002.
- [53] S. Candel, D. Thevenin, N. Darabiha, D. Veynante, *Progress in numerical combustion*, *Combustion Science and Technology* 149 (1999) 297–337.
- [54] S. Mahalingam, J. H. Chen, L. Vervisch, Finite-rate chemistry and transient effects in direct numerical simulations of turbulent nonpremixed flames, *Combustion and Flame* 102 (1995) 285–297.
- [55] N. D. Sandham, Introduction to direct numerical simulation, in: B. Launder, N. Sandham (Eds.), *Closure strategies for turbulent and transitional flows*, Cambridge University Press, 2002, Ch. 7, pp. 248–266.
- [56] R. Peyret, *Spectral Methods for Incompressible Viscous Flow*, Springer Verlag, Heidelberg, Germany, 2000.
- [57] J. C. Sutherland, Evaluation of mixing and reaction models for large-eddy simulation of nonpremixed combustion using direct numerical simulation, Ph.D. thesis, University of Utah (2004).
- [58] L. Vervisch, Using numerics to help the understanding of non-premixed turbulent flames, *Proceedings of the Combustion Institute* 28 (2000) 11–24.
- [59] R. Hilbert, F. Tap, H. El-Rabii, D. Thevenin, Impact of detailed chemistry and transport models on turbulent combustion simulations, *Progress in Energy and Combustion Science* 30 (2004) 61–117.
- [60] L. Vervisch, T. Poinso, Direct numerical simulation of non-premixed turbulent flames, *Annual Review of Fluid Mechanics* 30 (1998) 655–691.
- [61] R. Taylor, R. Krishna, *Multicomponent Mass Transfer*, John Wiley and Sons, Inc., New York, 1993.

- [62] P. Givi, C. K. Madnia, C. J. Steinberger, M. H. Carpenter, J. P. Drummond, Effects of compressibility and heat release in a high speed reacting mixing layer, *Combustion Science and Technology* 78 (1991) 33–67.
- [63] R. S. Miller, C. K. Madnia, P. Givi, Structure of a turbulent reacting mixing layer, *Combustion Science and Technology* 99 (1994) 1–36.
- [64] A. D. Leonard, J. C. Hill, Scalar dissipation and mixing in turbulent reacting flows, *Physics of Fluids A* 3 (5) (1991) 1286.
- [65] W. E. Mell, V. Nilsen, G. Kosaly, J. J. Riley, Direct numerical simulation investigation of the conditional moment closure model for nonpremixed turbulent reacting flows, *Combustion Science and Technology* 91 (1993) 179–186.
- [66] C. J. Montgomery, G. Kosaly, J. J. Riley, Direct numerical simulation of turbulent reacting flow using a reduced hydrogen-oxygen mechanism, *Combustion and Flame* 95 (1993) 247–260.
- [67] Y. Y. Lee, S. B. Pope, Nonpremixed turbulent reacting flow near extinction, *Combustion and Flame* 101 (1995) 501–528.
- [68] F. A. Jaber, R. S. Miller, F. Mashayek, P. Givi, Differential diffusion in binary scalar mixing and reaction, *Combustion and Flame* 109 (1997) 561–577.
- [69] W. K. Bushe, R. W. Bilger, Direct numerical simulation of turbulent non-premixed combustion with realistic chemistry, in: *Center for Turbulence Research, Annual Research Briefs*, 1998.
- [70] C. J. Montgomery, G. Kosaly, J. J. Riley, Direct numerical solution of turbulent nonpremixed combustion with multistep hydrogen-oxygen kinetics, *Combustion and Flame* 109 (1997) 113–144.
- [71] D. Thevenin, E. van Kalmthout, S. Candel, Two-dimensional direct numerical simulations of turbulent diffusion flames using detailed chemistry, in: J. P. Chollet, P. R. Voke, L. Kleiser (Eds.), *Direct and large eddy simulation II*, Dordrecht: Kluwer Academic Publishers, 1997, pp. 343–354.
- [72] R. Hilbert, F. Tap, D. Veynante, D. Thevenin, A new modelling approach for the autoignition of a nonpremixed turbulent flame using DNS, *Proceedings of the Combustion Institute* 29 (2002) 2079–2085.
- [73] M. Baum, T. J. Poinso, D. C. Haworth, N. Darabiha, Direct numerical simulation of  $H_2$ - $O_2$ - $N_2$  flames with complex chemistry in two-dimensional turbulent flows, *Journal of Fluid Mechanics* 28 (1994) 1–32.
- [74] E. Van Kalmouth, D. Veynante, Direct numerical simulations analysis of flame surface density models for nonpremixed combustion, *Physics of Fluids* 10 (9) (1998) 2347.
- [75] B. Bedat, F. N. Egolfopoulos, T. Poinso, Direct numerical simulation of heat release and  $NO_x$  formation in turbulent nonpremixed flames, *Combustion and Flame* 119 (1999) 69–83.

- [76] S. Sreedhara, K. N. Lakshminisha, Autoignition in a nonpremixed medium: DNS studies on the effects of three-dimensional turbulence, *Proceedings of the Combustion Institute* 29 (2002) 2067–2077.
- [77] D. Thevenin, O. Gicquel, J. de Charentrenay, R. Hilbert, D. Veynante, Two- versus three-dimensional direct simulations of turbulent methane flame kernels using realistic chemistry, *Proceedings of the Combustion Institute* 29 (2002) 2031–2039.
- [78] Y. Mizobuchi, S. Tachibana, J. Shinio, S. Ogawa, A numerical analysis of the structure of a turbulent hydrogen jet lifted flame, *Proceedings of the Combustion Institute* 29 (2002) 2009–2015.
- [79] C. Pantano, S. Sarkar, F. A. Williams, Mixing of a conserved scalar in a turbulent reacting shear layer, *Journal of Fluid Mechanics* 481 (2003) 291–328.
- [80] R. Sankaran, E. R. Hawkes, J. H. Chen, T. Lu, C. K. Law, Structure of a spatially developing turbulent lean methane-air bunsen flame, *Proceedings of the Combustion Institute* 31 (2007) 1291–1298.
- [81] E. R. Hawkes, R. Sankaran, J. C. Sutherland, J. H. Chen, Scalar mixing in direct numerical simulations of temporally-evolving plane jet flames with detailed CO/H<sub>2</sub> kinetics, *Proceedings of the Combustion Institute* 31 (2007) 1633–1640.
- [82] C. S. Yoo, J. H. Chen, R. Sankaran, Direct numerical simulation of a turbulent lifted hydrogen-air jet flame in heated coflow, in: D. Roekaerts (Ed.), *Computational Combustion, ECCOMAS Thematic Conference, Delft, The Netherlands, 2007*.
- [83] C. A. Kennedy, M. H. Carpenter, R. M. Lewis, Low-storage, explicit runge-kutta schemes for the compressible navier-stokes equations, *Applied Numerical Mathematics* 35 (3) (2000) 177–219.
- [84] C. A. Kennedy, M. H. Carpenter, A comparison of several new numerical methods for the simulation of compressible shear layers, *Applied Numerical Mathematics* 14 (4) (1994) 397–433.
- [85] J. C. Sutherland, C. A. Kennedy, Improved boundary conditions for viscous reacting compressible flows, *Journal of Computational Physics* 191 (2003) 502–524.
- [86] R. J. Kee, F. M. Rupley, J. A. Miller, Chemkin, Reaction Design, Inc., San Diego CA (2000).
- [87] R. J. Kee, G. Dixon-Lewis, J. Warnatz, M. E. Coltrin, J. A. Miller, H. K. Moffat, Transport, Reaction Design, Inc., San Diego CA (2000).
- [88] H. Lomax, T. H. Pulliam, D. W. Zingg, *Fundamentals of Computational Fluid Dynamics*, Springer Verlag, Heidelberg, Germany, 2004.
- [89] S. H. Lam, D. A. Goussis, Understanding complex chemical kinetics with computational singular perturbation, *Proceedings of the Combustion Institute* 22 (1988) 931–941.
- [90] J. C. Keck, Rate-controlled constrained-equilibrium theory of chemical reactions in complex systems, *Progress in Energy and Combustion Science* 16 (1990) 125–154.

- [91] T. Lu, C. K. Law, A directed relation graph method for mechanism reduction, *Proceedings of the Combustion Institute* 30 (2005) 1333–1341.
- [92] N. J. Brown, G. Li, M. L. Koszykowski, Mechanism reduction via principal component analysis, *International Journal of Chemical Kinetics* 29 (6) (1997) 393–414.
- [93] J. F. Griffiths, Reduced kinetic models and their application to practical combustion systems, *Progress in Energy and Combustion Science* 21 (1995) 25–107.
- [94] D. O. Lignell, J. H. Chen, P. J. Smith, T. Lu, C. K. Law, The effect of flame structure on soot formation and transport in turbulent nonpremixed flames using direct numerical simulation, *Combustion and Flame* 151 (1-2) (2007) 2–28.
- [95] Z. Qin, V. V. Lissianski, H. Yang, W. C. Gardiner, S. G. Davis, H. Wang, Combustion chemistry of propane: a case study of detailed reaction mechanism optimization, *Proceedings of the Combustion Institute* 28 (2000) 1663–1669.
- [96] T. Lu, Y. Ju, C. K. Law, Complex CSP for chemistry reduction and analysis, *Combustion and Flame* 126 (1-2) (2001) 1445–1455.
- [97] T. Lu, C. K. Law, On the applicability of direction relation graph to the reduction of reaction mechanisms, *Combustion and Flame* 146 (3) (2006) 472–483.
- [98] C. K. Westbrook, F. L. Dryer, Simplified reaction mechanisms for the oxidation of hydrocarbon fuels in flames, *Combustion Science and Technology* 27 (1981) 31–43.
- [99] Personal communication with Chun Sang Yoo, Sandia National Laboratories, Livermore, CA, March, 2006.
- [100] I. M. Kennedy, Models of soot formation and oxidation, *Progress in Energy and Combustion Science* 23 (1997) 95–132.
- [101] B. S. Haynes, H. G. Wagner, Soot formation, *Progress in Energy and Combustion Science* 7 (4) (1981) 229–273.
- [102] I. Glassman, Soot formation in combustion processes, *Proceedings of the Combustion Institute* 22 (1988) 295–311.
- [103] S. K. Friedlander, *Smoke Dust and Haze: Fundamentals of Aerosol Behavior*, 1st Edition, John Wiley and Sons, New York, 1977.
- [104] M. D. Smooke, C. S. McEnally, L. D. Pfefferle, Computational and experimental study of soot formation in a coflow, laminar diffusion flame, *Combustion and Flame* 117 (1999) 117–139.
- [105] S. E. Pratsinis, Simultaneous nucleation, condensation, and coagulation in aerosol reactors, *Journal of Colloid and Interface Science* 124 (2) (1987) 416–427.
- [106] M. Frenklach, S. J. Harris, Aerosol dynamics modeling using the method of moments, *Journal of Colloid and Interface Science* 118 (1) (1987) 252–261.
- [107] R. McGraw, Description of aerosol dynamics by the quadrature method of moments, *Aerosol Science and Technology* 25 (1997) 255–265.

- [108] H. M. Hulburt, S. Katz, Some problems in particle technology, *Chemical Engineering Science* 19 (1964) 555–574.
- [109] B. Zhao, Z. Yang, J. Wang, M. V. Johnston, H. Wang, Analysis of soot nanoparticles in a laminar premixed ethylene flame by scanning mobility particle sizer, *Aerosol Science and Technology* 37 (2003) 611–620.
- [110] W. H. Press, S. A. Teukolsky, W. T. Vetterling, B. P. Flannery, *Numerical Recipes in Fortran 77: The Art of Scientific Computing*, Press Syndicate of the University of Cambridge, New York, 1997.
- [111] R. G. Gordon, Error bounds in equilibrium statistical mechanics, *Journal of Mathematical Physics* 9 (5) (1968) 655–663.
- [112] S. Vemury, S. E. Pratsinis, Self-preserving size distributions of agglomerates, *Journal of Aerosol Science* 26 (2) (1995) 175–185.
- [113] P. R. Lindstedt, Simplified soot nucleation and surface growth steps for non-premixed flames, in: H. Bockhorn (Ed.), *Soot Formation in Combustion*, Springer-Verlag, New York, 1994, pp. 417–441.
- [114] L. R. Petzold, A description of dassl: A differential/algebraic system solver, Tech. Rep. SAND82-8637, Sandia National Laboratories, Livermore, CA (1982).
- [115] R. J. Kee, F. M. Rupley, J. A. Miller, Chemkin-II: A fortran chemical kinetics package for the analysis of gas-phase chemical kinetics, Tech. Rep. SAND89-8009B, Sandia National Laboratories (1991).
- [116] C. M. Ho, P. Huerre, Perturbed free shear layers, *Annual Review of Fluid Mechanics* 16 (1984) 365–424.
- [117] P. Givi, Model-free simulations of turbulent reactive flows, *Progress in Energy and Combustion Science* 15 (1989) 1–107.
- [118] L. M. Pickett, J. B. Ghandhi, Structure of a reacting hydrocarbon-air planar mixing layer, *Combustion and Flame* 132 (2003) 138–156.
- [119] L. M. Pickett, J. B. Ghandhi, Combustion generated instabilities in a hydrocarbon-air planar mixing layer, *Combustion and Flame* 129 (2002) 324–341.
- [120] R. W. Bilger, S. H. Starner, R. J. Kee, On reduced mechanisms for methane-air combustion in nonpremixed flames, *Combustion and Flame* 80 (2) (1990) 135–149.
- [121] N. T. Clemens, P. H. Paul, Effects of heat release on the near field flow structure of hydrogen jet diffusion flames, *Combustion and Flame* 102 (1995) 271–284.
- [122] U. Vandsburger, I. Kennedy, I. Glassman, Sooting counterflow diffusion flames with varying oxygen index, *Combustion Science and Technology* 39 (1984) 263–285.
- [123] C. R. Kaplan, C. R. Shaddix, K. C. Smyth, Computations of enhanced soot production in time-varying CH<sub>4</sub>/air diffusion flames, *Combustion and Flame* 106 (1996) 392–405.

- [124] J. Du, R. L. Axelbaum, The effect of flame structure on soot-particle inception in diffusion flames, *Combustion and Flame* 100 (1995) 367–375.
- [125] J. Du, R. L. Axelbaum, C. K. Law, The influence of carbon dioxide and oxygen as additives on soot formation in diffusion flames, *Proceedings of the Combustion Institute* 23 (1990) 1501–1507.
- [126] A. Atreya, C. Zhang, H. K. Kim, T. Shamim, J. Suh, The effect of changes in the flame structure on the formation and destruction of soot and NO in radiating diffusion flames, *Proceedings of the Combustion Institute* 26 (1996) 2181–2189.
- [127] K. C. Lin, G. M. Faeth, Effects of hydrodynamics on soot formation in laminar opposed-jet diffusion flames, *Journal of Propulsion and Power* 12 (4) (1996) 691–698.
- [128] B. H. Chao, S. Liu, R. L. Axelbaum, On soot inception in nonpremixed flames and the effects of flame structure, *Combustion Science and Technology* 138 (1998) 105–135.
- [129] K. T. Kang, J. Y. Hwang, S. H. Chung, Soot zone structure and sooting limit in diffusion flames: comparison of counterflow and coflow flames, *Combustion and Flame* 109 (1997) 266–281.
- [130] J. Y. Hwang, S. H. Chung, Growth of soot particles in counterflow diffusion flames of ethylene, *Combustion and Flame* 125 (2001) 752–762.
- [131] T. Passot, A. Pouquet, Numerical simulation of compressible homogeneous flows in the turbulent regime, *Journal of Fluid Mechanics* 181 (1987) 441–466.
- [132] C. H. Gibson, Fine structure of scalar fields mixed by turbulence. I Zero-gradient points and minimal gradient surfaces, *Physics of Fluids* 11 (1968) 2305–2315.
- [133] S. B. Pope, The evolution of surfaces in turbulence, *International Journal of Engineering Sciences* 26 (5) (1988) 445–469.
- [134] T. Echekki, J. H. Chen, Analysis of the contribution of curvature to premixed flame propagation, *Combustion and Flame* 118 (1999) 308–311.
- [135] W. Kollmann, J. H. Chen, Dynamics of the flame surface area in turbulent non-premixed combustion, *Proceedings of the Combustion Institute* 25 (1994) 1091–1098.
- [136] H. Guo, F. Liu, G. J. Smallwood, Soot and NO formation in counterflow ethylene/oxygen/nitrogen diffusion flames, *Combustion Theory and Modelling* 8 (2004) 475–489.
- [137] K. G. Neoh, J. B. Howard, A. F. Sarofim, Soot oxidation in flames, in: D. C. Siegla, G. W. Smith (Eds.), *Particulate Carbon: Formation During Combustion*, Plenum Pub Corp, New York, 1981, pp. 261–282.
- [138] D. Bradley, G. Dixon-Lewis, S. E. Habik, E. M. Mushi, The oxidation of graphite powder in flame reaction zone, *Proceedings of the Combustion Institute* 20 (1984) 931.

- [139] J. Nagle, R. F. Strickland-Constable, Oxidation of carbon between 1000-2000 °C, Proc. of the 5th Carbon Conference 1 (1962) 154–164.
- [140] H. Pitsch, N. Peters, A consistent flamelet formulation for non-premixed combustion considering differential diffusion effects, Combustion and Flame 114 (1998) 26–40.
- [141] L. K. Su, N. T. Clemens, The structure of fine-scale scalar mixing in gas-phase planar turbulent jets, Journal of Fluid Mechanics 488 (2003) 1–29.
- [142] H. Koseki, Combustion properties of large liquid pool fires, Fire Technology 25 (1989) 241–255.
- [143] A. N. Karpetis, R. S. Barlow, Measurements of flame orientation and scalar dissipation in turbulent partially premixed methane flames, Proceedings of the Combustion Institute 30 (2005) 665–672.
- [144] C. H. Gibson, Turbulence in the ocean, atmosphere, galaxy, and universe, Applied Mechanical Review 49 (1996) 299–315.
- [145] A. Kronenburg, R. W. Bilger, Modelling of differential diffusion effects in non-premixed nonreacting turbulent flow, Physics of Fluids 9 (1997) 1435–1447.
- [146] J. C. Hewson, A. J. Ricks, S. R. Tieszen, A. R. Kerstein, R. O. Fox, Conditional moment closure with differential diffusion for soot evolution in fire, in: Center for Turbulence Research, Proceedings of the Summer Program, 2006.
- [147] A. Beltrame, P. Porshnev, W. Merchan-Merchan, A. Saveliev, A. Fridman, L. Kennedy, Soot and NO formation in methane-oxygen enriched diffusion flames, Combustion and Flame 124 (2001) 295–310.
- [148] A. Heyl, H. Bockhorn, Flamelet modeling of NO formation in laminar and turbulent diffusion flames, Chemosphere 42 (2001) 449–462.
- [149] V. Gopalakrishnan, J. Abraham, Computed NO and soot distribution in turbulent transient jets under diesel conditions, Combustion Science and Technology 176 (2004) 603–641.
- [150] R. W. Bilger, Conditional moment closure for turbulent reacting flow, Physics of Fluids A 5 (1993) 436–444.
- [151] A. Kronenburg, M. Kostka, Modeling extinction and reignition in turbulent flames, Combustion and Flame 143 (2005) 342–356.
- [152] A. Michalke, Instability of the hyperbolic-tangent velocity profile, Journal of Fluid Mechanics 19 (1964) 543–556.